J. Astrophys. Astr. (1998) **19**, 1–18

Individual and Integrated Pulse Properties of PSR B0943+10 Involved in the Mode-Changing Phenomenon

Svetlana A. Suleymanova & Vera A. Izvekova, *Pushchino Radio Astronomy Observatory, P. N. Lebedev Physical Institute, Russian Academy of Sciences, Leninski Prospect, 53 Moscow 117924, Russia*

Joanna M. Rankin, *Department of Physics, University of Vermont, Burlington, VT 05405, USA*

N. Rathnasree, *Raman Research Institute, Sadashivanagar, Bangalore 560 080, India*

Received 1997 June 24; accepted 1997 December 17

Abstract. The characteristics of the "burst" (B) mode and "quiescent" (Q) mode pulse sequences—long known from studies at or below 103 MHz—are identified at 430 MHz for the first time. An 18-minute, Polarimetrie observation begins with a long Bmode sequence, which has a higher average intensity, regular drifting subpulses, and a preponderance of primary polarisationmode radiation. An abrupt transition to a Q-mode sequence is then marked by **a**) weaker average intensity, but occasional very bright individual subpulses, **b**) a complete cessation of drifting subpulses, with disorganized subpulses now being emitted over a much wider longitude interval, and **c**) near parity between the primary and secondary polarisation modes, resulting in pronounced depolarisation, both of individual pulses and the average profile.

Careful study, however, of profile changes before and after this mode change reveals slower variations which both anticipate the abrupt transition and respond to it. A slow attenuation of the intensity level of the dominant component is observed throughout the duration of the B-mode sequence, which then accelerates with the onset of the Q-mode sequence. This slow variation appears to represent a "preswitching transition" process; and the combination of effects on slow and abrupt time scales are finally responsible for the formation of the characteristic B and Q-mode average profiles.

Key words. Pulsars—B0943+10—mode changing—polarisation.

1. Introduction

Much of what is known about PSR B0943+10—including its discovery—has resulted from meter-wavelength observations at the Pushchino Observatory.[1] The remarkable burstlike emission attracted early attention (Vitkevich *et al.* 1969), and subsequent observations at 103 and 62 MHz first identified the two distinct average-profile forms associated with its more intensive burstlike (B) mode and "quiescent" (Q) mode (Suleymanova & Izvekova 1984)[2] Linear polarisation studies, on both an average and individualpulse basis, have also been carried out at the Pushchino Observatory at 103 MHz and below, by analyzing the spectral variations of 0943+10's Faradayrotated signal (Suleymanova *et al.* 1988; Suleymanova 1989).

Pulsar 0943+10 shows most of the properties which Bartel *et al.* (1982) have identified as characteristic of the "mode switching" phenomenon as follows:

- The components of its integrated pulse profile change their relative intensity, and the transformation of its double-resolved B-mode profile into an unresolved double in the Q-mode entails alterations in the longitudinal spacing of its components.
- The changes in 0943+10's integrated profile are accompanied by changes in the character of its subpulse-drift behaviour. The highly regular drift pattern with a P_3 value of about 2.1 cycles/period (Taylor & Huguenin 1971; Backer *et al.* 1975; Sieber & Oster 1975; Suleymanova & Izvekova 1984) is characteristic of the B-mode. On the other hand, observations at 103 MHz have shown no such feature in the Q-mode fluctuation spectrum (Suleymanova & Izvekova 1984).
- The fractional linear polarisation of the weaker Q-mode integrated profile is generally less than that of the B-mode.
- The mode switching occurs simultaneously at different frequencies—that is, at 40 and 103 MHz (this paper).
- In addition to these other characteristics, it is worth noting that the pulsar is nearly unique in exhibiting comparable lifetimes in its respective B and Q modes.

Helfand *et al.* (1975) have pointed out that "mode switching" pulsars are similar in being relatively old—that is, with periods $P>0.7$ s and characteristic ages $\tau = P/2P > 2.8 \times 10^6$yrs. With a period of 1.097 s and a τ of 4.9×10^6 yrs, pulsar 0943+10 is thus typical of this class.

All of these features, except the drifting behaviour, pertain to the integrated profile. We know rather little about how the mode-switching phenomenon is manifested on rotational-period time scales, so studies of long individual-pulse sequences are important for extending the range of our understanding. Unfortunately, observations at the Pushchino Observatory are limited to a few minutes duration by the transit

[1] The pulsar's unusually steep spectrum makes it both one of the strongest pulsars at low frequency and difficult to observe at higher frequencies. To our knowledge the pulsar has never been detected above about 600 MHz (Cornelia 1971), and we know of no published profiles at frequencies higher than 430 MHz. That one published by Rankin & Benson (1981) is typical of those at decimeter wavelengths; it has the simplest form and was classified as conal single (S_d) by Rankin (1986, 1993a, b). The extreme tangential traverse of our sightline through this pulsar's conal beam supports this classification and furthermore argues that it would ultimately miss the pulsar's beam at high enough frequency—a circumstance which goes far toward explaining its very steep spectrum.

[2] The designations of the two modes follow those given by Fowler *et al.* (1981) in discussing pulsar B1822–09.

nature of its BSA and DKR1000 instruments. Consequently, Pushchino observers are almost never able to "catch" the pulsar in the process of switching between its two modes, since the modal lifetime is estimated to be typically half an hour (Suleymanova & Izvekova 1984).[3]

Individualpulse polarimetry at 430 MHz of modest quality was carried out at Arecibo Observatory in 1974, and much improved observations at this frequency were conducted in October 1992. Fortunately, although pulsar 0943+10 is generally rather weak at this frequency, it exhibits periods of enhanced intensity, due to some combination of scintillation and intrinsic causes. Both observations were recorded during such "bursts", and the latter 18minute, fully Polarimetric observation—recorded when the pulsar was particularly bright—has been analyzed to compare with 103-MHz Pushchino observations.

Comparison of the 430- and 103-MHz observations has made it possible to —

(**a**) Identify 0943+10's two distinct emission modes in the 430MHz sequence of pulses for the first time. Groups of pulses at the higher frequency were found which appear analogous to those which constitute the characteristic B- and Q-mode profiles observed at and below 103 MHz, where a large body of observational data is at our disposal.

(**b**) Make both average and individualpulse polarisation measurements of pulse sequences belonging to the two distinct modes. Individualpulse polarimetry at 430 MHz, together with that at 103 MHz, has shown marked changes in the frequency of occurrence of the linear polarisation angle (PA). These polarization variations, together with alterations in the overall intensity, determine the structure and polarisation of the average profile.

(**c**) Study both rapid and slow variations in the intensity of individual pulses involved in the mode-switching process. One of the most salient characteristics of the mode-changing phenomenon is its rapid switching time—on the order of a pulsar period or less. Only in the case of one observation of one pulsar, PSR B0355+54, has evidence for a slower modal transition been suggested—there, a 12-minute onset of the abnormal mode at 11-cm wavelength (Morris *et al.* 1980).

The Arecibo observations of PSR 0943+10 provided a sequence of nearly 1000 pulses containing clear B- and Q-mode sequences as well as a transition interval of special interest. We shall show that 0943+10 exhibits changes on both long and short time scales during its modechanging process. A slow attenuation of the dominant B-mode component over 18 minutes (which can be regarded as a "pre-switching transition process") occurs before and for some time after the sudden enhancement of trailingedge radiation which is characteristic of the Q mode. The combination of these two effects, on completely different time scales, finally produces the observed integrated-profile changes.

This "pre-switching transition process" in pulsar 0943+10 is remarkable and constitutes one of the main results of our study, which we will discuss in detail below. The identification of gradual changes associated with a modal transition in PSR 0943+10, together with the similar phenomenon in 0355+54, sheds more light on the character of the modechanging phenomenon overall.

---

[3] Phillips & Wolszczan (1989) also estimated the time scale for mode changing as at least 30 minutes from observations at 25 MHz

2. Observations

The low frequency observations were conducted in 1990 using the 103MHz BSA and 40/61MHz DKR1000 telescopes at Pushchino Radio Astronomy Observatory, the 61-MHz observations in January and simultaneous 40- and 103MHz observations in December. The signals from these linearly polarised arrays were fed to radiometers with 64 × 20-kHz contiguous channels (at 61 and 103 MHz) and/or to 32× 5-kHz contiguous channels (at 40 MHz) in order to measure the total intensity and its spectral variations across the passband. The dedispersed signals were referred to the frequency of the first channel—that is, to 103.130, 61.194 and 39.898 MHz (hereafter 103, 61 and 40MHz).

By observing a linearly polarised pulsar signal at adjacent frequencies, the rotation measure (*RM*) canbe obtained,which for observing frequencies of 40,61 and 103MHz, gives a value of 15 ± 1 rad/m^2. The Faradaymodulation period Δf is related to the frequency f by $\Delta f = 1.748 \times 10^{-5} f^{3}/RM$ (Smith 1968). In that the total passband exceeded the Faraday-modulation period at each of the three frequencies, the total intensity of the dedispersed pulses provides a reasonable estimate of Stokes parameter *I*. The fractional linear polarisation and its associated position angle were then determined for each sample—using a technique developed at Pushchino (Suleymanova *et al.* 1988)—from the Faraday-rotation-induced, quasi-sinusoidal intensity modulation across the passband. The time resolutions were 6.9, 5.2 and 6.9 ms at 40, 61 and 103 MHz respectively. Each set of 0943+10 observations comprised some 280 individual pulses at 103 MHz and some 400 at 40 and 61 MHz. The individual-pulse analyses were carried out using the strongest 103-MHz, B-mode and Q-mode sequences available, those observed on 27th and 28th December 1990 respectively. Of these, pulses with sample intensities exceeding a threshold of five standard deviations in the off-pulse noise level were selected for the polarisation analysis presented below.

The 430-MHz observations were made at the Arecibo Observatory in a single observing session on the 19th October 1992. These individual-pulse observations used the Arecibo 40-MHz correlator in a gated mode, which "dumpted" the ACFs and CCFs of the right- and left-hand channel voltages at 1000 μs intervals during a window centred on the pulse.[4] Use of the 10MHz bandwidth and the retention of 32 lags reduced dispersion delay across the bandpass to negligible levels. The resolution was then essentially the correlator dump time or 0.33°. In all cases the measured correlation functions were scaled, 3-level-sampling corrected, and Fourier transformed to produce raw Stokes parameters, which were in turn corrected for dispersion, Faraday rotation, instrumental delays, and all of the known feed imperfections. This procedure will be described in a forthcoming paper (Rankin *et al.* 1998). The observational parameters are summarized in Table 1.

3. Identification of the B and Q modes at 430 MHz

The polarisation properties of a sequence of 103MHz individual pulses corresponding to the B- and Q-profile modes are given in the left-hand panels of Figs. 1 and 2,

[4] The Axecibo 40MHz correlator is described by Hagen (1987) and the observing software by Perillat (1988).

Table 1. Data acquisition information.

	102.5 MHz		430 MHz	
	B mode	Q mode	B mode	Q mode
Dates	27th Dec. 90	28th Dec. 90	19th Oct. 92	19th Oct. 1992
Total bandwidth, MHz	1.28	1.28	10	10
Post-detection smoothing, ms	3	3	none	none
Time resolution, ms	6.9	6.9	1.0	1.0
Number of pulses in histograms	264	224	817	169

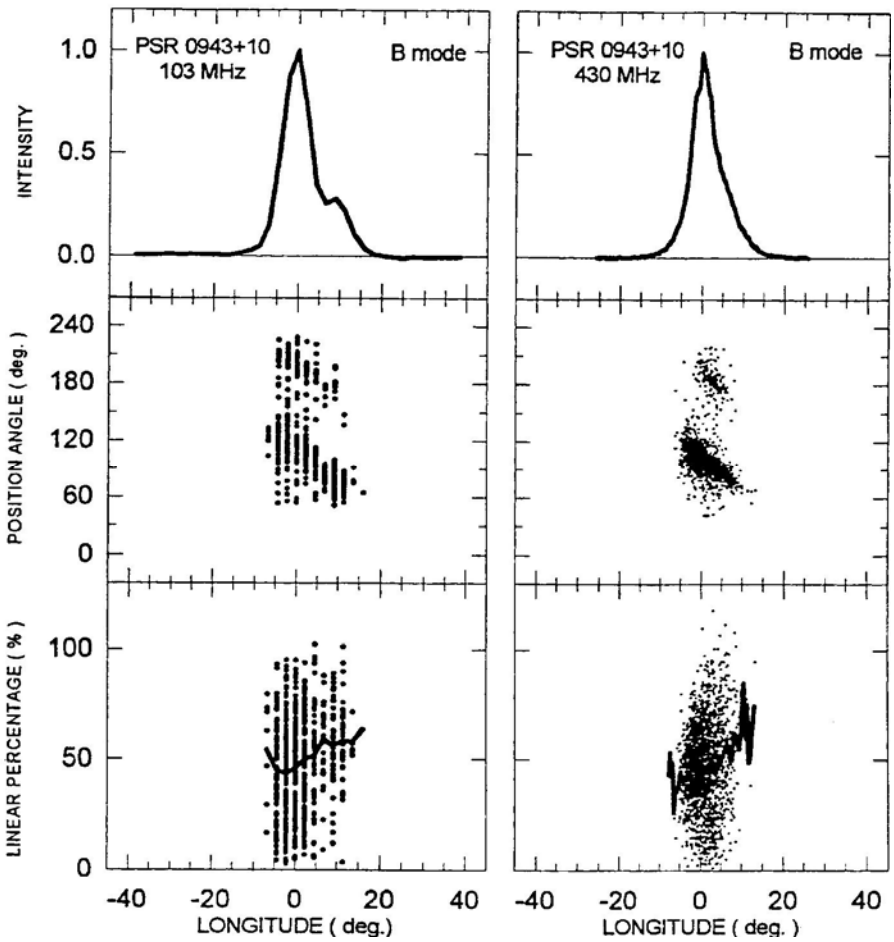

Figure 1. Polarisation displays for PSR 0943+10 in the B-mode profile at 103 MHz (left panels) and at 430 MHz (right panels). The integrated-intensity profiles (Stokes parameter *I*) are given in the top panels, the linear polarisation-angle histograms in the centre panels, and fractional linear-polarisation histograms along with their average value ($\langle L/I \rangle$) in the bottom panels. The 103-MHz displays are computed from 264 individual pulses recorded at Pushchino Observatory on the 27th December 1990, and those at 430 MHz from 817 pulses recorded using the Arecibo Observatory on the 19th October 1992. The profile 4peak intensities in the top panels have been normalized to unity, and the 430-MHz PAs rotated by about 90° so as to be easily compared with those at the lower frequency.

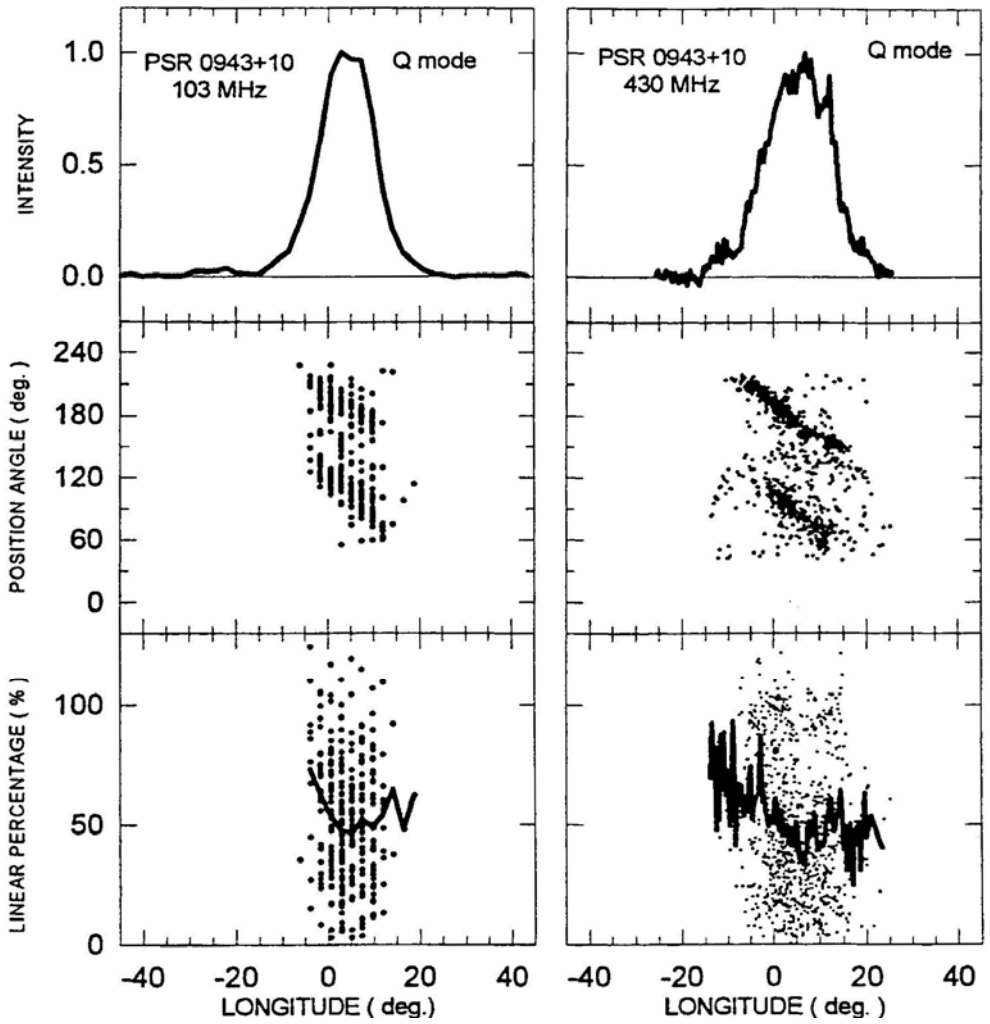

Figure 2. Polarisation displays for PSR 0943+10 in the Q mode as in Fig. 1. The 103-MHz displays are computed from 224 pulses recorded at the Pushchino Observatory on the 28th December 1990 and aligned in time according to the longitude scale in Fig. I ; the 430-MHz displays represent the last 100 pulses of the sequence recorded using the Arecibo Observatory as above.

respectively. Corresponding right-hand panels give the same information for 430 MHz.

The top-left panel of Fig. 1 shows the two-component profile characteristic of the B mode at 103 MHz and below. Its centre panel gives the PA histogram, and individual samples dominated by the primary (PPM) and secondary polarization modes (SPM) are in clear evidence and form two bands of PA sweep in longitude, typically separated by about 90°. Most B-mode longitude samples are dominated by the PPM; the overlapping of symbols makes this slightly difficult to see in Fig. 1, but some 70% of the points fall in the lower (PPM) band, whose PA sweeps from some 120 to 60°. Note further that the two polarisation modes have different distributions

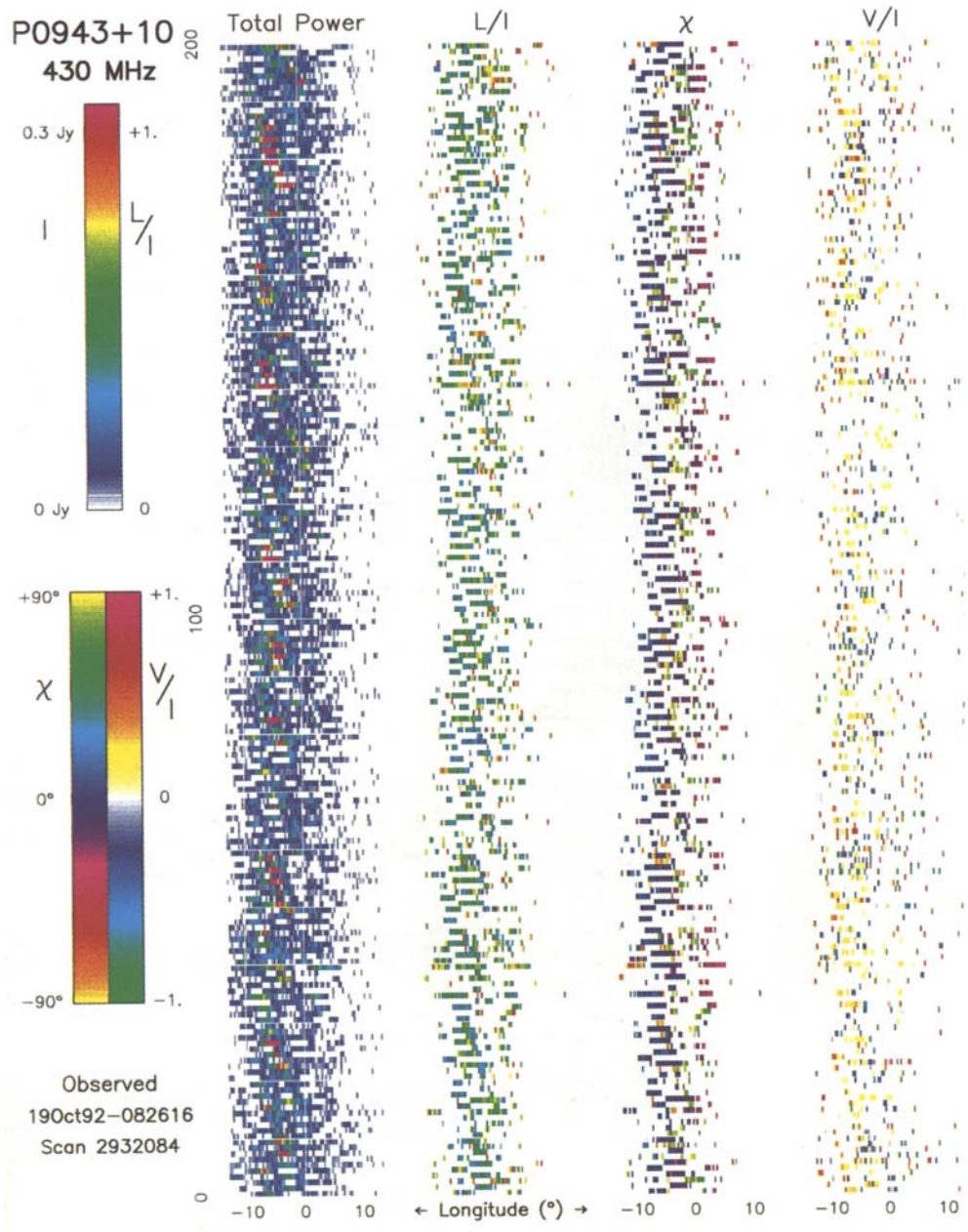
P0943+10
430 MHz
0.3 Jy
+1.
I
L/I
0 Jy
0
+90°
+1.
χ
V/I
0°
0
−90°
−1.
Observed
190ct92−082616
Scan 2932084
Total Power
L/I
χ
V/I
200
100
0
−10 0 10
← Longitude (°) →
−10 0 10
−10 0 10

Figure 3 (a)

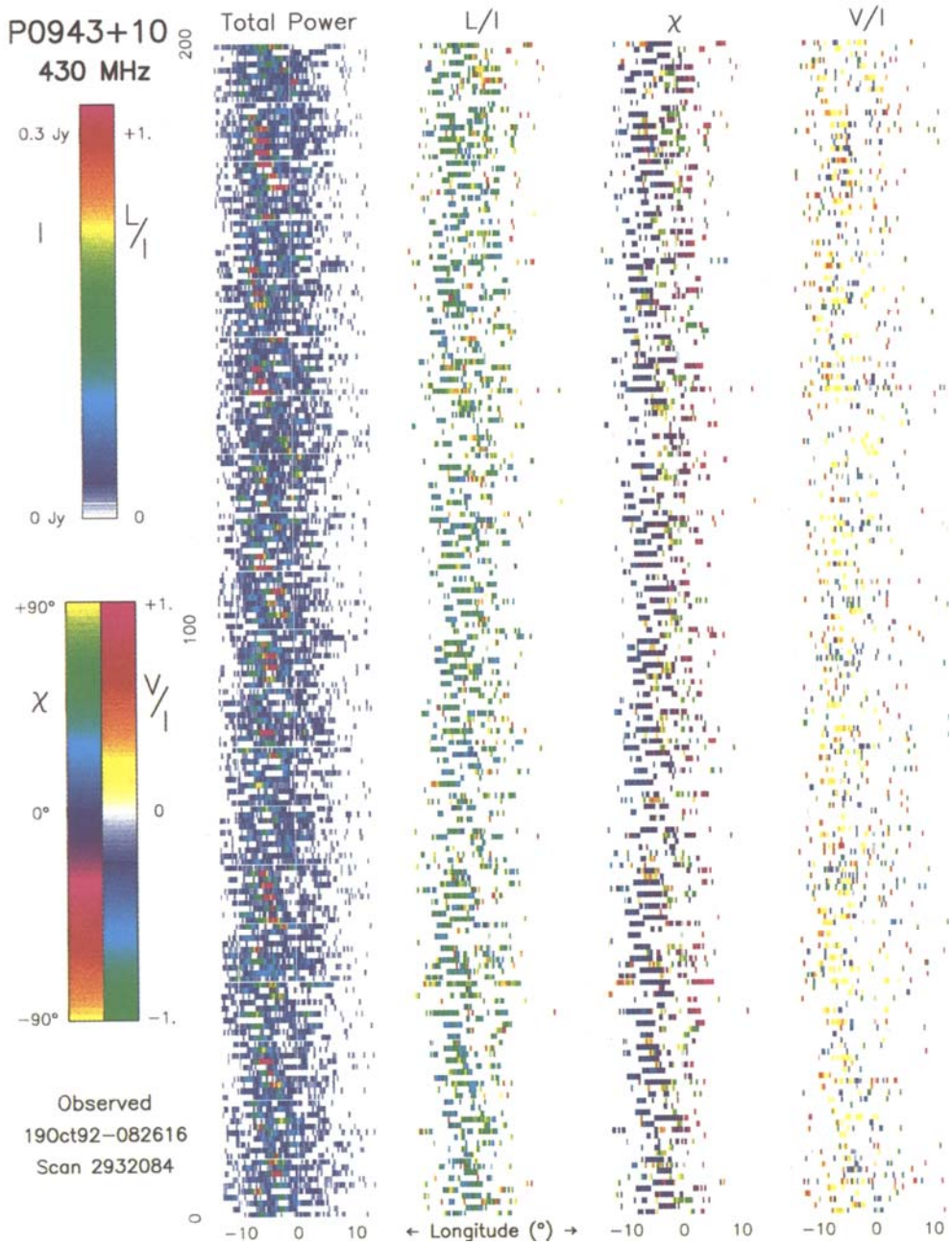
P0943+10
430 MHz
0.3 Jy
+1.
I
L/I
0 Jy
0
+90°
+1.
χ
V/I
0°
0
−90°
−1.
Observed
190ct92−082616
Scan 2932084
Total Power
L/I
χ
V/I
200
100
0
−10
0
10
← Longitude (°) →

Figure 3(b)

over the pulse window. PPM-dominated samples span the entire window, whereas SPM samples are found primarily under the main component. Clearly, the SPM becomes considerably weaker at longitudes corresponding to the second component. The PA sweep rate, computed over the entire band at 103 MHz is about 3.4° per degree of longitude.

The bottom-left panel of Fig. 1 gives the fractional linear polarisation associated with each Bmode longitude sample at 103 MHz. Values range fully from nearly complete to almost zero polarisation, suggesting that the time scale for polarization-mode mixing is comparable to the sample interval. The aggregate linear polarization-varies between about 40 and 60% and shows some tendency to increase under the extreme outer edges of the profile.

The lef-thand panels of Fig. 2 give similar information for the Q-mode profile at 103 MHz. Note that the profile is not only unimodal in form, but that its peak falls much later than that of the Bmode profile in Fig. 1. The PA distributions (centre panel) of the primary (lower) and secondary (upper) bands are here more nearly similar. They both span the entire longitude range under the pulse window, and the sample PAs are almost equally distributed between the two polarization-mode bands. About 46 and 54% of the samples are PPM and SPM dominated, respectively. The fractional linear polarisation of the samples again varies greatly, from zero to essentially 100%, with longitude-averaged values again falling between 40 and 60% within the window, just as did the B mode above. The different frequencies of occurrence of the PPM and SPM in the B and Q modes result, however, in significantly different levels of fractional linear polarisation in the modal profiles, 25% in the B mode and 15% in the Q mode.

Turning now to the Arecibo observation, the 18-minute or 986-pulse, fully polarimetric sequence recorded at 430 MHz in October 1992 was perhaps the longest such observation ever made of this pulsar. Fortunately, during this sequence a transition from the B mode to the Q mode was observed for the first time. Of the 986 recorded pulses, the first 817 clearly represent the B mode. We see this immediately from colour displays such as those in Fig. 3, wherein the normal, regular drifting-subpulse behaviour associated with the B mode is obvious (Fig. 3(a) gives a purely B-mode sequence comprised of pulses 1–200). Fig. 3(b), however, shows pulses 801–986 of the sequence in which the transition from the B mode to the Q mode occurs. An abrupt, dramatic change in the properties and organization of the subpulses begins with the 818th pulse, and we see that the final 169 pulses of the sequence correspond

---

Figure 3(a) & 3(b). Colour dislays of 200-pulse sequences of the 430-MHz observations in Figs. 1 and 2, (a) a B-mode sequence comprised of pulses 1–200 of the 19th October 1992 Arecibo observation, and (b) the transition region from B-mode to Q-mode emission comprised of pulses 801–986—note the abrupt change in properties at about pulse 817. The first column of the displays gives the total intensity(Stokes parameter I), with the vertical axis representing pulse number and the horizontal axis pulse longitude (a range encompassing the entire emission window is shown here), colour-coded according to the left-hand scale of the top bar to the left of the displays. The second and third columns give the corresponding fractional linear polarisation ($L/I=\sqrt{Q^2+U^2}/I$) and its angle ($\chi=\frac{1}{2}\tan^{-1} U/Q$), according to the scales at the top-right and bottom-left of the left-most panel. The last column gives the fractional circular polarisation (V/I), according to the scale at the bottom-right of the left-hand panel. No rotation has been applied to the PAs; therefore, their values are nearly orthogonal to those in Figs. 1 and 2.

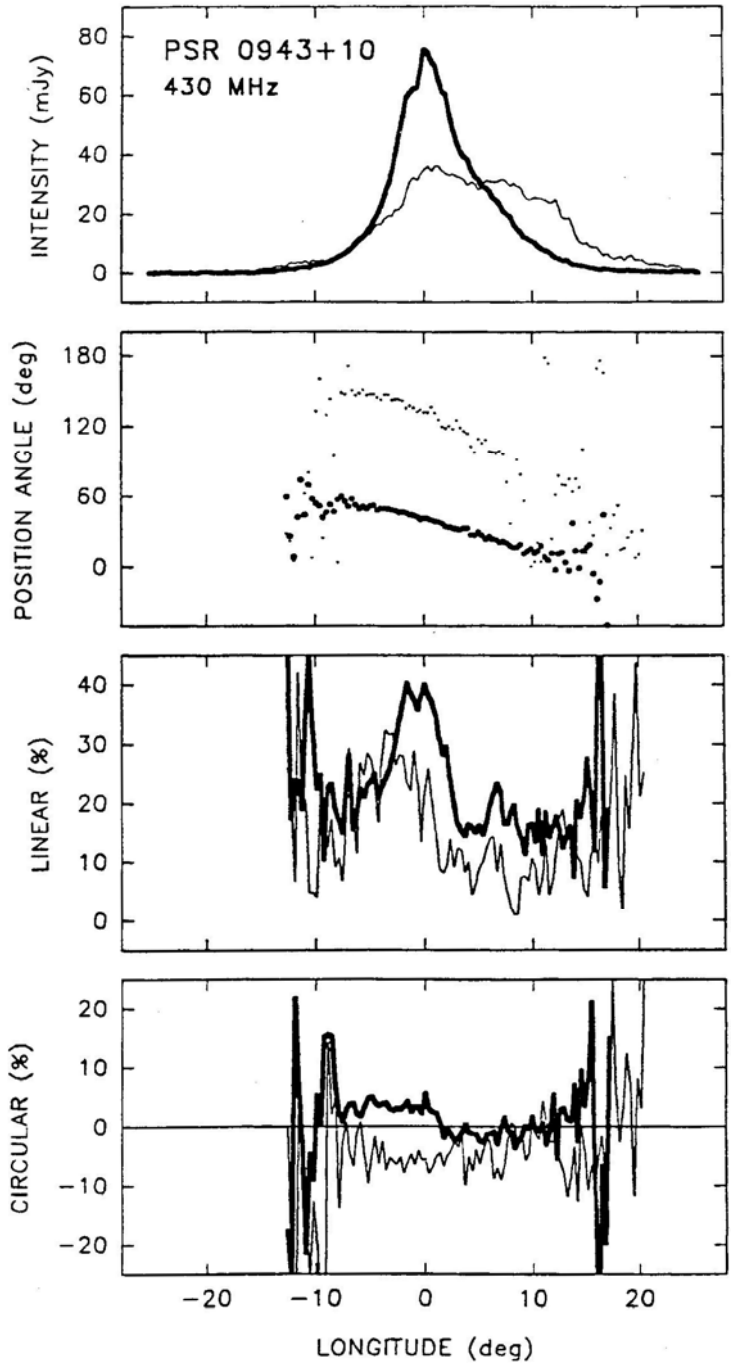

Figure 4. Average-polarisation characteristics of the pulse sequences identified as belonging to the B mode (thicker curves) and Q mode (thinner curves) at 430 MHz. Panels giving the total intensity, polarisation angle, fractional linear, and fractional circular polarisation are shown (defined as in Fig. 3). The peak intensities are not normalized. About 40° has been added to the PAs for ease of display.

Table 2. Characteristics of individual pulses.

	102.5 MHz		430 MHz	
	B mode	Q mode	B mode	Q mode
PA sweep rate, °/°	−3.4 ⟨−3.0⟩	−2.7	−2.4 ⟨−3.0⟩	−3.6
Fractional linear	48 ± 1	49 ± 1	47 ± 1	47 ± 1
Occurrence of PPM (number of samples)	808	235	5371	392
Occurrence of SPM	370	272	576	562

to the pulsar's Q mode. Here, the drifting-subpulse modulation characteristic of the B mode ceases entirely, and the Q-mode emission extends to much later longitudes than does that of the B mode.

Figure 4 gives average profiles computed from the 817 B-mode (heavy lines) and 169 Q-mode (lighter lines) pulses. The intensities are normalized by the numbers of pulses included in each, and thus the profiles clearly demonstrate the weaker, but broader overall character of the Q-mode profile. Note carefully how far the Q-mode emission extends in longitude: some subpulses are visible even at a longitude of 20° and significant emission is seen near longitude –12°.

The rotation of the average PA is shown in the second panel of Fig. 4, and the PA tracks corresponding to the B and Q modes are interesting. Both are comprised of differing contributions of PPM and SPM power. The B mode is dominated by the former and the Q mode by the latter, and this leads to average-PA tracks which are only roughly orthogonal. Note that the separation between the two tracks differs significantly from 90°. As summarized in Table 2, the different values of PA sweep rate corresponding to the B and Q modes combine to yield the average value of 3° /° characteristic of the total profiles at either frequency.

The fractional linear and circular polarisation are given in the bottom panels of the figure. The more comparable contributions of PPM and SPM power in the Q mode cause it to be more severely depolarised. The fractional linear polarisation of the B mode exhibits two minima at the edges of the main component, which are also observed in individual subpulses and correlate with ~ 90° PA "jumps" at these longitudes. The aggregate circular polarisation of the two modes is quite modest and has opposite senses in the two modes.

We can then carry out the same modal analysis of individual-pulse polarisation on the 430MHz sequence as for the 103MHz observation above. The results of this exercise are shown in the righ-thand panels of Figs. 1 and 2. Virtually every comment which was made about the 103-MHz observations can now be said of the 430-MHz ones.

Note the asymmetric, hardly double form of the B-mode profile in the top-right panel of Fig. 1 in contrast to the weak, broad, delayed form of the Q-mode profile in the corresponding position of Fig. 2. The Bmode PA distribution in the centre-right panel of Fig. 1 is again dominated by the PPM (90% of the samples), which is active over the full width of the profile, in contrast to the more limited longitude range of SPM activity; and in the corresponding Q-mode distribution in Fig. 2, the situation is reversed with SPM-dominated samples both predominating (59%) and occurring over a larger range of longitude. As a result the aggregate fractional linear polarisation is again weaker in the Q mode (14%) relative to the B mode (27%), just as at 103 MHz.

Overall, we see that the B- and Q-mode profiles, their polarisation properties, and their fluctuation characteristics, are very similar between 430 and 103 MHz. Hence we have every indication that pulse 818 in the 430-MHz sequence represents a clear and abrupt cessation of B-mode activity and a commencement of Q-mode emission.

4. Abrupt and slow changes accompanying the modal transition

Average profiles constructed from short subsets of the entire sequence further demonstrate the analogy with the B and Q modes identified at 103 MHz. The redistribution of power within the average-profile window is most evident over the

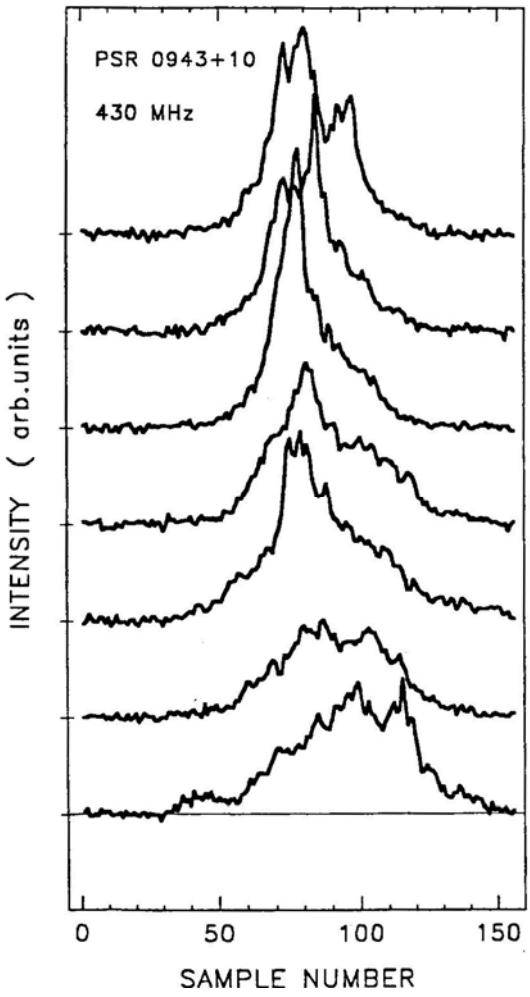

Figure 5. A sequence of integrated, totalpower profiles, calculated by averaging over 50 consecutive pulses (top: #s 637–686, and bottom #s 937–986). The middle profile (#s 787–836) includes 30 pulses before, and 20 pulses after, the mode change. The peak intensities have not been normalized relative to each other. The B-mode profile peak falls at sample 78, and the sample interval is 0.33°.

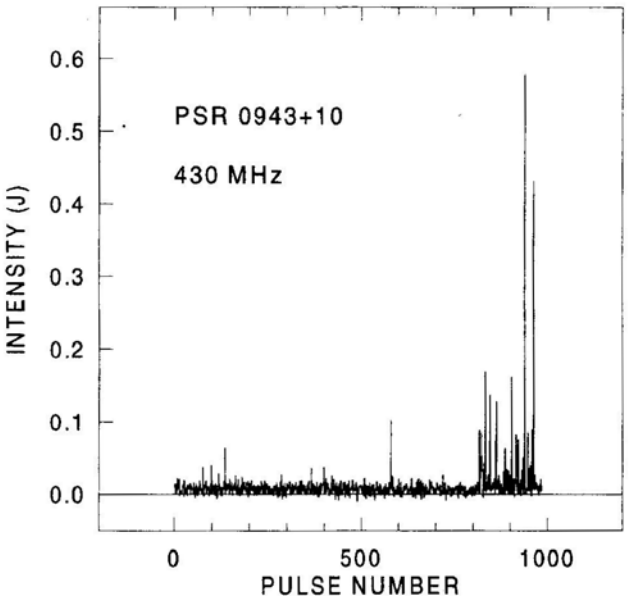

Figure 6. Intensity versus pulse number in a narrow longitude window near on the trailing edge of the B-mode profile (samples #s 112–114, 11.5 ± 0.5°) for the 986 pulses of the 430-MHz observation.

last 350 pulses of the 430MHz observation. Fig. 5 shows the result of consecutive 50-pulse integrations within this interval. Overall, it is clear that the transition from the B to the Q mode entails decreasing activity in the leading part of the profile and enhanced power emitted on the extreme trailing edge of the profile. The decrease in the average intensity of emission under the leading part of the profile is particularly marked in the last two subaverages. The profile corresponding to these last hundred pulses was shown in the top-right panel of Fig. 2 and closely resembles the 103-MHz Q-mode profile adjacent to it. Specifically, the overall shapes of these last several subaverages are more nearly that of a broad, weak, single component, whose centre is appreciably delayed relative to the B-mode profiles; if there are separate components within this overall form, they are not resolved.

The enormous intensity of certain individual pulses during intervals of Q-mode emission is evident in Fig. 6, where the power in a narrow window near the trailing edge of the Q-mode profile at about 11.5° is plotted against pulse number for all 986 pulses of the observation. Strong emission in this region of the pulse window is highly unusual in B-mode sequences, but *some* pulses are *remarkably* bright at this longitude after the transition to the Q mode. Note, however, that of the nearly 170 pulses after the mode change, no more than 20 or so are extraordinarily bright—and many of these only over limited ranges of longitude (see Fig. 3(b)). So, while the pulsar's emission is weaker in its Q mode, it is hardly quiescent!

Finally, we come to the most interesting aspect of our investigation of 0943+10's mode-switching phenomenon. Fig. 7 gives the intensity in three windows, averaged over successive groups of 10 pulses, resulting in 98 such averages in all. The "A" window is taken near the Bmode peak at about 0 ± 1.7° longitude (samples 73–83, see Fig. 5), the " B" window near the centre of the Q-mode profile at about 6.6 ± 1.7°

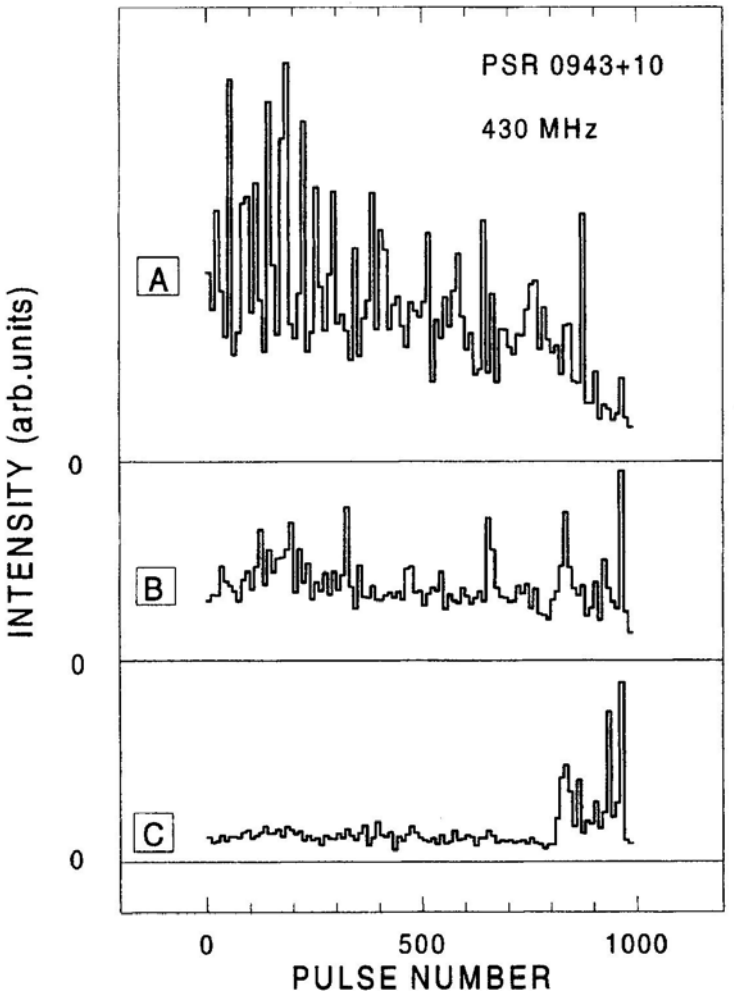

Figure 7. Secular variations in the intensity of PSR 0943+10 in three longitude windows at 430 MHz: **A**: (samples 73–83, 0±1.8°), **B**: (93–103, 6.6 ±1.8°) and **C**: (108–118, 11.5 ± 1.8°). Each value represents the average over 10 consecutive pulses for a total of 98 integrations. The mode change falls near the middle of the 82nd average as is seen clearly by the suddenly enhanced intensity in window C. Note that the power in window A slowly declines, while that in window B remains relatively constant.

(samples 93103), and the "C"window just before the trailing edge of the Q-mode emission at about 11.5 ± 1.7° (samples 108–118).[5]

The transition from B-mode to Q-mode emission falls near the middle of the 82nd average, and indeed, a sharp rise in intensity is seen in the C window (see also Fig. 6), pointing to the fact that the modal transition has a time scale as short as a pulsar period, as is observed for other "mode switching" pulsars. Rather little intensity change is seen in the B window near the peak of the Q-mode

[5] These windows were defined by a fitting procedure: a combination of three Gaussian-shaped components, centred at fixed longitudes, describes both the B and Q-mode profiles rather closely.

profile[6]—however, this point also corresponds to the mid-trailing edge of the B-mode profile (see Fig. 4, top panel).

What is arresting, however, is the behaviour of the A-window intensity. Here we see that its intensity falls gradually throughout the entire interval prior to the transition point, and then more rapidly following this modal transition. The modal change in A-window intensity is very considerable, but it is not at all abrupt. It appears, therefore, that the switching process in this pulsar involves both rapid and slower changes. This gradual decline of intensity centred on longitudes of enhanced Bmode emission—extending over at least 15 minutes—appears to represent some form of "preswitching transition process".

5. Frequency dependence of the two modal profiles

Since two distinct modes have been identified at 430 MHz, we can study the evolution of their respective integrated profiles over a wider frequency range. Fig. 8 displays integrated pulse profiles in the B mode (heavy lines) and Q mode (lighter lines) at five frequencies, 25, 40, 61, 103 and 430MHz. At all but the lowest frequency, the respective profile pairs are time aligned, and at 25 MHz they have been adjusted to span about the same longitude interval[7]

Several conclusions about the frequency evolution of 0943+10's pulse profile can be summarized as follows:

- The B-mode profile has two resolved components. The spacing between the components increases very rapidly between 25 and 103 MHz. This behaviour can be described by a power law with spacing $\Delta s \sim f^{-0\ 63\pm0\ 05}$.
- The relative intensity of the trailing component in the B-mode profile varies hardly at all with frequency in the range between 25 and 103 MHz, and then abruptly falls off between 103 and 430 MHz. This behaviour is reminiscent of the "absorption" phenomena seen in other stars (see Rankin 1983).
- The Q-mode profile has a simple and very similar shape at 61, 103 and 430 MHz At lower frequencies the profile bifurcates, and the two components become increasingly well resolved below 40 MHz.
- The peak of the Q-mode profile occurs some 4.5 ±1° earlier than the trailing component of the B-mode profile. It is remarkable that this shift is independent of frequency to within the (resolution-limited) accuracy of our measurements. It is worth noting that the 430-MHz windows B and C discussed above are also separated by some 4.9°; window C probably locates the (vestigial) B-mode trailing component, which becomes active in the Q-mode profile.

---

[6]While the relatively constant B-window intensity mitigates against diffractive-scintillation-induced intensity variations, we also note that our 10-MHz passband would tend to average out any such modulation. Little is known about 0943+10's dynamic spectrum, but its measured proper motion (Lyne *et al.* 1982) suggests a velocity as large as 200km/s. On this basis, its scintillation bandwidth at 430 MHz is probably well less than one MHz (see Cordes 1986).

[7]The two distinct modal profiles measured by Phillips & Wolszczan (1989) at 25 MHz were arbitrary aligned in their paper so that "the peak of the trailing component in each profile had the same pulse phase". Our alignment (although still arbitrary) reflects the observed alignment at higher frequencies (except 430 MHz), where the modes span about the same longitude interval.

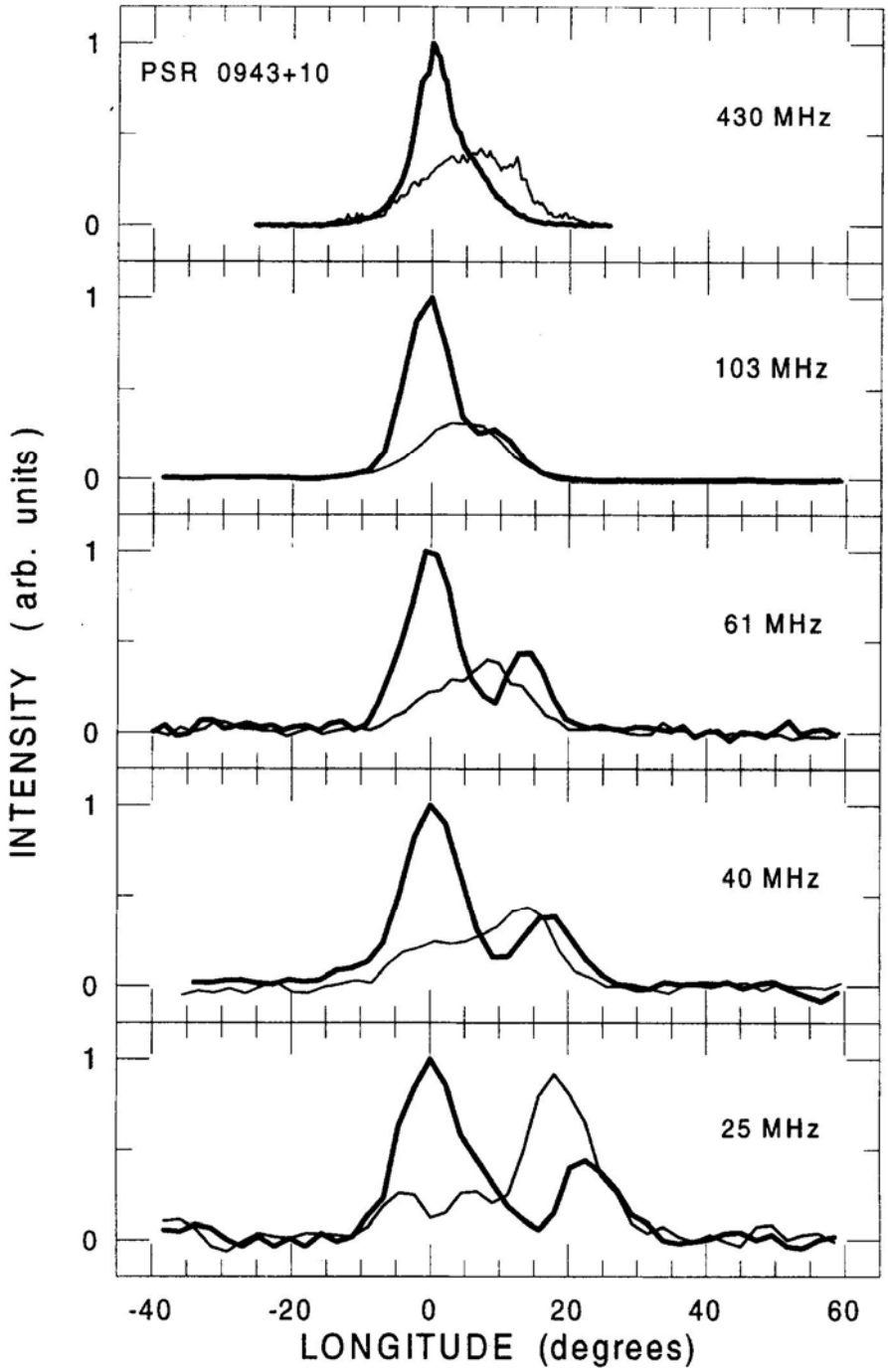

Figure 8. Evolution of the integrated pulse profile of pulsar 0943+10 in the B mode (heavy lines) and in the Q mode (lighter lines) with frequency. Each profile is normalized to its peak value in the B mode. The five profiles have been shifted in longitude so as to position their B-mode peaks at the longitude origin. The 40 and 103-MHz modal profiles were obtained during simultaneous observations on 27th and 28th December 1990, respectively.

- Generally, the integrated pulse profile of PSR 0943+10 has three components: components A and C form the double profile characteristic of the B mode, while central component B usually dominates in the Q-mode profile. The intensities of components A and C decrease, but do not vanish, during Q-mode sequences. Similarly, the intensity of component B seems to determine the amplitude level in the saddle region of the B-mode profile.

6. Summary and discussion

Two modes of subpulse organization are identified in an 18-minute pulse sequence at 430 MHz, and their properties correspond closely to the well known B and Q modes at 103 MHz. The B-mode sequence at 430-MHz is comprised of a highly regular, relatively intense pattern of drifting subpulses which is confined to the first half or two-thirds of the overall window of emission; whereas the Q mode entails a disorganized splatter of mostly weak subpulses, punctuated by a few extraordinarily bright ones, emitted over a broader longitude range, both earlier and particularly later than that of the B mode.

The polarisation behaviour is also similar to that observed at 103 MHz: the B mode exhibits a great preponderance of primary polarisationmode emission (and the little SPM emission is confined to a narrow region of longitude close to and just following the average-profile peak) and thus remains relatively highly polarised in the average; whereas the Q mode shows only a slight excess of secondary polarization-mode emission and thus is largely depolarised in the average. That the B-mode average profile exhibits a maximum fractional linear polarisation of no more than about 40% argues that significant mode mixing is occurring on scales smaller than the 1-ms sample interval. The integrated profiles also exhibit small amounts of circular polarisation over the first half or so of the emission window; lef-thand (positive) circular polarisation is associated with the B mode, and right-hand (negative) with the Q mode.

We find that the process of transition from the B mode to the Q mode is more complicated in PSR 0943+10 than for most other pulsars which exhibit the mode-changing phenomenon. While the overall organization of the subpulses "switches" abruptly at the B-mode/Q-mode boundary, it appears that other, slower changes, accompany this overall reorganization of the emission. Indeed, we find that the intensity of the main B-mode component declines progressively before the "switch" and more rapidly just following it. We know of only one other pulsar, 0355+54, in which there is also some evidence of slower changes concommitant with the sudden reorganization of emission which a "mode change" represents (Morris *et al.* 1980).

A clear example of the switching process from the Q mode to the B mode at 40 MHz has been given by Suleymanova *et al* (1996), which is something of the inverse of the B-mode-to-Qmode "switch" that we have observed at 430 MHz. Accounting for the broadband character of the modeswitching process, the complete scenario of mode switching at 430 MHz seems to be as follows: the onset of the Bmode sequence (which preceeded the beginning of our observation by some minutes) probably also occurred abruptly, via the reestablishment of bright, organized, drifting-subpulse emission within the longitude interval of the main component. This emission then slowly relaxes, as we have seen, with gradually decreasing pulse intensity on a time

scale of 1000 or more pulse periods. Then, at some later time, the electrostatic conditions in the polar-cap region can no longer sustain the intensive, organized subpulse emission, and it degenerates into a much weaker, more chaotic condition (punctuated by occasional extraordinarily bright individual subpulses) until conditions are again favourable for a renewed cycle of bright, organized emission.

We hope that in time it will be possible to understand the physical causes of these gradual and abrupt changes associated with the "mode changing" phenomenon, but as yet we know of no reliable theoretical structure into which they can be accommodated.

Acknowledgements

It is a pleasure to thank Amy Carlow and Kyriaki Xilouris for help with the 1992 observing, Phil Perillat for his remarkable software for the Arecibo 40-MHz Correlator, and Slava Pugachev for assistance in developing the programs used in the observations and analysis at 103 MHz. This work was supported in part by grants from the U. S. National Science Foundation (AST 89-17722 and INT 93-21974). Arecibo Observatory is operated by Cornell University under contract to the U. S. National Science Foundation.

References

Backer, D. C, Rankin, J. M., Campbell, D. B. 1975, *Astrophys. J.,* **197**, 481.
Bartel, N., Morris, D., Sieber, W., Hankins, T. H. 1982, *Astrophys. J.,* **258**, 343.
Cornelia, J. M. 1971, Ph. D. Thesis, Cornell Univ., Ithaca, New York, USA
Cordes, J. M. 1986, *Astrophys. J.,* **311**, 183.
Fowler, L. M., Wright, G. A. E., Morris, D. 1981, *Astr. Astrophys.,* **93,** 54.
Helfand, D. I, Manchester, R. N., Taylor, J. H. 1975, *Astrophys. J.,* **198**, 661.
Hagen, J. 1987. *NAIC Electronics Department Manual No. 8319*
Lyne, A. G., Anderson, B., Salter, M. J. 1982, *Mon. Not. R. astr. Soc,* **201**, 503.
Morris, D., Sieber, W, Ferguson, D. C, Bartel, N. 1980, *Astr. Astrophys.,* **84**, 260.
Perillat, P. 1988, *NAIC Computer Department Report #23*
Phillips, J. A., Wolszczan A. 1989, *Astrophys. J.,* **344**, L69.
Rankin, J. M. 1983, *Astrophys. I,* **274**, 359.
Rankin, J. M. 1986, *Astrophys. J.,* **301**, 901.
Rankin, J. M. 1993a, *Astrophys. J.,* **405**, 285.
Rankin, J. M. 1993b, *Astrophys. J. Suppl,* **85**, 145.
Rankin, J. M., Benson, J. M. 1981, *Astr. J.,* **86**(3), 418.
Rankin, J. M., Rathnasree, N., Xilouris, K. 1998 (in preparation).
Sieber, W, Oster, L. 1975, *Astr. Astrophys.,* **38,** 325.
Smith, F. G. 1968, *Nature,* **220**, 891.
Suleymanova, S. A., Izvekova, V. A. 1984, *Sov. Astron.,* **28**, 32.
Suleymanova, S. A., Volodin, Yu. V., Shitov, Yu. P. 1988, *Astron. Zh.,* **65**(2), 349.
Suleymanova, S. A. 1989, *Trudy FIAN, Moscow,"NAUKA" Series: Pulsars,* **199,** 42.
Suleymanova, S. A., Izvekova, V. A., Rankin, J. M. 1996, *ASP Conference Series,* **105**, 223.
Taylor, J. H., Huguenin, G. R. 1971, *Astrophys. J.,* **167,** 273.
Vitkevich, V. V., Alekseev, Yu. I., Zhuravlev, V. F., Shitov, Yu. P. 1969, *Nature,* **224**, 49.

J. Astrophys. Astr. (1998) **19,** 19–33

Local Pulsars: A Note on the Birth-Velocity Distribution*

A. Blaauw *Department of Astronomy, Kapteyn Institute, P.O. Box 800, 9700 AV Groningen, The Netherlands*

R. Ramachandran *Astronomical Institute "Anton Pannekoek", Kruislaan 403, 1098 SJ Amsterdam, The Netherlands*

Received 1997 December 26; accepted 1998 June 11

Abstract. We explore a simple model for the representation of the observed distributions of the motions, and the characteristic ages of the local population of pulsars. The principal difference from earlier models is the introduction of a unique value, *S,* for the kick velocity with which pulsars are born. We consider separately the proper motion components in galactic longitude and latitude, and find that the distributions of the velocity components parallel and perpendicular to the galactic plane are represented satisfactorily by S = 200 km/sec, and leave no room for a significant fraction of much higher velocities. The successful proposition of a unique value for the kick velocity may provide an interesting tool in attempts to understand the physical process leading to the expulsion of the neutron star.

Key words. Methods: statistical—stars: neutron, kinematics—pulsars: general.

1. Introduction: The model used

The early proper motion measurements have indicated that pulsars, on the average, have spatial velocities of the order of a few hundred km/sec (Lyne *et al* 1982). Subsequent measurements, over the past 15 years have provided evidence for speeds as high as a thousand km/sec (Bailes *et al* 1990; Fomalont *et al* 1992; Harrison *et al* 1993). Many models have been suggested to explain the spatial velocities of pulsars. Harrison & Tadimaru (1975) proposed the "rocket" theory which essentially stated that the pulsar is accelerated along the magnetic axis due to the radiation reaction soon after it was born. However, subsequent observations have failed to confirm the prediction of the model, that there is an alignment between the directions of proper motion and the magnetic axis. Gott *et al* (1970) proposed that pulsars derive their spatial velocities from their progenitor binary systems, when the binary disrupts due to the heavy mass loss during the supernova explosion (Blaauw 1961). Asymmetric supernova explosions were proposed by Shklowskii (1970). No fully satisfactory theory has been proposed yet.

Clearly, knowledge of the shape of the birth-velocity distribution is of basic importance for any theory that attempts to clarify the mechanism that causes the

*This paper is an extended analysis of the talk presented by A. Blaauw at the Raman Research Institute on 20th February, 1996.

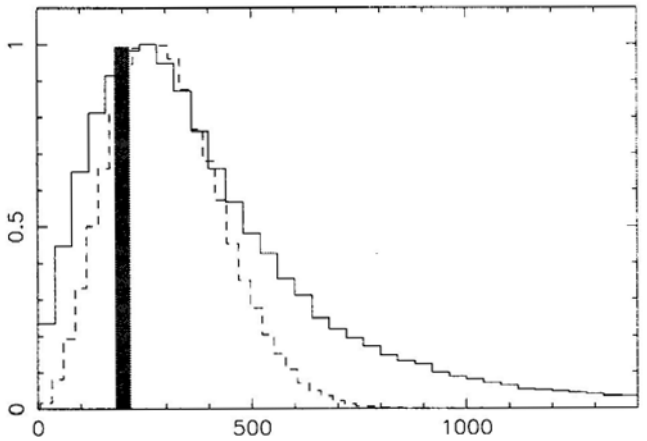

Figure 1. The birth speed distribution of pulsars as predicted by Lyne & Lorimer (1993) (solid line) and Hansen & Phinney (1997) (dash line), and as explored in the present paper (grey bar).

birth-velocities. The present paper is concerned with this problem. Among the most recent hypotheses for the birth-speed distribution are those by Lyne & Lorimer (1993) and Hansen & Phinney (1997), shown in Fig. 1. Hartman (1997) finds that a velocity distribution that has many more pulsars at low velocities than that of Lyne & Lorimer also describes the observations quite well.

Whereas these distributions are characterised by maximum density in velocity-space near zero-velocity, we assume all pulsars to have been ejected from the parent body with the same birth speed – henceforth denoted by S – isotropically distributed. Accordingly, in velocity space, velocity vector points define a spherical surface with radius S. We consider such an alternative worth exploring because it cannot be excluded at this stage of pulsar physics, that the birth (kick) velocities are spread around a (physically) preferred value rather different from zero. With regard to the space distribution of the progenitors, we assume these to be located in a layer of zero thickness at $z = 0$. This assumption is rather harmless because it is generally agreed that pulsars originate from the massive stars in the Galaxy which are confined to a layer the thickness of which is very small as compared to the scale-height of the z-distribution of the pulsars. Finally we assume an upper limit to the age, T, and we do not consider for this analysis pulsars with ages greater than T. Accordingly, the quantity to be solved for will be only S. Our analysis also differs from previous ones in that we separately consider the velocity components parallel and perpendicular to the galactic.plane.

Naturally, the assumed uniqueness of the birth speed cannot but be an approximation of the true situation, for even if there is uniqueness in the kick velocities with which the pulsars leave the parent body, these are vectorially added to the space motion of the parent body, i.e., in the case of components of binary systems, the orbital velocity and the systemic velocity. This implies that the birth-speed distribution is not a delta function but exhibits a certain width. However, since the birth speed we arrive at, S = 200 km/sec, generally dominates over these vector additions, the simplified model remains a good first approximation.

In section 2 we give analytical expressions for the expected distributions, and demonstrate why the pulsar velocities parallel to the plane provides a direct way to

estimate the velocity *S*. The observed pulsar population suffers from severe selection effects, which must be taken into account when comparing theoretical and observed distributions. We have done this through detailed Monte Carlo simulations described in section 3.

We compare our model with observations for the cylindrical volume of space defined by $|z| < 1$ kpc and projected distances $d \cos b$ smaller than 2kpc only. Within this volume we assume steady state for velocity and space distribution.

2. Definitions and analytical relations

We denote by,

S: the (unique) three dimensional speed at birth of the neutron star. In our analysis this will be the velocity with respect to the local standard of rest at the position of the Sun.

T: the (adopted) upper limit to the pulsar age; only those pulsars with characteristic ages less than T are considered for this analysis.

z : the distance from the galactic plane.

$K(z)$: the acceleration perpendicular to the plane due to the galactic gravitational field; K will be counted positive in the direction towards the plane.

d: the distance from the Sun.

w: the velocity component perpendicular to the galactic plane.

w_0:. the value of w at birth.

v: the velocity component (parallel to the plane) corresponding to the proper motion component in galactic longitude.

$G(S)$: the number of neutron stars generated per unit time per unit surface at $z = 0$.

$G_0(w_0)\, dw_0$: the number among these in the interval w_0 , $w_0 + dw_0$. Since the velocities at birth are distributed isotropically, this is a flat distribution:

$$G_0 (w_0)\, dw_0 = G (S)\, dw_0 / S = C\, dw_0 \qquad (1)$$

$G_z(w)\, dw$, the number passing level z with velocities w, $w + dw$ per unit surface per unit time.

We assume symmetry with respect to the galactic plane, hence the model deals only with positive values of z and w.

There is a subset of the pulsar population moving toward the plane after having reached maximum distance z. Table 1 gives this maximum distance, z_{max} for various values of w_0, and the quarter oscillation times $T_{1/4}$, computed with the adopted force field described in section 3.1. Objects with w_0 below about 52km/sec remain during their full lifetime below $z = 1$ kpc and hence, within the volume of space we study. For $S = 200$ km/sec these represent about one quarter of the population. For $T = 50$ Myr, roughly one half of them will be observed also after they have reached maximum distance from the plane. Objects with w_0 in excess of 50 km/sec will orbit beyond $z = 1$ kpc and re-enter the lower domain on their way back. In these upper parts of their orbits they dwell relatively long: for $w_0 = 60$ km/sec they reenter only at the age of about 50 Myr, for larger wo they dwell even longer beyond 1 kpc. Hence, it is

Table 1. The maximum height from the galactic plane (z_{max}) and the quarter oscillation time ($T_{1/4}$) for various initial z-velocities (w_0).

w_0 (km/sec)	10	20	30	40	50	60	70	80	90	100
z_{max} (kpc)	0.12	0.27	0.45	0.68	0.95	1.22	1.56	1.90	2.21	2.6
$T_{1/4}$ (Myr)	18	21	25	28	31.5	35	38	40	42	43.5

only in the interval of w_0 between 52 and 60 km/sec that we expect to find objects younger than 50Myr to re-appear in the domain below z = 1 kpc. Summarizing, for T = 50Myr, a small fraction of the observed population, about 15 per cent, will be on their way back to the plane. For lower values of T, this percentage is accordingly lower. The simulations take their presence into account.

2.1 *Velocities perpendicular to the plane*

The space density of neutron stars at z= 0 with w_0 , w_0 +f dw_0 is

$$D_0(w_0)\,\mathrm{d}w_0 = (1/w_0)G_0(w_0)\,\mathrm{d}w_0 = (C/w_0)\,\mathrm{d}w_0. \tag{2}$$

Since

$$w^2 = w_0^2 - 2\int_0^z K(z)\,\mathrm{d}z \tag{3}$$

for objects to reach level z, a minimum value of w_0, denoted by $w_{\min}$ is required:

$$w_{\min}^2 = 2\int_0^z K(z)\,\mathrm{d}z = 2P(z),$$

where,

$$P(z) = \int_0^z K(z)\,\mathrm{d}z. \tag{4}$$

The range of values w_0^2 for objects reaching level z and beyond is:

$$\text{Range in } w_0^2 = S^2 - w_{\min}^2 \tag{5}$$

This is also the range of the corresponding values w^2 at level z, since $w_{\min}$ becomes zero and S becomes w_s,

$$\text{where} \quad w_s^2 = S^2 - 2\int_0^z K(z)\,\mathrm{d}z = S^2 - 2P_z = S^2 - w_{\min}^2. \tag{6}$$

However, the range of w at level z, i.e., from zero to w_s, is broader than the corresponding range at birth in the ratio $w_s/(S–w_m)$ For instance, if we assume S = 180 km/sec, for reaching level 420 pc, wo should range from 30 to 180 km/sec, i.e., 150 km/sec, whereas the resulting range at level z = 420 pc becomes w= 0 to w_s=177km/sec.

Since for given z, from equation $3\Delta w^2 = \Delta_0\ (w_0^2)$, we have $w_0\ \Delta w_0 = w\ \Delta w$. Hence, the broadening for given w is in the ratio w_0/w.

Accordingly, whereas $G_o(w_0)\ dw$ is flat, for a given level z, $G_z(w)\ dw$ is proportional to w/w_o, with w and w_0 related by equation 3.

The number of objects per unit volume at level z with w in the interval w, $w + dw$ will be,

$$D_z(w)\ dw = (1/w)\ G_z\ (w)\ \mathrm{d}w \tag{7}$$

Due to the broadening just mentioned,

$$G_z(w) = (w/w_0)\ G_0(w_0). \tag{8}$$

Hence, $D_Z(w) = (C/w_0)$, and we have the well known relation, $D_Z(w)=D_0(w_0)$ for pairs of values w and W_0 related by equation 3.

The above relations do not take into account the disappearance from the sample of the pulsars older than age T. We denote by w_t the minimum velocity at $z = 0$ required for reaching level z within the time-span T. w_t is defined by:

$$T = \int_0^z \frac{\mathrm{d}z}{w(z)} = \int_0^z \frac{\mathrm{d}z}{\sqrt{w_t^2 - 2P}}. \tag{9}$$

Thus, there is an interval of velocities at level z from zero to w_z, in which no objects will occur. Again, we have,

$$w_z^2 = w_t^2 - 2P$$

Accordingly, at level z, the distribution of velocities w can be described by the above $D_z(w)\ dw$ truncated at the low velocity end by eliminating the interval $w = 0$ to $w = w_z$.

Figure 2 demonstrates this effect. They have been obtained numerically for an adopted value S =180 km/sec and T = 8 Myr. The five histograms correspond to five different z-slabs (between 0 and 1 kpc), each of width 200 pc. In the highest layer we note the absence of pulsars in the velocity range w = 0 to 90 km/sec. At lower z-levels the empty interval is accordingly smaller. At the high-velocity end the limiting velocity w_l is fixed by $w_l^2 = (S^2 — 2P)$. The fact that the cutoff is not sharp is due to the combination of all z-values within the slab.

2.2 *Velocities parallel to the plane*

We denote by:

v, the component of the velocity parallel to the galactic plane corresponding to the proper motion in galactic longitude:

$$v = d_{\mu_l} \cos b.$$

Since the distribution of v is symmetric we consider only the absolute value of v. At level z, for a given T, v ranges from 0 to $v_l = (S^2 - w_t^2)^{1/2}$ The predicted distribution will be shown to be:

$$D(v)\mathrm{d}v = C'\ S\left\{\pi/2 - \arcsin\left[\frac{w_t}{\sqrt{S^2 - v^2}}\right]\right\}\mathrm{d}v, \tag{10}$$

where C' is a constant defined below.

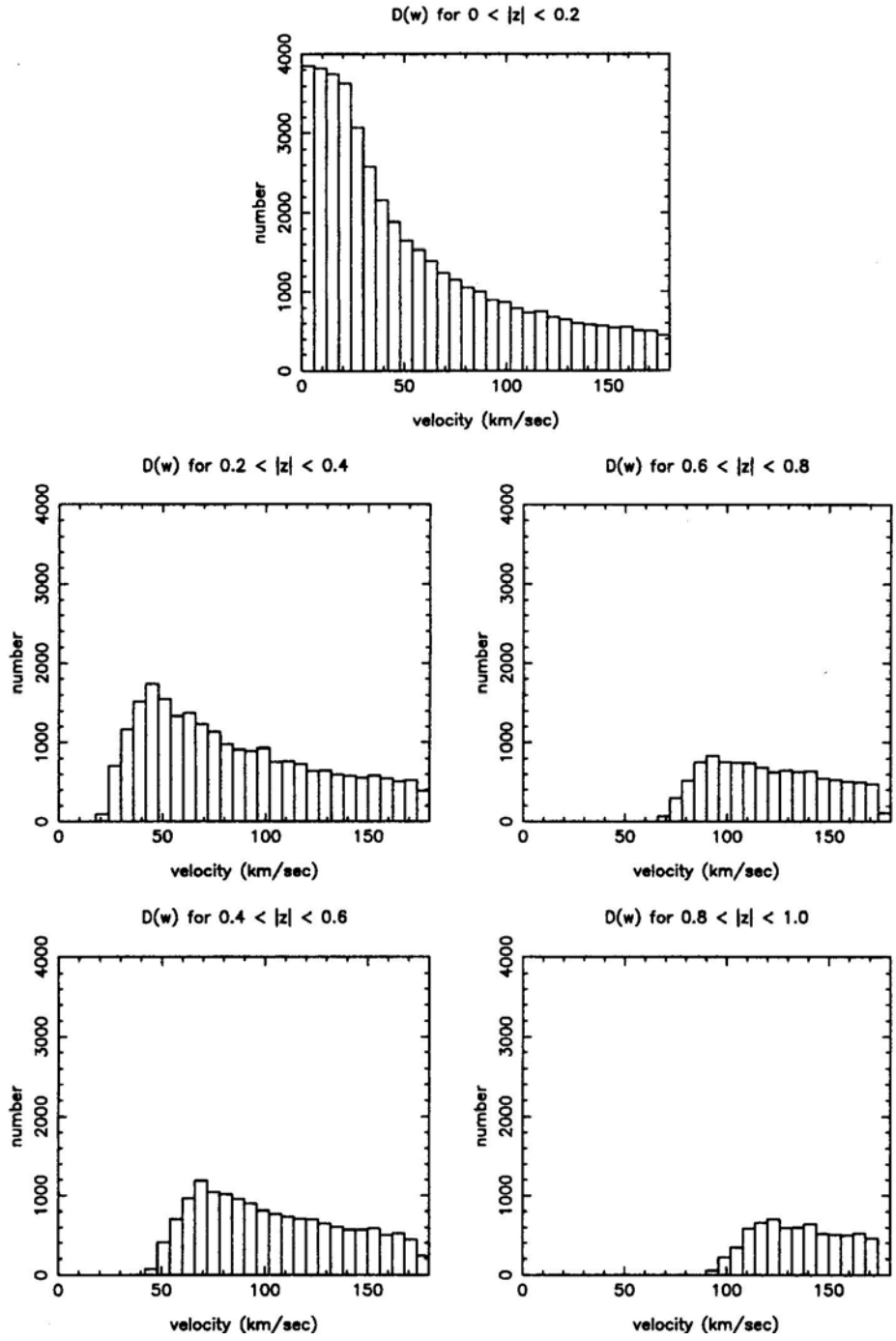

Figure 2. Distribution of velocities perpendicular to the plane of pulsars in different *z*-slabs after evolving in the potential for ages up to *T*. This plot corresponds to S = 180 km/sec and T= 8Myr.

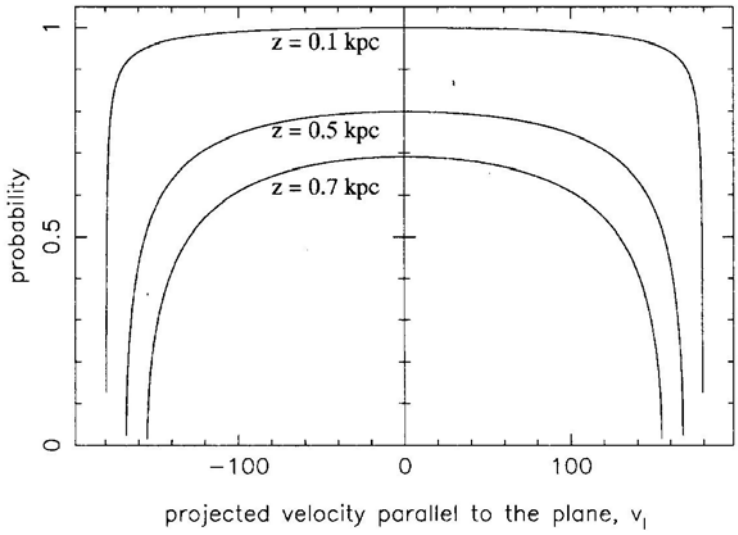

Figure 3. Distrubution of velocities D(v) parallel to the plane as given by equation 10 The three curves correspond to z = 0.1,0 0.5, and 0.7 kpc ,respectively for S =180 km/ sec and T = 8Myr.

We difine by N (v,w) the number of objects at level z per unit of v and of w Equation 10 then follows from

$$D(v)\,\mathrm{d}v = \mathrm{d}v \int_{w_t}^{w_l} N(v,w)\,\mathrm{d}w = \mathrm{d}v \int_{w_t}^{w_l} N(0,w)\frac{R\,\mathrm{d}w}{\sqrt{R^2 - v^2}},$$

where, $R^2 = (S^2 - w^2)$, $w_l^2 = (S^2 - v^2)$, and $N(0,w) = N(0,0)S/\sqrt{S^2 - v^2}$, so that

$$\begin{aligned} D(v)\,\mathrm{d}v &= \mathrm{d}v S N(0,0) \int_{w_t}^{w_l} \frac{\mathrm{d}w}{\sqrt{S^2 - v^2 - w^2}} \\ &= S N(0,0)\left[\pi/2 - \arcsin\frac{w_t}{\sqrt{S^2 - v^2}}\right]\mathrm{d}v, \end{aligned}$$

where $C' = N(0,0)$ is the number per unit v and unit w at v = 0, w = 0 at z = 0.

For low z-levels the distribution $D(\upsilon)\mathrm{d}\upsilon$ is nearly flat up to v close to υ_l. This is due to the fact that the second term in equation 10 becomes significant with respect to the first, constant term, only at high v. For instance, for S = 200 km/sec and T = 20 Myr, at $v = 0.9v_l$, the ratio between the second and the first term near z = 0 is only 0.036. For high z-levels the distribution becomes less flat. Fig. 3 demonstrates this effect. As we chose higher values of T, the nature of the curves for higher z becomes more similar to the one for the lowest z. The truncated nature of $D(v)$, particularly at low z, provides an important tool in estimating S; the extreme observed value, v_l is an approximate measure of S virtually independent of the assumed life time T.

3. Simulations

We did a Monte Carlo simulation to generate a large number of objects in the solar neighbourhood (with initial value of z = 0), keeping the surface density constant. As

mentioned in the previous sections, we assumed a simplistic model with all neutron stars being ejected out isotropically with a constant speed (S). This assumption corresponds to having initial velocities in the z-direction ranging from zero to S with uniform probability. We evolve them in an assumed local gravitational potential to get their velocity and spatial distributions, and in addition we studied the distributions of their characteristic ages. Each object was assigned an age chosen randomly with uniform probability between zero and T. Given the distribution of characteristic ages öf known pulsars, we chose a value of T = 50 Myr as an optimal choice in order to include a sufficiently large sample, and at the same time describe the kinematics with our potential model. The presence of the objects which turn over after reaching their maximum z-amplitude of oscillation within their age are accounted for.

3.1 *Local gravitational potential*

To study the kinematics of the generated objects we assumed the local gravitational potential function given by Kuijken & Gilmore (1989). The vertical acceleration due to this potential is given by (Bhattacharya *et al.* 1991)

$$g_z = 1.04 \times 10^{-3}\left[\frac{1.26\,z}{\sqrt{z^2+0.18^2}} + 0.58\,z\right], \tag{11}$$

where g_z is in units of kpc/Myr^2 and z in kpc. We use this function to evolve every one of the generated objects from their initial position and velocity to their current value after a time t.

3.2 *Further assumptions for simulation*

We assumed a Gaussian distribution of fields in logarithmic scale, with$\langle \log B(\mathrm{G})\rangle$ = 12.2 with a root mean square spread around the mean of 0.3. The choice of initial periods will be discussed in section 4.4. With an assumption that the magnetic field does not decay significantly within the time scales of our interest (~50Myr) the final rotational period of the pulsar can be easily calculated with the simple dipole formula

$$B^2 = \frac{3Ic^3}{8\pi R^6}\,P\dot{P}, \tag{12}$$

where c is the velocity of light, I is the moment of inertia of the neutron star, and $\dot{P}$ is the time derivative of the rotation period P.

The simulation was repeated for various values of S (ranging from 90 km/sec to 350 km/sec) and T (from 15 Myr to 50 Myr). At the end of the evolution, pulsars which have the quantity $(B/P^2) < 2 \times 10^{11}$ were neglected from the simulation, since it is believed that the pulsar activity ceases to continue below this limit.

3.3 *Selection filter*

After evolving the generated objects in the galactic potential, their final position, velocity components, rotation period and characteristic age are noted down. After compensating for observational selection effects a subset of this population was

selected to compare with the known sample. The procedure we have adopted for this task is the same as the one described by Deshpande *et al.* (1995). We selected only those pulsars which are, in principle, detected by any one of the eight major pulsar surveys considered, namely (**1**) Jodrell Bank survey, (**2**) U. Mass-Arecibo survey, **(3)** Second Molonglo survey, (**4**) U. Mass–NRAO survey, (**5**) Princeton–NRAO Phase I survey, (**6**) Princeton–NRAO Phase II survey, (**7**) Princeton–Arecibo survey, and (**8**) Jodrell Bank-1400MHz survey. Since our analysis deals with only the solar neighbourhood (projected distance onto the plane less than 2 kpc, and $|z| < 1$ kpc) the effect due to interstellar scattering and dispersion are ignored. While comparing the results of the simulation with the known sample, only the subset of the simulated sample (*detectable* simulated sample) was used.

For consistency, even the sample of known pulsars were passed through this filter to select a subsample, which was finally used for comparison with the simulated sample.

4. Comparison with observations

4.1 *Velocities parallel to the plane*

As the first step, we consider the distribution of velocity components parallel to the plane, $D(v)$, because as it was explained in section 2.2, these provide the estimate of S. From the compilation of Taylor *et al.* (1993) we use those proper motion measurements for which the quantity $d \times \sigma < 94$ km/sec (20 A.U./yr), where σ is the formal error in the proper motion quoted by those authors. We do not apply corrections for solar motion and differential galactic rotation, since within the range of distances considered, these are negligible as compared to the true proper motions and their observational errors. Fig. 4(a) gives the distribution of these velocities, and Fig. 4(b) gives their distribution as a function of the height from the galactic plane. We note that with the exception of 5 objects, all are confined within ±210 km/sec. In comparison with Fig. 3 we may conclude that the value of the unique velocity must be roughly around about 200 km/sec. Clearly, values of S in excess of 250 km/sec are incompatible with the proper motions.

4.2 *Density distribution perpendicular to the plane*

Hartman & Verbunt (1994), from their study of evolution of neutron stars in various models of the local gravitational potential, demonstrate the effect of observational selection for understanding the distribution of pulsars perpendicular to the plane. Since observations tend to detect more luminous pulsars (which are younger and closer to the plane), irrespective of the nature of the *true* distribution the *observable* distribution is roughly the same. This has been seen in our simulations too. While comparing the simulated sample (after compensating for the selection effects) with the observed, a satisfactory KolmogorovSmirnov probability was achieved for many different combinations of S and T. For $S = 180$ km/sec and $T = 50$ Myr (Fig. 5) the KS probability was 59.6%, and for many other combinations of (S, T), like (250,50), (350,50) the KS probability was roughly as high as for (180,50). Therefore, one can conclude that the density distribution perpendicular to the galactic

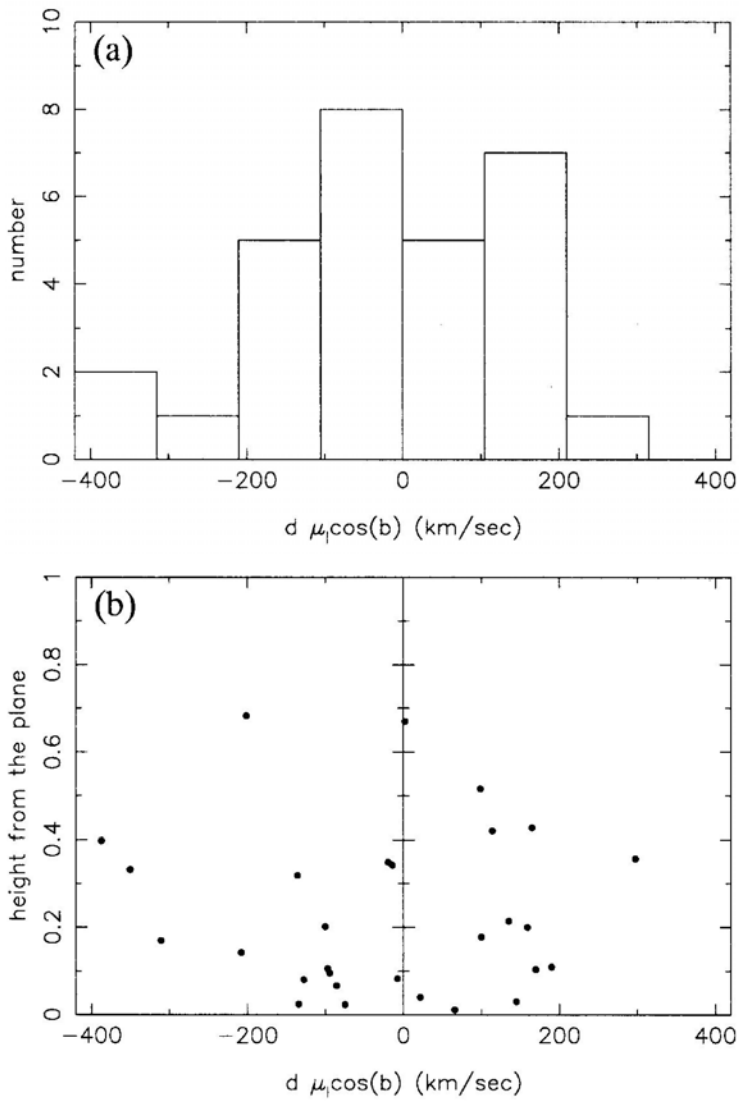

Figure 4. Velocities parallel to the plane corresponding to the proper motions in galactic longitude. (**a**) Distribution of these velocities; (**b**) distribution of velocities as a function of height from the galactic plane. Only those pulsars whose proper motion errors (1σ) are less than 94 km/sec (20 A.U./yr) are considered for this figure.

plane alone is not a severe constraint on the kinematic properties of pulsars, and one needs to study other properties like the velocity components and the distribution of characteristic ages, etc.

4.3 *Velocities perpendicular to the plane*

We do not have measured *w,* since there is no way of measuring the radial component of the velocity vector. However, for pulsars with sufficiently low galactic latitude

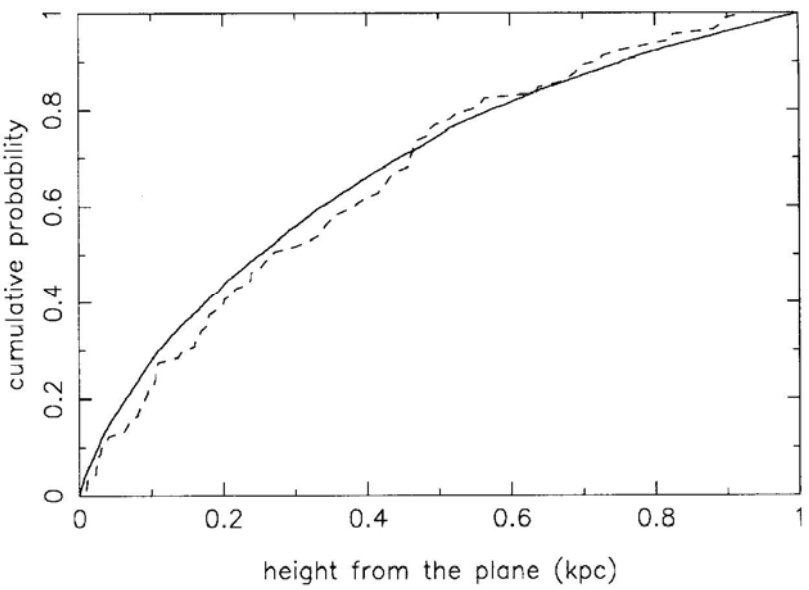

Figure 5. The cumulative number distribution of pulsars as a function of height from the galactic plane. Dash line is for the known sample and the solid line is the best fit corresponding to S = 180 km/sec and T = 50Myr.

(say, $|b| < 50°$), we can approximate $w = \mu_b \times d$ provided cos b is close to unity. Out of the 30 pulsars selected, 23 have cos $b > 0.87$, 5 have cos $b = 0.78 - 0.87$, and 2 have cos $b = 0.72 - 0.78$. Fig. 6(a) gives the distribution of ($\mu_b \times d$). Fig. 6(b) shows the distribution of $\mu_b \times d$ against the height from the galactic plane. Objects at negative z are plotted with reversed z and reversed $\mu_b \times d$. The asymmetry in the distribution of $\mu_b \times d$ in Fig. 6(a) shows the flow of objects away from the galactic plane.

Once a considerably richer sample of accurate pulsar proper motions is available, it will be of great interest to make the detailed comparison between the observed distribution and the theoretical one of Fig. 2, and check its rapidly varying shape with increasing z. The predicted run of the mean velocity υ with increasing z is in harmony with observations, as shown in Fig. 6(b).

4.4 *Distribution of characteristic ages*

As described in section 3.2 we have assumed that the magnetic fields at birth are distributed as a Gaussian in log B around 12.2 with an r m.s. of 0.3. Since many of the earlier works (Vivekanand & Narayan 1981; Srinivasan *et al.* 1984; Narayan 1987; Narayan & Ostriker 1990; Deshpande *et al.* 1995) suggest that pulsars are born with rotation periods as long as a few hundred milliseconds, for the simulation, all pulsars were assumed to be born with a rotation period of 0.1 sec. With the assumption that the magnetic field does not decay with time, the period was evolved with the simple dipole formula 12. Objects were evolved in the local gravitational potential for their corresponding ages (distributed between zero and T with uniform probability). At the end of the simulation pulsars with $B/P^2 < 2 \times 10^{11}$ Gs^{-2} were neglected, since the pulsar activity is believed to cease below this limit. After applying the *selection effect*

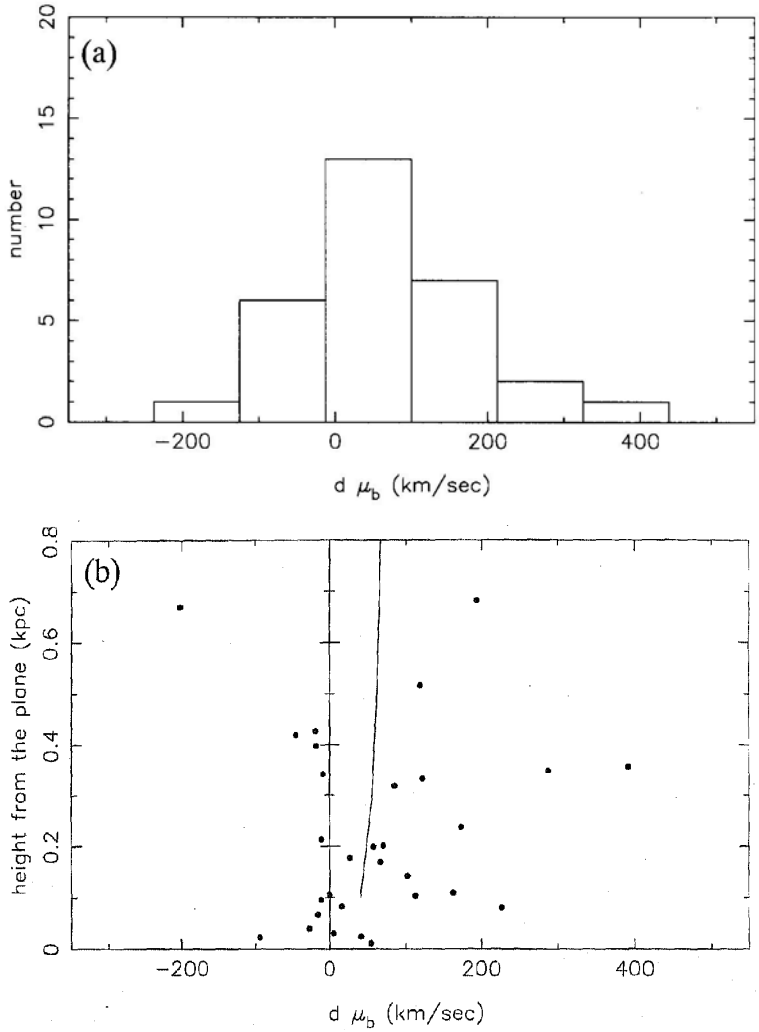

Figure 6. (**a**) Distribution of $d \times \mu_b$ of known pulsars; (**b**) distribution of known pulsars as a function of $d \times \mu_b$ and the height from the plane. Only those pulsars with $|b| < 50°$ and velocity error less than 94 km/sec are included. The solid line gives the mean of the simulated sample for S = 180 km/sec, T = 50Myr.

filter, a subset of the simulated sample (detectable subset of the simulated sample) was selected for comparison with the known sample.

Fig. 7 gives the distribution of known pulsars in the z — log τ_{ch} plane (where τ_{ch} is the characteristic age of the pulsar). The 'dash' line gives the observed mean value of logτ_{ch} in the five different z-slabs from zero to 1 kpc, and the solid line gives the corresponding mean value of the "detectable" simulated sample for the combination of S = 180 km/sec and T = 50Myr. The "dotted" line gives the possible lower limit of τ_{ch} for a given height from the plane i.e., with initial velocities, w_0, ranging from zero to S, the object can reach a given height z, only if its age is greater than a certain value. As one can see from this figure, our model fits with the observed distribution of logτ_{ch} as a function of z, quite satisfactorily. The fact that the envelope in Fig. 7

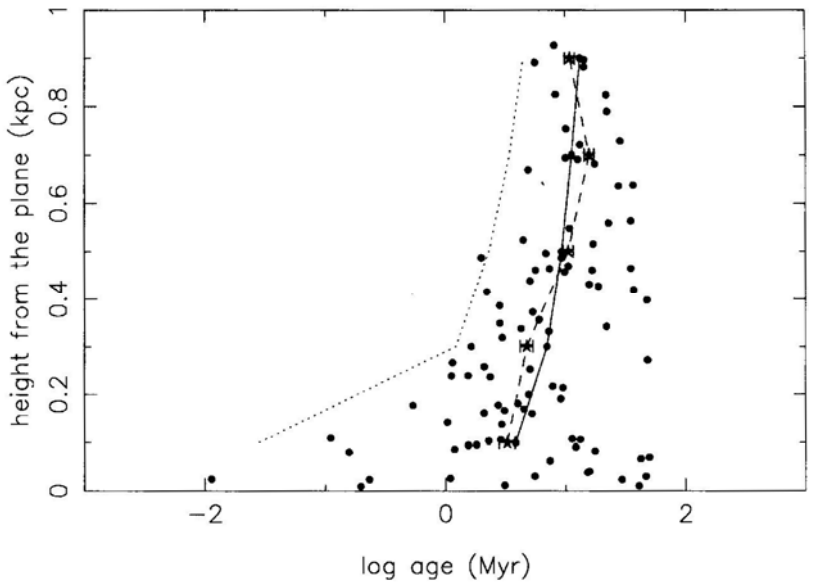

Figure 7. Distribution of known pulsars in z-logτ_{ch} plane. The dash line indicates the average log τ_{ch} as a function of z, for the known sample. Solid line indicates the corresponding quantity for the simulated sample for S = 180 km/sec and T = 50 Myr. The dotted lines give the predicted lower bound for τ_{Ch} as a function of z. The error bars indicate the uncertainty in the mean value.

(given by the dotted line) encloses all the pulsars means that almost all pulsars are born close to the plane and they migrate by the virtue of their velocities. As it turns out, to constrain the combination of S and T, the distribution of log τ_{ch} can be used effectively.

Ideally we would have liked to compare the distribution of log τ_{ch} in each z-slab with the corresponding observed distribution. However, a small number of the observed sample prevents us from doing so.

5. Conclusions

We have explored the hypothesis that pulsars are born in the galactic plane with a unique kick velocity S, distributed isotropically. We therefore investigate the pulsars in the solar neighbourhood by studying the distributions of the velocity components parallel and perpendicular to the galactic plane, and the characteristic age distribution. We find that the known sample of pulsars in the solar neighbourhood is consistent with kick velocities of about 200 km/sec.

We wish to emphasise that our analysis of the nearby pulsars leaves no room for the existence of an appreciable fraction of pulsars with velocities much higher than 200 km/sec. These should have shown up in the plots of Figs. 4 and 6. Evidence for very high velocities came from a few reliable proper motion measurements (Bailes *et al.* 1990; Fomalont *et al* 1992; Harrison *et al* 1993) and velocities inferred from the association of a few pulsars with supernova remnants (Caraveo 1993; Frail *et al.* 1994). The reliability of such associations has been questioned by Kaspi (1996).

The analysis by Brandt & Podsiadlowski (1995) shows that the assumed kick speeds of the order of 450 km/sec are inconsistent with the eccentricity-orbital period distribution of binaries which contain neutron stars, and it is consistent with kick speeds of 200 km/sec. This supports our result.

The velocity distribution derived by Lyne & Lorimer (1993) and Hansen & Phinney (1997), referred to in the introduction and Fig. 1, shows a considerable fraction of pulsars with velocities around 200 km/sec, the value of S we arrived at. They differ from our model in two respects:

1. Both of them show maximum density in velocity space around velocity zero, whereas our model gives zero density at zero velocity.
2. Both of them show a long tail towards the high-speed end. This is recognised in our plots of the velocity components v and w (Figs. 4 and 6), but this represents a small fraction only of the total distribution.

The recent paper by Fomalont *et al.* (1997) has brought out improved proper motion measurements for about fifteen pulsars. Among those pulsars with distance less than 2kpc and galactic latitude less than 50 degrees, on the basis of the earlier measurements we had ignored 155-644 and 1749-28, since they had errors greater than 20 A.U./yr. For 1919+21 and 2045-16 the improved proper motion measurements seem to be quite different from the earlier measurements. However, since these changes are unlikely to change the results in this paper we have done our analysis on the basis of the earlier measurements.

To summarise the main result, we show that if pulsars are postulated to derive a unique isotropic supernova kick speed at their birth around 200 km/sec, the distribution of the proper motions and the characteristic ages of pulsars in the solar neighbourhood can then be understood satisfactorily.

Acknowledgement

We would like to thank Dipankar Bhattacharya for his very valuable comments which have helped us a great deal to improve the manuscript.

References

Bailes, M., Manchester, R. N., Kasteven, M. J., Norris, R. P., Reynolds, J. E. 1990, *Mon. Not. R. Astr. Soc,* **247**, 322.

Bhattacharya, D.,Wijers,R. A. M. J.,Hartman, J. W.,Verbunt, F.1991, *Astron. Astrophys.,* **254,** 198.

Blaauw, A.1961, *Bull. Astr. Inst. Netherlands,* 15, 265.

Brandt,N., Podsiadlowski, P.1995, *Mon. Not. R. Astr. Soc,* **274**, 461.

Caraveo, P.A.1993,*Astrophys. J.*, **415**, L111.

Deshpande, A. A., Ramachandran,R.,Srinivasan, G.1995, *J. Astrophys. Astr.,***16**,53.

Fomalont, E. B., Goss, W. M., Lyne, A. G., Manchester, R. N., Justtanont, K. 1992, *Mon. Not. R. Astr. Soc,* **258**, 497.

Fomalont, E. B., Goss, W. M., Manchester, R. N., Lyne, A. G. 1997, *Mon. Not. R. Astr. Soc,* **286**,81.

Frail, D. A., Goss, W. M., Whiteoak, J. B. Z. 1994, *Astrophys. J.,* **437,** 781.

Gott, J. R., Gunn, J. E., Ostriker, J. P. 1970, *Astrophys. J.,* **160**, L91.

Hansen, B. M. S., Phinney, E. S. 1997, *Mon. Not. R. Astr. Soc,* **291**, 569.
Harrison, P. A., Lyne, A. G., Anderson, B. 1993, *Mon. Not. R. Astr. Soc.,* **261**, 113
Harrison, E. R., Tadimaru, E. 1975, *Astrophys. J.,* **201**, 447.
Hartman, J. W. 1997, Ph. D. thesis, Utrecht University.
Kaspi, V. M. 1996, in *Pulsars: Problems & Progress,* eds. S. Johnston, M. A. Walker, & M. Bailes, *Astron. Soc. Pac. San Francisco,* ASP Conf. Ser. Vol. **105**, p. 375.
Kuijken, K., Gilmore, G. 1989, *Mon. Not. R. Astr. Soc,* **239**, 571.
Lyne, A. G., Lorimer, D. R. 1993, *Nature* (*London*)*,* **369**, 127.
Lyne, A. G., Anderson, B., Salter, M. J. 1982, *Mon. Not. R. Astr. Soc,* **201**, 503.
Narayan, R. 1987, *Astrophys. J.,* **319**, 162.
Narayan, R., Ostriker, J. P. 1990, *Astrophys. J.,* **352**, 222.
Shklovskii, I. S. 1970, *Astr. Zu.,* **46,** 715.
Srinivasan, G., Bhattacharya, D., Dwarakanath, K. S. 1984, *J. Astrophys. Astr.,* **5**, 403.
Taylor, J. H., Manchester, R. N., Lyne, A. G. 1993, *Astrophys. J. Suppl,* **88,** 529 (modified version in the Princeton PSR Catalogue, 1995).
Vivekanand, M., Narayan, R. 1981, J. *Astrophys. Astr.,* **2,** 315.

J Astrophys. Astr. (1998) **19,** 35–53

A Low Frequency Radio Telescope at Mauritius for a Southern Sky Survey

K Golap[1], N. Udaya Shankar[2,1], S. Sachdev[2,1], R. Dodson[2,4] & Ch. V. Sastry[3,1]
[1] *Departments of Physics, University of Mauritius, Reduit, Mauritius.*
[2] *Raman Research Institute, Sadashivanagar, Bangalore 560 080, India.*
[3] *Indian Institute of Astrophysics, Koraimangala, Bangalore 560 034, India.*
[4] *Physics Department, University of Durham, Durham, U.K.*

Received 1998 May 18; accepted 1998 August 3

Abstract. A new, meter-wave radio telescope has been built in the north-east of Mauritius, an island in the Indian Ocean, at a latitude of –20.14°. The Mauritius Radio Telescope (MRT) is a Fourier Synthesis T-shaped array, consisting of a 2048 m long East-West arm and an 880 m long South arm. In the East-West arm 1024 fixed helices are arranged in 32 groups and in the South arm 16 trolleys, with four helices on each, which move on a rail are used. A 512-channel digital complex correlation receiver is used to measure the visibility function. At least 60 days of observing are required for obtaining the visibilities up to 880 m spacing. The Fourier transform of the calibrated visibilities produces a map of the area of the sky under observation with a synthesized beam width $4' \times 4.6' \sec(\delta + 20.14°)$ at 151.5 MHz.

The primary objective of the telescope is to produce a sky survey in the declination range —70° to —10° with a point source sensitivity of about 200 mJy (3σ level). This will be the southern sky equivalent of the Cambridge 6C survey. In this paper we describe the telescope, discuss the array design and the calibration techniques used, and present a map made using the telescope.

Key words. Radio telescope—low frequency—imaging—southern sky—Fourier Synthesis.

1. Introduction

Surveying the sky and compiling catalogs of celestial objects has been a major part of astronomical research for centuries. The first systematic survey of the radio universe was carried out by Grote Reber (1944) using a backyard telescope with a resolution of 12° operating at a frequency of 160 MHz. With the quest for higher angular resolution the exercise of surveying soon shifted to higher frequencies. Even so' many low frequency surveys were carried out after Reber's survey some of which are summarized in Table 1. The table clearly indicates that the sixth Cambridge survey (6C) (Baldwin *et al* 1995) is by far the most extensive

Table 1. Surveys below 1 GHz.

Freq.	Observatory	Resol.	Dec. coverage	Sensit.	No. of sources
Northern declination surveys					
408 MHz	Effelsberg	$0.85° \times 0.85°$	$-10° + 50°$	0.2 Jy	—
178 MHz	Cambr. 3CR	$2' \times 2'$	$-5° + 90°$	9 Jy	328
178 MHz	Cambr. 4C	$7.5' \times 7.5'$	$-7° + 80°$	2 Jy	4843
38 MHz	Cambr. WKB	$45' \times 45'$	$-45° + 35°$	14 Jy	1000
34.5 MHz	GEE TEE	$30' \times 30'$	$-30° + 60°$	5 Jy	≈ 3000
151 MHz	Cambr. 6C	$4' \times 4'$	$+30° + 90°$	0.12 Jy	$> 10^5$
Southern declination surveys					
38 MHz	Cambr. WKB	$45' \times 45'$	$-45° + 35°$	14 Jy	1000
34.5 MHz	GEE TEE	$30' \times 30'$	$-30° + 60°$	5 Jy	≈ 3000
408 MHz	Parkes	$0.85° \times 0.85°$	$-60° + 10°$	1 Jy	–
408 MHz	Molongolo	$2' \times 2'$	$-60° + 18°$	0.6 Jy	> 12000
843 MHz	MOST	$0.4' \times 0.4'$	$-90° - 30°$	–	ongoing
151.5 MHz	MRT	$4' \times 4'$	$-70° - 10°$	0.2 Jy	ongoing

survey at low frequencies. This survey provides a moderately deep radio catalog reaching a source density of about 2×10^4 sr^{-1} over most of the sky north of $\delta = +30°$ with an angular resolution of 4.2' × 4.2' cosec(6) and a limiting flux density of 120 mJy at 151 MHz. An equivalent of the 6C survey for the southern sky does not exist.

Since the survey of Mills *et al.* (1958) at 80 MHz there has not been much effort at low frequencies to map the southern sky apart from the Parkes 408 MHz survey. The Culgoora (Slee 1977) observations at 80 and 160 MHz were made mainly to study known sources and determine their spectral indices. The largest existing radio survey of the southern sky is the Parkes-MIT-NRAO survey (Griffith & Wright 1993) at 5 GHz. There is an obvious need to survey the southern sky at a frequency around 150 MHz. At this frequency synchrotron sources show up much better than at higher frequencies, such as 408 MHz, due to their spectra. Sources also show up better at 150 MHz than at lower frequencies since the absorption due to the interstellar gas is much less than at deca-meter wavelengths. For this purpose a radio telescope operating at 150 MHz has been constructed at Bras d'Eau, Mauritius.

The Mauritius Radio-Telescope (MRT) has been constructed and is operated collaboratively by the Raman Research Institute, the Indian Institute of Astrophysics and the University of Mauritius. It is situated in the North-East of Mauritius (latitude 20.14° South, longitude 57.74° East), an island in the Indian Ocean. It is a T-shaped array with an East-West (E-W) arm of length 2048 m having 1024 helical antennas and a South (S) arm of length 880 m consisting of a rail line on which 16 movable trolleys each with four helical antennas are placed (Fig. 1). The helical antennas respond to frequencies between 80 and 160 MHz. Presently the telescope is operated at 151.5 MHz which allows maximum interference-free observations. The helices are mounted with a tilt of 20° towards the south so that they point towards a declination of –40° at the meridian. The declination coverage corresponding to the Half Power Beam Width (HPBW) of the helices is from –70° to –10°. Fig. 2 shows an aerial view of the telescope and Fig. 3 shows a closer view of the helices used.

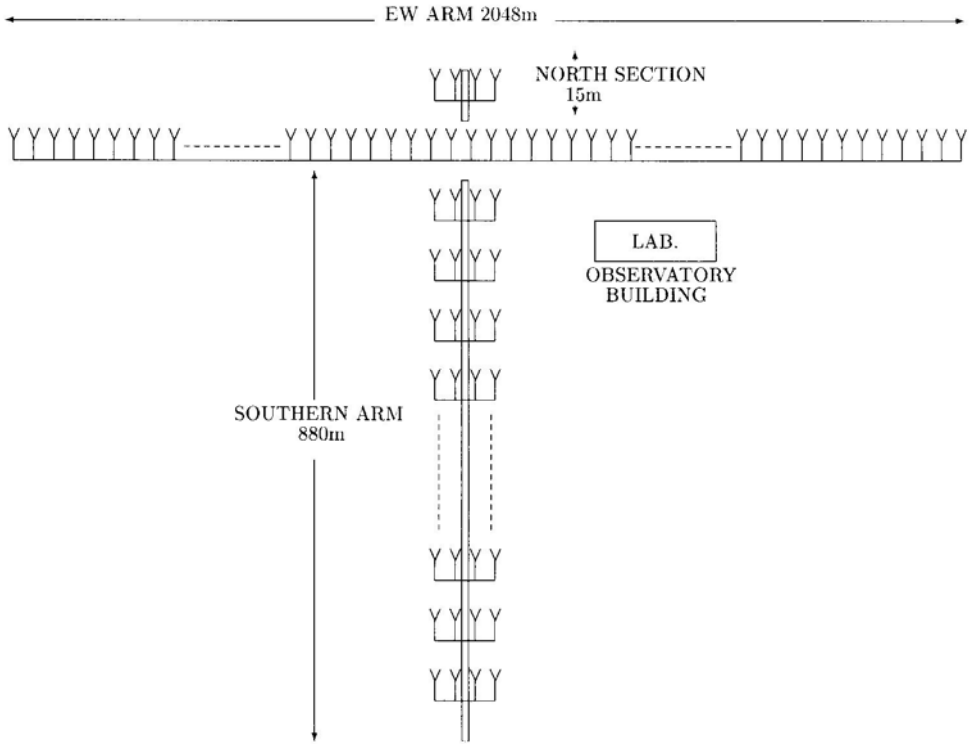

Figure 1. A schematic of the array. The E-W arm has 1024 helices which are divided in 32 groups of 32 helices each. The N-S arm has 16 trolleys each with 4 helices.

The E-W arm is divided into 32 groups of 32 helices each. All the E-W groups are not at the same height, a situation imposed by the uneven terrain. Each trolley in the S arm constitutes one S group. Both E-W and S group outputs are heterodyned to an intermediate frequency (IF) of 30 MHz, using a local oscillator (LO) at 121.6 MHz. The 48 group outputs are then amplified and brought separately to the observatory building via coaxial cables. In the observatory, the 48 group outputs are further amplified and down-converted to a second IF of 10.1 MHz. The 32 E-W and 16 S group outputs are fed into a 32 x 16 complex, 2-bit 3-level digital correlator sampling at 12MHz. The 512 complex visibilities are integrated and recorded at intervals of 1 second. At the end of 24 hours of observation the trolleys are moved to a different position and new visibilities are recorded. A minimum of 60 days of observing are needed to obtain the visibilities up to the 880 m spacing.

The Fourier transform of the phase corrected visibilities obtained after the complete observing schedule produces a map of the area of the sky under observation with a synthesized beam width of $4' \times 4.6' \sec(\delta \pm 20.14^0)$. The phase corrections mentioned above take into consideration the non-coplanarity of the baselines. The expected root mean squared (RMS) values of the background in the synthesized images, arising from the system noise with a 1 MHz bandwidth and an integration time of 8 seconds and from the confusion noise are expected to be around 200 mJy (3σ) and 10 mJy respectively.

Table 2 summarizes the MRT specifications.

Figure 2. An aerial view of the Mauritius Radio Telescope.

Figure 3. A closer view of the helices used.

Table 2. MRT specifications.

Observing frequency	151.5 MHz.
Telescope configuration	T-shaped 2048 m E-W arm and 880 m N-S arm.
Basic element	Helical antenna.
Polarization	Right Circular.
HPBW of helix	$60^\circ \times 60^\circ$.
Declination coverage	-70° to -10°.
Collecting area of helix	$4\,m^2$ at 150 MHz.
East-West arm	32 groups with 32 helices each.
North-South arm	15 trolleys each with 4 helices.
1st IF frequency	30 MHz.
2nd IF frequency	10.1 MHz.
Instrumental bandwidths	0.15,1.0,1.5,3.0 MHz.
Digitization before correlation	2-bit 3-level.
Correlation receiver	32×16 complex channels.
No. of baselines measured per day	32×16.
Minimum and maximum baselines	0, 1024 λ.
Time to get full resolution image	60 days.
Synthesized beam-width	$4' \times 4.6'\sec(\delta + 20.14^\circ)$.
Point source sensitivity	200 mJy (3 σ).

2. The telescope

2.1 *Design criteria*

The array was designed by considering the availability of the 512 channel Clark Lake correlator system' (Erickson *et al* 1982), the constraints due to the available terrain and the presence of man-made interference.

Configuration: A T-shaped configuration was chosen for its simplicity. Aperture synthesis with fixed antennas in the E-W arm and movable elements (trolleys) in the S arm were chosen to minimize the hardware required. An abandoned old railway line running North-South was rebuilt for use as the South arm. This new rail line, slopes downwards at about 1/2° to the horizontal till about 655 m, and then slopes upwards at about 1° to the horizontal. On this rail the trolleys cannot approach the E-W arm nearer than 11 m.

To ensure that the array responds to structures of all sizes in the sky, the array should provide all spacings available in a square aperture. To meet this requirement at MRT, a 15 m North extension with one trolley almost touching the E-W arm has been built and is used to measure the low spatial frequencies. However, this trolley cannot approach the E-W array nearer than 2 m. Hence baselines with 1 m spacing in the S direction are not measured. Non-zero E-W baselines with zero-spacing along the S direction are obtained by multiplying the groups of the eastern arm with the output of four helices which are a part of the first group (closest to the center) of the western arm. This has the same primary beam as a trolley and ensures a weighting similar to baselines with non-zero spacing along the S direction.

[1]After the closure of the Clark Lake radio-telescope the two-bit three-level 512 channel complex correlation receiver was kindly donated to the MRT.

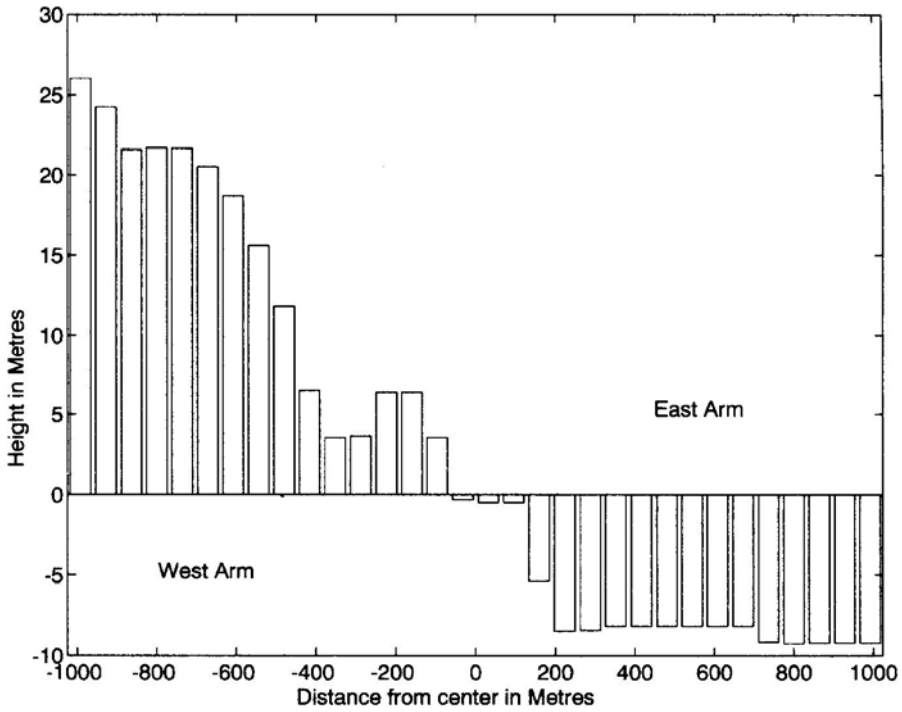

Figure 4. The E-W height profile. The maximum height difference in the E-W arm is 35 m.

Terrain: The locale, terrain is rocky and very uneven, especially along the E-W arm with height differences of up to 35 m. To minimize the problems of non-coplanarity, it was decided to level the E-W arm in multiples of 64 m (32λ) so that the antennas in each group will be at the same height. The height profile of the groups is shown in Fig. 4. For optimal use of the 512-channel complex correlation receiver, several schemes were considered before arriving at a configuration consisting of 16 movable trolleys in the N-S arm and 32 groups in the E-W arm. Details of these considerations are given by K Golap (1998).

Interference: When this telescope was conceived, man-made interference in Mauritius was very low. By the time the array became operational, the increased use of many local communication networks, had increased man-made interference. The front end of the receiver system has been built with sufficient bandwidth so that the observing frequency can be shifted (within 145-155 MHz) to an interference-free zone by tuning the LO. The 1 MHz band around 151.5 MHz has been found to be relatively quiet and is therefore presently being used.

2.2 *The MRT array*

Helix: The primary element is a peripherally fed monofilar[2] axial-mode helix of 3 turns with a diameter of 0.75 m and a height of 1.75 m (Fig. 5). This is mounted above

[2] Monofilar: A term used to distinguish single conductor helix from helices with two or more conductors.

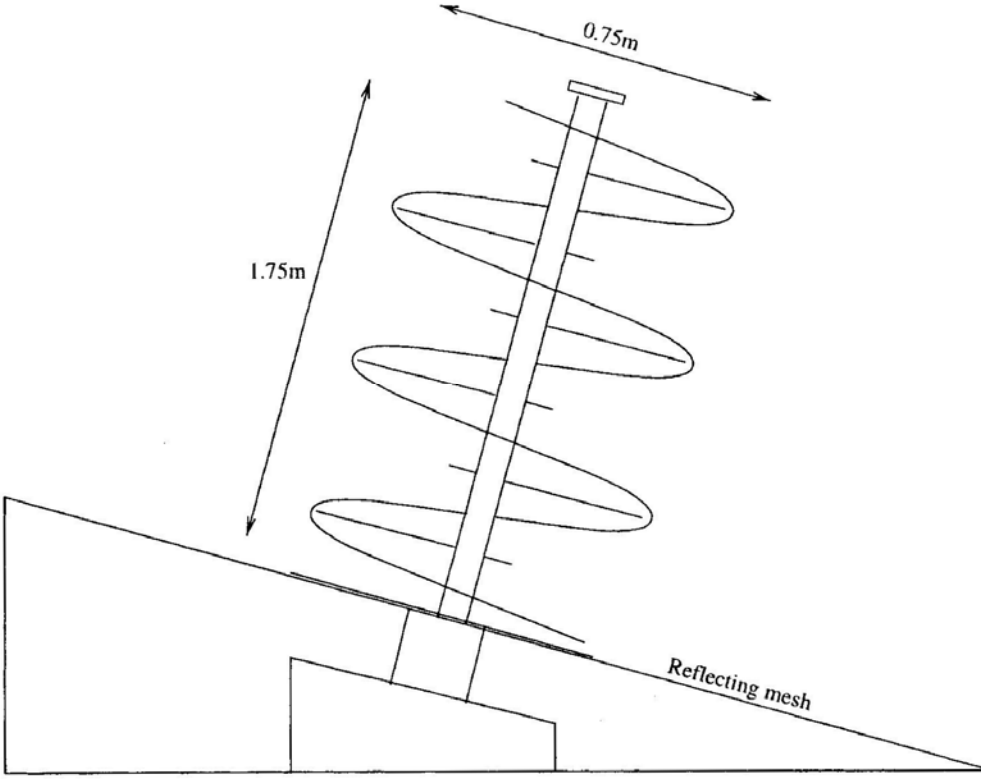

Figure 5. The MRT helix is a peripherally fed monofilar axial mode helix of 3 turns. The helices are mounted with a tilt of 20° to allow a better coverage of the southern sky.

a stainless steel reflector mesh of grid size 2″ × 2″. The helix is wound using a 1.5 cm diameter round aluminium tubing supported with a central UV (Ultra Violet) stabilized, light-weight PVC (Poly Vinyl Chloride) cylinder and radial PVC rods. The axial mode provides maximum radiation along the helix axis.

The helix responds to frequencies between 100 and 200 MHz with right circular polarization (IEEE definition). A quarter-wave transformer used in the feed network optimizes the VSWR to ≤1.5 around 150 MHz. The helical antenna, with its reflector, has a canonical collecting area of about λ^2 (4 m^2 at 150 MHz) with a HPBW of about 60° × 60°. The helices are mounted with a tilt of 20° towards the South to get a better coverage of the southern sky (–70° to –10° dec) including the southern-most part of the galactic plane, a region largely unexplored at meter wavelengths.

E-W and S arms: The E-W arm consists of 1024 helices mounted on a 2 m wide ground plane with an inter-element spacing of 2 m (λ at 150 MHz) and is divided into 32 groups of 32 helices each. As already mentioned, due to the uneven terrain all the E-W groups are not at the same height. The HPBW of the primary beam of each E-W group is 1.8° × 60° and allows observation of a source for roughly 7 × sec(δ) minutes. In each group, four helices are combined using power combiners and the combined output is pre-amplified in a low noise amplifier (noise temperature ≈300K). Eight such amplified outputs are further combined and amplified to form a group output in the E-W array.

Four helices mounted on a trolley with a 4 m-wide ground plane constitute a group in the S array with a primary beam of HPBW 15° × 60°. Each of the 32 E-W and 16 S group outputs are heterodyned to an IF of 30 MHz, amplified and transmitted, using coaxial cables, to the observatory building situated close to the center of the array. Equal lengths of coaxial cables are used irrespective of the distance of the groups from the observatory to ensure that the interferometer outputs are not affected much by changes in the ambient temperature. The configuration of the E-W group is shown in Fig. 6. Each N-S trolley has a similar signal flow path except that there are only 4 helices and 1 pre-filter unit.

Local Oscillator System: Low loss (2.4 dB/ 100 m at 120 MHz) heliax cables running parallel to the East, West and South arms of the array are used to distribute the LO signal required for heterodyning. The 121.6 MHz LO signal at each group is obtained by using directional couplers. To maintain a more or less constant power level for the LO signal (–5 dBm to –7 dBm) across the array, broad-band high-power amplifiers are placed at several places along the heliax cable.

To minimize the spurious correlations in the visibility measurements, the following hardware features are built into the LO system.

- The first LO is phase switched to minimize the effects of cross coupling. The Clark Lake correlator has the facility for generating the Walsh functions required for switching. But it is not practical to use many independent switching waveforms in a series fed LO system owing to the problem of distribution. Hence, we use a simple arrangement in which the LO to the first eight southern groups remain unswitched while, the eastern, the western and the remaining southern groups are switched with orthogonal square waves. The disadvantage of this scheme is that the products of the outputs from groups having the same switching signal are prone to spurious correlations (e.g., the product of any two eastern arm group outputs).
- The signal generator used to produce the LO also generates spurious signals at other frequencies. The spurious signals around 30 MHz, which is our first IF frequency, leaks to the IF port from the LO port of the mixer and results in correlation several times the detection limit. This is minimized by using a band rejection device centered around 30 MHz in the LO path. Band rejection is achieved using a band-pass filter centered around 30 MHz and a power-splitter (Fig. 6). The filter absorbs the signal around 30 MHz and reflects the LO required for heterodyning.

2.3 *The receiver system*

2.3.1 *Second IF and correlator modules*

In the observatory building the 48 group outputs are further amplified. Each of the 32 E-W group outputs are split into two using power dividers. One set of the outputs is combined to form a fan beam of 4′ × 60° using phase-shifter modules. This single beam forming receiver provides a two degree tracking system. Details of pulsar observations carried out using this system are described by N. Issur (1997).

The second set of 32 E-W group outputs and the 16 S outputs are down-converted to 10.1 MHz (second IF). Four IF bandwidths, ranging from 0.15 to 3 MHz are selectable. Signals are then fed to an. Automatic Gain Control (AGC) module which keeps the output power level constant. Each of the 16 group outputs of the S arm and

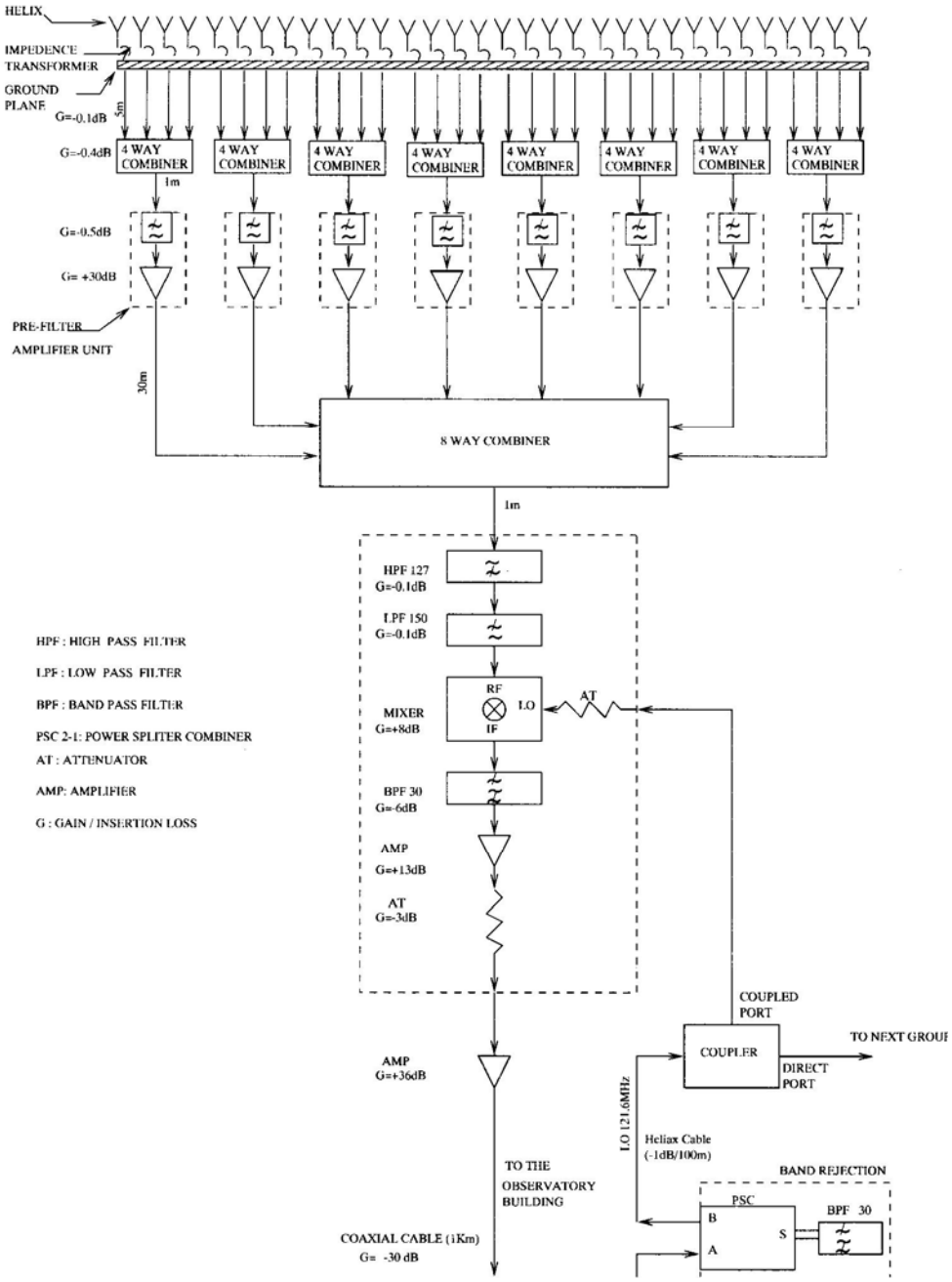

Figure 6. Signal path of an E-W group. The N-S trolley has a similar flow path except that there are only 4 helices and 1 pre-filter unit.

the 16 group outputs of the E arm is split in a quadrature hybrid to obtain the in-phase and quadrature components. Then the signals are digitized to 2-bit 3-level, sampled at 12 MHz and fed into the 32 × 16 complex correlator to obtain the E-W × S outputs. The high sampling rate is to reduce the loss of sensitivity due to quantization. More

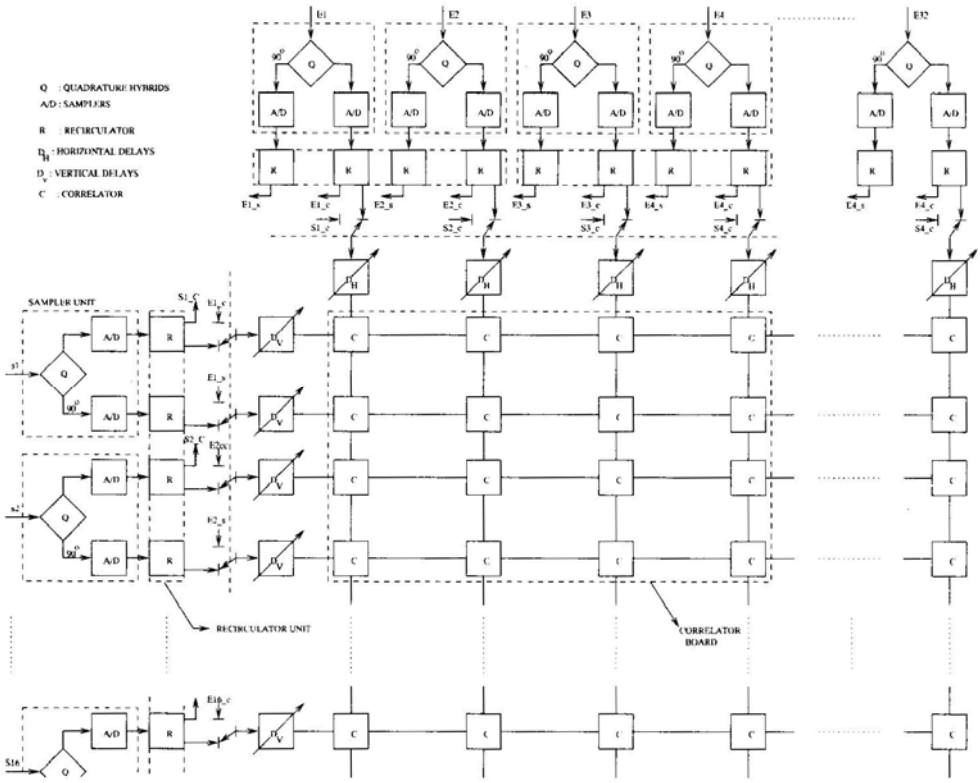

Figure 7. Diagram showing the general layout of the signals to the correlators.

details of the system are given by Erickson *et al.* (1982). Fig. 7 shows the general layout of the samplers, delay lines and correlators.

The last group of the East array (E16) is fed to the correlator in the place of the 16th trolley. This gives a set of baselines formed between E16 and the E-W array on all observing days. This helps to check the repeatability of data. These baselines with each trolley give 31 independent closure information which are used in the calibration. This mode of observing reduces the number of usable trolleys to only 15.

Many observing programs require the formation of fan beams (Issur 1997) corresponding to each arm of the array. The correlator can also be configured to obtain E × E-W and S × S correlations.

Self-correlators: Sixty four self-correlators are available in the receiver system. This provides the necessary information for obtaining the normalized correlation coefficient from the measured digital correlation counts using the correction given by D'Addario *et al.* (1984).

$$\rho = \gamma - \frac{\gamma^3(\alpha_1^2 - 1)(\alpha_2^2 - 1)}{6} \tag{1}$$

where $\gamma = (\pi/2)(N/N_{\max}) \exp(\alpha_1^2 + \alpha_2^2)/2$. α_1 and α_2 are the V_{th}/σ- of the two channels being correlated and $N / N_{\max}$ is the ratio of the correlation value to the maximum value possible out of the 2-bit 3-level system (V_{th} is the threshold-voltage for digitization and σ is RMS value of the signal fed to the digitizer).

The AGCs maintain a constant power level to the samplers, even though the brightness distribution of the sky changes. Therefore we do not get the amplitude informations of the signal from the sky. This results in identical correlation for a weak source in a weak background and a stronger source in a correspondingly stronger background. To measure the absolute brightness while using the AGC there is a need to measure the gains. In many telescopes this is done by adding a fixed amount of a known signal at each antenna. At the MRT, however, the variation in the background radiation as seen by the E-W and the S groups are measured separately by switching off the AGCs, one in each of the E-W and the S arms and using the self-correlators to measure the total power output of these groups.

The self correlators of the MRT are wired such that they measure the probability (P) that the input signal amplitude, V, is between the threshold levels used for digitization. This probability for a zero-mean Gaussian signal with RMS fluctuation of σ and a symmetric 2-level digitizer with voltage threshold levels $\pm V_{\rm th}$, is given by

$$P = \frac{1}{\sigma\sqrt{2\pi}} \int_{-V_{\rm th}}^{+V_{\rm th}} e^{-(V/\sqrt{2}\sigma)^2} \mathrm{d}V = \mathrm{erf}\left(\frac{V_{\rm th}}{\sqrt{2}\sigma}\right), \tag{2}$$

knowing P, the RMS fluctuation σ of the signal can be obtained. The analog correlation p_a is obtained using the relation

$$\rho_a = \rho \times \sigma_1 \times \sigma_2 \tag{3}$$

where σ_1 and σ_2 are the RMS of the signals correlated.

In a 2-bit 3-level correlator, sampling the digitized signal at Nyquist rate, the maximum sensitivity obtainable relative to an analog correlators is 0.81. This is obtained when $V_{\rm th} / \sigma$ is 0.61. The sensitivity changes by only 5% from this optimal value when the signal power changes by 40% (Bowers & Klinger 1974). Hence, switching off the AGC does not affect the signal-to-noise ratio (SNR) of the channels used to measure the total power as the variation of the sky brightness is less than 40%.

Recirculator: Although the use of larger bandwidths results in better sensitivity of a telescope, it restricts the angular range over which an image can be made if the relative delays between the signals being correlated are not compensated. When the uncompensated delay between the signals becomes comparable to the inverse of the bandwidth used, the signals will be decorrelated. At MRT we normally use a bandwidth of 1 MHz. Since the E-W group has a narrow primary beam of two degrees in RA, this bandwidth does not pose a problem for synthesizing the primary beam in this direction. However both the E-W and N-S groups have wide primary beams in declination extending from –70° to –10°. For signals arriving from zenith angles greater than 10 degrees on N-S baselines longer than 175 m, the uncompensated delay results in bandwidth decorrelation greater than 20%.

To overcome this loss of signal one has to measure visibilities with appropriate delay settings, while imaging different declination regions. To keep the loss of signal for a bandwidth of 1MHz to less than 15% in the entire declination range –70° to –10°, the longer baselines have to be measured with four delay settings.

With the existing correlator system this implied observations for four days at trolley locations measuring long baselines. Furthermore, to be able to make inter ference free maps, observations have to be repeated approximately 3 times at each location. This would make the time required to complete the survey very large.

To solve this problem, a recirculator system which measures visibilities with different delay settings using the available correlators in a time multiplexed mode has been incorporated in the receiver system (Sachdev 1998). In this system, the data are sampled at 3 MHz, stored in a buffer memory and the correlations are measured at 12 MHz rate. Such processing by the correlator at a higher speed than the input sampling rate allows correlations to be measured with four delay settings. This ensures that the observations at each trolley allocation, even at longer baselines, can be carried out in one day, thereby, improving the surveying sensitivity. The loss of sensitivity due to the decrease in the input sampling rate from 12 MHz to 3 MHz is not serious. The recirculator system is described in detail by Sachdev (1998).

The recirculator system can configure the correlator in the (E + W) and S × S modes for one integration time (roughly 100 ms in every second of data collection). Since both E-W and S arrays are linear, this mode provides visibilities on several redundant baselines to calibrate the array using the Redundant Baseline Calibration technique (Noordam & Bruyn 1982). Presently the software at MRT does not make use of this data for array calibration.

2.4 *Observations*

In the T configuration, we are interested in sampling baselines with North-South components from 0 m to 880 m with a sampling of 1 m (except the 1 m spacing [section 2.1]). This ensures that the grating response will be confined well outside the primary beam response. To measure the visibilities with a 1 m spacing using 15 trolleys however requires 60 days of observing. Each day the trolleys are spread over 84 m with an inter-trolley spacing of 6 m. 512 complex visibilities are recorded with 1 sec of integration. After obtaining data for 24 sidereal-hours the trolleys are moved by one meter. After 6 days of successful observing we get visibilities measured over 90 m. The trolleys are then moved *en bloc* to measure the next set of visibilities.

3. Imaging with the MRT

The visibilities measured are processed off-line using MARMOSAT[3], the MAuRitius Minimum Operating System for Array Telescopes (Dodson 1997). This is designed in-house to transfer the visibilities to images which can be ported to AIPS. The flow diagram showing the various processing stages is shown in Fig. 8.

The programs in MARMOSAT cater to the following needs: detection of bad data, determination of complex gain of the antennae, position calibration of antennas, combining data of different days, transforming the visibilities to get brightness distribution.

The program **Online** presents an uncalibrated view of the data. It is designed to read visibilities from several baselines and offers to display many functions such as phase, magnitude, closure and fringe frequencies of the visibility measured. The program **Health** monitors the signal-to-noise ratio of the visibilities, correlator offsets, magnitudes of the visibility of all the baselines and displays the mean and the scatter. This helps to detect gross errors quickly. The program **Interference Detection** detects the

[3] A marmosat is a small monkey, distantly related to the ape.

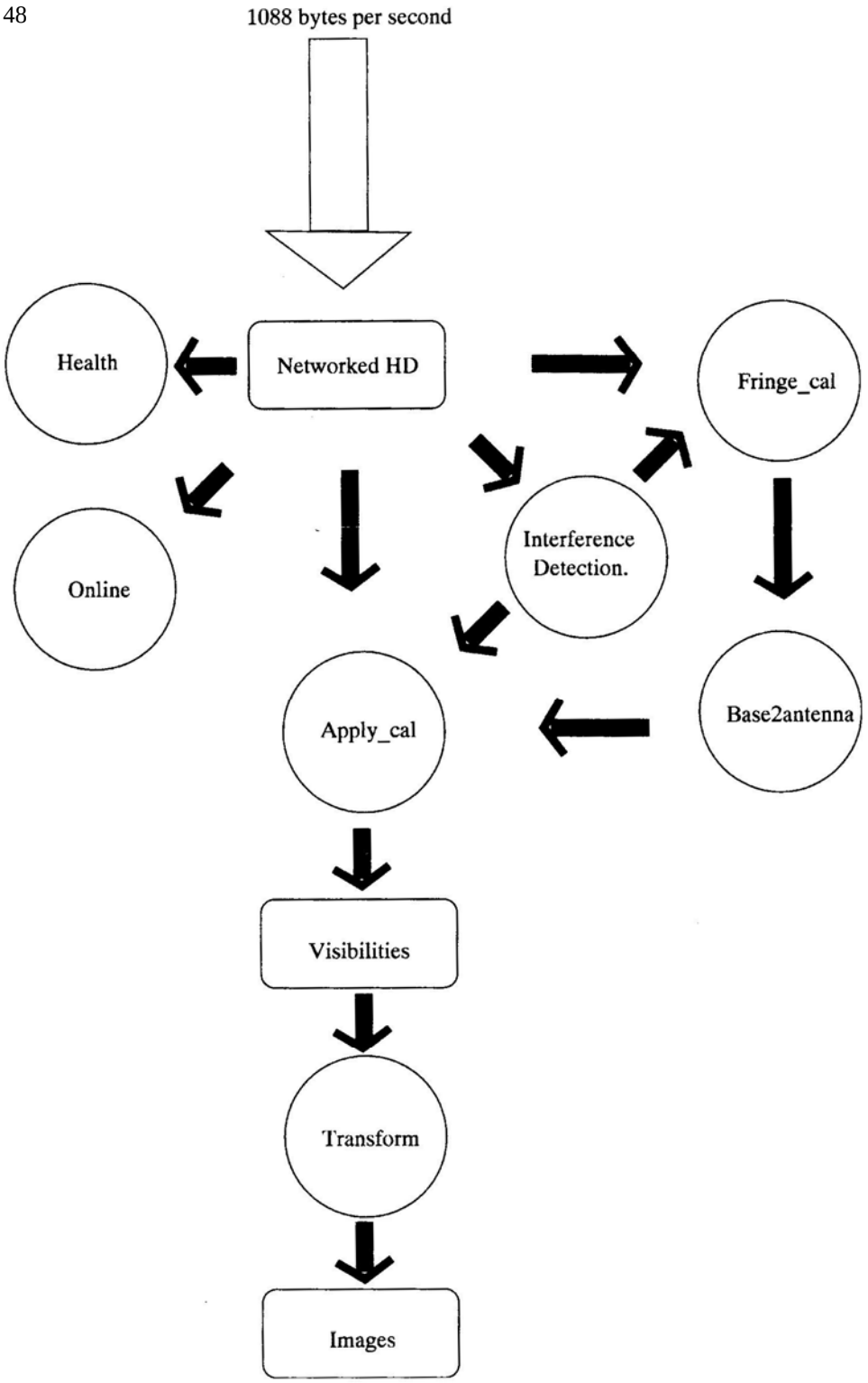

Figure 8. Flow diagram of data acquisition, checking and processing.

interference points which are rejected in subsequent processing. The details of interference detection and their statistics at MRT are given by Sachdev (1998). The programs **Fringe-cal** and the **Transform** are very special to the MRT due to its non-coplanarity and configuration. The following sections describe the concepts behind these programs. Further details of these programs are given by Dodson (1997).

3.1 *Antenna calibration*

The complex gains of the 47 antennae[4] are estimated using the measured visibilities for the calibrators MRC0915-119, MRC1932-464 and MRC2211-173. The sensitivity per baseline is 30 Jy for an integration time of one second. In the 1.8° E-W-group primary beam, the above sources are observable in each baseline with a minimum SNR of about 35.

One of the advantages of observing in the southern sky is that the two very strong sources, Cyg A and Cas A are not in the primary beam, where they would dominate the system temperature causing dynamic range problems.

The disadvantage, however, is a paucity of strong sources required for reliable calibration. This leaves us with a situation where we can calibrate the array only a few times in a sidereal day.

The visibility phase is estimated by fringe fitting (hence the name **Fringe-cal** for the program), where we assume that the sky in the primary beam is dominated by the calibrator. The instrumental phase estimated is simply the difference between the phase of the observed visibilities and the expected geometric phase due to the point source calibrator (or calibrators). The instrumental gain is estimated by measuring the relative amplitudes of the fringes on different baselines. The instrumental phase is insensitive to short term interference and also to fringes due to other sources in the sky, provided their fringe rate is significantly different from that of the calibrator for a given baseline. Therefore, at short baselines where there are less than two fringes in the E-W-group beam due to the calibrator, satisfactory calibration cannot be obtained.

This is tackled at MRT by calculating 47 antenna complex gains from the measured 512 complex visibilities (**base2antenna** in Fig. 8). At this stage we reject those baselines with short E-W components (essentially the first four E and W group outputs with the S array) and input the closure information obtained from multiplying the E16 group with the E-W and S array group outputs.

We have found that the day-to-day RMS variation per baseline in phase is about ±7° and the RMS amplitude variation is about ±0.1 dB. The RMS variation of phase from one calibrator to another (e.g. MRC1932-464 and MRC0915-119) is about ±10°.

Transforming visibilities to brightness: The *u, v* coverage of MRT (E-W and the N-S components of the baseline) can be thought of as a pleated sheet, extended in both *u* and *v*, with discrete steps in *w* (height) as we move from one E-W group to the one at a different height. As we are imaging a very large field of view (60° field), the approximate coplanar approach, wherein the phase term due to the heights is assumed to be a constant over the synthesized field of view, is invalid. Thus for MRT, a 3D imaging method is required.

[4] Since the last group of the eastern array (E16) is used as an input to the correlator in the place of the sixteenth trolley.

Here we transform the visibilities using a Fast Fourier Transforms (FFT) along the regularly sampled v axis, apply a Direct Fourier Transform (DFT) along the w axis and finally sum along u to obtain the image on the meridian. A DFT on w is required as the sampling is not uniform. The direct transform corrects every term along the zenith angle on the meridian for the group heights. This is equivalent to phasing the groups to a common (and artificial) 2D plane.

The N-S array slopes downwards at about 1/2° to the horizontal till about 655 m, and then slopes upwards at about 1° to the horizontal. These two parts are treated separately while transforming. The slope is taken into account by assuming an instrumental zenith appropriate to the slope of the track. While combining contributions from different parts we introduce necessary corrections to get an instrumental zenith equal to the latitude of the place.

The sampling of the visibilities on the E-W grid is at intervals equal to the size of each E-W group. This gives a grating response which falls on the nulls of the primary beam while synthesizing on the meridian. For synthesis away from the meridian, one of the grating response starts moving into the primary beam. This leads to the synthesized beam being a function of the hour angle. Hence to simplify matters, imaging is presently done on the meridian only.

3.2 *Initial results*

One set of observations for all the 880 trolley positions have been made. Because of the presence of the Sun and the day time interference, the data set is not complete for the full RA coverage. A second set of data is being taken to cover the complete accessible sky. The observations are expected to be completed in 1998.

For imaging on the meridian with all the 880 m baselines, the point source sensitivity will be about 200 mJy (3σ) at the peak of primary beam with 8 seconds of integration and a bandwidth of 1 MHz. The confusion limit for an instrument of resolution $4' \times 4'$ is about 13 mJy. For extended structures the surface brightness sensitivity is about 5 mJy/arcmin.^{2}.

While the data collection is underway, we are processing the available data to make a low resolution survey of the sky. Observations up to a baseline of 178 m do not require the recirculator. We have taken this as a natural cutoff and have made low resolution images using only 8 central groups of the E-W arm and trolley positions up to 178 m in the N-S. A part of the survey covering the RA range 18:00 to 24:00 hrs and 00:00 to 05:00 hrs has been completed. In Fig. 9, we present a deconvolved image of the region extending from 0100 hrs to 0200 hrs in RA and –62° and –42° in declination, with a resolution of $13' \times 18'$ sec (σ + 20.14°). MRC1932-464, with a flux density of 81 Jy/beam was used as the primary flux calibrator (Golap 1998). The expected RMS noise due to confusion and system temperature (with an integration time of 19 seconds) is expected to be 0.7 Jy. The noise seen on the-map is 0.8 Jy and is very close to the expected value. A list of 25 point sources in the flux density range 3 to 20Jy seen in the map is given in Table 3. Many of them have been identified with Molongolo and Culgoora sources. A comparison of the flux densities of the sources common to MRT and Culgoora lists showed that the error on the estimated flux densities is less than 25%. The vertical line at RA 01h55m and the feature at RA 01h55m, Dec –59° are due to man-made interference. The image has been

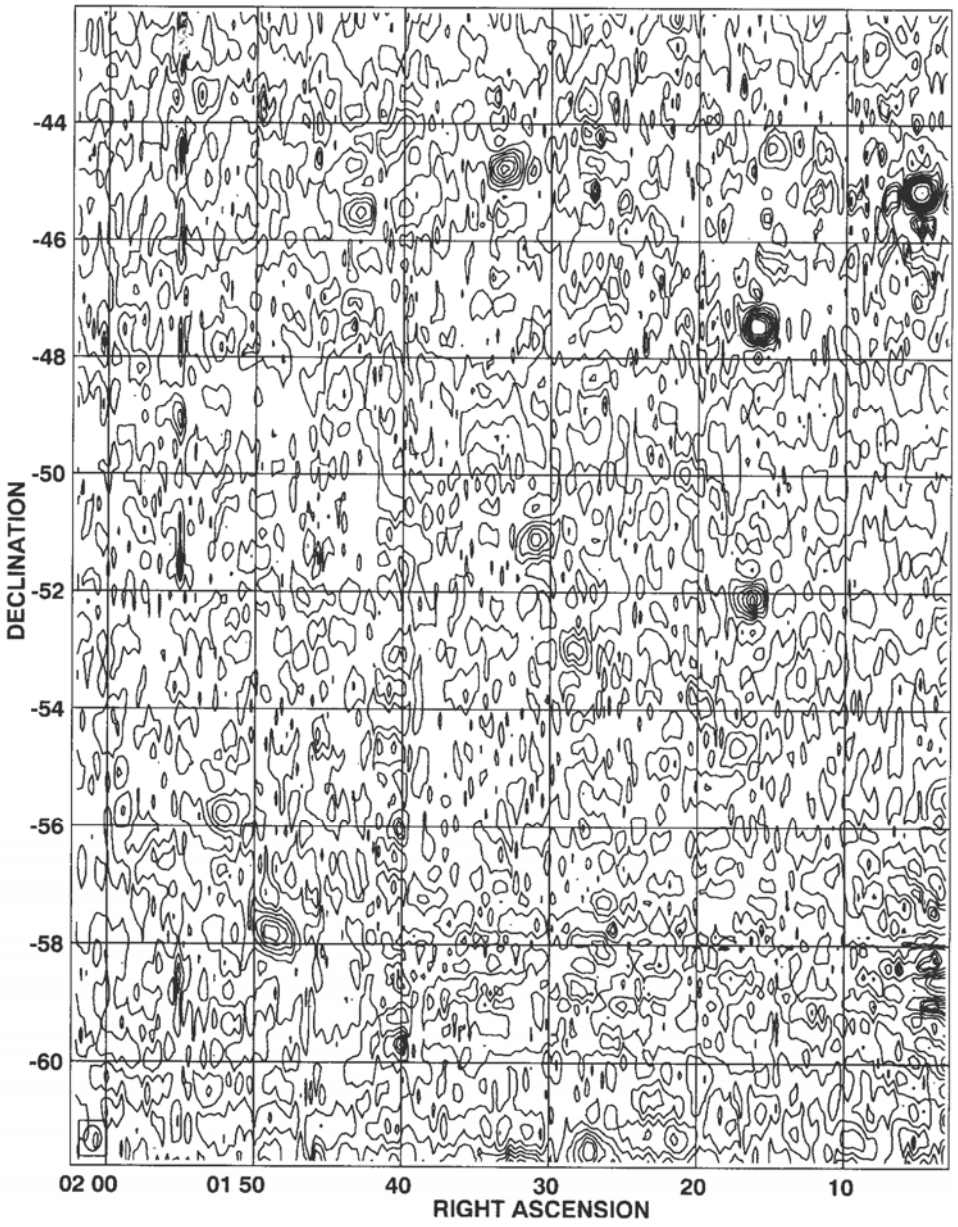

Figure 9. Map at 13′ × 18′ resolution of a typical region away from the galactic plane.The contours are -9 -7 -5 -4 -3 -2 -1 1 2 3 4 5 7 9 11 13 15 17 19 23 27 31 35 45 55 65 Jy/beam. The coordinates are for epoch 2000.

presented here for completeness and to illustrate the success of the methods developed for imaging. A separate paper on the low resolution survey will discuss more details such as the deconvolution procedure for a non-coplanar array like MRT, method used for detecting point sources, measurement of the zero spacing and the flux density scale used.

Table 3. Table giving point sources detected in the image of Fig. 9. The coordinates are for epoch 2000.

RA	Declination	Flux density (Jy)
01:05:26	−45:04	20
01:07:51	−42:40	6
01:08:53	−52:20	4
01:13:23	−53:23	3
01:15:29	−44:23	4
01:16:30	−47:24	15
01:16:51	−52:08	10
01:17:53	−54:39	3
01:18:54	−62:42	7
01:19:58	−53:48	3
01:21:22	−49:59	4
01:23:27	−50:42	5
01:27:15	−51:37	4
01:27:34	−61:32	9
01:27:57	−48:17	4
01:28:38	−52:58	5
01:31:24	−51:06	8
01:31:44	−61:53	12
01:33:30	−44:40	10
01:43:13	−45:27	6
01:49:04	−57:47	8
01:52:33	−55:49	4
01:54:19	−43:32	5
01:55:41	−49:05	4
01:59:30	−47:30	5

Acknowledgements

We thank V. Radhakrishnan for his interest and encouragement right from the initial stages of the project. Our special thanks are due to W. E. Erickson for gifting the CLRO correlator to MRT. We are grateful to M. Modgekar, C. M. Ateequlla and H. A. Aswathapa of the Raman Research Institute; R. Somanah and N. Issur of the University of Mauritius; and G. N. Rajashekar of the Indian Institute of Astrophysics for their efforts in this project. Many other colleagues at the Raman Research Institute, Indian Institute of Astrophysics, and the University of Mauritius also contributed to this project in numerous ways, and we extend our thanks to them. ChVS thanks J. E. Baldwin for many useful discussions and suggestions.

References

Baldwin, J. E., Boysen, R C., Hales, J. E., Jennings, S. E. G., Waggett, P. C., Warner, P. J., Wilson, D. M. A. 1985, The 6c survey of radio sources –1; *Mon. Not. R. astr. Soc.*, **217**, 717-730.

Bowers, F. K., Klinger, R. J. 1974, Quantization noise of correlation spectrometers; *Astr. Astrophys. Suppl.*, **15**, 373-380.

D'Addario, L. R., Thompson, A. R., Schwab, F. R., Granlund, J. 1984, Complex cross correlators with 3-level quantization – design tolerances; *Radio Science*, **19(3),** 931-945.

Dodson, R. 1997, The Mauritius Radio Telescope and a Study of Selected Super Nova Remnants Associated with Pulsars. PhD thesis, University of Durham.

Frickson, W. C., Mahoney, M. J., Erb, K. 1982, The Clark Lake teepee-tee telescope; *Astrophys. J. Suppl.*, **50,** 403-419.

Golap, K. 1998, Synthesis Imaging at 151.5 MHz using the MRT. PhD thesis, University of Mauritius.

Griffith, M. R., Wright, A. E. 1993, *Astron. J.*, **105,** 1666.

Issur, N. 1997, Pulsar Observation with MRT; *Bull. Astr. Soc. India*.

Mills, B. Y., Slee, O. B., Hill, E. R. 1958, A Catalogue of Radio Sources; *Aust. J. Phys.*, **11**, 360.

Noordam, J. E., de Bruyn, A. G. 1982, High Dynamic Range Mapping of Strong Radio Sources, with Application to 3c84. *Nature*, **299**, 597.

Reber, G. 1944, *Astrophys. J.*, **100,** 279.

Sachdev, S. 1998, Wide Field Imaging with the Mauritius Radio Telescope (under preparation). PhD thesis, University of Mauritius.

Slee, O. B., 1977, Culgoora-3 List of Radio Source Measurements; *Aust. J. Phys. Astrophys Suppl.*, **43**, 1-123.

J. Astrophys. Astr. (1998) **19,** 55–61

Low Frequency Quasi-Periodic Oscillations in the Hard X-ray Emission from Cygnus X-1

B. Paul, P. C. Agrawal & A. R. Rao, *Tata Institute of Fundamental Research, Homi Bhabha Road, Mumbai 400 005, India.*
e-mail: bpaul@ tifr.res.in; pagrawal@ tifr.res.in; arrao@ tifr.res. in

Received 1998 June 5; accepted 1998 June 18

Abstract. The observations of the black hole binary Cygnus X-l were made in the energy band of 20-100keV with a balloon-borne Xenon-filled multiwire proportional counter telescope on 5th April 1992. Timing analysis of the data revealed the presence of Quasi-Periodic Oscillations (QPO) in the hard X-ray emission from the source. The QPO feature in the power density spectrum is broad with a peak at a frequency of 0.06 Hz. This result is compared with similar reports of QPOs in Cyg X-l in soft and hard X-rays. Short time scale random intensity variations in the X-ray light curve are described with a shot noise model.

Key words. X-rays: stars — stars: individual Cygnus Xl.

1. Introduction

Cyg X-l, the brightest hard X-ray source in the sky, is one of the best studied binary X-ray sources. The mass function of the companion star clearly indicates the presence of a massive compact object (about 16 $M_{\odot}$), and therefore is often referred to as the first source with observational evidence of a black hole (Webster & Murdin 1972; Bolton 1972). This X-ray source is noted for its peculiar features in several respects, like bimodal behaviour of the spectrum (Zhang *et al.* 1997a), large intensity variations over a wide range of time scales, time lag between soft and hard X-rays (Miyamoto & Kitamoto 1989), dependence of the shape and absolute value of the power density spectrum on the intensity states etc. (Belloni *et al.* 1996; Cui *et al.* 1997; Rao *et al* 1998). Most of the time the source is found to be in a low intensity and hard spectral state. Many of the X-ray properties of this source are also present in other black hole candidates and they are therefore considered to be the distinguishing characteristics of black hole binaries (Tanaka & Lewin 1995).

Black hole sources exhibit many different types of temporal variations in their X-ray intensity. Very rapid variability, flickering, irregular fluctuations and strong quasi-periodic oscillations (QPOs) are often observed in the X-ray light curves of black hole sources (see van der Klis 1995 for a review). Rapid and large amplitude variabilities in the intensity carry information about the irregular accretion flows in the vicinity of the compact object. Quasi-periodic oscillations in the X-ray flux have been observed in several black hole candidates in a wide frequency range. A variety of physical mechanisms have been considered which can produce the observed intensity variations in the black hole sources.

Cyg X-l shows X-ray intensity variations on time scales from milliseconds to months in both the soft X-rays and the hard X-rays. The intensity variations are found to be less pronounced in the high state of the source compared to the same in its low state. The X-ray variabilities have been explained as the sum of randomly occurring X-ray shots and a steady emission (Weisskopf *et al.* 1975). The shots are assumed to be symmetric in shape with exponential rise and decay, or asymmetric with sharp rise and exponential decay. The shots are probably due to the formation of local 'hot spots' in the accretion disks. The structure of the X-ray shots of Cyg X-l in its low state were studied in detail by Negoro *et al.* (1994) with the large area proportional counters onboard the GINGA satellite. Statistics of the X-ray shots including distributions of the shot duration and amplitude and also the temporal distribution of the shots were investigated in the Cyg X-l observations of GINGA (Negoro *et al.* 1995) and with the IXAE (Rao *et al.* 1998).

In some of the low state observations of Cyg X-l, in addition to the random variations, QPOs were also observed in the soft energy band with the EXOSAT (Angelini *et al.* 1992) and in the hard energy band with the SIGMA (Vikhlinin *et al.* 1992) and the BATSE experiments (Kouveliotou *et al* 1992). The QPO phenomena in Cyg X-l. is transient in nature and the peak frequency of the broad QPO signature lies between 0.04 and 0.07 Hz. Of the 13 observations of Cyg X-l with the EXOSAT ME detectors, QPOs were observed only on 4 occasions. The appearance of the QPOs in hard X-rays was found to be correlated with the energy flux whereas in soft X-rays no such correlation was observed. In the BATSE observations, the QPO feature in the power spectrum is broad, centered at a frequency of about 0.04 Hz, and was detected independently in several energy bands ranging from 20 to 320 keV. At high energy the fractional rms variation at the QPO frequency is about 10–15% of the total intensity.

We have performed hard X-ray observation of Cygnus X-l with a low background and good energy resolution telescope to study the energy spectrum and temporal properties of this source in detail. Here we report the detection of a low frequency QPO and random intensity variations in this source.

2. Observation and results

The observations were carried out with a balloon-borne hard X-ray telescope consisting of two xenonfilled multilayer proportional counters (XMPCs). The balloon flight was carried out on 5th April 1992, and the observation was made at a ceiling altitude corresponding toa residual atmospheric column density of 4 gm cm^{-2}. CygX-l was observed continuously for a duration of one hour followed by 4 cycles of 20 minutes source and 10 minutes background observations. The source was in a low state during our observation. The two identical xenon-filled proportional counters (XMPC) have a total effective area of 2400 cm^2 with a $5° \times 5°$ field of view defined by a passive tin-copper graded collimator. The average detection efficiency in the energy range of 20 and 100keV is 50%. For details of the Xray telescope refer to Rao *et al.* (1991). The telescope, mounted on an orientation platform, can be preprogrammed to track a given source by an onboard automated tracking system.

The count rate profile of Cyg X-l and background observation is shown in Fig.1 where summed light curve from the two detectors is plotted. The background count rate was constant during the entire balloon flight. The source count rate changed with

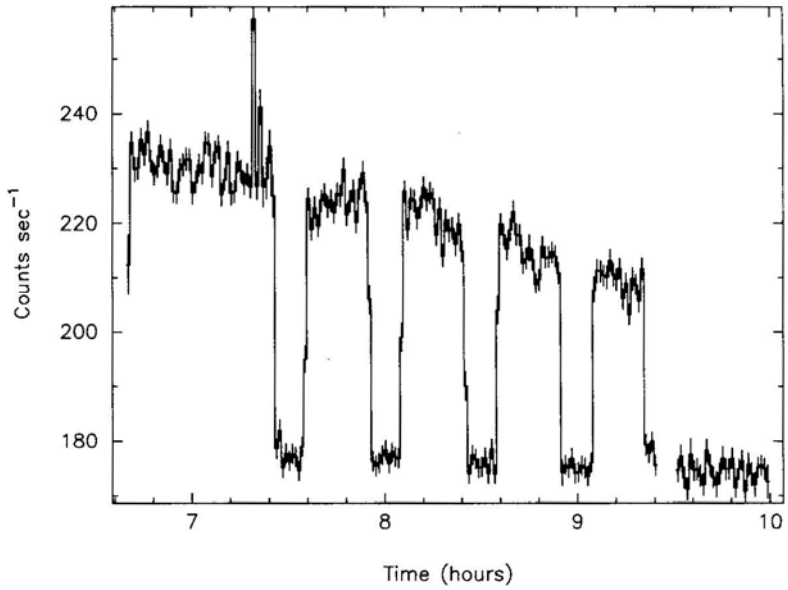

Figure 1. The 20–100 keV light curve of the 5th April 1992 observation of Cyg X-l showing the source and the background count rates in the two XMPC detectors.

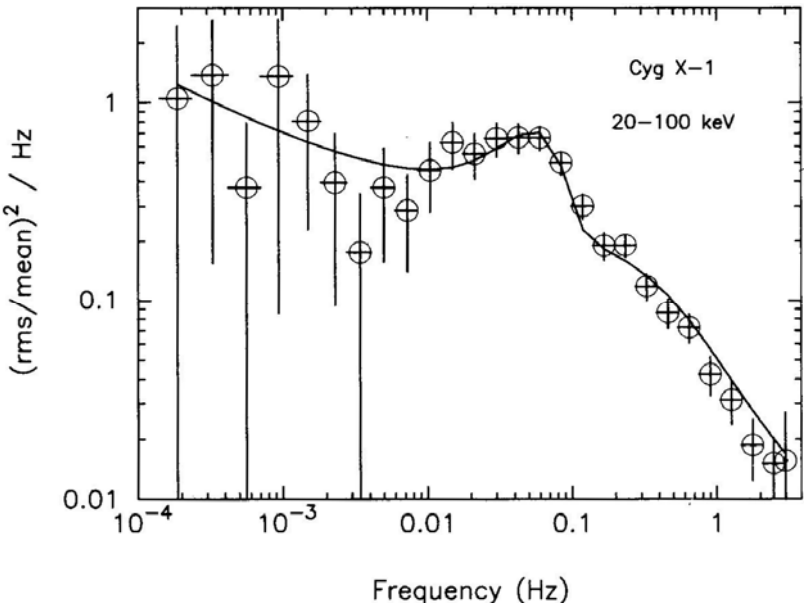

Figure 2. Power density spectrum of Cyg X-l in the 20–100 keV energy band.The continuous line shows the best fit which includes sum of three components, a zero centered Lorentzian, a Gaussian and a power-law component at very low frequency.

the zenith angle because of change in the atmospheric depth along the line of sight. Average Cygnus X-1 count rate near the meridian transit was 51.0 ± 0.8 counts s^{-1}. The energy spectrum in the 20–100 keV range has a power-law shape with a photon index 1.62 ± 0.07 (Chitnis *et al.* 1998).

2.1 *The power density spectrum*

To calculate the power density spectrum (PDS), we generated count rate profile of Cyg X-1 in the 20–100 keV band with a time resolution of 163 ms. The PDS, generated from this light curve in the frequency range of 10^{-4} to 3 Hz is shown in Fig. 2.

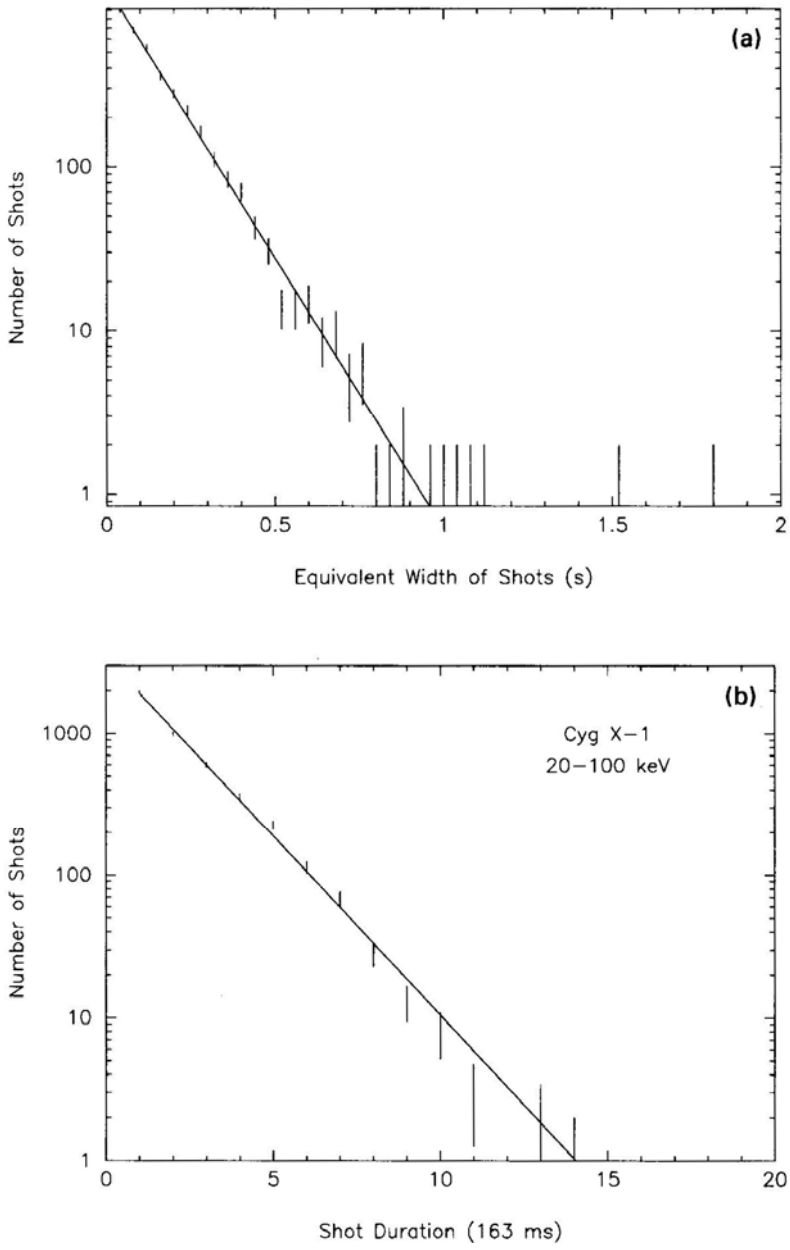

Figure 3. Statistics of the shots in the hard X-rays. (**a**) The number distribution of the shots as a function of equivalent width of the shots. The straight line shows the best fit exponential through the data points. (**b**) The number distribution of shots as a function of shot duration is also exponential in nature.

The PDS is white noise subtracted and is normalized to the mean count rate. Data from the two XMPC detectors were added to improve the statistics. A broad quasi-periodic oscillation peak centered around a frequency of 0.06 Hz is clearly observed in the figure. Apart from the QPO feature, the PDS appears to have a power-law shape which becomes steeper above a frequency of 0.2 Hz. The overall PDS fits well with a model comprising three components, a zero centered Lorentzian of width 0.7 Hz, a Gaussian of width 0.03 Hz centered at 0.06 Hz for the QPO peak and a power-law component of index —0.3 at lower frequencies with the following features:

- A power-law shape above 0.l Hz with index of –0.96;
- A Gaussian type broad QPO peak centered at 0.06 Hz; and
- Increasing power towards very low frequency (< 0.01 Hz). The PDS is similar to the one obtained in other low state observations in hard X-rays (Vikhlinin *et al.* 1992, 1994; Kouveliotou *et al.* 1992; Angelini *et al.* 1992) of Cyg X-1.

2.2 *Shot noise description of the light curve*

We give here a statistical description of the rapid intensity variations observed in Cyg X-1 in its low state. The X-ray variability is assumed to be a result of randomly occurring X-ray shots with a steady emission. To quantify the variations in the intensity as a sum of shots in the light curve of Cyg X-1, we have adopted the following method. Every data bin of the light curve is compared to a running average around it, and if the successive data bins are found to be above the average, a shot is presumed to have occurred. The total excess counts in the individual shots above the average are calculated and the same divided by the averaged intensity gives the equivalent width of the shots. The number distribution of the shots as a function of the equivalent width is shown in Fig. 3(a). It is found that the distribution fits very well with an exponential function with a time scale of 0.13 s. The number distribution of the shots as a function of the duration of the shots is shown in Fig. 3(b), and it also has an exponential form with a time constant of l.7 s.

The distribution of shots in the X-ray light curve of black hole candidates has been explained in the self-organized criticality (SOC) model (Mineshige *et al.* 1994). Negoro *et al.* (1995) have examined this model by analyzing the GINGA data for the hard state of Cyg X-1. Rao *et al.* (1998) found that in the soft X-ray band the shots have an exponential distribution in terms of their strength and duration. The time scales were found to be different in the two intensity states. In the present work we have found that in the hard X-ray band also the shots have similar exponential distribution.

3. Discussion

The QPOs and chaotic intensity variations in black hole sources are likely to provide better understanding of the physical processes taking place in the innermost part of the accretion disk. We have detected quasi-periodic oscillations with a frequency of ~0.06 Hz in the hard X-rays emitted from Cygnus X-1 in our observation on 5th April 1992. QPOs, in the frequency range of 0.04-0.07 Hz were observed from this source in the low intensity state on several occasions both in the hard X-ray band (Vikhlinin

et al. 1994) and in the soft X-ray band (Angelini *et al.* 1994). Quasi-periodic oscilla tions-have also been observed in some other black hole sources LMC X-l, GX 339-4, GS 1124-68, GRO J0422+32 and GRS 1915+105 in the similar low frequency range. Some of these sources e.g. GX 339-4, *GS* 112468 and Cyg X-l also have shown higher frequency QPOs in the range of 1–12 Hz at different intensity states. The frequency of the QPOs detected in these sources is usually lower than the frequency of the QPOs observed in LMXBs and this appears to be characteristic of black hole candidates. There are two black hole candidates namely GRS 1915+105 (Morgan *et al.* 1997) and GRO 1655-40 (Remillard *et al.* 1997), both superluminal jets sources, in which high frequency transient QPOs (67 Hz and 300 Hz respectively) have been observed and are interpreted as signature of the Keplerian motion of material at the innermost stable orbit around the black hole.

Recently Cui *et al.* (1998) have brought into light the relation of QPOs with one very important aspect of the black hole accretion disks, namely dragging of the relativistic frame. They have suggested that QPOs can be produced by X-ray modulation at the precession frequency of the accretion disk. Given the mass of a black hole and the QPO frequency, the specific angular momentum (described as $a_* = J/mcr_g$, where J is the angular momentum and m is the mass) of the black hole can be determined. In the low state of Cyg X-l, the spectrum consists of a hard power-law component and a very low temperature (0.1–0.2 keV) black-body component whereas in the high state the black-body component becomes stronger and the temperature is also higher. In the case of Cygnus X-l, they suggested that the high and the low intensity states in this source are due to the presence of a prograde and retrograde disk respectively (Zhang *et al.* 1997b). The high frequency QPOs (9 Hz) observed in the high state suggests that for a black hole mass of $\sim 10M_\odot$, the specific angular momentum is $a_* \sim 0.5$. With this spin parameter, the QPO frequency for a retrograde disk (in the low state) is expected to be about 2 Hz, whereas the QPOs observed in the low state including the present observation, are in the frequency range of 0.04–0.07 Hz. Additionally, for this hypothesis to explain the observed intensity and spectral changes, the specific angular momentum of the black hole should be $a_* \sim 0.75$. These differences can be reconciled with the fact that there is a large uncertainty in the mass of the black hole and inclination of the system. One important point to note about this model is that the observed changes in the QPO frequency of the black hole sources can also be explained by moderate changes in the inner radius of the disk which may arise due to radiation pressure. Both the low and the high frequency QPOs, also observed in some other black hole sources, may arise due to similar change in the sign of rotation of the accretion disk. It is very important now to do a detailed study of the QPO properties of black hole candidates in different intensity levels which will lead to a better understanding of the disk precession phenomena around the black hole sources.

Acknowledgement

It is a pleasure to acknowledge the contributions of Shri M. R. Shah, Electronics Engineer-in-charge of this experiment, Shri D. K.Dedhia, Shri K. Mukherjee, Shri V. M. Gujar and Shri S. S. Mohite, for their support in the fabrication and testing of the payload and conducting the balloon experiment. We thank the Balloon Support

Instrumentation Group and the Balloon Flight Group led by Shri M. N. Joshi, under the overall supervision of Prof. S. V. Damle.

References

Angelini, L., White, N. E., Stella, L. 1992, *IAU Circ No. 5580.*

Angelini, L., White, N. E., Stella, L. 1994, *New Horizons of X-ray Astronomy: First results from ASCA,* Ed. F. Makino & T. Ohasi, (Tokyo, Japan: Universal Academy Press) p. 429.

Belloni, T., Mendez, M., van der Klis, M., *et al.* 1996, *Astrophys. J.,* **472,** L107.

Bolton, C. T. 1972, *Nature* (*London*), **235,** 271.

Chitnis, V. R., Rao, A. R., Agrawal, P. C. 1998, *Astr. Astrophys.,* **331,** 251.

Cui, W., Zhang, S. N., Focke, W, Swank, J. H. 1997, *Astrophys. J.,* **484,** 383.

Cui, W., Zhang, S. N., Chen, W. 1998, *Astrophys. J.,* **492,** L53.

Kouveliotou, C., Finger, M. H., Fishman, G. J., *et al.* 1992, *IAU Circ No. 5576.*

Morgan, E., Remillard, R., Greiner, J. 1997, *Astrophys. J.,* **482,** 993.

Mineshige, S., Takeuchi, M., Nishimori, H. 1994, *Astrophys. J.,* **435,** L128

Miyamoto, S., Kitamoto, S. 1989, *Nature* (*London*)*,* **342,** 773.

Negoro, H., Miyamoto, S., Kitamoto, S. 1994, *Astrophys. J.,* **423,** L127.

Negoro, H., Miyamoto, S., Kitamoto, S. 1995, *Astrophys. J.,* **452,** L49.

Rao, A. R., Agrawal, P. C, Manchanda, R. K., *et al.* 1991, *Astr. Astrophys.,* **241,** 127.

Rao, A. R., Agrawal, P. C, Paul, B., *et al.* 1998, *Astr. Astrophys.,* **330,** 181.

Remillard, R. A., Morgan, E. H., McClintock, J. E. *et al.* 1997, in *Proceedings of the 18th Texas Symposium on Relativistic Astrophysics,* Ed. A. Olinto, J. Frieman & D. Schramm (Chicago: Chicago University Press), in press.

Tanaka, Y., Lewin, W. H. G. 1995, in X-Ray Binaries, Ed. W. H. G. Lewin, jan van Paradijs & E. P. J. van den Heuvel, (Cambridge University Press) p 126.

Vikhlinin, A., Churazov, E., Gifanov, M. *et al.* 1994, *Astrophys. J.,* **424,** 395.

Vikhlinin, A., Finoguenov, A., Sitdikov, A. *et al.* 1992, *IAU Circ No. 5576.*

van der Klis, M. 1995, in *X-ray Binaries,* Ed. W. H. G. Lewin, jan van Paradijs & van den Heuvel, (Cambridge University Press) p 252.

Webster, B. L., Murdin, P. 1972, *Nature* (*London*), **235,** 37.

Weisskopf, M. C, Khan, S. M., Sutherland, P. G. 1975, *Astrophys. J.,* **199,** L147.

Zhang, S. N., Cui, W, Harmon, B. A. *et al.* 1997a, *Astrophys. J.,* **477,** L95.

Zhang, S. N., Cui, W, Chen, W. 1997b, *Astrophys. J.,* **482,** L155.

J. Astrophys. Astr. (1998) **19**, i–ii

Vijay K. Kapahi

(21st January 1944 – 16th March 1999)

The sad demise of Vijay Kapahi on 16th March, 1999 at the age of 55 is a great loss to the radio astronomy community, particularly so because the Giant Metrewave Radio Telescope near Pune to which he made an essential contribution is about to become fully operational.

Vijay Kapahi was born on 21st January, 1944 in Quetta. He was educated in Meerut, Madras and Bangalore. After his graduation from St. Joseph's College in Bangalore in 1962, he joined the Physics Course of the Training School of the Atomic Energy Establishment in Bombay. In August 1963 he joined the newly formed Radio Astronomy Group of the Tata Institute of Fundamental Research in Bombay. Within two years this group led by G. Swarup set up a 32-element grating interferometer in Kalyan (near Bombay) for solar studies. Subsequently Kapahi contributed to many major aspects of the design and development of the Ooty Radio Telescope (ORT). In particular, he was principally responsible for the development of the complex feed system of the ORT consisting of 968 dipoles with phase shifters operating at 327 MHz.

During the 1970s Vijay Kapahi used the ORT for studying the structure of a large number of radio sources exploiting the technique of Lunar Occultations. These observations yielded the brightness distribution of hundreds of weak radio sources with arcsecond resolution. His first major paper appeared in *Nature* (1971) in which he identified the second BL Lac object AP Lib (1514–24) based on the observations made at Ooty. His studies provided strong evidence in favour of cosmological evolution of the average property of radio sources. In 1975 he showed, for the first time, that not only was the number density of powerful radio galaxies higher at earlier cosmic epochs, but that their linear sizes were considerably smaller. Later, he was able to convincingly demonstrate that the conclusion about the cosmic evolution was not affected by any inverse correlation between the linear size and radio luminosity.

In 1981 Kapahi identified a major class of radio sources – the *compact steep – spectrum sources*. In 1982, along with one of his colleagues, he made a pioneering

statistical analysis of the flux in the compact cores of quasars with a view to unifying models of quasars on the basis of the relativistic beaming hypothesis.

During the past ten years he and his collaborators carried out an important *multi-wavelength* study of a complete sample of 558 radio sources with a flux density above 1 Jy at 843 MHz selected from a 10° wide strip observed with the Molongolo Synthesis Radio Telescope. These extensive series of observations have provided a major source of information about the nature of radio galaxies and quasars at high redshifts, and will remain a lasting tribute to his scientific foresight.

Kapahi was an important member of the team responsible for setting up the Giant Metrewave Radio Telescope about 70 km north of Pune. He was closely associated with the selection of a suitable site, antenna design, surface measurement, array configuration and many other important aspects of the project. In 1994 he became the Director of the National Centre for Radio Astrophysics at Pune which integrates all the radio astronomy activities of TIFR. Among his many achievements in this phase was to successfully lead the team which made GMRT operational. It is a great pity that Kapahi did not live to see the fruits of this major endeavour.

Vijay Kapahi was not only a brilliant astronomer and an able administrator, he was also a committed teacher. Since 1997 he was the President of the Astronomical Society of India. The Indian astronomical community has been impoverished by his untimely death.

Govind Swarup

J. Astrophys. Astr. (1998) **19,** 63–77

The Redshift Dependence of Spectral Index in Powerful Radio Galaxies

Ramana M. Athreya[1] & Vijay K. Kapahi[†], *National Centre for Radio Astrophysics (TIFR), P.O. Bag 3, Pune University Campus, Pune 411 007, India.*
e-mail: *ramana@gmrt.ernet.in*

Received 1997 April 30; accepted 1999 February 9

Abstract. We present and discuss in this paper the rest frame radio spectra (1–25 GHz) of a sample of fourteen radio galaxies at $z > 2$ from the newly defined MRC/1Jy complete sample of 558 radio sources. These galaxies are among the most powerful radio sources known and range in luminosity from 10^{28}–$10^{28.8}$ watt Hz^{-1} at 1 GHz. We find that the median rest frame spectral index of this sample of galaxies at $z > 2$ is significantly steeper than that of a matched luminosity sample of 3CRR galaxies which are at a much lower redshift ($0.85 < z < 1.7$). This indicates that spectral index correlates primarily with redshift, at least in the luminosity range considered here. The difference between the distributions of rest frame spectral curvatures for the two samples does not appear to be statistically significant.

We suggest a new explanation for the steeper spectra of radio galaxies at high redshift involving steeper electron energy spectra at injection. Electron energy spectra are expected to steepen in a first-order Fermi acceleration process, at both non-relativistic and relativistic shock fronts, as the upstream fluid velocity decreases. This may well be the case at high redshifts: the hotter and denser circum-galactic medium at high redshifts could result in slower speeds for the hotspot and the jet material behind it. The smaller sizes of radio sources at higher redshifts provide support to this scenario.

Key words. Galaxies: radio spectra, high redshift radio—synchrotron electron acceleration.

1. Introduction

We have undertaken a multifrequency radio polarisation study of a sample of fifteen radio galaxies at $z > 2$. These galaxies were selected from the newly defined MRC/1Jy complete sample of 558 radio sources (McCarthy *et al.* 1996; Kapahi *et al.* 1998a, b). This project has resulted in several interesting and surprising discoveries including steep spectrum radio cores and large rotation measures in many of the sources (Athreya 1996; Athreya *et al.* 1997, 1998). We discuss in this paper the rest frame radio spectra of these high redshift radio galaxies.

[1] Presently at the l'lnstitut d' Astrophysique de Paris, 98 bis Bd Arago, 75014 Paris. e-mail: athreya@iap fr
[†] Since deceased.

Since Whitfield (1957) first reported that the more distant radio galaxies appeared to have steeper radio spectra, several workers have confirmed and improved the statistics of the correlation between radio spectral index (α: $S_\nu \propto \nu^{-a}$) and radio luminosity (P) or redshift (z). The correlation has in fact been very successsfully exploited to search for high redshift galaxies among radio sources with steep spectral indices (e.g. Chambers & Miley 1990; McCarthy *et al.* 1991; Rottgering *et al.* 1994). Due to the strong P–z correlation in flux-limited radio samples, there has been much debate on whether α correlates primarily with P or with z, though most initial workers have tended to favour an α–P correlation (Laing & Peacock 1980; Macklin 1982; Gopal-Krishna 1988; Wieringa & Katgert 1991).

Using spectral indices defined at a constant rest frame frequency instead of the usual spectral index defined between two fixed observed frequencies Gopal-Krishna (1988) drew attention to the importance of K-correction in spectral index studies because of the steeper spectral index at higher frequencies for many sources. However, all the correlation between α and P cannot be attributed to high frequency spectral steepening, as indeed had been suggested by a much earlier work in which radio sources with straight spectra (same α at all frequencies) also showed an α–P correlation (Bridle *et al.* 1972). Using spectral indices at 1.4 GHz (rest frame) van Breugel & McCarthy (1990) have shown that 3CR galaxies at $z \sim 1.5$ are steeper on the average by ~ 0.1 than galaxies at $z < 0.5$.

The reason for the observed α–P (or α– z) correlation is, however, not clear. Gopal-Krishna & Wiita (1990) have suggested that intrinsically more powerful jets undergo multiple shocks before they are completely randomised and the successive shocks lead to steeper and steeper spectra, resulting in a luminosity correlation. Krolik & Chen (1991) suggest that the increase in the energy density of the cosmic microwave background radiation at higher redshifts would result in faster depletion of high energy electrons and hence steeper spectra due to increased inverse Compton scattering of CMBR photons. Alternatively, they suggest that the correlation may be a selection effect in which the P–z correlation in flux limited samples selects higher magnetic fields (to increase emissivity) which leads to more rapid spectral steepening. Kapahi & Kulkarni (1990) explore the possibility that the correlation is an artifact of the high flux density limits of low frequency radio samples and predict a weaker α–z correlation at fainter flux limits.

The 3CRR sample of extragalactic radio sources happens to be the only large sample with complete optical identification and redshift content; but, the strong P–z correlation in the sample makes it difficult to disentangle the luminosity and redshift dependences of radio source properties. We have been involved with a major observational programme to define and study a new complete sample of 558 extra-galactic radio sources from the Molonglo Reference Catalogue (McCarthy *et al.* 1996; Kapahi *et al.* 1998a, b). The sources in the sample satisfy $S_{408\ \mathrm{MHZ}} > 0.95$ Jy, $-20° > \delta > -30°$ and Galactic latitude $|b| > 20°$. About 96 per cent of the MRC/1Jy sources have already been optically identified. We have obtained spectroscopic redshifts for about 60 per cent of the 447 galaxies so far (the other 111 sources are quasars) and another 21 per cent of the galaxies have redshift estimates from the K-band Hubble relation (McCarthy *et al.* 1999). An important feature of this sample is that more than a third of the galaxies are at $z > 1$, with a substantial fraction extending to $z > 2$. The MRC/1Jy sample is on the average about five times fainter in flux density than the 3CRR. Consequently, at similar redshifts, the 3CRR sources

are five times more luminous than the MRC/1Jy sources. However, the MRC/1Jy sample goes to much higher redshifts than the 3CRR. A comparison of sources in the 3CRR and MRC/1Jy samples should therefore facilitate the disentangling of the redshift and luminosity dependences of source properties. In particular, the nature of the spectral index correlation was one of the questions which motivated this project.

While redshifts are not yet available for all the sources, we have attempted to distinguish between redshift and luminosity as the primary spectral index correlate using a sample of MRC/1Jy galaxies at $z > 2$. In this paper we have compared the spectra of these high redshift radio galaxies (HRRG) with those of a matched luminosity sample of 3CRR galaxies at lower redshifts. The analysis indicates that the primary correlation of spectral index is with redshift and not luminosity.

2. Sample selection

2.1 *High redshift radio galaxy (HRRG) sample at $z > 2$*

Seventeen MRC/1Jy galaxies had been spectroscopically confirmed to have $z > 2$ by 1993. Fifteen of these were observed using the VLA radio telescope in early 1993; the other two had to be left out due to constraints of the range of LST allocated to our project. Subsequently, four more galaxies have been discovered in the sample at $z > 2$. Infrared K-band magnitudes of another twenty galaxies indicate that they are also likely to be at $z > 2$. However, the analysis in this paper is confined to the data on the 15 MRC/1Jy galaxies at $z > 2$ which were observed using the VLA in 1993. The lack of spectroscopic redshifts and/or the insufficient frequency coverage for the others made them unsuitable for inclusion in this work. The possible biases introduced by the incompleteness of the HRRG sample is discussed in detail in section 5.1. The GHz spectra of compact radio sources are often modified by synchrotron self-absorption. For this reason, the compact source 0030–219 was left out of this analysis.

The 14 HRRGs in this study have $P_{1\ GHz}$ (luminosity at 1 GHz) of $10^{28{\cdot}0}$–$10^{28{\cdot}8}$ wattHz^{-1} (median value of 28.37) and range in redshift from 2.0 to 3.13 (median value of 2.38)[2].

2.2 *Matched luminosity 3CRR radio galaxies – IRRG samples*

We have chosen a statistically complete subset of 3CRR radio galaxies which match the $P_{1\ GHz}$ of the HRRG sample. There are 37 3CRR galaxies with $P_{1\ GHZ} > 10^{28}$ watt Hz^{-1}, the most powerful at $P_{1\ GHz} = 10^{28{\cdot}71}$ watt Hz^{-1}. Two of the radio galaxies are smaller than 10 kpc in linear size and have been excluded for the reason given before. The rest of the 35 sources range in redshift from $z = 0.25$ to 1.8.

The MRC/1Jy sample is defined at 408 MHz which corresponds to ~ 1–2 GHz in the rest frame for HRRGs. However, the 3CRR sample was selected at 178 MHz i.e. 0.3–0.5 GHz in the rest frame. Since the original selection frequency of 3CRR is not the one at which the luminosity criterion has been applied in this work, there is the

[2] H_o = km sec^{-1} Mpc^{-1} and $\Omega_o = 1$ used throughout this paper.

possibility that any subset of 3CRR that we choose will be biased towards flatter spectral indices. This is because 3CRR galaxies with a spectrum steeper than a critical value would have $L_{1G} < 10^{28}$ and hence would not be selected by us. However, all the galaxies in the 3CRR with $z > 0.81$ have $P_{1\ GHz} > 10^{28}$ watt Hz^{-1}. So, selecting 3CRR sources at $z > 0.81$ will take care of this bias.

The chosen subsample should contain all the galaxies within a certain range in z for achieving completeness; this subsample should also be statistically similar to the HRRG sample in its $P_{1\ GHz}$ distribution. Further, the range of z must satisfy the conflicting requirements of large sample size as well as distinctness from the redshift distribution of the HRRG sample (since we are examining the redshift dependence of α). Taking all these factors into consideration, we define the Intermediate Redshift Radio Galaxy (IRRG) sample which comprises all the 21 3CRR galaxies at $0.85 < z < 1.7$ and linear size > 10 kpc. These sources have $P_{1\ GHz}$ in the range 10^{28}–$10^{28.68}$; the median value is 28.37 and the difference between the luminosity distribution of the IRRG and HRRG samples is not statistically significant (from a Kolmogorov-Smirnov test).

It is likely that the IRRG sample, as defined here, is biased towards a steeper median spectral index. This is because sources with $P_{1\ GHz} > 1028$ watt Hz^{-1} and a spectral index flatter than a certain value will not be selected into the 3CRR and hence will not be in the IRRG sample. However the lack of radio samples selected at

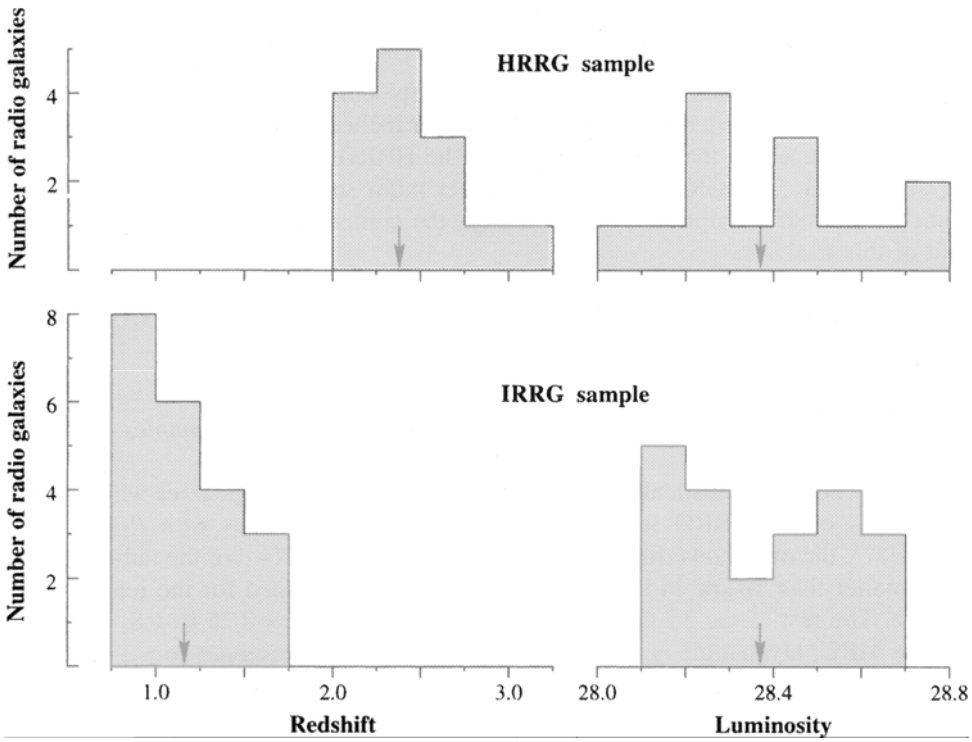

Figure 1. The redshift and luminosity distributions of the radio galaxy samples. The luminosity (at 1 GHz) is in units of log(wattHz^{-1}). The arrowheads indicate the median values.

around 1 GHz with complete redshift information makes it difficult to estimate this effect. We have elaborated on this aspect in section 5.1.

The redshift and luminosity distributions of the galaxies are shown in Fig. 1.

3. The data

The flux densities of HRRGs and the details of the observations from which they were obtained are given in Athreya (1999). In brief, the flux densities were available for most sources at 408 MHz (Large *et al.* 1981), 843 MHz (Subrahmanya & Hunstead, pers. comm), 1.43 GHz, 4.71 GHz, 4.86 GHz, 8.21 GHz and 8.44 GHz (the last 5 from VLA observations). The flux density scale for the VLA observations was that of Baars *et al.* (1977) along with the corrections determined and incorporated into the AIPS[3] package (version 15OCT95) by Perley. The fluxes at the first two frequencies were measured with a telescope beam larger than the sizes of the HRRGs. The high resolution radio images obtained at the higher frequencies did not show any other confusing source in the vicinity of the HRRGs strong enough to affect the estimated flux densities significantly. So neither over-resolution nor contribution from an unrelated source are expected to have corrupted the values at 408 MHz and 843 MHz. The same holds for the flux densities at 1.425 and 4.8 GHz which were estimated from observations with resolutions of 3–4″ arc. The observations at 4.71, 8.21 and 8.4 GHz with a higher resolution of 0″.5 arc are insensitive to structures larger than ~20″ arc. However the considerably smaller total sizes of most of the HRRGs (only 1 source is larger than 12″ arc) make it unlikely that there is a significant underestimation of the flux densities at these frequencies. The standard error in the flux densities of all sources is estimated to be ~5%, most of which is due to the uncertainty in the primary flux density scale itself.

The spectra are plotted in Fig. 2 and Table 1 lists the parameters of the analytic functions used to fit the flux densities. Four different functions of log (ν_{GHZ}) were tried for fitting the log (S_{Jy}) data for each source, viz. (**i**) $A_0 + A_1 \log(\nu)$, (**ii**) $A_0 + A_1 \log(\nu) + A_2[\log(\nu)]^2$ (**iii**) $A_0 + A_1 \log(\nu) + A_2 \exp[+\log(\nu)]$ and (**iv**) $A_1 \log(\nu) + A_2 \exp[-\log(\nu)]$. The last two functions were found to provide the best fit (least χ^2) to the data in each source. The best fits were chosen for calculating the flux densities at other frequencies. The form of the fitting functions is *not* expected to reflect on the nature of the underlying phenomena; they were solely used as aids in interpolation (and perhaps extrapolation a little way beyond the extreme points on either side). The fits are fairly good with 65 per cent of the residuals being less than 3 per cent of the observed values and only 4 per cent of the residuals larger than 10 per cent. The spectrum of 0349–211 is rather poorly fit even by the best fitting function. The concave spectral curvature seen in this source is likely to be due to the inverted spectrum ($\alpha < 0$) of its prominent core. The fitting functions were used to calculate the spectral indices (tangents to the functions) of the HRRGs at various frequencies to investigate the shape of their spectra.

A similar procedure was adopted for the IRRG sample. The analytical fits to the spectra were calculated from the flux densities at 0.178, 0.750, 1.4, 2.695, 5.0, 10.7 and 14.9 GHz (observed) listed in Laing & Peacock (1980), which are also based on

[3] Astronomical Image Processing Systems, distributed by the NRAO.

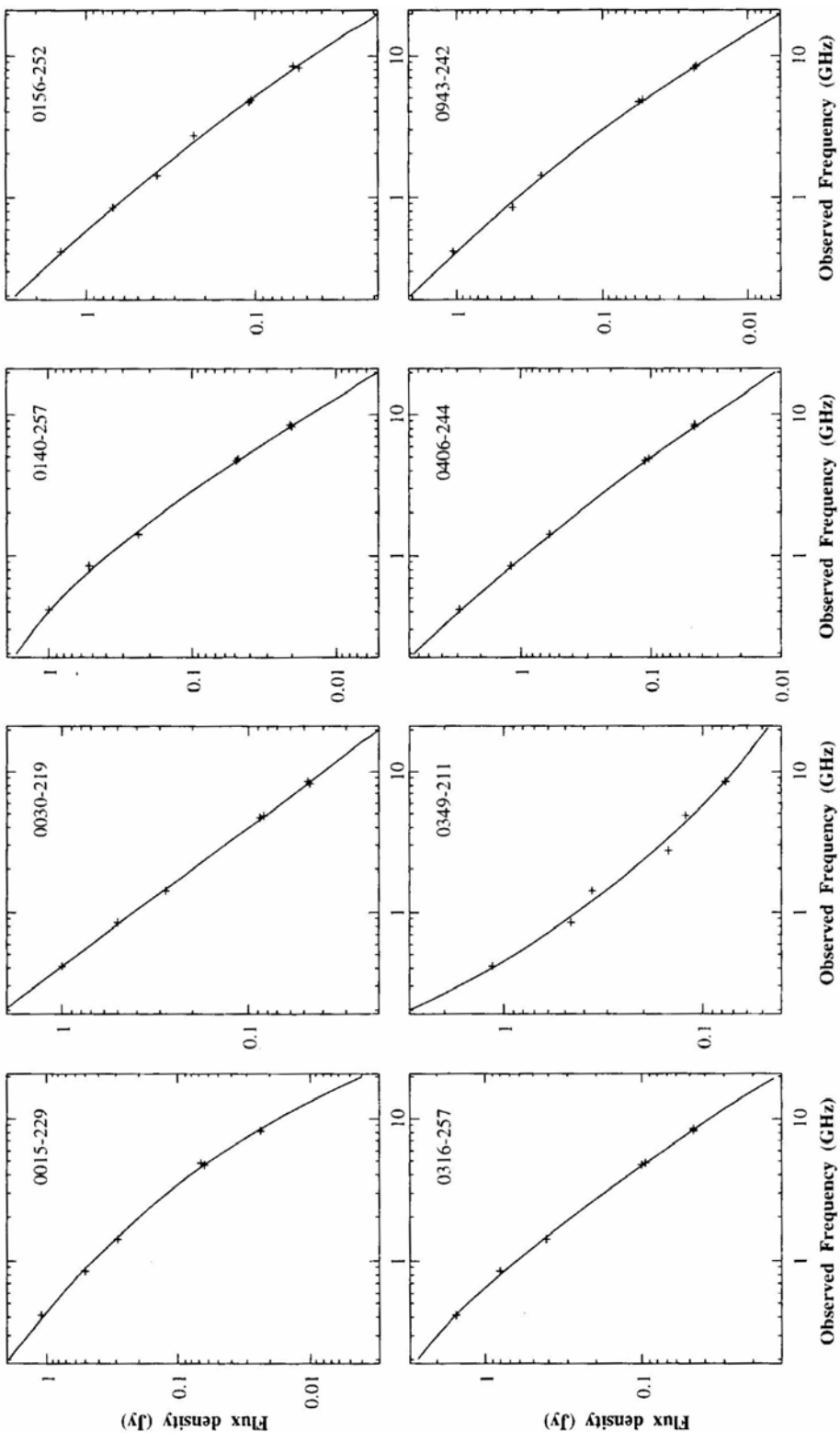

Figure 2. (*Continued*)

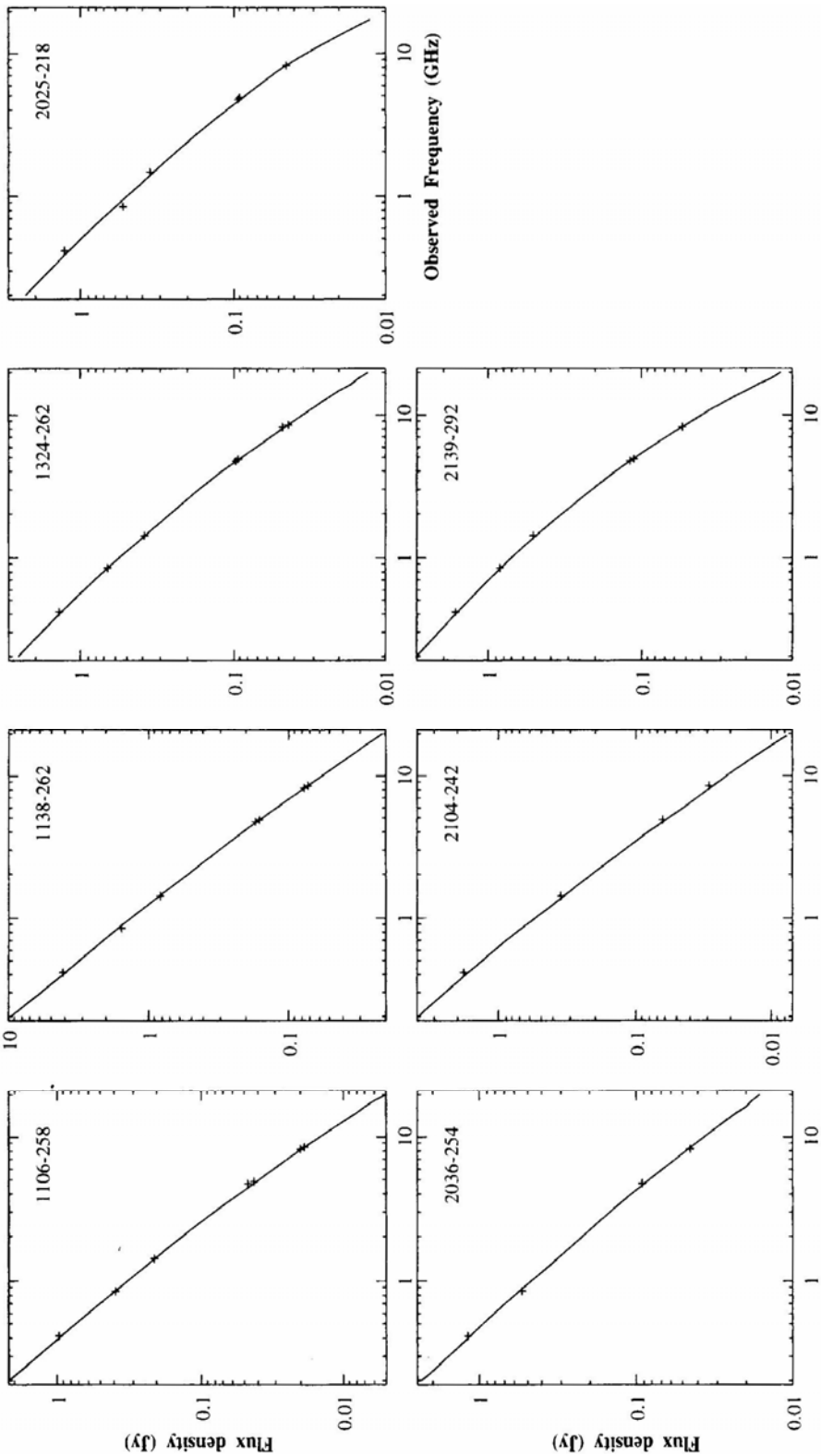

Figure 2. The radio spectra of MRC/1Jy galaxies at $z > 2$ (HRRG sample).

Table 1. Some properties of MRC/1Jy high redshift radio galaxies.

Source	z	$P_{1\,\mathrm{GHz}}$	Size	Co-effs. of the spectral fits				$\alpha^{I}_{1.4G}$	C^{α}_{4G}
		watt Hz^{-1}	arcsec	$e^{\pm}$	A_0	A_1	A_2		
0015–229	2.01	28.07	11.2	+	0.130	−0.573	−0.481	0.92	0.54
0030–219	2.17	28.14	<0.1	+	−0.390	−1.016	0.002	1.01	0.00
0140–257	2.64	28.29	3.8	−	0.246	−1.825	−0.643	0.86	0.62
0156–252	2.09	28.23	6.9	+	−0.072	−0.829	−0.162	0.94	0.18
0316–257	3.13	28.64	6.9	−	0.207	−1.491	−0.403	0.85	0.41
0349–211	2.31	28.28	7.2	−	−0.893	−0.460	0.519	1.21	−0.48
0406–244	2.44	28.75	7.4	+	0.181	−1.095	−0.205	1.23	0.22
0943–242	2.93	28.43	3.6	+	−0.146	−0.857	−0.277	1.03	0.28
1106–258	2.43	28.25	3.6	+	−0.326	−1.066	−0.159	1.17	0.17
1138–262	2.17	28.76	11.4	+	0.240	−1.152	−0.122	1.24	0.14
1324–262	2.28	28.32	1.7	+	−0.025	−0.816	−0.225	0.97	0.24
2025–218	2.63	28.40	4.1	+	−0.135	−0.860	−0.166	0.97	0.17
2036–254	2.00	28.12	5.9	+	−0.221	−0.921	−0.108	1.00	0.12
2104–242	2.49	28.53	21.7	−	−0.009	−1.579	−0.249	1.21	0.23
2139–292	2.55	28.49	7.3	+	0.215	−0.644	−0.360	0.89	0.38

Notes:

1. $P_{1\,\mathrm{GHz}}$: Luminosity at 1 GHz.
2. Size: Linear distance between the outer hotspots.
3. The analytical fits to the observed spectra are of the form $\log(S) = \pm A_0 A_1 \log(\nu) + A_2 \exp(\pm \log(\nu))$, where S is the flux density in Jy, ν is the observed frequency in GHz and the sign of the exponential is listed in column 5.
4. $\alpha^{T}_{1\,4G}$: Spectral index ($\equiv$ d log S/d log ν) at 1.4 GHz (rest frame).
5. C^{α}_{4G}: Spectral curvature ($-\mathrm{d}^2(\log S)/(\mathrm{d}\ \log\ \nu)^2$) at 4 GHz (rest frame).

the flux density scale of Baars *et al.* (1977). The spectral fits for these galaxies are listed in Table 2.

The flux densities used in this work arc the total flux densities for the sources and not that of just the extended emission. While it appears from previous studies that the spectral index correlation is a property of the extended emission (Laing & Peacock 1980), very few radio sources have been observed with sufficiently high resolution over a wide frequency range for obtaining the radio spectra of their cores. The discovery of steep spectrum radio cores in the HRRG sample (Athreya *et al.* 1997) at GHz frequencies did not allow us the liberty of assuming the same flux density for the cores at all frequencies (i.e. $\alpha = 0$) as has hitherto been done for radio sources. Nevertheless, this is unlikely to affect the analysis as the fraction of the total flux density contributed by the core in most sources in less than 1 per cent.

We have compared the distribution of the spectral indices of the HRRG and the IRRG samples at rest frame frequencies of 1, 2, 4, 8 and 16 GHz. These frequencies lie within the range of rest frame frequencies used to fit the spectra for both the samples. Given the strong spectral curvature, it is not clear how dependable are extrapolations of the spectra outside the observed range.

The spectral index values used here are $\alpha^{T}_{\nu} = -(\mathrm{d}\log S/\mathrm{d}\log \nu)_{\nu}$ instead of the usual $\alpha^{\nu 2}_{\nu 1} = -(\log S_{\nu 1} - \log S_{\nu 2})/(\log \nu 1 - \log \nu 2)$. The tangent to the spectrum at $\nu(\alpha^{T}_{\nu})$ is the proper definition of spectral index, of which $\alpha^{\nu 2}_{\nu 1}$ is only an

Table 2. The observed spectra of the intermediate redshift radio galaxy sample.

Source	z	$P_{1\,\mathrm{GHz}}$ watt Hz^{-1}	$e^{\pm}$	Co-effs. of the spectral fits A_0	A_1	A_2	$\alpha^T_{1.4G}$	C^{α}_{4G}
3CR 13	1.351	28.48	−	0.701	−1.337	−0.278	0.99	0.22
3CR 22	0.937	28.17	+	0.636	−0.736	−0.129	0.85	0.18
3CR 65	1.176	28.52	−	1.151	−1.452	−0.504	0.84	0.39
3CR 68.2	1.575	28.54	+	0.519	−1.028	−0.296	1.26	0.36
3CR 175.1	0.920	28.10	+	0.617	−0.734	−0.171	0.88	0.24
3CR 184	0.994	28.25	+	0.759	−0.693	−0.244	0.90	0.33
3CR 217	0.898	28.15	−	0.962	−1.508	−0.474	0.97	0.34
3CR 252	1.104	28.16	−	0.299	−1.143	−0.035	1.10	0.03
3CR 266	1.275	28.32	−	0.321	−1.098	−0.027	1.07	0.02
3CR 267	1.140	28.37	+	0.539	−0.885	−0.042	0.92	0.06
3CR 268.1	0.974	28.56	+	1.097	−0.480	−0.176	0.63	0.24
3CR 280	0.998	28.53	+	0.966	−0.678	−0.143	0.80	0.19
3CR 289	0.967	28.22	−	0.798	−1.247	−0.292	0.91	0.21
3CR 322	1.681	28.66	−	0.782	−1.373	−0.364	0.89	0.31
3CR 324	1.206	28.48	+	0.766	−0.766	−0.223	0.95	0.29
3CR 325	0.860	28.28	−	1.137	−1.362	−0.441	0.87	0.32
3CR 356	1.079	28.18	+	0.449	−0.941	−0.134	1.05	0.18
3CR 368	1.132	28.22	−	0.334	−1.413	−0.102	1.29	0.08
3CR 437	1.480	28.68	−	0.712	−1.029	−0.132	0.86	0.11
3CR 469.1	1.336	28.43	+	0.507	−0.901	−0.128	1.00	0.16
3CR 470	1.653	28.64	+	0.760	−0.580	−0.309	0.81	0.37
3CR 6.1	0.840	28.22	+	0.887	−0.628	−0.220	0.82	0.31
3CR 226	0.818	28.10	+	0.752	−0.764	−0.224	0.97	0.32
3CR 239	1.781	28.71	+	0.417	−1.047	−0.089	1.11	0.10
3CR 263.1	0.824	28.21	−	0.858	−1.213	−0.223	0.96	0.16
3CR 265	0.811	28.18	−	0.809	−1.254	−0.204	1.03	0.14
3CR 294	1.786	28.63	+	0.485	−0.890	−0.215	1.05	0.25

1. See the notes under Table 6 for an explanation of the columns.
2. The 6 sources in a separate block at the bottom are not part of the IRRG sample but have been used for determining the redshift dependence of spectral index (Fig. 4).

approximation necessitated by lack of data at sufficiently large number of frequencies. It is possible to examine spectral properties in finer detail using α^T_ν. We have also investigated the differences in the spectral curvature ($C^{\alpha} \equiv -\mathrm{d}^2(\log S)/(\mathrm{d}\log \nu)^2$) distributions for the two samples.

4. Results

The median spectral indices of the radio galaxy samples at different rest frame frequencies are plotted in Fig. 3. The 1-tailed Kolmogorov-Smirnov test shows that the spectra of HRRGs are steeper than those of IRRG galaxies at all frequencies though at different levels of significance (Table 3); in fact, the alternative hypothesis

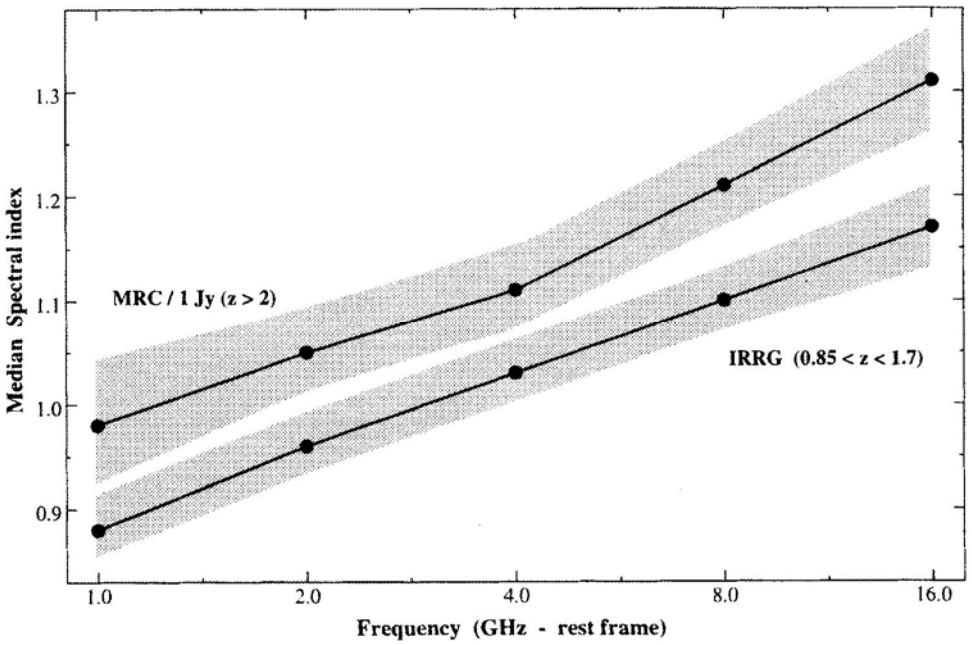

Figure 3. A plot of median spectral index (α_u^T) *versus* frequency for the radio galaxy samples. The shaded area indicates the error on the median values.

Table 3. Kolmogorov-Smirnov tests of the spectral differences between the HRRG and the IRRG samples.

	Spectral index				**Spectral curvature**			
$\nu_{\rm Ghz}$	$\alpha^T_{\rm HRRG} > \alpha^T_{\rm IRRG}$		$\alpha^T_{\rm HRRG} < \alpha^T_{\rm IRRG}$		$C^\alpha_{\rm HRRG} > C^\alpha_{\rm IRRG}$		$C^\alpha_{\rm HRRG} < C^\alpha_{\rm IRRG}$	
	Δ	Σ	Δ	Σ	Δ	Σ	Δ	Σ
1.0	0.381	>0.90	0.095	~0.15	0.143	nc	0.167	nc
2.0	0.357	>0.85	0.095	~0.15	0.143	nc	0.095	~0.15
4.0	0.286	nc	0.048	<0.05	0.238	nc	0.095	~0.15
8.0	0.429	>0.95	0.048	~0.05	0.262	nc	0.071	<0.10
16.0	0.476	~0.98	0.071	<0.10	0.403	>0.90	0.071	<0.10

Notes:

1. Δ: The maximum difference between the cumulative probability distributions.
2. Σ: The probability that the above difference is not due to chance. A value close to 1 recommends the acceptance of the hypothesis (listed in the header of the column) while a value close to 0 recommends rejection of the same; 'nc' indicates that the test was not conclusive (Σ = 0.2-0.8).

that the spectra of IRRGs are steeper may be rejected at a high level of significance. However, the distributions at different frequencies are not strictly independent.

A surprising result is that differences in the spectral curvatures of the two samples are not statistically significant except possibly at the highest frequency of 16 GHz. Though median spectral indices changed by ~0.3 over the frequency range, the differential steepening between the two samples is $\lesssim$ 0.04. The median value of the

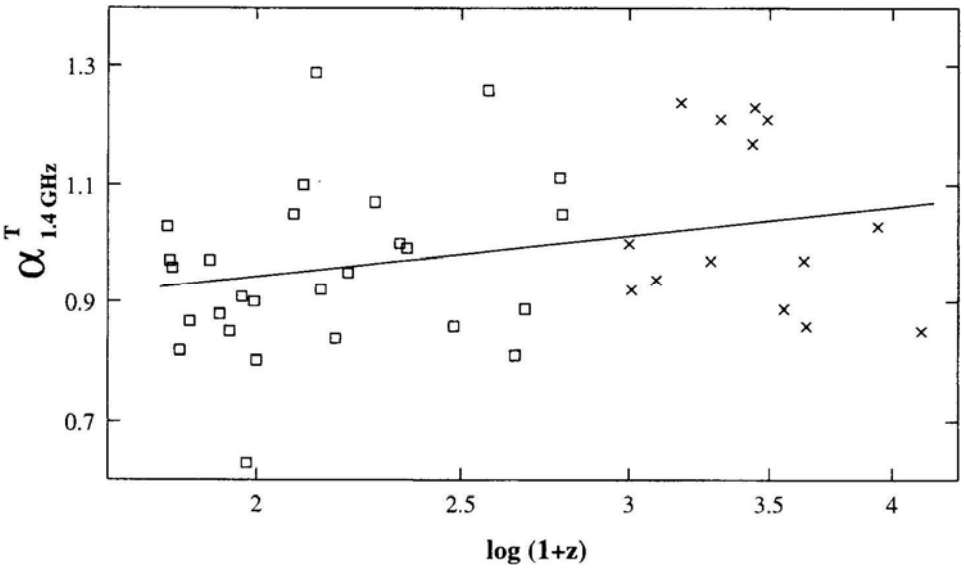

Figure 4. A plot of spectral index *versus* redshift for radio galaxies. The '×' are HRRGs while the open squares are IRRGs. The spectral index values are calculated at 1.4 GHz in the rest frame. The solid line is the best fit for the data.

spectral curvature is 0.23 ± 0.04 for HRRG and 0.18 ± 0.04 for IRRG samples at 1.4 GHz.

The α at 1.4 GHz (rest frame) of 41 radio galaxies is plotted against their redshift in Fig. 4. These 41 galaxies consist of all the sources in the HRRG and IRRG samples and an additional six sources from the 3CRR sample with $P_{1\ GHz} > 10^{28}$ watt Hz^{-1} and $0.81 < z < 0.85$ or $z > 1.7$. The data may be fitted by a linear function of the form $\alpha = (0.82 \pm 0.08) + (0.40 + 0.20) \log (1 + z)$ at 1.4 GHz. The fit has a correlation co-efficient of 0.301, the confidence co-efficient of the correlation being >95 per cent. The plot (and the correlation co-efficient) shows that the scatter about the best fit line is considerable. However, we find that the residuals of the fits are not correlated with luminosity (correlation co-efficient of –0.067, confidence co-efficient 33 per cent).

5. Discussion

5.1 *The α–z correlation*

Since the two samples used here are matched in luminosity, our result indicates a primary relationship between a and z in the luminosity range of 10^{28}–10^{29} watt Hz^{-1}. The fit is consistent with a spectral index difference of 0.1 at 1.4 GHz between 3CR galaxies at $z < 0.5$ and $z \sim 1.5$ reported by van Breugel & McCarthy (1990)—i.e. the redshift dependence is sufficient to explain the change of spectral index within the 3CRR. This, together with the lack of a residual luminosity-spectral index correlation in our study (although the statistics are not sufficient to rule out the correlation either) suggests that the luminosity dependence of spectral index, if any, is not important.

However, the best way of confirming this would be to select sources at a fixed redshift but spanning a wide range in luminosity.

One of the principal objectives behind the definition and study of the MRC/1Jy sample was the discovery and study of high redshift radio galaxies (see McCarthy *et al.* 1991; Athreya 1996, 1999; Athreya *et al.* 1997, 1998). To this end, spectroscopy was first carried out for those MRC/1Jy sources more likely to be at high redshifts, i.e. small angular sized sources with steep radio spectra between 408 and 843 MHz ($\alpha > 0.9$). The spectroscopy of most of the other *normal spectrum* ($\alpha < 0.9$) galaxies was carried out subsequently. All the 38 MRC/1Jy $z > 2$ galaxies presently known are from the steep spectrum sample only and none of the 121 normal spectrum galaxies have been found to be at $z > 2$. Therefore, though the initial selection of the HRRG sample suggested a strong steep spectrum bias, subsequent results show that the HRRG sample is likely to be representative of the complete set of MRC/1Jy $z > 2$ galaxies as far as their radio spectra are concerned.

We have already explained in section 2 that the median spectral index of the IRRG sample may be biased towards a steeper value and also the problem associated with quantifying this effect. However, any such bias would only make our conclusion more significant. We tried to estimate this bias using sources in the MRC/1Jy sample. We selected all the sources satisfying $0.85 < z < 1.75$, $P_{1\ \mathrm{GHz}} > 10^{28}$ watt Hz^{-1} and with $S_{178} < 10$ Jy. The redshift range is identical to that of the IRRG sample but the median redshift of the sample is ~ 1.6 which is considerably higher than ~ 1.2 of the IRRG sample. The MRC selection frequency of 408 MHz corresponds to a rest frame frequency of ~1 GHz for these sources which is appropriate for our purpose. These sources should represent the 1 GHz selected population which would not be in the 3CRR because of the above bias. We only have $\alpha_{5\mathrm{G}}^{408\mathrm{G}}$ (observed frame) for these sources, which to first order corresponds to $\alpha_{1.4G}^{T}$ (observed) or $\alpha_{3.7G}^{T}$ (rest frame). The median spectral index of this sample is 1.06. Compensating for the higher redshift (using our α-z relationship) reduces this median value to 1.03 which is the same as that of the IRRG sample. Given the incompleteness of this subsample, the inadequate frequency coverage and the error bars, we can only say that the bias is unlikely to be significant.

One other question is how significant is the use of a particular cosmological model for this result. The increase in the luminosity of sources is larger for more distant sources as the deceleration parameter decreases. This would affect our result by modifying the selection of sources. For example, using $q_0 = 0.2$ (instead of 0.5), would brighten the sources at $z = 1.2$ and 2.3 by factors of ~4.5 and 2, respectively. As a result we would have to eliminate some of the lower luminosity (and hence redshift) sources from the IRRG sample and some of the higher luminosity/redshift sources from the HRRG sample to ensure that the luminosity distributions are the same. Doing so, we found that the median value of $\alpha_{1\ 4\mathrm{G}}^{T}$ remained unchanged at 0.91 for the IRRG sample despite the removal of five sources; the median reduced by 0.02 for the HRRG sample with the elimination of three sources. However the difference in the redshifts of the two modified samples is less than before and the change is sufficient to account for the reduction in the spectral index difference. But the change of 0.02 in the median value is not statistically significant and we believe it is as likely to be due to statistical noise as due to a change in the redshift distribution. It would be safe to say that cosmology is not a critical parameter here (excepting that more extreme cosmologies would sharply reduce the number of useful sources in the two

sub-samples!)—given the small numbers of sources involved we feel that a more elaborate analysis of the effect of cosmological parameters would not be useful.

5.2 *Steeper electron energy spectra at high redshifts*

The similar spectral curvature seen in the two samples is rather surprising. All the explanations for the spectral steepening with redshift invoke an increased steepening of the spectrum *in the rest frame* at higher redshifts due to a more rapid evolution of the synchrotron spectral break to lower frequencies which is not indicated by this data. Perhaps, one must also consider the possibility of steeper electron injection spectra at higher redshifts.

Synchrotron electrons are believed to be accelerated to ultrarelativistic energies by a first-order Fermi process at the shock front between the hotspot and the ambient medium. In the case of non-relativistic shocks, the index of the electron injection spectrum in this process, s (i.e $N(E) \propto E^{-s}$)is related to the Mach number, M, (through the compression ratio) of the shock front by $s = 2(M^2+1)/(M^2 - 1)$ for a monotomic gas (Longair 1994). The injection spectral index is given by $\alpha_i = (s - 1)/2$. This expression provides a lower limit of $\alpha_i = 0.5$ (for strong shock conditions, i.e. $M \gg 1$). The observed lack of extended radio sources with spectral indices flatter than 0.5 is explained by this acceleration process.

A similar result has been shown in the case of relativistic shocks. For example, Kirk & Schneider (1987) show that the electron energy index is a very sensitive function of the bulk velocity upstream of the shock. Starting with $s \approx 2$ ($\alpha = 0.5$) for velocity $\sim c$, the spectrum steepens to $s = 2.8$ and 3.6 (i.e. $\alpha = 0.9$ and 1.3) for velocities of 0.9c and 0.8c respectively.

Thus, in the case of radio sources, any reduction in the bulk velocity of plasma, would result in the production of electrons with a steeper energy distribution. This would be true in the diffuse regions in radio lobes (non-relativistic shocks) as well as in the vicinity of hotspots (relativistic shocks).

The conditions at higher redshifts may well result in steeper electron spectra. We know that linear sizes of radio sources decrease with redshift (Oort *et al.* 1987; Kapahi 1987; Athreya 1996). This is usually taken as evidence of lower expansion speeds due to higher gas density at high redshifts (for e.g. Swamp & Subramanian 1990; Gopal-Krishna & Wiita 1990). The phenomenon of cluster cooling flows suggests that the temperature of the ambient medium evolves with redshift. At higher redshifts, the radio jet would have to work against the higher pressure of the denser and hotter circumgalactic medium. This would slow down the hotspot propagation speed as well as the bulk flow of the jet material behind the hotspot. Consequently, Fermi acceleration would lead to steeper electron energy distributions. In this model, the large scatter seen in the redshift-spectral index plot reflects the object-to-object variation of the temperature and density of the circumgalactic (or intracluster) medium.

It also follows from this model that one should not see any correlation between redshift and spectral index at very low redshifts which is indeed the case (for example, Laing & Peacock 1980). As the circumgalactic gas density and temperature decrease at low redshift, the electron index rapidly tends towards the asymptotic value.

An additional pointer to steeper electron injection spectra at high redshifts is the steep spectral index values at high frequencies. Synchrotron radiation results in a faster depletion of high energy electrons and a progressive steepening of the high frequency spectrum from its initial a corresponding to the injected (i.e. unmodified) electron spectrum. Under conditions of a continuous replenishment of ultra-relativistic particles, as is most probably the case in these active radio sources, it has been shown that the spectral index at high frequencies cannot be steeper by more than 0.5 of the value corresponding to the initial electron spectrum (Pacholczyk 1970). The median α of 1.31 at 16 GHz (rest frame) suggests that the median α corresponding to the initial electron spectrum is ≥ 0.8.

6. Conclusion

- A comparison of the spectra of sub-samples of matched luminosity radio galaxies from the 3CRR and the MRC/1Jy samples indicates that spectral index correlates primarily with redshift; the luminosity dependence, if any, is not likely to be significant.
- It is suggested in this paper that the electron energy spectrum at injection itself may be steeper at higher redshifts; we have also shown that the typical values of the relevant parameters for radio sources are indeed in the right ballpark to make such a model plausible. However, the idea needs to be worked out in detail.

Acknowledgements

We would like to thank the referee for helpful comments and suggestions. The VLA is operated by the Associated Universities Inc. under co-operative agreement with the National Science Foundation, USA.

References

Athreya, R. M. 1996, Ph.D Thesis, University of Bombay.

Athreya, R. M. 1999, *Astr. Astrophys. Suppl.* (submitted).

Athreya, R. M., Kapahi, V. K., McCarthy, P. J., van Breugel, W. 1997, *Mon. Not. R. Astr. Soc.*, 289, 525.

Athreya, R. M., Kapahi, V. K., McCarthy, P. J., van Breugel, W. 1998, *Astr. Astrophys.*, **329,** 809.

Baars, J. W. M., Genzel, R., Pauliny-Toth, I. I. K., Witzel, A. 1977, *Astr. Astrophys.*, **61,** 99.

Bridle, A. H., Kesteven, M. J. L., Guindon, B. 1972, *Astrophys. Lett.*, **11,** 27.

Chambers, K. C., Miley, G. K. 1990, in *The evolution of galaxies*, ed. R. G. Kron (Hubble Centennial Symp., ASP Conf. Ser. 10) pg 372.

Gopal-Krishna 1988, *Astr. Astrophys.*, **192,** 37.

Gopal-Krishna, Wiita, P. J. 1990, *Astr. Astrophys.*, **236,** 305.

Kapahi, V. K. 1989, *Astr. J.*, **97,** 1.

Kapahi, V. K., Athreya, R. M., Subrahmanya, C. R., van Breugel, W., McCarthy, P. J. 1998a, *Astrophys. J. Suppl.*, **118,** 275.

Kapahi, V. K., Athreya, R. M., Subrahmanya, C. R. Baker, J. C., Hunstead, R. W., McCarthy, P. J., van Breugel, W. 1998b, *Astrophys. J. Suppl.*, **118,** 327.

Kapahi, V. K., Kulkarni, V. K. 1990, *Astr. J.*, **99,** 1397.

Kirk, J. G., Schneider, P. 1987, *Astrophys. J.*, **315,** 425.
Krolik, J. H., Chen, W. 1991, *Astr. J.*, **102,** 1659.
Laing, R. A., Peacock, J. A. 1980, *Mon. Not. R. Astr. Soc.*, **190,** 903.
Large, M. I., Mills, B. Y., Little, A. G, Crawford, D. F., Sutton, M. J. 1981, *Mon. Not. R. Astr. Soc.*, **181,** 194.
Longair, M. S. 1994 in *High Energy Astrophysics*, (Cambridge University Press) **2,** p 359.
Macklin, J. T. 1982, *Mon. Not. R. Astr. Soc.* **199,** 1119.
McCarthy P. J., Kapahi, V. K., van Breugel W., Persson, S. E., Athreya, R. M., Subrahmanya, C. R. 1996, *Astrophys. J. Suppl.*, **107,** 19.
McCarthy, P. J., van Breugel, W., Kapahi, V. K., Subrahmanya, C. R. 1991b, *Astr. J.*, **102,** 522.
McCarthy, P. J., van Breugel, W., Kapahi, V. K., Athreya, R. M. 1999, (under preparation).
Oort, M. J. A., Katgert, P., Windhorst, R. A. 1987, *Nature*, **328,** 500.
Pacholczyk, A. G. 1970, *Radio Astrophysics* (San Fransisco: W. H. Freeman & Co.).
Rottgering, H. J. A., Lacy, M., Miley, G. K., Chambers, K. C., Saunders, R. 1994, *Astr. Astrophys. Suppl.*, **108,** 79.
Swarup, G. 1975, *Mon. Not. R. Astr. Soc.* **172,** 501.
van Breugel, W., McCarthy, P. J. 1990 in *The evolution of galaxies*, ed. R. G. Kron (Hubble Centennial Symp., ASP Conf. Ser. 10) pg 359.
Whitfield, G. R. 1957, *Mon. Not. R. Astr. Soc.*, **117,** 680.
Wieringa, H. M., Katgert, P. 1991, *Astr. Astrophys.*, **248,** L31

J. Astrophys. Astr. (1998) **19,** 79–96

Molecular Gas Associated with the IRAS-Vela Shell

Jayadev Rajagopal & G. Srinivasan

Raman Research Institute, Bangalore 560 080, India
email: jaydev@rri.ernet.in, srini@rri.ernet.in

Received 1998 June 29; accepted 1998 September 28

Abstract. We present a survey of molecular gas in the $J = 1 \rightarrow 0$ transition of ^{12}CO towards the IRAS Vela Shell. The shell, previously identified from IRAS maps, is a ring-like structure seen in the region of the Gum Nebula. We confirm the presence of molecular gas associated with some of the infrared point sources seen along the shell. We have studied the morphology and kinematics of the gas and conclude that the shell is expanding at the rate of ~ 13 km s^{-1} from a common center. We go on to include in this study the Southern Dark Clouds seen in the region. The distribution and motion of these objects firmly identify them as being part of the shell of molecular gas. Estimates of the mass of gas involved in this expansion reveal that the shell is a massive object comparable to a GMC. From the expansion and various other signatures like the presence of bright-rimmed clouds with head-tail morphology, clumpy distribution of the gas etc., we conjecture that the molecular gas we have detected is the remnant of a GMC in the process of being disrupted and swept outwards through the influence of a central OB association, itself born of the parent cloud.

Key words. ISM: structure, clouds.

1. Introduction

The IRAS Vela Shell is a ring-like structure seen clearly in the IRAS Sky Survey Atlas (ISSA) in the 25, 60 and 100 micron maps. This large feature extending almost 30 degrees in Galactic longitude (l^{II} = 245° to 275°), and discernible from the galactic plane till galactic latitude –15°, was first noticed by A. Blaauw. Subsequently, a detailed study of this region formed the major part of the thesis by Sahu (1992). This infrared shell is seen in projection against the Gum Nebula as a region of enhanced Hα; emission in the southern part of the nebula. But it is quite likely that whereas the IRAS shell may be located in the vicinity of the Gum Nebula, it is unrelated to it. The main reason for supposing this is that the kinematics of the shell is quite different from that of the Gum Nebula as a whole. The evidence comes from emission line studies of this region (e.g., lines of NII). Whereas there is no conclusive evidence of any expansion of the Gum Nebula, in two directions towards approximately the centre of the shell the emission lines have a "double-peaked" structure, consistent with an expansion with a velocity ~ 10 ± 2 km s^{-1} . Moreover, the Gum Nebula does not appear as a discernible feature in the IRAS maps.

The shell roughly envelopes the Vela OB2 stellar association (Brandt *et al.* 1971). Two of the brightest known stars, ζ Puppis (spectral type 04If) and γ^2 Velorum a Wolf-Rayet binary are also located close to the shell on the sky. Based on the symmetric location of the shell with respect to the Vela OB2 association, Sahu argued that this group of stars is associated with the shell. The distance estimate to Vela OB2 association is ~ 450 pc, and this has been taken as the distance to the shell as well (Sahu 1992).

The IRAS Point Source Catalogue (IPSC) also reveals a ring-like structure, although slightly offset in position from the ISSA shell. From its emissivity in the infrared, and assuming the standard 1 : 100 ratio of dust to gas, Sahu estimated the total mass of the shell to be ~10^6 solar masses. Presumably much of this mass must

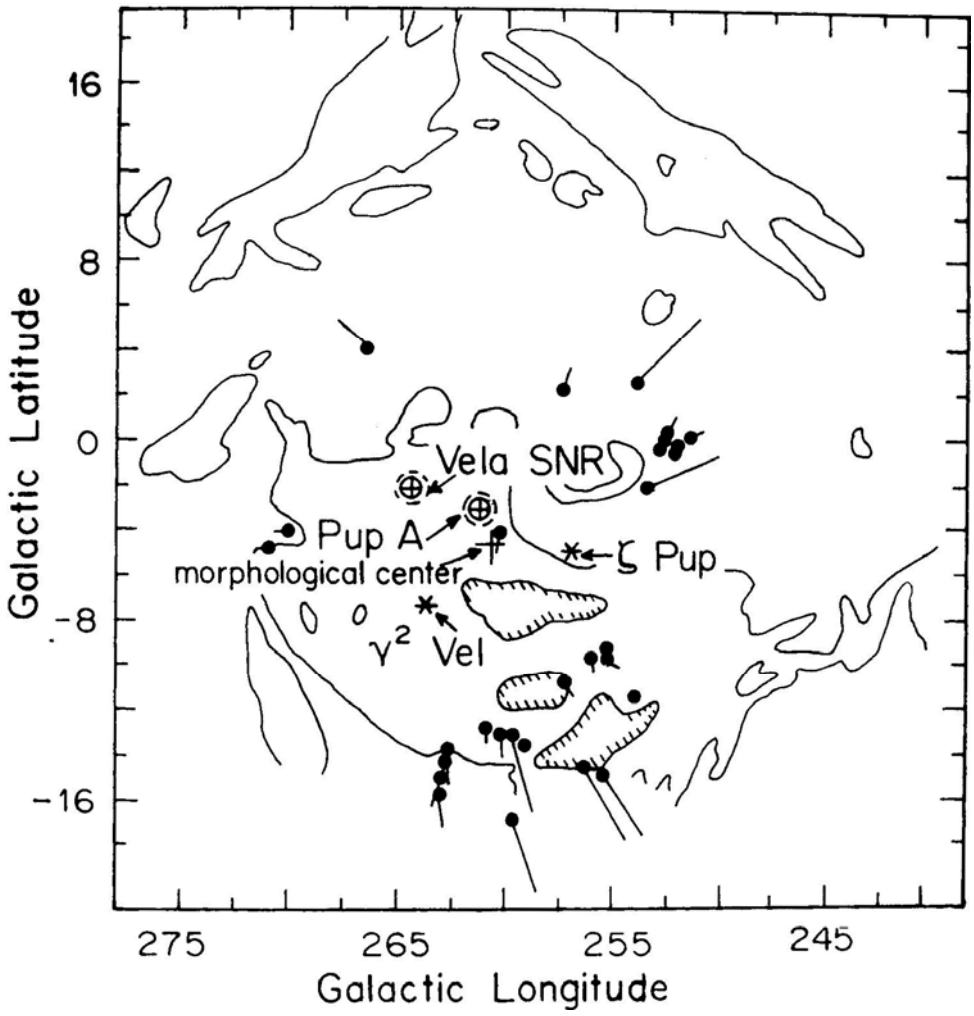

Figure 1. Overall picture of the Gum-Vela region showing the Hα emission as solid lines, the cometary globules as filled circles with tails (scaled up 10 times for clarity), and other important objects in the region. The morphological centre of the system of cometary globules is indicated by a + sign. From Sridharan (1992b).

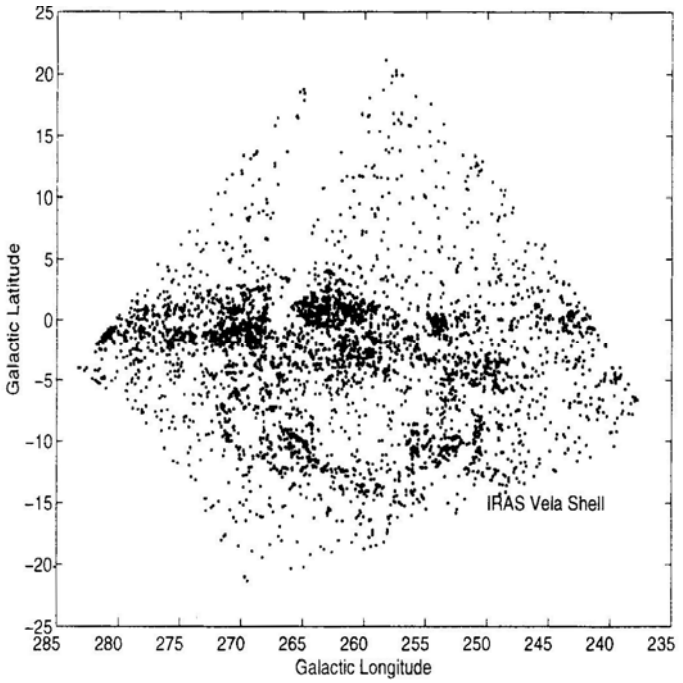

Figure 2. IRAS Point Sources between l = 240° and l = 280°. These sources satisfy the criteria for Young Stellar Object candidates listed in the text. The IRAS Vela Shell is noticeable below the Galactic plane.

be in the form of molecular gas. The only evidence for this so far is restricted to the ~ 35 or so cometary globules in the region. These, with head-tail structures, are distributed in the region of the shell in a manner which suggests a physical association. From a comprehensive study of these globules Sridharan (1992a,b) concluded that these small molecular clouds are expanding about a common centre with a velocity ~ 12 kms^{-1}. It turns out that this centre of expansion is roughly centred on the infrared shell as delineated by the IRAS point sources. This strengthens the case for the cometary globules being associated with the IRAS Vela Shell. Even so, this would account for only a few thousand solar masses of molecular gas since the mass of each of the globules is less than ~$100M_{\odot}$ (Sridharan 1992b).

The main objective of the investigation reported in this paper was to make an extensive survey for molecular gas possibly associated with the IRAS shell. A second objective was to study the kinematics of this gas. For future reference we show in Fig. 1 a schematic of the Gum-Vela region, and in Fig. 2 the distribution of the IRAS point sources.

2. Source selection

In order to increase our chances of detecting molecular gas we chose a sample of point sources in the IPSC which were candidates for Young Stellar Objects (YSO); it had been noted by earlier workers that the shell-like structure in the distribution of the IRAS point sources was more pronounced if one restricted oneself to those which are

likely to be associated with YSOs. Prusti (1992), for example, used a certain "Classifier III" criteria to pick out the YSO candidates in the IPSC. In addition to colour and statistical criteria Prusti used certain "crowding" properties which tended to enhance the "shell-structure". Since the use of such a filter would excessively bias the distribution of sources selected for our survey, we used instead a less restrictive criteria used by Sridharan (1992b), and which are originally due to Emerson (1987) and Parker (1988). These are listed below:

- Detection at 25 μm and 60 μm, with [60 – 25] > 0.
- [25 – 12] > 0, if also detected at 12μm.
- Detection only at 60 μm
- Detection at 60 μm and 100 μm only with [100 – 60] > 0.6.
- [100 – 25] > 0.

Here the notation [25 – 12], for example, refers to the 25 to 12 μm *colour ratio,* defined to be $\log[S_{25}/S_{12}]$· The flux density in Jansky at 25 μm is denoted by S_{25}, etc.. We used the filter specified above on the IPSC sources in the RA range seven hours to nine hours which covers the shell (see Fig. 2).

3. The observations

In March–April 1996 we undertook millimeter-wave observation in the $J = 1 \rightarrow 0$ rotational transition of the ^{12}CO molecule at 115.271 GHz. The observations were done with the 10.4 m telescope located in the campus of the Raman Research Institute. It has an altitude-azimuth mount with the receiver at the Nasmyth focus. The receiver is a Schottky diode mixer cooled to 20 K. Further details about the telescope and the subsystems may be found in Patel (1990). The backend used was a

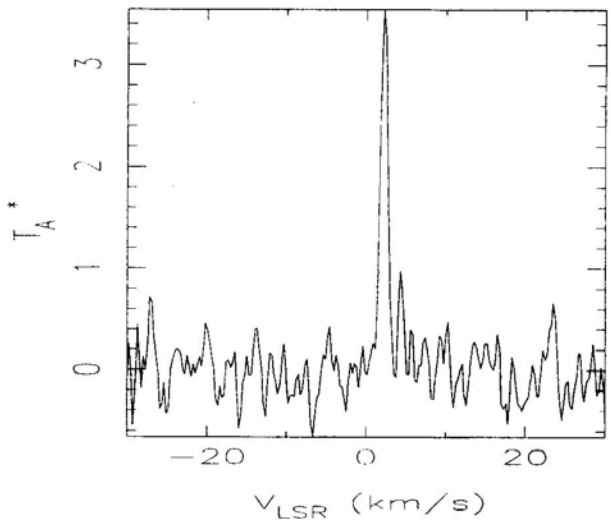

Figure 3. A typical spectrum showing ^{12}CO emission ($J = 1 \rightarrow 0$ transition, λ = 2.6 mm, υ_0 = 115.271 GHz) after removal of a polynomial fit to the baseline. The spectrum was obtained towards the IRAS point source IR 56549 in the shell. The vertical axis shows T_A^* (calibrated antenna temperature) in K. The effective integration time was ~ 20 minutes.

hybrid type correlation spectrometer configured for a bandwidth of 80 MHz with 800 channels giving a resolution of ≈ 100 kHz when using both polarizations. This corresponds to a velocity resolution of 0.26 kms^{-1}.

The observations were done in the frequency switched mode. This had the advantage that no time is spent looking at source-free regions. Moreover, since our sources were not point sources "off-source" regions are not well defined for beam switching schemes. A frequency offset of 15.25 MHz was chosen between ON and OFF spectra since that is the frequency of the observed baseline ripple. With this scheme only a polynomial fit was required to remove any residual baseline curvature. The switching rate was 2 Hz. Calibration was done using an ambient temperature load at intervals of several minutes. The pointing error was within 20" (as determined by observing Jupiter). The frequency stability of the correlator was checked by observing the head of the cometary globule CG1 each day. The rms of this distribution was 0.3 km s^{-1}, and hence that will be the error on the velocities quoted by us. A comparison of the velocities measured by us towards the heads of several cometary globules with those measured by Sridharan (1992b) showed good agreement.

Due to the limited observing season we selected about 100 IPSC sources out of about 3750 which satisfied the various criteria mentioned before. The sources selected for observations covered the shell although not uniformly. In addition, we observed in several directions (within the shell) where there were no IPSC sources. Each observing run consisted of typically ten minutes of integration. The spectra in the vertical and

Table 1. Summary of molecular detections toward IRAS Point Sources: Column 1 lists the IRAS Point Source Catalogue number for the source. Columns 2 and 3 give the LSR velocity and the corrected antenna temperature. Column 4 gives the rms noise level for each source. **The table is continued in Columns 5 to 8.**

Source	V_{lsr}	T_A^*	T_{rms}	Source	V_{lsr}	T_a^*	T_{rms}
	km s^{-1}	*K*	*K*		km s^{-1}	*K*	*K*
51704	−1.2	0.6	0.12	61322	8.4	2.2	0.22
52594	−2.5	0.9	0.18	61322	13.2	1.5	0.22
53668	−0.5	0.5	0.13	61351	8.1	1.2	0.26
53829	−3.4	0.4	0.13	61428	7.7	3.0	0.14
54473	−1.2	0.8	0.18	61837	3.0	4.6	0.20
54599	−2.2	3.3	0.23	62100	9.9	7.7	0.12
54769	−3.1	1.7	0.13	62578	14.9	0.6	0.15
55878	−5.0	4.5	0.13	62717	3.9	3.3	0.21
55884	4.4	2.8	0.18	62841	−1.0	2.1	0.45
55925	5.5	0.9	0.24	62847	5.4	0.7	0.17
55932	21.5	0.8	0.14	63338	14.4	0.7	0.17
56549	2.2	3.6	0.27	63338	9.4	1.9	0.17
56831	−1.5	1.2	0.17	63927	4.6	1.4	0.20
57035	16.4	1.5	0.16	64029	8.8	3.7	0.16
57035	28.6	1.9	0.16	64154	14.1	1.4	0.16
57898	1.4	5.2	0.37	64388	0.9	2.2	0.14
58784	−8.2	1.1	0.18	64728	10.6	1.2	0.27
58793	8.6	0.3	0.12	64999	−4.0	1.1	0.25
58793	9.6	0.3	0.12	65728	7.0	2.4	0.27
59579	−7.5	0.9	0.24	65877	4.9	9.3	0.31
59584	5.7	0.8	0.18	66001	1.8	1.3	0.36
59891	−6.3	0.9	0.24	67910	6.0	3.3	0.30
60933	0.3	1.3	0.18	69185	3.5	2.0	0.30

horizontal polarizations were then averaged after removing the baseline curvature. The effective integration time was therefore typically ~ 20 minutes. The rms of the noise over such an integration period was ~ 0.2 K. In Fig. 3 we show a typical spectrum after correcting for the baseline curvature. The reduction of the data was done using the UNIPOPS package. The temperature scale T^*_A is telescope dependent but we shall not convert it to an absolute scale since in this paper we are only interested in detection (or otherwise), and the velocities if molecular material is detected.

4. Results

We detected ^{12}CO emission towards 42 of the 100 or so sources observed. Table 1 lists the measured antenna temperatures and LSR velocities found by fitting gaussians to the spectra. In some cases multiple features were detected at different velocities. The distribution of the observed sources in galactic coordinates is shown in Fig. 4; the circles denote detection of CO emission and the crosses indicate non-detections. While the distribution of the open circles suggests a ring-like structure it is not convincing. A gap in the distribution of detections in the lower right hand side of Fig. 4 is conspicuous. Interestingly, a number of cometary globules are located in this region. They, however, were not included in our sample selected from the IPSC.

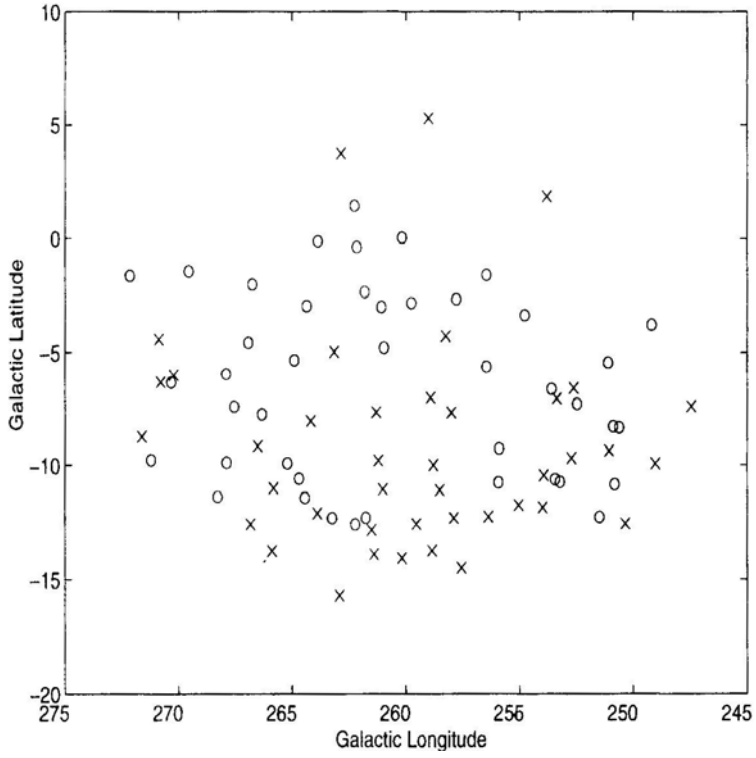

Figure 4. IPSC sources observed by us for CO emission are shown in Galactic coordinates. The circles denote detections and the crosses indicate non-detections. We have 42 detections from ~ 100 pointings. The sensitivity limit was ~ 0.6 K.

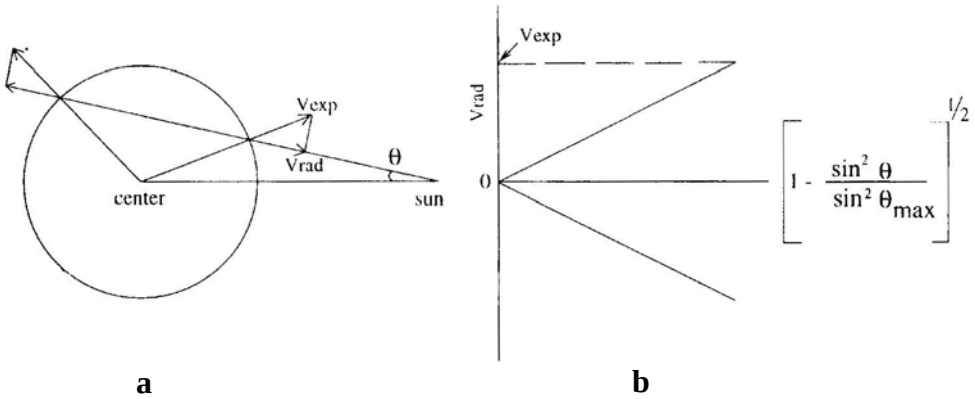

Figure 5. (**a**) A schematic for deriving expected radial velocities from an expanding shell. υ_{exp} is the expansion velocity, υ_{rad} is the radial component and Θ is the angular separation of any point on the shell from the center, (**b**) υ_{rad} plotted against $(1 - \sin^2 \theta / \sin^2 \theta_{max})^{1/2}$.

Since molecular gas has earlier been detected in these globules, their inclusion would fill in this gap (as we shall see in Fig. 5).

5. The kinematics of the molecular gas

In this section we wish to present an analysis of the kinematics of the molecular gas detected by us in the region of the IRAS Vela Shell. As already mentioned, there are two independent pieces of evidence to suggest that the shell-like structure may be in a state of expansion. To recall, the ionized gas possibly associated with the IRAS shell, as well as the cometary globules, both show evidence of expansion with a velocity ~ 12 km s^{-1}. If this is a general feature of the region under discussion then one would expect the more widely distributed molecular gas also to be in a state of expansion. Our analysis confirms this.

Sridharan's study revealed that the system of cometary globules are expanding with the centre of expansion roughly coincident with the "morphological centre", i.e., the point towards which the tails of the maximum fraction of the globules extrapolate to. This is located roughly at l = 260° and b = –4°. It is reasonable to assume that if the molecular gas detected by us is also expanding then it is likely to be with respect to the same "centre". The analysis presented below is predicated on this assumption.

Fig. 5 illustrates the analysis procedure. The first step is to remove the contribution to the observed radial velocity due to the differential rotation of the Galaxy. Since we are looking for a possible expansion with respect to a common centre, we subtracted from the measured LSR velocity of each detection the radial velocity component at the assumed centre of expansion (viz., the morphological centre of the system of cometary globules) due to galactic differential rotation. The radial component of the rotation velocity was determined from the well known relation

$$\upsilon_r = \mathrm{Ad} \sin 2l \cos^2 b.$$

As already mentioned, the co-ordinates of the assumed centre of expansion are l = 260°, b = –4°. Following Kerr and Lynden-Bell (1986) we assumed a value of

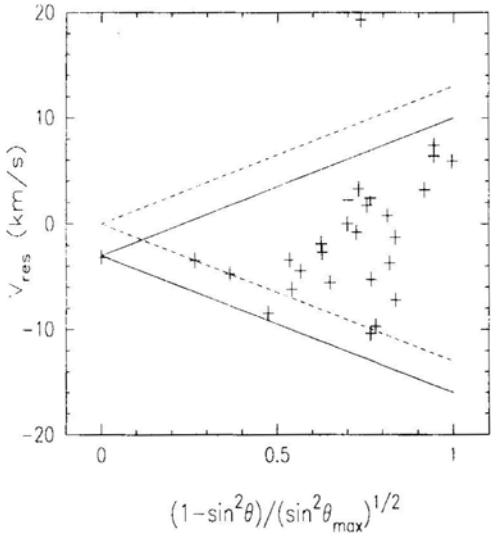

Figure 6. The residual radial velocity after removing the contribution from Galactic differential rotation plotted against the "expansion parameter" i.e., $(1 - \sin^2 \theta/\sin^2 \theta_{\max})^{1/2}$. θ is the angular separation of the source from the assumed center of expansion. If the objects form an expanding shell, the points will lie on the two straight lines (the "envelope") shown. If they are distributed in a volume, the points would tend to lie within the envelope, as is the case here. The envelope in solid lines is for an expansion velocity of 13 km s^{-1} with an offset of –3 km s^{-1}. The points are better "enclosed" by the solid lines than the envelope defined by the dashed lines (no offset).

14.5 kms^{-1} kpc^{-1} for Oort's constant *A*. As for the heliocentric distance *d* to the centre of the shell, we adopted a value of 450 pc. This is consistent with the recent distance estimate to the Vela OB2 association based on the data from Hipparcos (de Zeeuw *et al.* 1997). It is also consistent with the distance estimate to the young star embedded in the head of the cometary globule CGI (Brand *et al* 1983).

It may be seen from Fig. 5 that if the objects expanding about the common centre with a velocity v_{exp} are distributed on a thin *shell* with a hollow interior then the residual radial velocity v_{res} (i.e., after allowing for galactic rotation) will be related to the expansion velocity by

$$v_{res} = \pm v_{exp} (1 - \sin^2 \theta_{max})^{\frac{1}{2}}$$

where θ is the angular separation of the object from the centre of expansion, and θ_{max} is (half) the angular size of the shell (~ 12.5° in the present case). If the sources are distributed on a thin shell then in a plot of the residual radial velocity *versus* $(1 - \sin^2 \theta/ \sin^2 \theta_{max})^{\frac{1}{2}}$ the points would lie along two straight lines as shown in Fig. 5. If, on the other hand, the objects in question were distributed over the whole expanding volume then the points would lie *within* the envelope defined by the two lines (provided, of course, the inner objects are moving slower than the outer ones).

Our data are shown in Fig. 6. In this plot we have included only those detections that are in the lower part of the shell (i.e. $b < 0$) so as to avoid the confusing region near the galactic plane, for example, the Vela Molecular Ridge. Although its estimated distance of ~ 1 kpc would put the ridge well beyond the region under study here, there

will be blending in velocity space towards these longitudes. As may be seen in the figure, the IRAS point sources (with which the molecular gas we have detected is associated) are expanding about a common centre. The filled nature of the cone suggests that the gas is not confined to a thin shell but rather distributed over a volume, with the outer regions expanding faster. From the slope of the two lines enveloping the data points we deduce that the outer regions are expanding with a velocity ~ 13km s^{-1}. Thedata also suggest that there may be offset of ~ –3km s^{-1}, i.e. the expansion is more *symmetric* with respect to a residual radial velocity of –3 km s^{-1} than about zero velocity. If this is significant then it would imply that the gas has an overall drift. We shall return to this presently.

5.1 *The southern dark clouds*

It may be recalled that our search for molecular gas was motivated by a shell-like structure seen in the distribution of IRAS point sources. Indeed, our candidates were a sample of these point sources; due to the limited observing season at the site of the telescope we used we could only observe about 100 of these sources. Nevertheless, due to fortuitous circumstances, molecular observations of a different class of objects – some of which are possibly related to the feature we were investigating – became available to us. Recently a general survey of the population of *dark clouds* in the southern sky was undertaken in the $J = 1 \rightarrow 0$ line of ^{12}CO using the Mopra antenna (Otrupcek, Hartley and Wang Jing-Sheng 1995). These clouds listed in the Catalogue of Dark Clouds by Hartley *et al.* (1986) appear as dark patches of obscuration in optical photographs. Interestingly, the extinction map made from the ESO/SERC Southern Sky Survey by Feitzinger and Stüwe (1984) shows a shell-like structure just in the region of the IRAS shell. In view of this we decided to enlarge our database of molecular gas in the region of the IRAS shell by including the southern dark clouds. *The radial velocities from the Mopra Survey were very kindly made available to us by Otrupcek.*

In Fig. 7 we have replotted the molecular gas detected in this region, this time including the dark clouds, as well as the cometary globules. Since the molecular detections of the Southern Dark Clouds are not yet published, we have given in the Appendix an extensive Table of the coordinates and measured LSR velocities of the subset of the Dark Clouds within the IRAS Vela Shell (i.e., within 12.5° from the assumed centre of expansion). The corresponding data for the cometary globules were taken from Sridharan (1992b). In Fig. 7, the IRAS point sources observed by us are shown as plus signs, and the rest as open circles. The tip of the *arrow* represents the point with respect to which both the IRAS point sources as well as the cometary globules appear to be expanding. Since the distribution of the dark clouds also suggests a shell-like structure it is conceivable that they, too, are in a state of expansion. This is indeed the case. Fig. 8 clearly shows that the molecular clouds associated with the young stellar objects in the region, the cometary globules, and a subset of the southern dark clouds are members of a common family, and that they are expanding with respect to a common centre. As in the analysis presented earlier in Fig. 6, to avoid confusion with unrelated objects near the galactic plane we have included only those dark clouds with latitudes greater than –4°. We have, however, included all the cometary globules; in view of their distinctive morphology there is less chance of confusion.

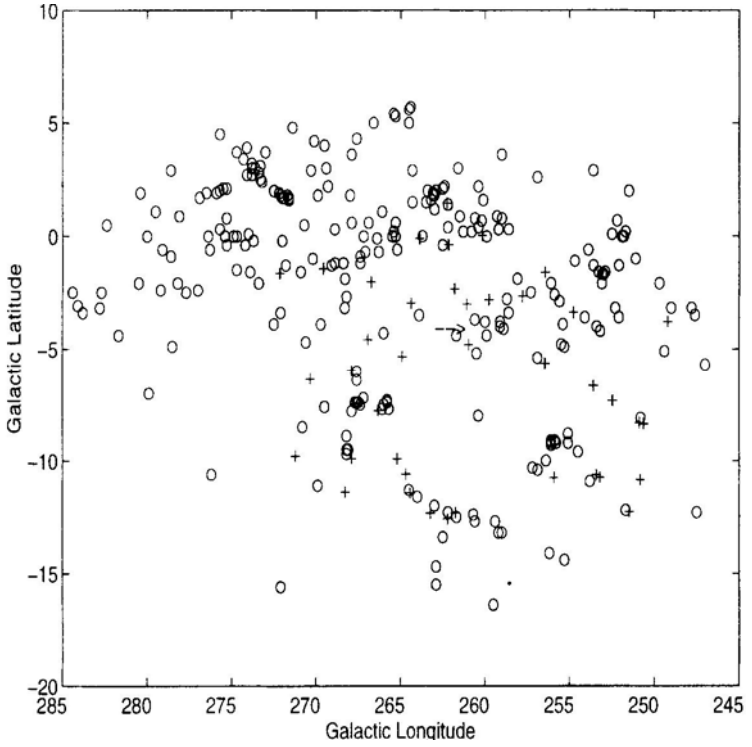

Figure 7. The figure shows the molecular detections towards IRAS point sources (plus signs), and the Southern Dark Clouds including cometary globules in the region of the IRAS Vela Shell shown as open circles. The arrow indicates the morphological center of the cometary globule system.

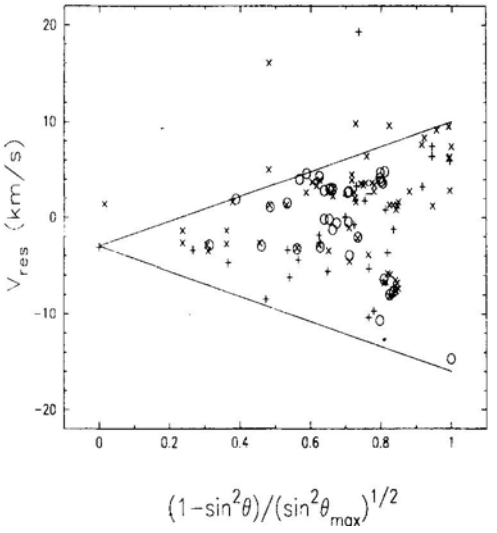

Figure 8. The residual velocity plotted against $(1 - \sin^2 \theta / \sin^2 \theta_{max})^{1/2}$ for *all* objects. The crosses denote SDCs, the open circles are cometary globules and the plus signs show molecular detections towards IPSC sources. The "expansion envelope" is for an expansion velocity of 13 kms^{-1} and offset of –3 kms^{-1}.

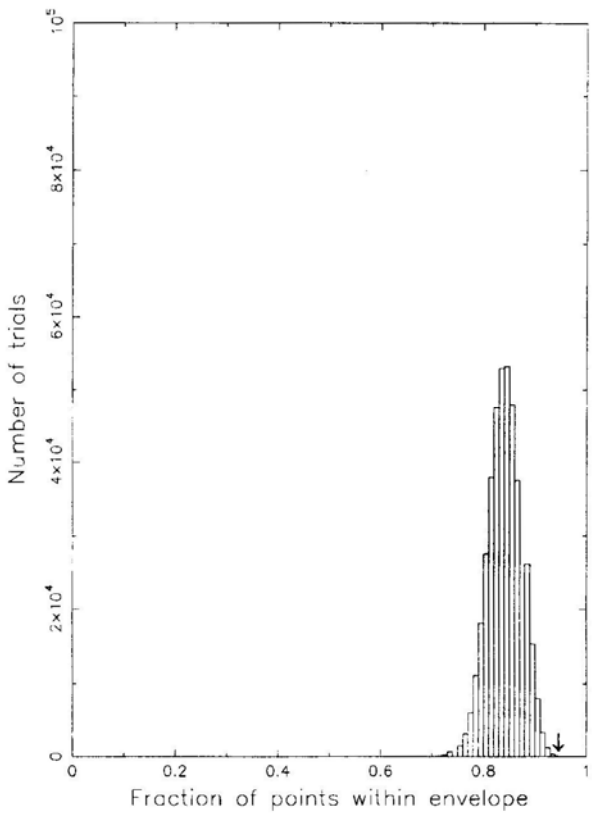

Figure 9. Result of significance tests done for an expansion velocity of 13 km s^{-1} and offset of –3kms^{-1}. In these tests, the velocity axis in the V_{LSR} vs $(1–\sin^2 \theta/ \sin^2 \theta_{max})^{1/2}$ diagram was "scrambled" and the number of points within the "expansion envelope" computed for each trial. The peak of the histogram shows the most likely fraction of points within the "expansion envelope" for a *random sample.* The arrow points to the fraction of points within the "expansion envelope" for the *observed sample.* This point lies 3.3σ away from the peak for the random samples.

5.2 *A Statistical test*

To rule out the possibility that the signature of expansion seen in Fig. 8 is spurious we did the following test. It essentially involved *scrambling* the observed (residual) radial velocities among the objects in the sample, and determining the *fraction of points which lie within the envelope* defined by an expansion velocity υ_{exp} and an offset υ_{offset} For every assumed value of the 'offset' we determined the minimum value of υ_{exp} for which > 95% of the observed points fell within the expansion envelope. Given a pair (υ_{exp}, υ_{offset})so determined, we generated a large set of random samples and determined for each set the fraction of random samples that fall within the wedge-shaped region in Fig. 9. If the mean of this distribution of fractions is not significantly different from the fraction of the *actual* observed sample that lies within the defined envelope, then the expansion deduced by us would not be statistically significant. The most statistically significant values we obtained were υ_{exp} = 13 km s^{-1} and υ_{offset} =–3 kms^{-1}. The results of 400,000 simulations for this pair of values is

shown in Fig. 9. As may be seen, one can say with a confidence at 3.3σ level that the observed radial velocities (after correcting for contribution from galactic rotation) indicates an expansion. For completeness we mention that we also did simulations for offsets of 1, 0, 2 and 4 kms^{-1}, all with v_{exp} = 13 km^{-1}. As mentioned above, the most significant value for the offset in the residual velocity was –3 k m s^{-1}, with the significance decreasing on either side of this value.

6. Summary and discussion

We first summarize our main conclusions:

(i) There is a significant amount of molecular gas associated with the IRAS point sources defining the shell-like feature. Our observations thus confirm the expectation that molecular gas must be associated with these Young Stellar Objects.

(ii) Perhaps more importantly, these point sources which delineate the "IRAS Vela Shell" are expanding about a common centre, with the sources in the outer region moving with a velocity ~ $13kms^{-1}$.

(iii) Our study has established that a subset of the "Southern Dark Clouds" in this region are also part of this "shell" since they, too, are participating in the systematic motion mentioned above.

(iv) Earlier observers had found that the dozen or so cometary globules in this region, as well as some ionized gas, showed evidence of similar expansion with roughly the same velocity. One can therefore safely conclude that the cometary globules and the expanding ionized gas are also part of the "IRAS Vela Shell".

6.1 *The mass of the shell*

We shall now attempt to estimate the mass of the shell. From its infrared emissivity Sahu (1992) estimated the amount of dust in the shell, and assuming the standard dust-to-gas ratio she estimated the mass of the shell to be ~ 10^6 $M_\odot$ As we shall presently see, our estimates yield a mass an order of magnitude less than this.

As already discussed, the lower half ($b < -4°$) of the IRAS Vela Shell is more clearly defined, and has an angular radius of ~ 12.5°. Using the criteria explained earlier, we estimate that there are ~ 1000 Young Stellar Objects in the lower half of the shell. We shall now assume that these are of roughly the same mass as the typical cometary globules. The mass of a typical globule has been estimated to be $\leq 100M_\odot$ (Sridharan 1992b, and references therein). Adopting this value we estimate that the mass of the molecular gas associated with the entire IRAS Vela Shell must be $\sim 10^5 M_\odot$. In deriving this estimate we have allowed for the fact that we detected molecular gas in only ~ 50% of the IPSC sources towards which we looked.

An alternative mass estimate can be made as follows. It has been argued that in the local giant molecular cloud complexes such as Orion, Ophiuchus and Taurus-Auriga the *efficiency* with which gas is converted to stars is ~ 1% (Evans and Lada 1990). If this is also the case in the small molecular clouds under discussion, and if the typical

mass of the stars formed in these clouds is ~ $1M_{\odot}$,then the presence of approximately 1000 Young Stellar Objects in the shell suggests a total mass ~ 10^5 $M_{\odot}$, consistent with the earlier estimate. But if the star forming efficiency is much higher in the small globules, as has been argued, for example, by Bhatt (1993), then the mass of the molecular gas could be smaller.

To derive the total mass of the shell one must, of course, add the mass of the ionized gas, as well as neutral atomic gas associated with the shell. While there is clear evidence for some ionized gas (HII, NII, SII etc.) it is difficult to estimate its mass. As for HI associated with the Vela Shell, the picture is far from clear.

6.2 *On the origin and evolution of the IRAS Vela Shell*

Based on the fact that the Vela OB2 association of stars appears centrally located with respect to the shell, Sahu (1992) attributed the expansion of the gas in the shell to the combined effect of stellar wind from the massive stars and supernova explosions in the association. Sridharan (1992a) invoked the same explanation to account for the expansion of the system of cometary globules. We endorse these suggestions, and our observations lend more credence to the scenario that the Vela Shell is the remnant of the giant molecular cloud from which the Vela OB2 association itself formed.

Although the Vela OB2 association is more or less symmetrically located with respect to the IRAS Vela Shell, there are two points to consider: (**i**) whether the group of stars are members of a genuine "association", and (**ii**) whether the shell and the association are at the same distance from us. As for the first point, the recent proper motion measurements by the Hipparcos satellite firmly establishes this group of stars as a genuine association with 116 members, including the O star γ^2 Veloram, at a mean distance of 415 ± 10 pc (de Zeeuw *et al* 1997). Hipparcos data also lend support to the idea that it is a fairly evolved association approximately 10^7 years old (Schaerer, Schmutz & Grenon 1997). In comparison, the distance estimate to the shell is indirect. Earlier we presented arguments to support the hypothesis that the system of cometary globules in the region is part of the expanding shell. The estimated distances to a number of these globules roughly agrees with the Hipparcos distance to the Vela OB2 association (Brand *et al.* 1983; Pettersson 1987). There is also a piece of circumstantial evidence which may be more reliable. A recent photometric study of the $H\alpha$ emission from the bright rim of the globule CG22 (Rajagopal 1997) clearly indicates that the ionizing source is ζ-Puppis· The Hipparcos measurements yield a distance of 429^{+120}_{-77}pc to ζ–Puppis (van der Hucht *et al.* 1997). This would suggest that the distance to CG22 is of this order, and consistent with the distance to the Vela OB2 association.

If one accepts the premise that the Vela OB2 association and the IRAS Vela Shell are at the same distance, then one has to ask if it is plausible that the expansion of the shell is causally connected with the group of stars. Adapting the model due to McCray and Kafatos (1987) for the formation of "supershells" by OB associations, Sahu (1992)has argued that if Vela OB2 is a "standard association" of the type found within 1 kpc of the Sun then it could account for the observed expansion with a kinetic energy ~ 10^{50} – 10^{51} erg. A closer examination of this important question is warranted in the light of the Hipparcos observation, and we hope to undertake it.

There is an increasing body of evidence to suggest that the break up of giant molecular clouds may be quite common. Many of the giant molecular clouds in our

neighbourhood show evidence of streaming flows of ionized gas, clumpy distribution of the molecular gas, large velocity fields etc.. These phenomena are consistent with these giant clouds disintegrating under the influence of nearby OB associations (Leisawitz, Bash and Thaddeus 1989). Such clouds may represent an *earlier* stage of evolution of the IRAS Vela Shell. As for its future evolution, it is conceivable that as the expanding molecular gas sweeps up enough interstellar matter it will develop into a classical "supershell".

Acknowledgements

The basis for this study emerged from a series of discussions with Prof. Blaauw who continued to guide us throughout. We wish to thank T. K. Sridharan for his help at several stages. The data from the Mopra survey were invaluable; we are indebted to R. Otrupcek and co-workers for giving us timely access to it. Finally, the support from the staff at the Raman Institute Millimeter Wave Observatory is gratefully acknowledged.

References

Bhatt, H. C . 1993, *Mon. Not. R. astr. Soc,* **262**, 812.

Brand, P. W. J. L., Hawarden, T. G., Longmore, A. J., Williams, P. M., Caldwell, J. A. R. 1983, *Mon. Not. R. astr. Soc,* **203**, 215.

Brandt, J. C, Stecher, T. P., Crawford, D. L., Maran, S. P. 1971, *Ap. J. (Lett),* **163**, L99.

de Zeeuw, P. T., Brown, A. G. A, de Bruijne, J. H. J, Hoogerwerf, R., Lub, J., Le Poole, R. S., Blaauw, A. 1997, *ESA SP,* **402**, 495.

Emerson, J. P. 1987, in *Star Forming Regions,* ed. M. Piembert & J. Jugaku (D. Riedel Publishing Company) pp 19.

Evans Π, N. J., Lada, E. A. 1990, in *IAU Symp. No. 147* on Fragmentation of Molecular Clouds and Star Formation, eds. E. Falgarone, F. Boulanger & G. Duvert (Dordrecht: Kluwer).

Feitzinger, J. V., Stuwe, J. A. 1984, *Astr. Astrophys. Suppl,* **58**, 365.

Hartley, M., Manchester, R. N., Smith, R. M., Tritton, S. B., Goss, W. M. 1986, *Astr. Astrophys. Suppl.,***63**,27.

Kerr, F. J., LyndenBell, D. 1986, *Mon. Not. R. astr. Soc,* **221***,* 1023.

Leisawitz, D., Bash, F. N., Thaddeus, P. 1989, *Ap. J. Suppl,* **70**, 731.

McCray, R., Kafatos, M. 1987, *Ap. J,* **317**, 190.

Otrupcek, R. E., Hartley, M., Jing-Sheng, W. 1995 (private communication, Otrupcek).

Parker, N. D. 1988, *Mon. Not. R. astr. Soc,* **235**, 139.

Patel, N. A. 1990, Ph.D. Thesis, Indian Institute of Science, Bangalore.

Pettersson, B.1987,*Astr. Astrophys.,***171**, 101.

Prusti, T. 1992, Ph.D. Thesis, University of Groningen.

Rajagopal, J. 1997, Ph.D. Thesis, Jawaharlal Nehru University, New Delhi.

Sahu, M. S. 1992, Ph.D. Thesis, University of Groningen.

Schaerer, D., Schmutz, W., Grenon, M. 1997, *Ap. J. (Lett.),* **484**, L153.

Sridharan, T. K. 1992a, *JA&A,* **13**, 217.

Sridharan, T. K. 1992b, Ph.D. Thesis, Indian Institute of Science, Bangalore,

van der Hucht, K.A., Schrijver, H., Stenholm, B., Lundstrom, I., Moffat, A. F. J., Marchenko, S. V., Seggewiss, W., Setia Gunawan, D. Y. A., Sutyanto, W., van den Heuvel, E. P. J, de Cuyper, J. P., Gomez, A. E. 1997, *New Astr.,* **2***,* 245.

Appendix

In the following set of tables, we present the Galactic co-ordinates, measured velocities (LSR) of the ^{12}CO emission, and projected separation from the assumed center of the shell for the Southern Dark Clouds (SDCs). Only those SDCs within 12.5° of the center have been included.

Table Southern Dark Clouds within 12.5° of the center of the IRAS Vela Shell, from the Mopra Survey (Otrupcek *et al.* 1995) kindly made available to us by R. Otrupcek: Columns 1 and 2 give the galactic co-ordinates; Column 3 shows the LSR velocity and; Column 4 shows the projected angular separation between the source and the center of the shell. **The table is continued in Columns 5 to 8.**

l^{II}	b^{II}	V_{lsr}	θ	l^{II}	b^{II}	V_{lsr}	θ
Deg.	Deg.	km/s	Deg.	Deg.	Deg.	km/s	Deg.
247.80	−3.2	18.7	12.40	253.40	−4.0	11.8	6.77
249.00	−3.2	17.2	11.20	253.60	−1.3	11.2	7.12
249.00	−3.2	26.2	11.20	253.60	2.9	5.9	9.57
249.40	−5.1	7.2	10.82	253.80	−10.9	−1.3	9.36
249.40	−5.1	18.2	10.82	253.90	−0.6	10.8	7.16
249.70	−2.1	15.6	10.65	253.90	−0.6	35.8	7.16
250.80	−8.1	−1.0	10.21	254.10	−3.6	10.6	6.09
251.10	−1.0	9.6	9.57	254.50	−9.6	−1.7	7.94
251.50	2.0	25.1	10.57	254.70	−1.1	9.8	6.22
251.70	0.2	5.1	9.48	254.70	−1.1	37.1	6.22
251.70	−12.2	−1.3	11.76	255.10	−9.2	−4.6	7.23
251.80	0.0	5.6	9.30	255.10	−8.8	−6.0	6.95
251.90	0.0	5.4	9.21	255.30	−14.4	3.8	11.44
252.10	−3.6	−2.0	8.08	255.30	−4.9	9.8	4.95
252.10	−3.6	7.2	8.08	255.40	−3.9	9.8	4.77
252.10	−3.6	14.5	8.08	255.50	−4.8	10.5	4.73
252.10	−1.3	12.9	8.53	255.60	−2.9	8.9	4.71
252.20	0.7	1.6	9.28	255.80	−9.2	−5.6	6.76
252.30	−3.2	8.5	7.92	255.90	−9.1	−5.4	6.62
252.30	−3.2	12.5	7.92	255.90	−2.6	9.8	4.51
252.50	0.1	4.4	8.72	256.10	−2.1	9.0	4.51
252.90	−1.6	5.9	7.67	256.10	−9.3	−4.3	6.64
252.90	−1.6	11.2	7.67	256.10	−9.2	−4.6	6.57
253.00	−1.7	5.7	7.55	256.10	−9.1	−5.2	6.49
253.00	−1.7	10.3	7.55	256.20	−14.1	3.5	10.81
253.10	−2.1	11.6	7.34	256.40	−10.0	−3.6	7.05
253.10	−1.7	5.4	7.45	256.90	−10.4	−4.5	7.14
253.10	−1.7	9.9	7.45	256.90	−5.4	11.3	3.54
253.20	−4.2	11.8	6.97	256.90	2.6	10.6	7.41
253.30	−1.6	5.2	7.30	257.20	−10.3	−3.7	6.92

(*Continued*)

Southern Dark Clouds within 12.5° of the assumed center of the IRAS Vela Shell, from the Mopra Survey (Otrapcek *et al.* 1995): Columns 1 and 2 give the galactic co-ordinates; Column 3 shows the LSR velocity and; Column 4 shows the projected angular separation between the source and the center of the shell.

l^{II}	b^{II}	V_{lsr}	θ	l^{II}	b^{II}	V_{lsr}	θ
Deg.	Deg.	km/s	Deg.	Deg.	Deg.	km/s	Deg.
257.30	−2.5	15.9	3.26	260.40	0.4	6.3	4.46
258.10	−1.9	10.3	2.99	260.40	0.4	9.2	4.46
258.10	−1.9	43.2	2.99	260.40	−8.0	3.4	3.96
258.60	0.3	7.9	4.63	260.40	2.2	7.5	6.25
258.60	0.3	17.3	4.63	260.50	−5.2	5.0	1.20
258.60	−3.4	8.9	1.70	260.60	0.8	5.2	4.87
258.60	−3.4	15.1	1.70	260.60	−3.7	4.5	0.55
258.70	−2.8	10.3	1.93	260.60	−3.7	6.4	0.55
258.90	−4.1	8.5	1.27	260.60	−12.7	−2.4	8.66
259.00	−13.2	4.4	9.23	260.70	−12.4	0.0	8.37
259.00	0.8	5.9	4.99	260.80	0.2	5.8	4.30
259.00	3.6	2.6	7.74	260.80	0.2	8.0	4.30
259.00	3.6	6.4	7.74	260.80	0.2	12.2	4.30
259.10	−4.0	9.5	1.07	261.30	0.2	5.7	4.40
259.10	−3.8	9.5	1.10	261.30	0.2	7.6	4.40
259.20	0.3	4.4	4.46	261.30	0.2	10.9	4.40
259.20	0.3	6.5	4.46	261.50	0.9	6.4	5.12
259.20	0.3	12.3	4.46	261.60	3.0	11.2	7.19
259.20	−13.2	5.2	9.20	261.70	−4.4	8.4	1.57
259.30	0.9	3.6	5.03	261.70	−4.4	11.7	1.57
259.30	0.9	6.7	5.03	261.70	−12.5	6.1	8.59
259.30	0.9	4.5	5.03	262.20	0.4	8.4	4.89
259.40	−12.7	1.1	8.68	262.20	−12.3	4.8	8.50
259.50	−16.4	3.6	12.37	262.20	1.4	4.8	5.81
259.90	−4.4	9.6	0.44	262.40	2.2	6.5	6.63
259.90	0.0	7.9	4.06	262.40	2.2	8.4	6.63
260.00	−3.8	−12.7	0.30	262.50	−13.4	−0.7	9.64
260.10	1.6	5.6	5.65	262.50	−0.4	7.6	4.33
260.10	1.6	6.8	5.65	262.50	−0.4	39.3	4.33
260.20	0.7	5.3	4.75	262.50	2.1	8.4	6.58

(*Continued*)

Southern Dark Clouds within 12.5° of the assumed center of the IRAS Vela Shell, from the Mopra Survey (Otrupcek *et al.* 1995): Columns 1 and 2 give the galactic co-ordinates, Column 3 shows the LSR velocity and; Column 4 shows the projected angular separation between the source and the center of the shell.

l^{II}	b^{II}	V_{lsr}	θ	l^{II}	b^{II}	V_{lsr}	θ
Deg.	Deg.	km/s	Deg.	Deg.	Deg.	km/s	Deg.
262.90	−14.7	−0.5	10.99	265.50	0.0	−6.8	6.69
262.90	2.0	5.0	6.64	265.70	−7.7	3.0	6.62
263.00	1.8	7.1	6.50	265.80	−7.3	3.8	6.50
263.00	1.8	26.9	6.50	265.80	−7.4	3.4	6.55
263.00	1.2	7.8	5.96	266.00	−7.5	3.5	6.77
263.00	−12.0	3.8	8.44	266.00	−4.3	4.9	5.83
263.10	1.8	5.6	6.54	266.10	1.1	2.1	7.85
263.10	1.9	3.8	6.63	266.10	1.1	5.4	7.85
263.20	1.6	5.4	6.41	266.10	1.1	8.4	7.85
263.40	2.0	3.0	6.86	266.10	1.1	12.0	7.85
263.50	1.5	4.8	6.47	266.10	1.1	21.6	7.85
263.50	1.5	8.7	6.47	266.10	−7.7	3.5	6.96
263.70	0.0	5.4	5.37	266.30	−0.7	3.8	6.98
263.70	0.0	9.9	5.37	266.30	−0.7	6.2	6.98
263.90	−3.5	2.8	3.77	266.30	−0.7	10.0	6.98
263.90	−3.5	5.2	3.77	266.40	−0.1	3.8	7.37
264.00	−11.6	4.2	8.47	266.40	−0.1	5.7	7.37
264.30	2.9	11.3	8.08	266.60	5.0	2.5	11.10
264.30	1.5	6.6	6.92	266.90	0.6	5.3	8.18
264.40	5.7	8.9	10.63	267.10	−0.7	1.4	7.70
264.50	5.6	10.0	10.58	267.10	−0.7	6.0	7.70
264.50	5.0	2.5	10.03	267.10	−0.7	18.8	7.70
264.50	−11.3	12.0	8.44	267.20	−7.2	4.9	7.70
265.20	−0.6	5.7	6.10	267.20	0.0	4.5	8.11
265.30	0.0	6.5	6.53	267.20	0.0	6.7	8.11
265.30	5.3	3.0	10.66	267.20	0.0	8.8	8.11
265.30	0.6	4.7	6.92	267.40	−0.9	4.0	7.88
265.30	0.6	6.7	6.92	267.40	−0.9	6.6	7.88
265.40	0.2	6.0	6.74	267.40	−0.9	8.3	7.88
265.40	0.2	7.7	6.74	267.40	−7.5	8.6	8.01

(*Continued*)

Southern Dark Clouds within 12.5° of the assumed center of the IRAS Vela Shell, from the Mopra Survey (Otrupcek *et al.* 1995): Columns 1 and 2 give the galactic co-ordinates; Column 3 shows the LSR velocity and; Column 4 shows the projected angular separation between the source and the center of the shell.

l^{II}	b^{II}	V_{lsr}	θ	l^{II}	b^{II}	V_{lsr}	θ
Deg.	Deg.	km/s	Deg.	Deg.	Deg.	km/s	Deg.
267.50	−7.4	5.8	8.06	269.40	3.0	−1.4	11.61
267.60	−6.4	5.8	7.79	269.50	−7.6	4.8	9.98
267.60	−6.0	5.6	7.68	269.50	4.0	−3.8	12.32
267.60	4.3	1.3	11.18	269.70	−3.9	2.2	9.53
267.60	−7.4	5.6	8.15	269.90	−11.1	−0.5	12.01
267.70	−7.4	5.7	8.24	269.90	−11.1	0.8	12.01
267.90	0.6	0.1	9.02	269.90	1.8	−3.0	11.35
267.90	0.6	2.7	9.02	269.90	1.8	4.2	11.35
267.90	3.6	0.5	10.87	270.20	−1.0	1.8	10.48
267.90	3.6	2.1	10.87	270.20	−1.0	7.2	10.48
267.90	−7.8	6.7	8.59	270.20	−1.0	9.6	10.48
268.00	1.8	−5.4	9.77	270.30	2.9	−4.2	12.28
268.00	1.8	−0.6	9.77	270.60	−4.7	3.5	10.45
268.10	−9.5	6.1	9.62	270.70	0.5	−0.2	11.47
268.20	−9.7	5.9	9.82	270.70	0.5	6.2	11.47
268.20	−8.9	4.8	9.38	270.80	−8.5	−0.6	11.52
268.20	−9.5	5.5	9.70	270.80	−8.5	0.8	11.52
268.20	−2.7	7.5	8.14	270.90	−1.6	5.6	11.00
268.20	−2.7	14.4	8.14	271.80	−1.3	−3.9	11.95
268.30	−3.2	1.1	8.17	271.80	−1.3	−1.4	11.95
268.30	−1.9	3.1	8.41	271.80	−1.3	2.7	11.95
268.40	−1.2	4.7	8.71	272.00	−0.2	−0.8	12.44
268.90	0.3	0.7	9.75	272.00	−0.2	4.8	12.44
268.90	0.3	4.8	9.75	272.10	−3.4	8.2	11.95
268.90	0.3	8.4	9.75	272.50	−3.9	4.8	12.33
268.90	−1.2	4.7	9.18	272.50	−3.9	6.2	12.33
269.10	−1.3	2.6	9.34				
269.10	−1.3	6.0	9.34				
269.10	−1.3	7.7	9.34				
269.10	−1.3	9.1	9.34				

J. Astrophys. Astr. (1998) **19,** 97–116

The Interstellar Clouds of Adams and Blaauw Revisited: An HI Absorption Study – I

Jayadev Rajagopal, G. Srinivasan & K. S. Dwarakanath

Raman Research Institute, Bangalore 560 080, India
email: jaydev@rri.ernet.in, srini@rri.ernet.in, dwaraka@rri.ernet.in

Received 1998 August 4; accepted 1998 November 2

Abstract. This investigation is aimed at clarifying the nature of the interstellar gas seen in absorption against bright O and B stars. Towards this end we have obtained for the first time HI absorption spectra towards radio sources very close to the lines of sight towards twenty five bright stars previously studied. In this paper we describe the selection criteria, the details regarding our observations, and finally present the absorption spectra. In the accompanying paper we analyse the results and draw conclusions.

Key words. ISM: clouds, structure—radio lines: ISM.

1. Introduction

We have carried out an absorption study in the 21 cm line of atomic hydrogen in twenty five directions in the Galaxy. These directions have been selected from previous optical absorption studies in the lines of singly ionized calcium (CaII) and neutral sodium (NaI). In this paper, we describe the observations and present the data obtained by us. A discussion of the results and the conclusions drawn from the study are in the accompanying paper (Rajagopal, Srinivasan & Dwarakanath 1998; Paper II).

Our observations were primarily intended to study the velocities of the HI absorption features, their linewidths, and in combination with existing HI emission measurements obtain the spin temperature of the absorbing gas. Our study was motivated by the following questions:

- How are interstellar clouds seen in optical absorption related to those seen in HI absorption and emission?
- What is the nature of the relatively fast clouds so commonly seen in the absorption lines of NaI and CaII?

To clarify these and related issues we briefly summarize the salient historical background. Some of the earliest information about the Interstellar Medium (ISM) came from observations of optical absorption in the H and K (λλλ3933,3968Å) lines of CaII, and the D_1 and D_2 (λλ5889,5895 Å) lines of NaI towards bright stars. Adams (1949) made an extensive study of the absorption lines of CaII towards nearly 300 O and B stars. These observations were later extended to the D lines of NaI (Routly & Spitzer 1952; Hobbs 1969), and to high latitude stars (Munch & Zirrin 1961). In the

simplest model, these lines were attributed to interstellar gas in the form of clouds. The existence of a *hot intercloud medium* was conjectured by Spitzer (1956) and the theoretical basis for a two-phase model followed (Field 1965; Field, Goldsmith & Habing 1969).

Independently, a global picture of the ISM emerged from radio observations of the 21 cm HI line (Clark, Radhakrishnan & Wilson 1962; Clark 1965; Radhakrishnan *et al.* 1972). These and later studies have established that an important constituent of the ISM are cool diffuse clouds in pressure equilibrium with a warmer intercloud medium. The notion of interstellar "clouds" was thus invoked to explain both optical and radio observations. *But one was left speculating as to whether the two populations were the same.* Surprisingly the answer to the above question still remains incomplete. Many properties of the two populations seem to differ. In particular the number of clouds per kiloparsec (Blaauw 1952; Radhakrishnan & Goss 1972; Hobbs 1974; Radhakrishnan & Srinivasan 1980), and the velocity distributions deduced from optical and radio observations, respectively, do not agree. The latter discrepancy is discussed in more detail in a subsequent section.

In this study, we have attempted a direct comparison by doing HI absorption measurements towards the bright stars themselves. Of course, this can be done only in those lines of sight (towards stars studied previously) where there are strong enough radio sources. We were actually able to do this in about twenty five directions. From this data we obtain the velocities of the absorbing gas, and in combination with previous emission measurements in the same directions, the spin temperature of the HI gas in the very entities seen in optical absorption. This is the first attempt at such a direct comparison.

Identifying the optical absorption lines with 21 cm absorption features is particularly important because of a long standing puzzle. Optical absorption along many lines of sight reveals two sets of absorption features. One set occurs at near zero (low) velocities and another at higher velocities with respect to the local standard of rest. The faster clouds have measured velocities well in excess of the radial component of Galactic rotation one could attribute to them. In a classic study of Adams' data, Blaauw (1952) clearly showed the existence of a high velocity tail extending up to as high as 100 km s^{-1} in the distribution of random velocities of the optical absorption features. Thus the existence of a high velocity population of clouds was firmly established. There was also a hint that these "fast" clouds may belong to a different population. They exhibited the well known Routly-Spitzer effect (Routly and Spitzer 1952) i.e., the NaI to CaII ratios in these clouds were significantly lower than those in the lower velocity clouds.

In the decade following the discovery of the 21 cm line attempts were made to detect the gas seen in optical absorption. These involved measuring HI emission in the direction of stars which show optical absorption features in their spectra in order to compare the HI spectra with the CaII and NaI spectra (Takakubo 1967; Habing 1968, 1969; Goldstein and MacDonald 1969; Goniadzki 1972; Heiles 1974 and others). Habing's study in particular targeted selected stars to attempt a direct face off. The results of these early studies threw up another intriguing fact. The low velocity features appeared to be well correlated in HI emission and optical absorption i.e. whenever the optical spectra showed a low velocity absorption feature (v < 10km s^{-1}), there was HI emission at the corresponding velocity. However the high velocity features were in general *absent* in HI emission down to low limits

(T_b < 1 K). This seemed to be the case in all directions in the sky.

The typical beam sizes in the early experiments to measure HI emission were ~ 0.5°. The angular size of the absorbing gas could have been much smaller leading to considerable beam dilution. This could be the reason why the clouds were not detected in HI emission. This exemplifies the difficulties in comparing the features seen in optical absorption with arc-second resolution with those seen in radio emission using a comparatively large beam. This is one of the major factors which led us to attempt an HI *absorption study.* The resolution achieved is of the same order as in optical absorption enabling a surer comparison.

Despite the failure of the early emission measurements to detect the "fast" clouds there is some indication for a population of high velocity clouds from an independent HI absorption study, though this is far from being firmly established. Radhakrishnan and Srinivasan (1980) from a detailed analysis of the 21 cm absorption profile towards the Galactic centre suggested that the peculiar velocities of HI clouds cannot be understood in terms of a single Gaussian distribution with a dispersion of about 5–7 kms^{-1}, the velocity distribution for "standard" HI clouds. There was an indication of a second population of weakly absorbing clouds with a velocity dispersion ~ 35kms^{-1}. But this has not been confirmed by other studies. Our study is an attempt to address this important but neglected problem.

2. Scope of the present observations

We chose twenty five stars towards which both low and high velocity absorption features have been seen (from CaII or NaI atoms or both). Two of the stars HD 14134 and 14143 happen to be in the same field (in our radio observations) and hence we have measured absorption in only twenty four fields. The positions of all the selected stars as projected on the plane of the Galaxy are shown in Fig. 1. The Galactic spiral arms shown in this figure are from the electron density model by Taylor and Cordes (1993). In thirteen of these directions HI emission measurements had been carried out earlier by Habing (1968, 1969). Most of the fields studied by Habing were chosen at |b| > 20° to avoid complicated HI emission arising in the plane. Four stars, however, have |b| < 10° and were selected since they show CaII velocities well outside the limits of Galactic rotation at the estimated distances. Out of the remaining twelve fields, three have been investigated by Goniadzki (1972) for HI emission and one by Takakubo (1967). The rest of the fields have not been investigated in the radio. However, we have been able to get the brightness temperatures and column densities of HI in these directions also from the Leiden-Green Bank survey (Burton 1985).

In the observations described in this paper we have obtained HI absorption spectra towards a radio source whose line of sight is close to that of the star in each of the twenty four fields. We have been able to identify fairly strong radio sources (in most cases 50 mJy at 21 cm) within 30′ to 40′ of the star in every field. In more than half the fields the radio sources are within 10′ and several within 5′ of the star in question. If the cloud is halfway to the star, then given a 10′ separation between the star and the radio source one will sample a cloud of size less than 2 pc even for the farthest stars in the sample which are about 2 kpc away. This is well within the range of accepted sizes for standard clouds (Spitzer 1978). In some fields we had to arrive at a compromise between the minimum cloud size we could sample (i.e., the proximity of

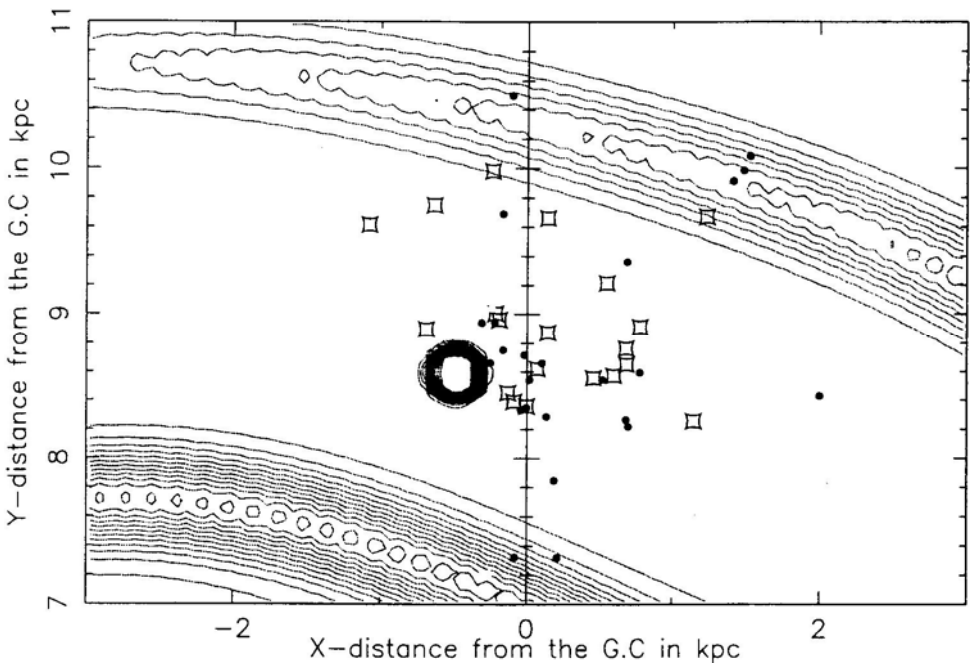

Figure 1. Twenty four of our sample of twenty five stars (HD 119608 lies outside the region shown) are shown as dots on the contour plot of the Galactic spiral arms from Taylor and Cordes. The squares show the local OB associations from Blaauw (1985). The Sun is at 8.5 kpc from the Galactic center. The object with dense contours to the left of the sun is the Gum Nebula. The outer arm shown is the Perseus arm, while the inner one is the Sagittarius arm. The three stars bunched together well inside the Perseus arm are HD 14134, 14143 and 14818. The Perseus OB1 cluster is seen close to them. The two stars seen projected on the Sagittarius arm are HD 166937 and 159176. These fields show high velocity HI absorption.

the projected position of the background source to the star) and the optical depth sensitivity we could achieve. The latter constrains us to fairly strong radio sources for reasonable integration times. This flux density requirement limits the number of sources that one can find close to the star and hence the trade off. Most of the background sources selected are from the NRAO/VLA Sky Survey (Condon *et al.* 1996). We aimed at an optical depth sensitivity of $\tau = 0.1$ and have done better than that in several cases. The worst case limit on the optical depth is 0.4.

3. Observations and data analysis

We obtained the absorption spectra using the Very Large Array (VLA[1]) in the ~ 1 km and ~ 11 km configurations with a synthesized beam size of 44″ and 4″, respectively, at 21 cm. The observations were carried out with a total bandwidth of 1.56 MHz using both polarizations and 128 channels. We used 0134 + 329 as the primary flux

[1] The VLA is operated by the National Radio Astronomy Observatory (NRAO). The NRAO is a facility of the National Science Foundation operated under cooperative agreement by Associated Universities, Inc.

calibrator. For each source we observed a nearby secondary calibrator to do a phase and bandpass calibration. The calibrator was observed with the frequency band shifted by 1.5 MHz, corresponding to a velocity shift ~ 300 km s^{-1}. This shift in velocity is sufficient to move the band away from any Galactic feature which might affect the bandpass calibration. Typically, each of these calibrators were observed for ~ 10 minutes. The typical strengths of these calibrator sources being > 1 Jy, 10 minutes of integration time was sufficient to achieve a signal-to-noise ratio greater than that on the source by a factor of 2. After on line Hanning smoothing over 2 channels, the frequency resolution obtained was ~ 12kHz which corresponds to a velocity resolution of ~ 2.5 kms^{-1}. The integration time on each source was chosen to give an optical depth sensitivity of $\tau \sim 0.1$, and ranged from a few minutes to more than an hour. In all a total of ~ 30 hours were spent on the sources, split over several sessions of observing.

The analysis was carried out using the Astronomical Image Processing System (AIPS) developed by the National Radio Astronomy Observatory (NRAO). The first step was to make continuum images of each field and examine them for bright sources, including the target source. Our observations coincided with the ongoing NRAO/VLA Sky Survey (in the B and D configurations) and most of our observations were carried out during the daytime. Hence we had to contend with moderate to strong levels of interference over most of the band owing to which approximately 10% of the data was lost. The next stage involved removing the continuum level from all channels. The task used for this was UVLIN. The continuum level to be removed is determined from a linear fit to the visibility levels in selected channels, which are chosen to be free of interference as well as any spectral features. Finally the image cubes were made. The imaging was typically done over an area of 512 by 512 pixels. In some cases several cubes were synthesised for different areas to cover all the sources of interest in the field. The spectra towards each of the sources were analysed with the Groningen Image Processing System (GIPSY; van der Hulst *et al.* 1992).

4. Results

Table 1 lists the details of all the fields observed. In most of these fields there were several radio sources within the primary beam in addition to the source initially targeted. We have obtained spectra towards these sources as well if they turned out to be strong enough to detect reasonable optical depths (~ 0.1). Column 1 gives the HD number of the star. Columns 2 and 3 give the distance to the star (as listed in the SKY 2000 catalogue of bright stars) and its galactic coordinates, respectively. Column 4 gives the angular separation of the star from the radio source(s) towards which absorption has been detected. Column 5 lists the HI absorption velocities (LSR). These velocities have been derived by fitting Gaussian profiles to the absorption features. Column 6 shows the detection limit in τ (towards the strongest source in the field). Column 7 shows the radial component of the Galactic rotation velocity at the distance to the star.

The optical absorption velocities are likely to suffer from blending of features due to lack of resolution. A discussion of this and associated problems can be found in Welty, Morton & Hobbs (1996). Moreover, the correction for the solar motion adopted by different authors may differ leading to errors of ~ 1 kms^{-1} (see for example

Table 1. Summary of HI absorption: Column 1 gives the HD number of the star. Columns 2 and 3 show the distance to the star (as listed in the Sky Catalogue 2000.0, Vol 1, Hirshfield & Sinnott 1982) and its galactic coordinates, respectively. Column 4 gives the angular separation of the star from the radio source(s) towards which absorption has been detected. Column 5 lists the HI absorption velocities (LSR). Column 6 shows the detection limit in τ (towards the strongest source in the field). Column 7 shows the approximate radial component of the Galactic rotation velocity at the distance to the star. < 0 and > 0 are used to indicate velocities with magnitude less than 5 km s^{-}1.

Field	d	l^{II}, b^{II}	θ	V_{lsr}	τ	V_{Gal}
	pc		arcmin	km s^{-1}		km s^{-1}
14143*	2000	135, −4	10.0	−52.8, −50.3, −46.1, −11.2, −8.2	0.09	−25
14818	2200	136, −4	10.0	−55.8, −14.0, −3.7	0.05	−25
21278	190	148, −6	37.0	2.8	0.08	>0
21291	1100	141, 3	36.0	−31.2, −7.0, −4.9	0.07	−10
24912	46	160, −13	2.2	4.3, 6.0, −82.0	0.39	−5
25558	220	185, −33	26.0	8.1	0.10	<0
34816	540	215, −26	40.0	6.0, 8.0	0.10	<0
37742	500	206, −16	15.0	9.5	0.03	5
38666	300	237, −27	21.5	none	0.02	5
41335	300	213, −13	3.0	1.0, 10.0	0.04	>0
42087	1200	188, 2	42.0, 32.0	4.4, 6.5, 12.4	0.13	−5
93521	2000	183, 62	27.0	none	0.11	<0
119608	3400	320, 43	16.0	−5.4	0.09	−20
141637	170	346, 21	11.0	0.5, −0.2	0.28	∼0
148184	150	358, 21	0.82	3.4	0.26	∼0
156110	720	71, 36	<10.0	2.2	0.18	5
159176	1180	356, 0	5.3	−20.8, −74.0	0.28	∼0
166937	1200	10, −2	5.0, 7.0	34.6, 47.2, 35.7	0.39	5
175754	680	16, −10	<10.0	6.8	0.09	10
199478	2000	88, 1	8.0	5.0 to −75.0	0.21	−7
205637	250	32, −45	18.4	none	0.30	5
212978	520	95, −15	12.0	0.3, −12.3	0.04	−5
214680	780	97, −17	12.0	−4.8, 1.4	0.28	−5
220172	750	68, −63	2.9	none	0.33	10

*The stars 14134 and 14143 are in the *same* field referred to above as 14143*.

Blaauw 1952). In some cases, we have smoothed the absorption spectra to a resolution of 5 km s^{-1} to facilitate the convergence of the Gaussian fit. Narrow absorption features are known to have widths less than this (Crovisier 1981). We have checked the unsmoothed data to ensure that there are no serious effects of blending in the estimates for velocities for the features discussed below. However, crowding in velocities inevitably causes some of the absorption widths to be suspect. The formal error in the fitting procedure for our HI absorption velocities is in most cases ∼1 kms^{-1} or less. The errors add to $\lesssim$ 2 km s^{-1}. However, it must be stated that the blending of features in both optical and radio could easily lead to larger errors than this formal value. *Hence we consider a feature in the optical spectrum as "coincident" with one seen in HI absorption or emission if the magnitude of the*

Table 2. Summary of coincident velocities: Column 2 lists the LSR velocities of all the optical absorption features seen in each line of sight (most of the listed velocities are from CaII observations). Velocities of the matching HI absorption features are given in Column 3. Column 4 shows the radial component of the Galactic rotation velocity at the distance to the star. Column 5 has the reference for the optical absorption velocities which are from **A:** Adams (1949), **B:** Buscombe and Kennedy (1962), **M:** Münch (1957) and **MZ:** Münch and Zirrin (1961).

Field	V_{lsr}(optical, all)	V_{lsr}(HI, coincident)	V_{Gal}	Ref.
	km s^{-1}	km s^{-1}	km s^{-1}	
14143*	−62.3, −46.8, −6.3 −65.3, −50.8, −10.3	−46.1, −50.3, −11.2	−25	M
14818	−42.6, −33.6, −6.6	−3.7	−25	M
21278	−0.2, 48.6	2.8	>0	A
21291	−34.0, −7.5	−31.2, −7.0, −4.9	−10	M
24912	4.7, 20.7	4.3	−5	A
25558	10.1, 19.0	8.1	<0	A
34816	−14.0, 4.14	6.0	<0	A
37742	−21.0, 3.6	none	5	A
38666	1.0, 20.2	no absorption	5	MZ
41335	−20.8, 0.2	1.0	>0	A
42087	−37.7, −4.8, 10.2	12.4	−5	A
93521	−55.0, −34.0, −10.3, 6.8	no absorption	< 0	MZ
119608	1.3, 22.4	none	−20	MZ
141637	−22.0, 0.0	0.5, −0.2	0	B
148184	14.2, 2.2	3.4	0	A
156110	−19.7, 0.4	2.2	5	MZ
159176	3.5, −22.5	−20.8	0	A
166937	−5.5, 5.9, 25.3, 41.1	5.4, 47.2, 35.7	5	A
175754	−73.0, 5.9, 29.5	6.8	10	A
199478	−2.1, 8.7, 42.3, 61.2	3.8 (blend)	−7	A
205637	−13.9, 1.8	no absorption	5	A
212978	−73.0, 0.6	0.3	−5	A
214680	−23.7, −14.7, 0.1	1.4	−5	A
220172	−21.5, −0.8, 13.5	no absorption	10	MZ

difference in velocities is less than 3 *km s*$^{-1}$. This is roughly the same criterion adopted by Habing (1969) and Howard *et al.* (1963) for comparing HI emission profiles with optical absorption.

Table 2 lists the "matching" features i.e., HI absorption features whose velocities agree with the velocity of the optical absorption feature. Column 2 shows the LSR velocities of all the optical absorption features seen in each line of sight (most of the listed velocities are from CaII observations). Velocities of the matching HI absorption features follow in column 3. Column 4 shows the radial component of the Galactic rotation velocity at the distance to the star to facilitate comparison with the optical absorption velocities. Column 5 has the reference for the optical absorption velocities which are from Adams (1949); Münch (1957) and Münch and Zirrin (1961). We have used later compilations of these by Takakubo (1967), Siluk and Silk (1974), and Habing (1969).

We present the HI optical depth towards all the observed fields at the end of the paper. The coordinates of the radio source (epoch 1950) towards which the spectrum is obtained is labelled at the top right of each panel. The HD number of the star towards which the corresponding optical spectrum is obtained is at the top left. The star co-ordinates (epoch 1950) are given immediately below this. The star co-ordinates have not been repeated if there are several radio sources in the same field. In all the spectra the velocities at which optical absorption is seen is indicated by arrows on the velocity axis (top). The conclusions we draw from these observations and a detailed discussion of the implications for the models of the ISM are presented in Paper II.

Acknowledgement

We wish to thank Adriaan Blaauw for extensive discussions which led to this investigation. His continued interest and critical comments have been invaluable to us. We are also indebted to Hugo van Woerden for guiding us through the literature pertaining to the early HI observations by the Dutch group.

References

Adams, W. A. 1949, *Astrophys. J.*, **109,** 354, 131.
Blaauw, A. 1952, *Bull Astr. Inst. Netherland*, **11**, 459.
Blaauw, A.1985, in *IAU Symp. 106*, *The Milky Way Galaxy*, eds.H. vanWoerden, R. J.Allen & W. B. Burton, p. 335.
Burton,W.B.1985,*Astr. Astrophys. SuppL.*,**62**,365.
Buscombe, W.,Kennedy, P.M.1962, *Mon. Not. R. astr. Soc.*,**125**, 195.
Clark, B. G. 1965, *Astrophys. J.*, **142**, 1398.
Clark, B. G., Radhakrishnan, V., Wilson, R. W. 1962, *Astrophys. J.*, **135**, 151.
Condon, J. J., Cotton, W. D., Greisen, W. E., Yin, Q. F., Perley, R. A., Taylor, G. B., Broderick, J. J. 1996, *Astr. J.*, **115**, 1693.
Crovisier. J.1981, *Astr. Astrophys.*, **94**, 162.
Field, G.B.1965, *Astrophys. J.*, **142**, 531.
Field, G. B., Goldsmith, D. W., Habing, H. J. 1969, *Astrophys. J. (Lett.)*, **155**, L149.
Goniadzki, D.1972, *Astr. Astrophys.*,**17**,378.
Goldstein, S. J., MacDonald, D. D. 1969, *Astrophys. J.*, **157**, 1101.
Habing, H.J.1968,*B.A.N.*, **20**,120.
Habing, H. J.1969,*B.A.N.*,**20,** 171.
Heiles, C. 1974, *Astrophys. J. (Lett.)*, **193**, L31.
Hirshfield, A., Sinnott, R. W. 1982, (eds), *Sky Catalogue 2000.0*, **Vol 1**, Sky Pub. Corp. and Cambridge University Press.
Hobbs, L. M. 1969, *Astrophys. J.*, **157**, 135.
Hobbs, L. M.1974, *Astrophys. J.*, **191**, 395.
Howard III,W.E., Wentzel, D.G.,McGee, R.X. 1963, *Astrophys. J.*, **138**, 988.
Münch, G. 1957, *Astrophys. J.*, **125,** 42.
Münch, G., Zirrin, H. 1961, *Astrophys. J.*, **133,** 11.
Radhakrishnan, V., Goss, W.M. 1972, *Astrophys. J. SuppL*, **24,** 161.
Radhakrishnan, V., Goss, W. M., Murray, J. D., Brooks, J. W. 1972, *Astrophys. J. SuppL*, **24,** 49.
Radhakrishnan, V., Srinivasan, G. 1980, *J. Astrophys. Astr.*, **1**, 47.
Rajagopal, J., Srinivasan, G., Dwarakanath, K. S. (Paper II) 1998,*J. Astrophys. Astr.*, **19**, 117.
Routly, P. M., Spitzer, L. Jr. 1952, *Astrophys. J.*, **115,** 227.

Siluk, R. S., Silk, J. 1974, *Astrophys. J.*, **192**, 51.
Spitzer, L. Jr. 1956, *Astrophys. J.*, **124**, 20.
Spitzer, L. Jr. 1978, *Physical Processes in the Interstellar Medium* (New York: Wiley Interscience).
Takakubo, K. 1967, *B.A.N.*,**19**, 125.
Taylor, J. H., Cordes, J. M. 1993, *Astrophys. J.*, **411**, 674.
van der Hulst, J. M., Terlouw, J. P., Begeman, K., Zwitzer, W., Roelfsema, P. R**.** 1992, in GIPSY in *Astronomical Data Analysis Software and Systems I*, eds. D. M. Worall & C. Biemesderfer,
Welty, D. E., Morton, D. C., Hobbs, L. M. 1996, *Astrophys. J. Suppl.*, **106,** 533.

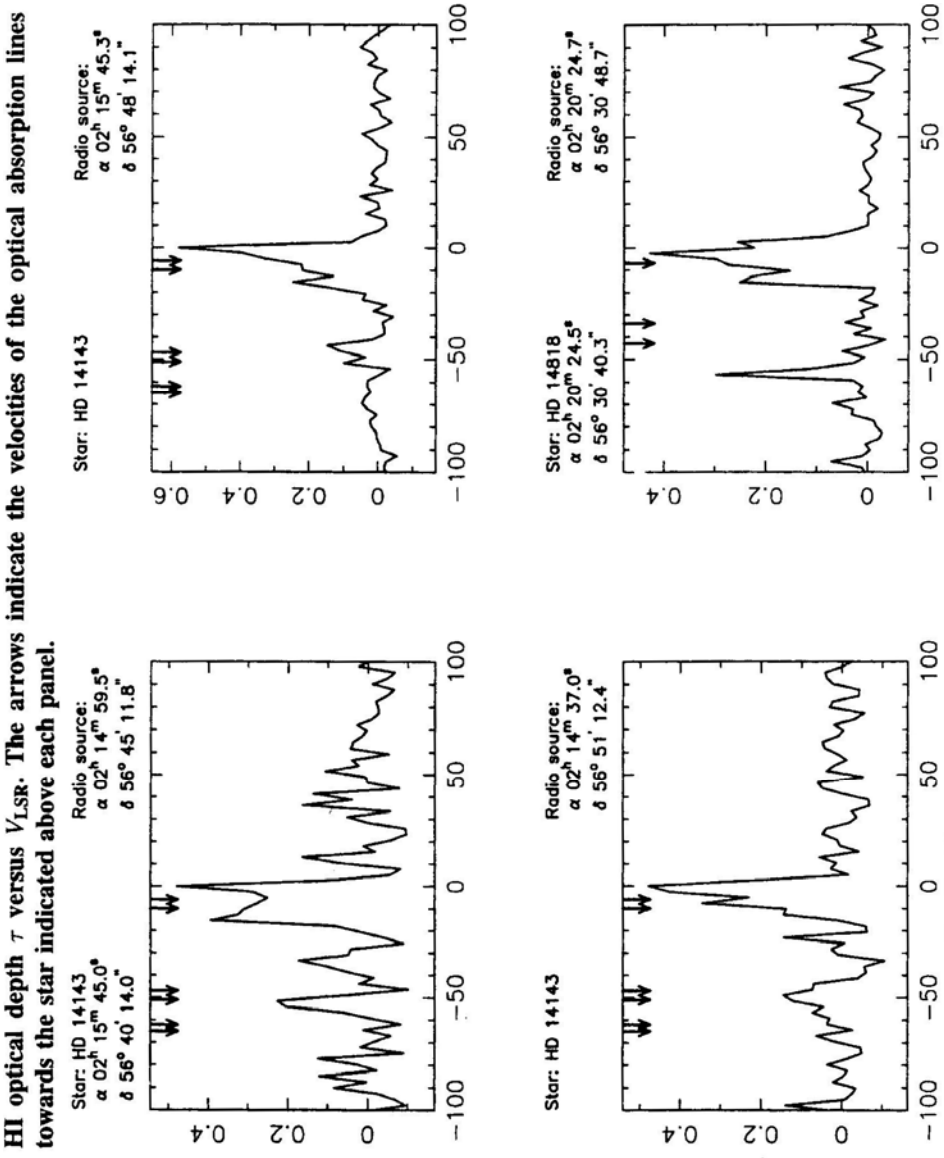

HI optical depth τ versus V_{LSR}. The arrows indicate the velocities of the optical absorption lines towards the star indicated above each panel.

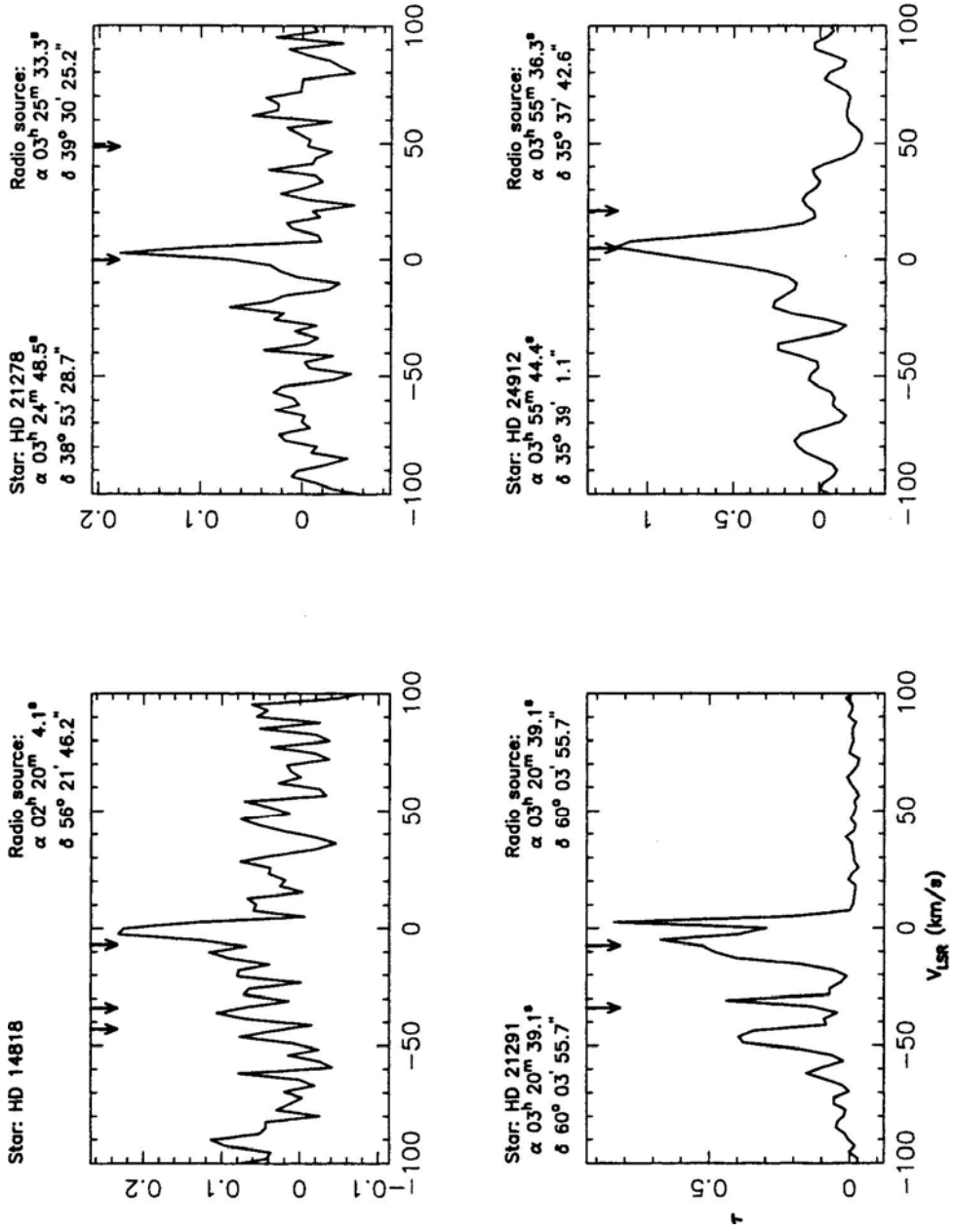
Star: HD 14818
Radio source:
α 02h 20m 4.1s
δ 56° 21' 46.2"
Star: HD 21278
α 03h 24m 48.5s
δ 38° 53' 28.7"
Radio source:
α 03h 25m 33.3s
δ 39° 30' 25.2"
Star: HD 21291
α 03h 20m 39.1s
δ 60° 03' 55.7"
Radio source:
α 03h 20m 39.1s
δ 60° 03' 55.7"
Star: HD 24912
α 03h 55m 44.4s
δ 35° 39' 1.1"
Radio source:
α 03h 55m 36.3s
δ 35° 37' 42.6"
τ
VLSR (km/s)

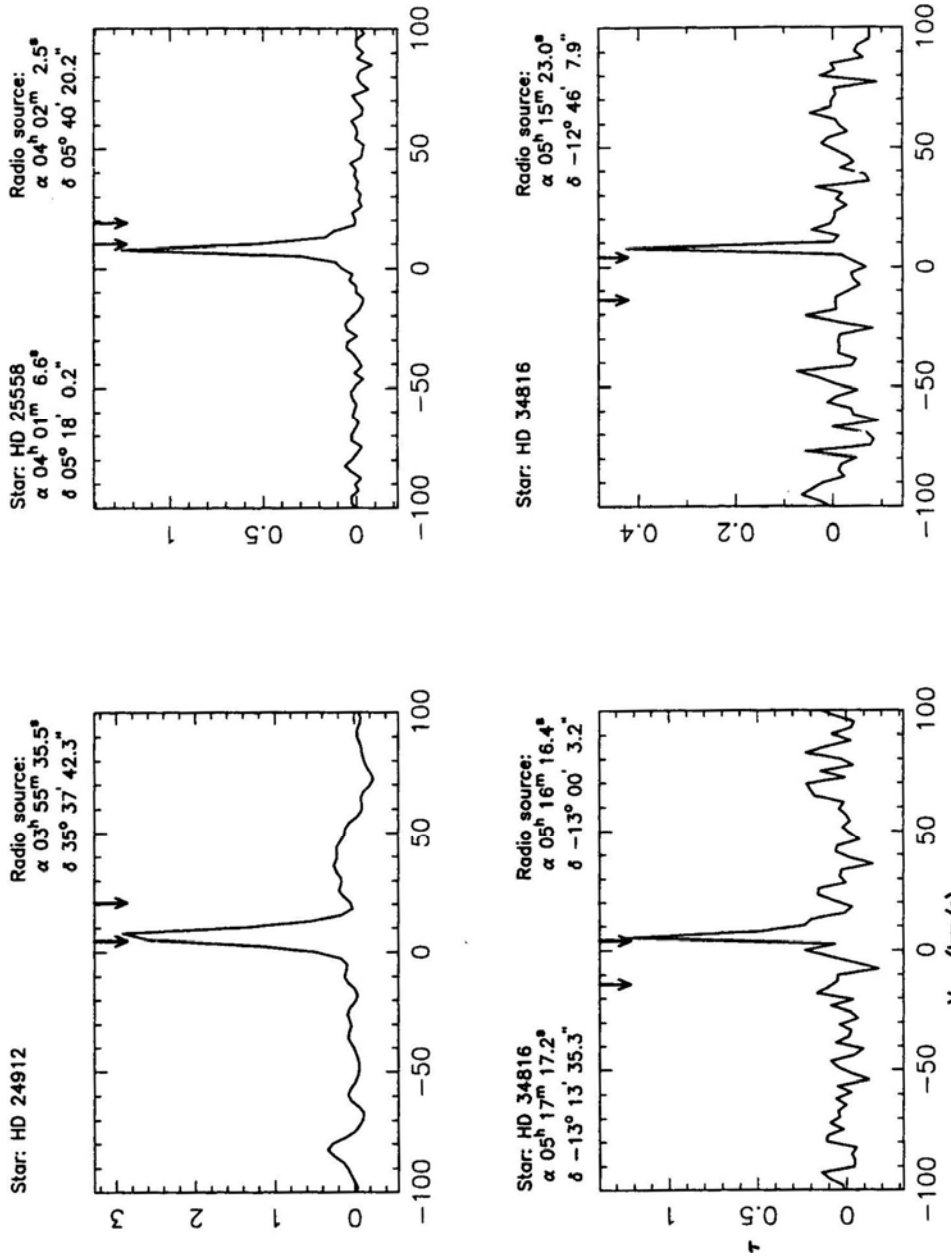
Star: HD 24912
Radio source:
α 03h 55m 35.5s
δ 35° 37' 42.3"
Star: HD 25558
α 04h 01m 6.6s
δ 05° 18' 0.2"
Radio source:
α 04h 02m 2.5s
δ 05° 40' 20.2"
Star: HD 34816
α 05h 17m 17.2s
δ −13° 13' 35.3"
Radio source:
α 05h 16m 16.4s
δ −13° 00' 3.2"
Star: HD 34816
Radio source:
α 05h 15m 23.0s
δ −12° 46' 7.9"
τ
V_LSR (km/s)

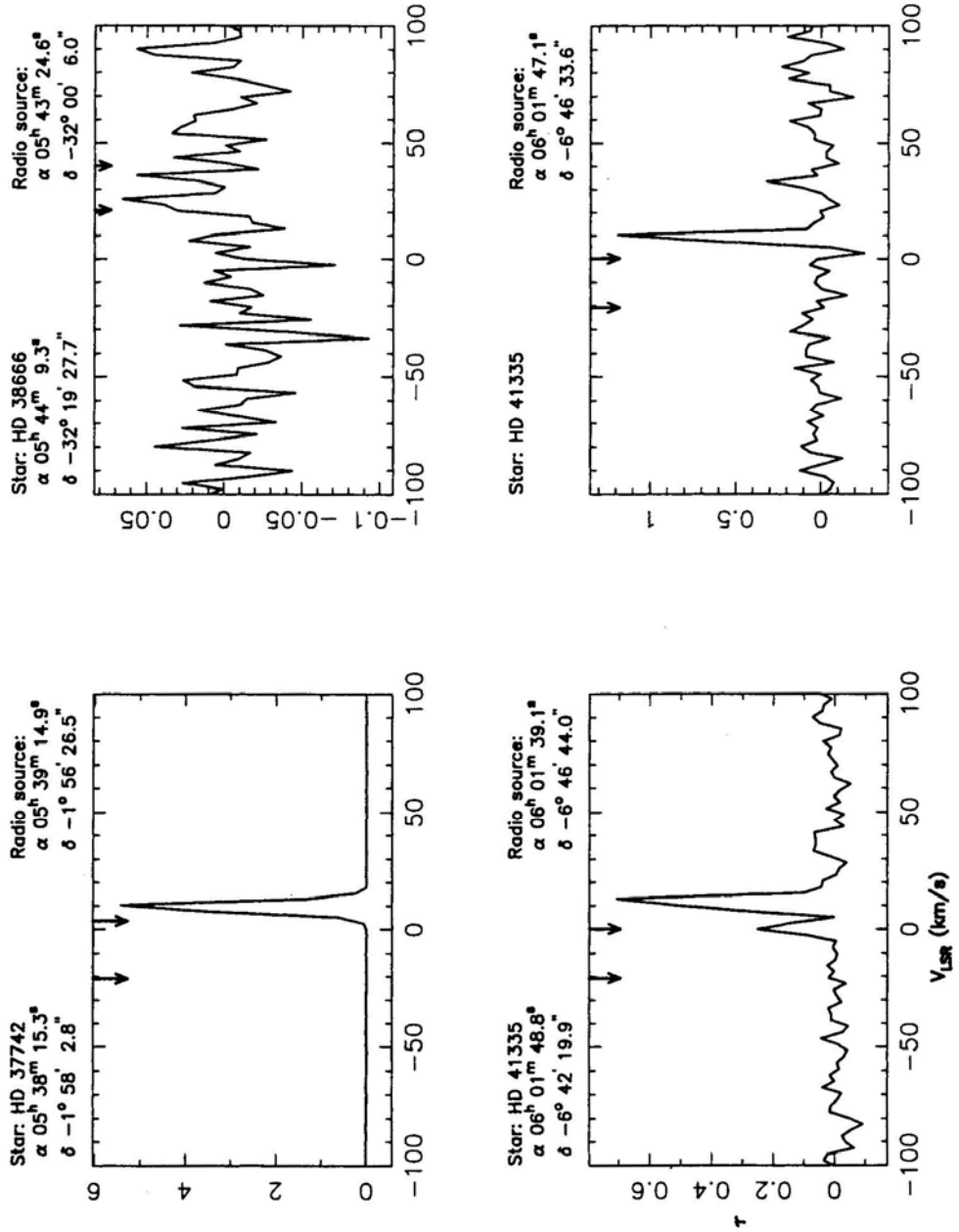
Star: HD 37742
α 05h 38m 15.3s
δ −1° 58' 2.8"
Radio source:
α 05h 39m 14.9s
δ −1° 56' 26.5"
Star: HD 38666
α 05h 44m 9.3s
δ −32° 19' 27.7"
Radio source:
α 05h 43m 24.6s
δ −32° 00' 6.0"
Star: HD 41335
α 06h 01m 48.8s
δ −6° 42' 19.9"
Radio source:
α 06h 01m 39.1s
δ −6° 46' 44.0"
Star: HD 41335
Radio source:
α 06h 01m 47.1s
δ −6° 46' 33.6"
τ
VLSR (km/s)

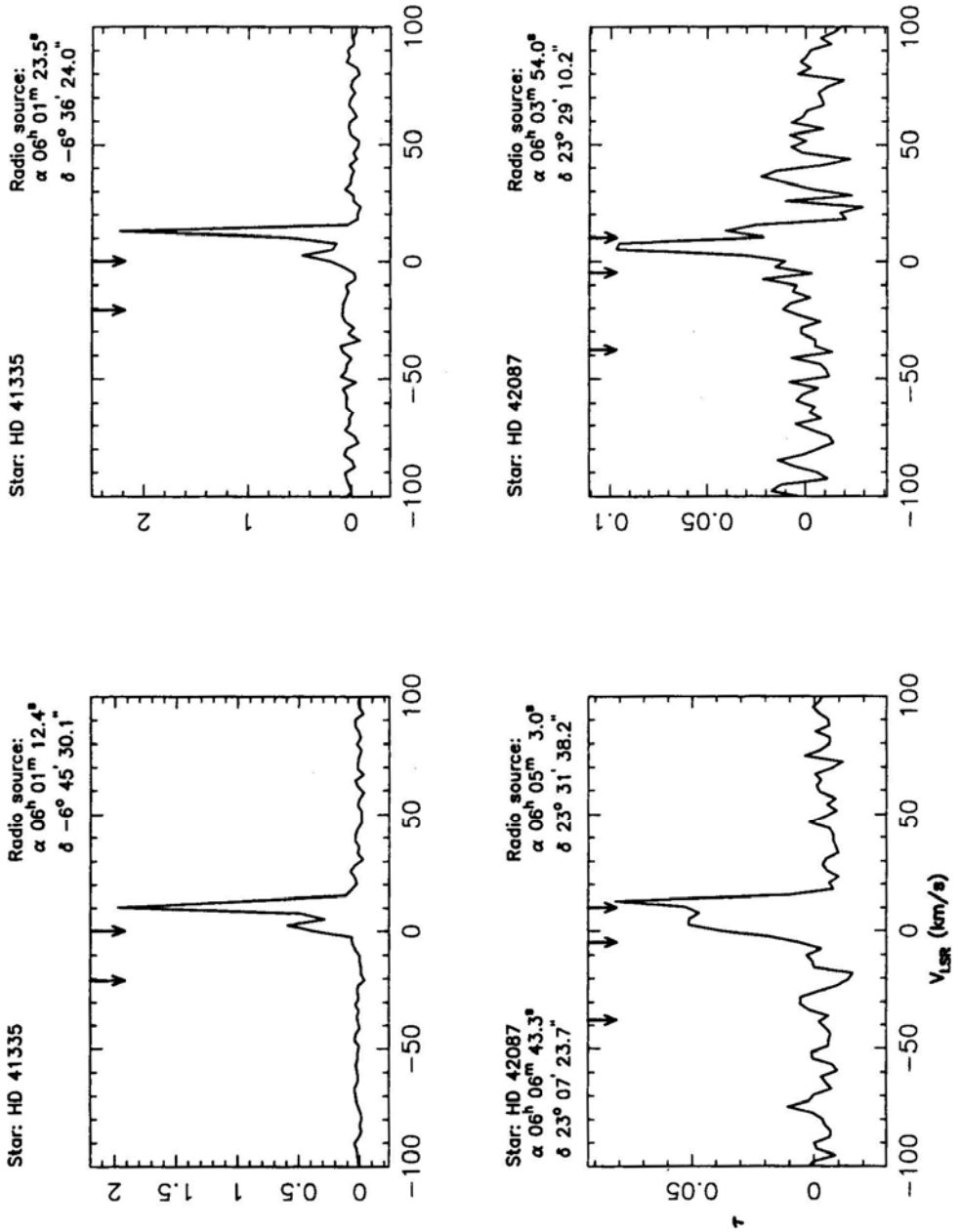
Star: HD 41335
Radio source:
α 06h 01m 12.4s
δ −6° 45′ 30.1″
Star: HD 41335
Radio source:
α 06h 01m 23.5s
δ −6° 36′ 24.0″
Star: HD 42087
Radio source:
α 06h 06m 43.3s
δ 23° 07′ 23.7″
Star: HD 42087
Radio source:
α 06h 05m 3.0s
δ 23° 31′ 38.2″
Star: HD 42087
Radio source:
α 06h 03m 54.0s
δ 23° 29′ 10.2″
τ
V_LSR (km/s)

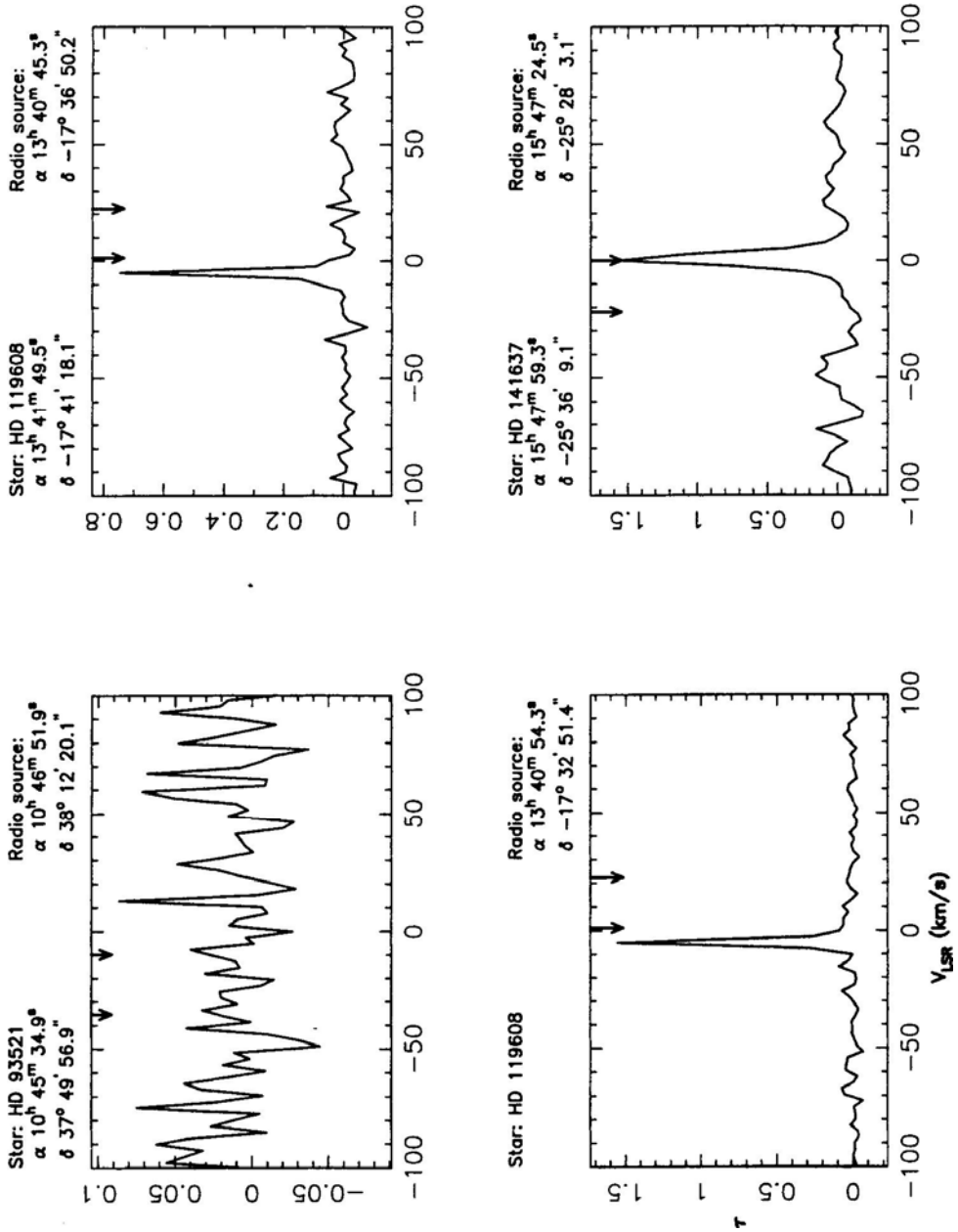
Star: HD 93521
α 10h 45m 34.9s
δ 37° 49' 56.9"
Radio source:
α 10h 46m 51.9s
δ 38° 12' 20.1"
Star: HD 119608
α 13h 41m 49.5s
δ −17° 41' 18.1"
Radio source:
α 13h 40m 45.3s
δ −17° 36' 50.2"
Star: HD 141637
α 15h 47m 59.3s
δ −25° 36' 9.1"
Radio source:
α 15h 47m 24.5s
δ −25° 28' 3.1"
Star: HD 119608
Radio source:
α 13h 40m 54.3s
δ −17° 32' 51.4"
τ
V_LSR (km/s)

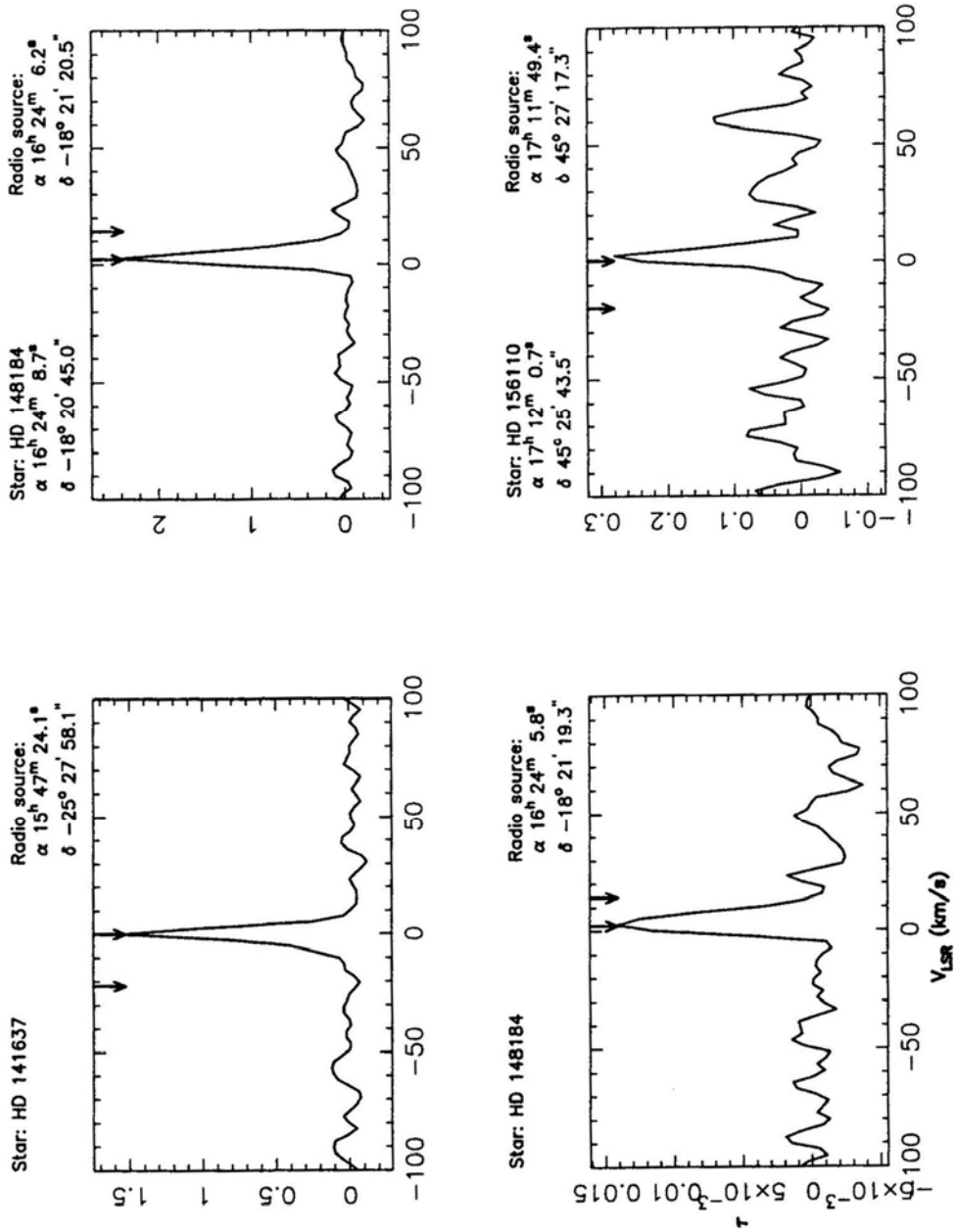
Star: HD 141637
Radio source:
α 15h 47m 24.1s
δ −25° 27′ 58.1″
Star: HD 148184
α 16h 24m 8.7s
δ −18° 20′ 45.0″
Radio source:
α 16h 24m 6.2s
δ −18° 21′ 20.5″
Star: HD 156110
α 17h 12m 0.7s
δ 45° 25′ 43.5″
Radio source:
α 17h 11m 49.4s
δ 45° 27′ 17.3″
Star: HD 148184
Radio source:
α 16h 24m 5.8s
δ −18° 21′ 19.3″
τ
V_LSR (km/s)

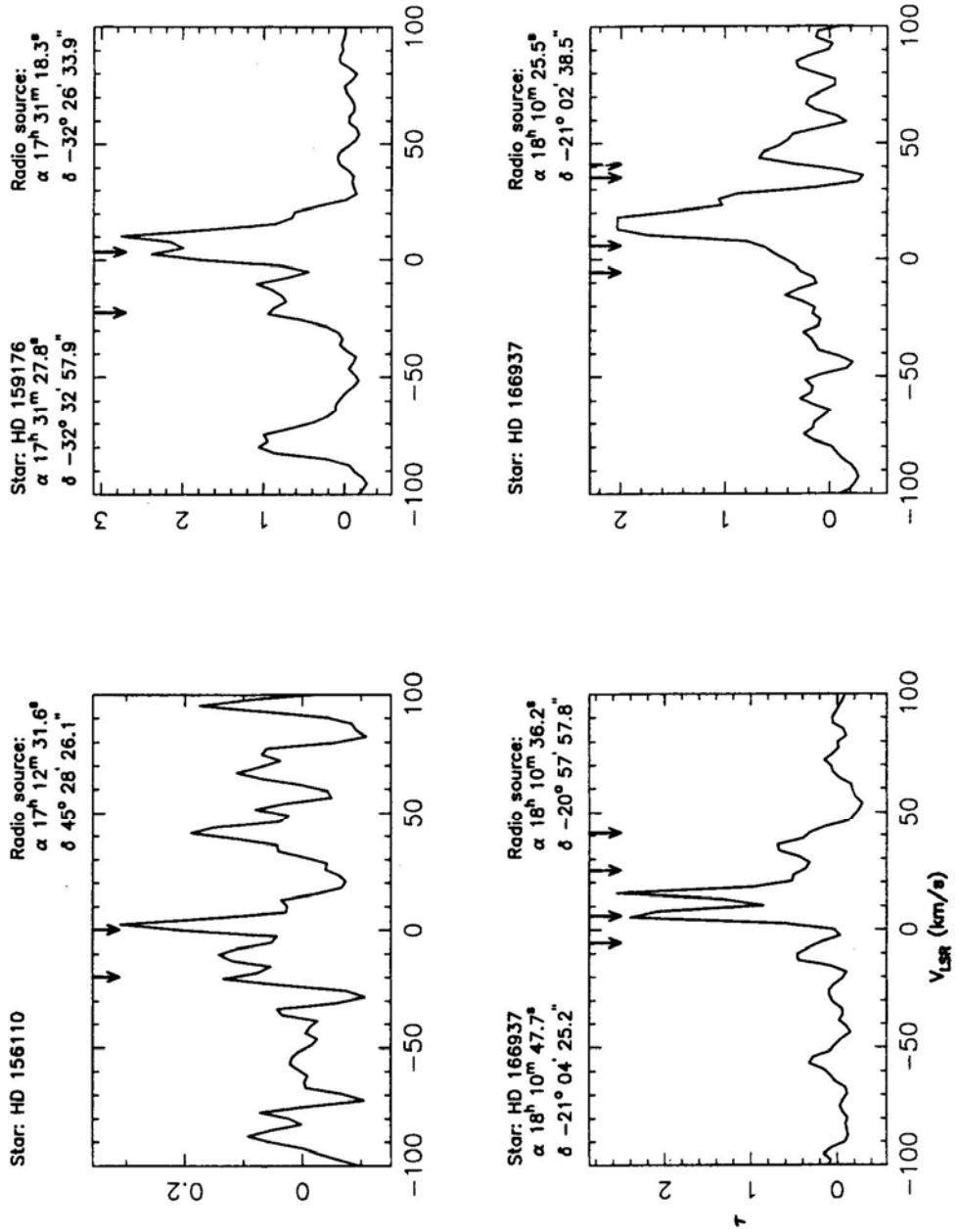
Star: HD 156110
Radio source:
α 17h 12m 31.6s
δ 45° 28' 26.1"
Star: HD 159176
α 17h 31m 27.8s
δ −32° 32' 57.9"
Radio source:
α 17h 31m 18.3s
δ −32° 26' 33.9"
Star: HD 166937
α 18h 10m 47.7s
δ −21° 04' 25.2"
Radio source:
α 18h 10m 36.2s
δ −20° 57' 57.8"
Star: HD 166937
α 18h 10m 25.5s
δ −21° 02' 38.5"
τ
V_LSR (km/s)

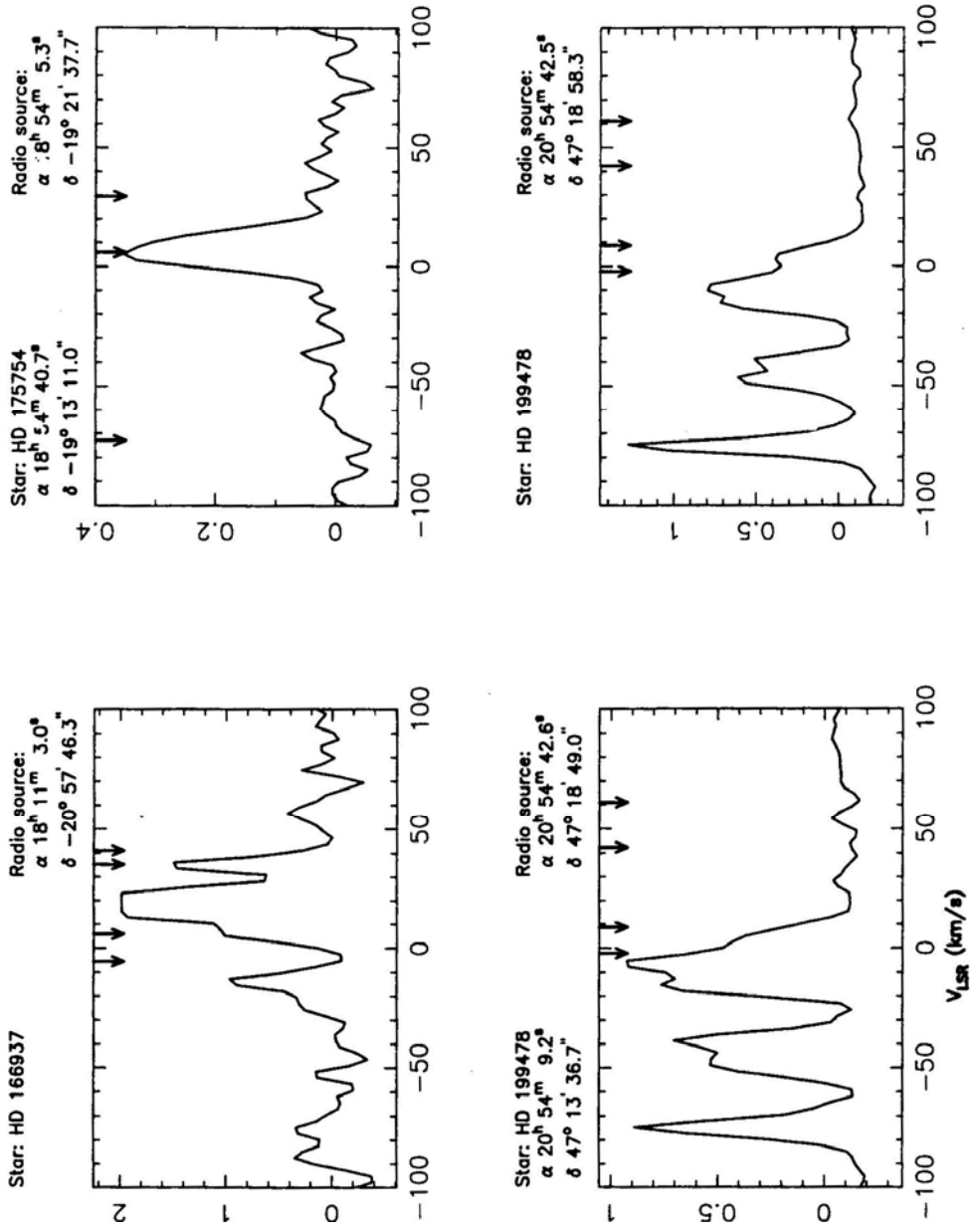
Star: HD 166937
Radio source:
α 18h 11m 3.0s
δ −20° 57' 46.3"
Star: HD 175754
α 18h 54m 40.7s
δ −19° 13' 11.0"
Radio source:
α 18h 54m 5.3s
δ −19° 21' 37.7"
Star: HD 199478
α 20h 54m 9.2s
δ 47° 13' 36.7"
Radio source:
α 20h 54m 42.6s
δ 47° 18' 49.0"
Star: HD 199478
Radio source:
α 20h 54m 42.5s
δ 47° 18' 58.3"
VLSR (km/s)

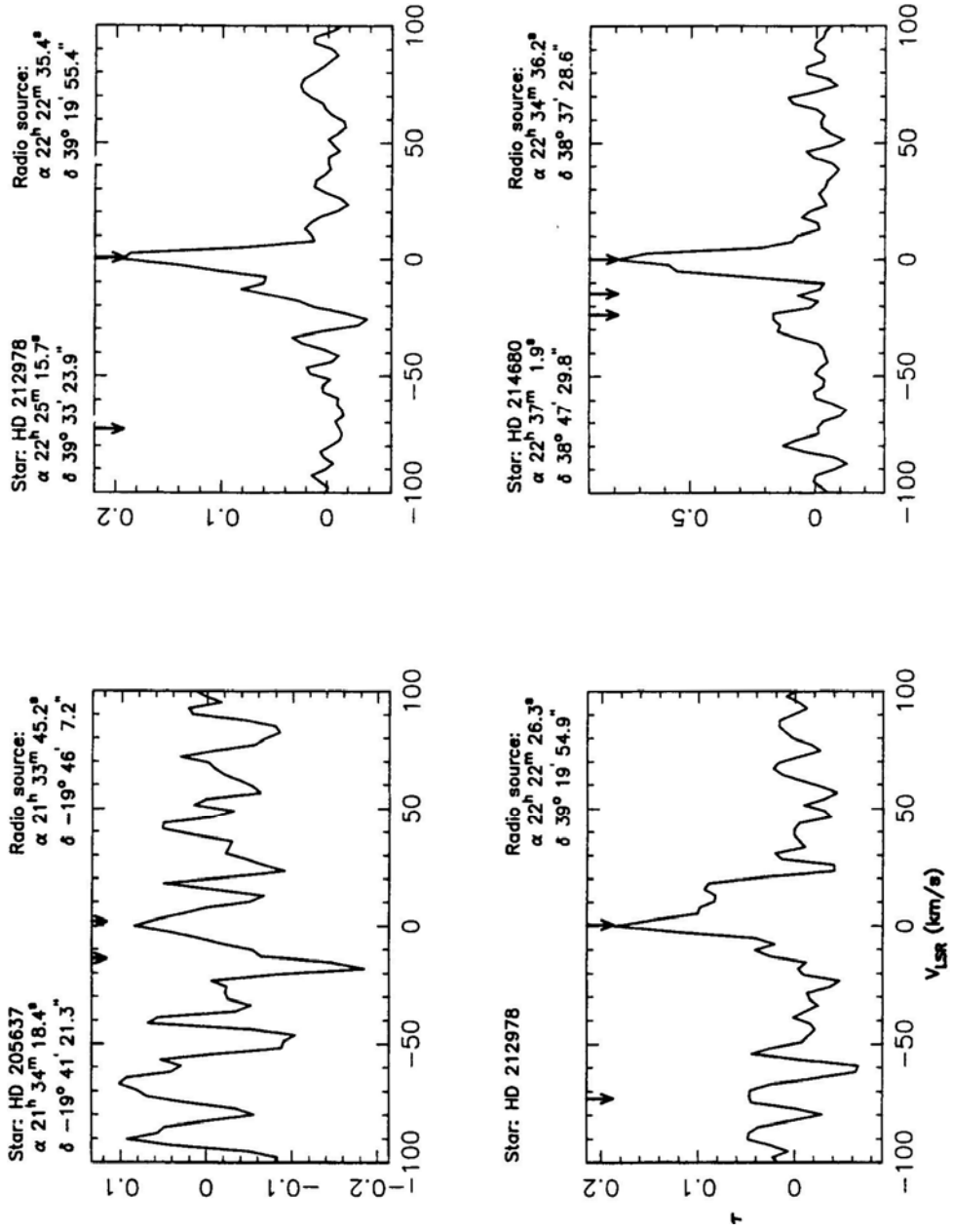
Star: HD 205637
α 21h 34m 18.4s
δ −19° 41′ 21.3″
Radio source:
α 21h 33m 45.2s
δ −19° 46′ 7.2″
Star: HD 212978
α 22h 25m 15.7s
δ 39° 33′ 23.9″
Radio source:
α 22h 22m 35.4s
δ 39° 19′ 55.4″
Star: HD 214680
α 22h 37m 1.9s
δ 38° 47′ 29.8″
Radio source:
α 22h 34m 36.2s
δ 38° 37′ 28.6″
Star: HD 212978
Radio source:
α 22h 22m 26.3s
δ 39° 19′ 54.9″
τ
v_{LSR} (km/s)

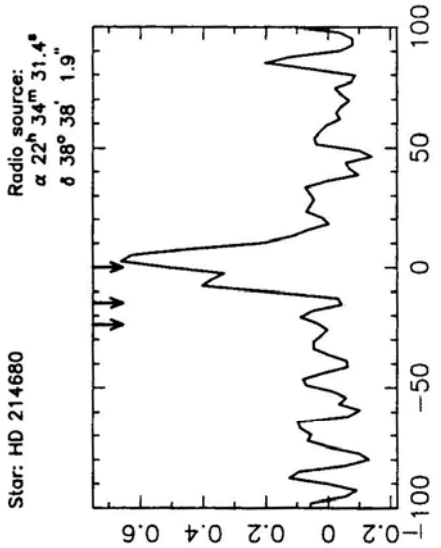
Star: HD 214680
Radio source:
α 22h 34m 31.4s
δ 38° 38' 1.9"
0.6
0.4
0.2
0
0.2
100
50
0
−50
−100

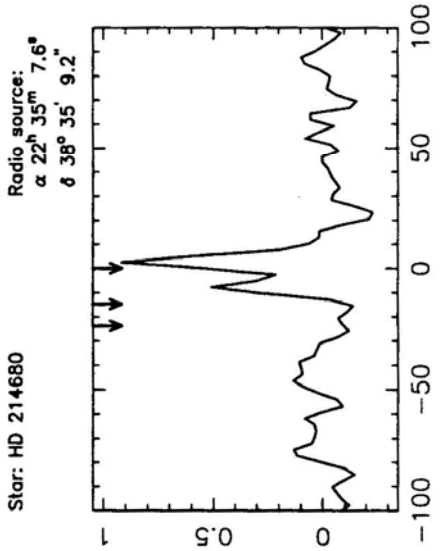
Star: HD 214680
Radio source:
α 22h 35m 7.6s
δ 38° 35' 9.2"
1
0.5
0
−100
−50
0
50
100

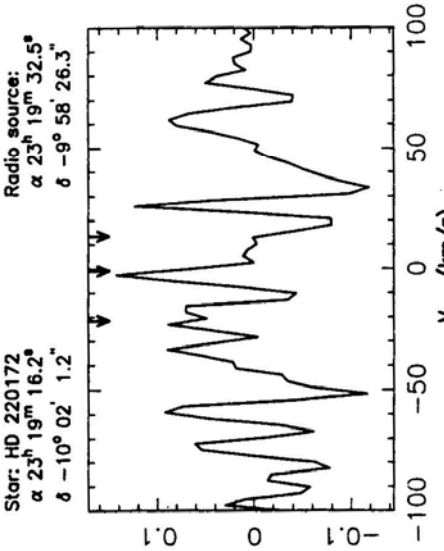
Star: HD 220172
α 23h 19m 16.2s
δ −10° 02' 1.2"
Radio source:
α 23h 19m 32.5s
δ −9° 58' 26.3"
τ
0.1
0
−0.1
−100
−50
0
50
100
VLSR (km/s)

J. Astrophys. Astr. (1998) **19,** 117–131

The Interstellar Clouds of Adams and Blaauw Revisited: An HI Absorption Study – II

Jayadev Rajagopal, G. Srinivasan & K. S. Dwarakanath

Raman Research Institute, Bangalore 560 080, India.
email: jaydev@rri.ernet.in, srini@rri.ernet.in, dwaraka@rri.ernet.in

Received 1998 August 4; accepted 1998 November 20

Abstract. In the preceding paper (Paper I), we presented HI absorption spectra towards radio sources very close to the lines of sight towards twenty five bright stars against which optical absorption spectra had been obtained earlier, In this paper we analyse the results and draw some conclusions.

To summarize briefly, in most cases we found HI absorption at velocities corresponding to the optical absorption features provided one restricted oneself to velocities $\lesssim$10 kms$_{-1}$. At higher velocities we did not detect any HI absorption down to an optical depth limit of 0.1 (except in four cases which we attribute to gas in systematic motion rather than clouds in random motion). After discussing various scenarios, we suggest that this trend should perhaps be understood in terms of the high velocity interstellar clouds being accelerated, heated and ablated by expanding supernova remnants.

Key words. ISM: clouds, structure, kinematics and dynamics.

1. Introduction

In the preceding paper (Rajagopal, Srinivasan & Dwarakanath 1998; Paper I) we presented the results of a program to obtain the HI absorption profiles towards a selected sample of bright stars. As mentioned there, detailed optical absorption studies exist in the direction of these stars in the lines of NaI and CaII. The motivation for such an observational program was also described in the previous paper. In the present paper, we wish to discuss the results obtained by us. There are two major issues that we wish to address and discuss later:

- Are the properties of interstellar clouds seen in optical absorption the same as those seen in HI emission and absorption in general?
- What is the origin and nature of the faster clouds seen in optical and UV absorption?

Let us elaborate a bit on the first issue. Although the general picture of the ISM that emerged from optical and radio observations, respectively, is the same, viz., clouds in pressure equilibrium with an intercloud medium, it has not been possible to directly compare the inferred properties. Whereas both the column densities and the spin temperatures of the clou ds have been estimated from HI observations, there have only

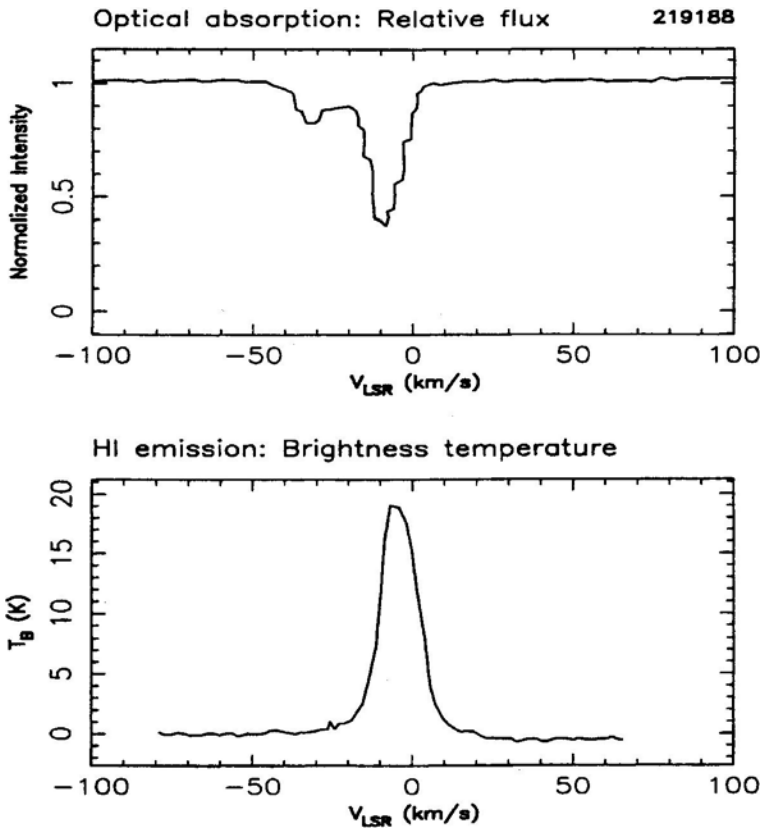

Figure 1. Comparison of optical absorption (top) from CaII towards HD219188 (Sembach, Danks and Savage 1993) and HI emission (Habing 1968) in the same direction. The absorption feature at higher velocity is missing in the HI profile.

been indirect and often unreliable estimates for the clouds seen in optical absorption. Our HI absorption measurements, combined with HI emission measurements in the same directions will enable us to directly estimate for the first time the column densities and spin temperatures of the clouds seen in optical absorption.

The second question mentioned above arises as follows. The existence of a *high velocity tail* in the distribution of random velocities of clouds was firmly established by Blaauw (1952) from the data obtained by Adams (1949). As mentioned in Paper I, it was noticed quite early on by Routly and Spitzer (1952) that the faster clouds have a smaller NaI to CaII ratio than the lower velocity clouds. Early HI emission measurements (see Paper I for references) in the direction of the bright O and B stars provided an added twist. Whereas the lower velocity clouds clearly manifested themselves in the HI emission measurements, the higher velocity clouds were not detected. To illustrate this point, we show in Fig. 1 the optical absorption features and the HI emission profiles towards the star HD219188. It may be seen that there is no counterpart in HI emission to the higher velocity optical absorption feature.

In the next two sections (sections 2 and 3) we will discuss the results of our absorption survey presented in Paper I. We shall classify the HI absorption features into two broad classes, viz., “low velocity” and “high velocity”. It is of course

difficult to define a sharp dividing line between "low" and "high" velocities. But based upon earlier analyses of Nal to CaII ratios, as well as HI emission measurements, we adopt a velocity of the order of 10km s^{-1} as the dividing line. The main conclusions from our study are summarized in section 4. Section 5 is devoted to a detailed discussion of the nature and origin of the high velocity clouds.

2. The low velocity clouds

In this section we discuss the low velocity absorption features (i.e., $\upsilon \lesssim$ 10km s^{-1}). To recall from Paper I, we detected HI absorption in all but four of the twenty four fields we looked at. We will discuss these four unusual fields at the end of the next section.

2.1 *Coincident absorption features*

All the lines of sight in our sample show optical absorption from CaII at both low and high velocities. In most of the fields where we have detected HI absorption, they occur at roughly the same velocities as the optical absorption lines for $\upsilon \lesssim$ 10 km s^{-1}. Not surprisingly, the HI absorption features have one-to-one correspondence with the HI emission features in the fields for which earlier emission measurements exist. In Table 1 we have listed all the fields with "matching" velocities in optical absorption and HI emission and absorption.

For illustration we have shown in the upper panels of Fig. 2 the HI absorption spectra (optical depth) in three fields; HI optical depth is plotted as a function of V_{LSR}. The arrows indicate the velocities of the optical absorption lines. For comparison, we have shown in the lower panels the HI emission in these 3 fields: the data obtained by Habing (1968) has been digitized and re-plotted. The first field contains the star HD34816. The optical spectrum obtained by Adams (1949) towards this star shows CaII absorption at – 14.0 and +4.1 km s^{-1}. The HI absorption profile shows a prominent feature at 6 km s^{-1} (we have obtained spectra towards two radio sources in this field but only one of them is shown here). As may be seen from the lower panel, there is a corresponding emission feature at this velocity. As mentioned in Paper I, absorption features in the optical and HI spectra may be taken to be at "matching" velocities provided they are within ~ 3km s^{-1} of one another (this window is to account for blending effects in the optical spectra and different corrections adopted for solar motion). In view of this one may conclude that the optical absorption at +4.1 km s^{-1} and HI emission and absorption at 6 km s^{-1} arise in the same cloud, even though the radio source is 20′ away from the star.

The second panel pertains to the field containing the star HD42087. In this field also we have two radio sources within the primary beam, and the spectrum towards one of them is shown. The absorption features are clearly seen at 4.4 km s^{-1} and 12.4 km s^{-1}, with the latter being much stronger. The HI emission spectrum (shown in the panel below) shows a broad peak centred at ~ 15 kms^{-1}. The absorption feature at 12.4 km s^{-1} may be taken to be the counterpart of the optical absorption at 10.2 km s^{-1}. There is no HI absorption at negative velocities corresponding to the other optical absorption lines indicated by the arrows. This may be due to the fact that the two radio sources in the field are 32′ and 42′ respectively from the star in

Table 1. Summary of coincident low velocities: Column 1 lists the HD number for the field. Columns 2 and 3 give the LSR velocities for the "matching" optical and HI absorption features respectively. Columns 4 and 5 list the optical depth and width for the HI absorption derived from the fitted gaussian. Column 6 lists the spin temperature T_S. These values have been derived by using the optical depth from our observations along with the emission brightness temperatures from Habing (1968). Where this was not available we used brightness temperatures from the Leiden-Green Bank survey (Burton 1985). Those fields where emission measurements were not available are marked NA in column 6.

Field	V_{lsr}(opt)	V_{lsr}(HI)	τ	ΔV	T_s
	km s^{-1}	km s^{-1}		km s^{-1}	K
14143–14134	−10.3	−11.2	0.18	11.8	283^{+}
14818	−6.6	−3.7	0.43	13.7	143
21278	−0.2	2.8	0.18	5.1	250
21291	−7.5	7.0	0.60	6.2	180
24912	4.7	4.3	0.80	14.9	73
25558	10.1	8.1	1.13	5.6	73
34816	4.1	6.0	1.50	3.2	45
41335	0.2	1.0	0.22	7.2	342
42087	10.2	12.4	1.26	3.5	211
141637	0.0	0.5	1.60	8.0	NA
148184	2.2	3.4	4.90	3.4	50
156110	0.4	2.2	0.28	7.5	102
159176	−22.5	−20.8	1.15	15.3	NA
166937	5.9	5.4	1.70	5.7	NA
175754	5.9	6.8	0.35	17.7	135
199478	−2.1, 8.7	3.8^{+}	0.60	11.4	121
212978	0.6	0.3	0.20	9.0	NA
214680	0.1	1.4	*	2.1	NA

$^{+}$ The feature is a blend.
* The feature is saturated.

question. Given that the star is at a distance of 1.3 kpc (Paper I, Table 1) it is conceivable that we are not sampling all the gas seen in optical absorption.

The spectra towards HD148184 is shown in panel 3. Again there is good agreement between the HI spectrum and the optical spectrum as far as the lower velocity optical absorption is concerned. As in the previous two cases there is no counterpart of the higher velocity optical absorption in the HI spectrum. These two examples will suffice to illustrate the general trend in Table 1 viz., there is reasonably good agreement at low velocities ($\upsilon \lesssim 10$km s^{-1}) between the optical absorption features and the HI spectra.

Returning to Table.1, we have listed the derived optical depths in column 4 and the velocity width of the HI absorption in column 5. In the last column we have given the derived *spin temperatures*. These are obtained by supplementing our HI absorption measurements with brightness temperatures derived from emission measurements (mostly from Habing 1968; and in some cases from Burton 1985). To the best of our knowledge, this is the first direct determination of the temperatures of the interstellar clouds seen in optical absorption. To be precise, the temperature derived by us is the spin temperature which may be taken to be an approximate measure of the kinetic temperature.

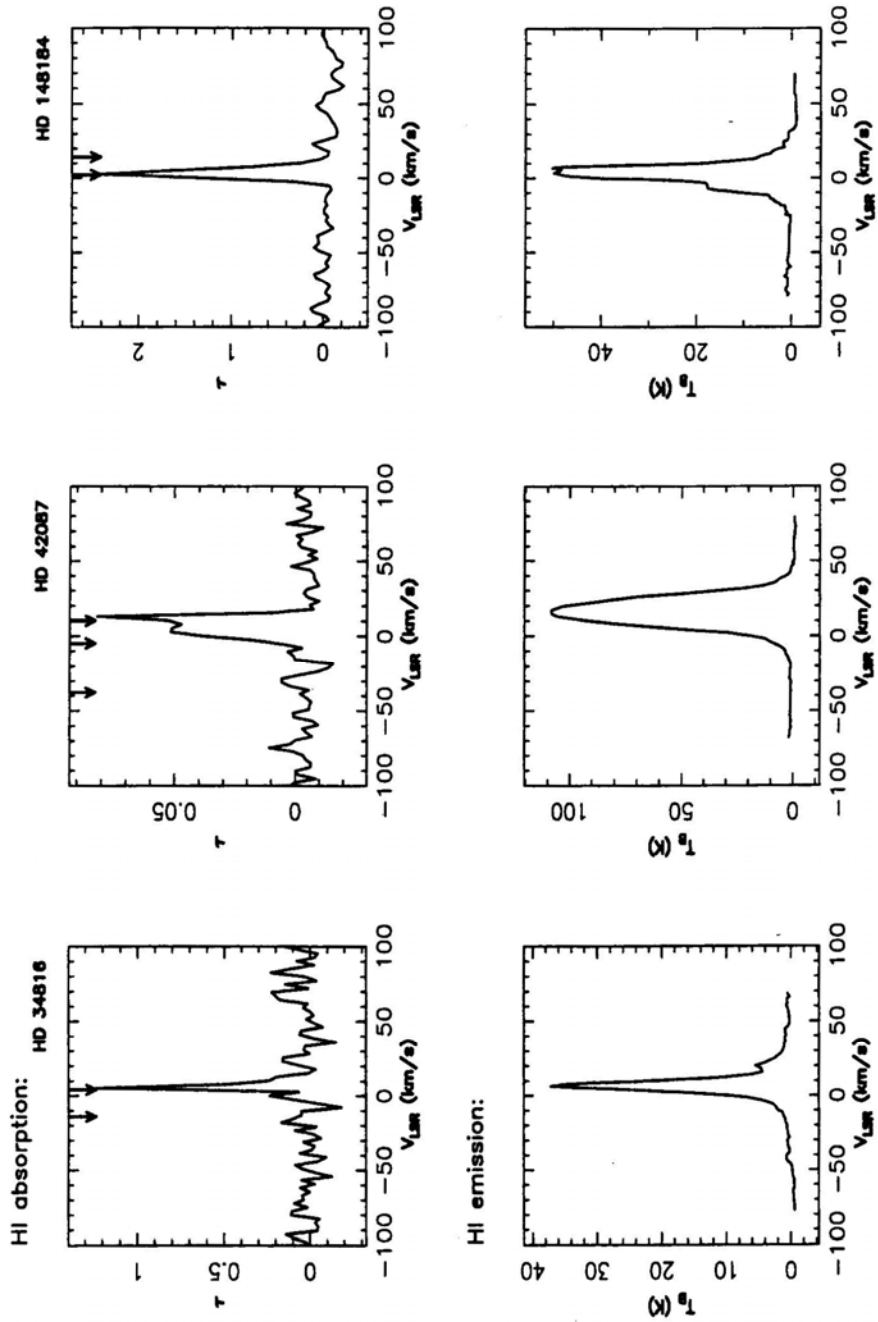

Figure 2. HI absorption (top) and emission (bottom) spectra towards three stars demonstrating the correspondence in *low* velocity emission in optical absorption, HI emission and HI absorption. The arrows on the velocity axis of the optical depth plot mark the velocities at which optical absorption is seen. The emission spectra are digitized from Habing (1968).

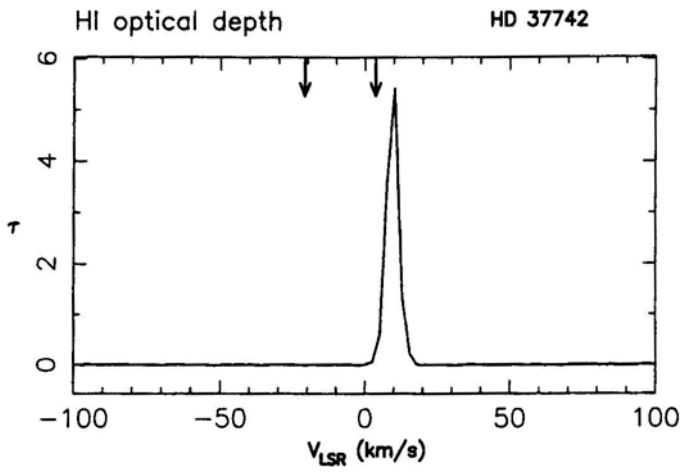

Figure 3. Spectram towards HD37742. The arrows on the velocity axis mark the velocities at which optical absorption is seen.

The correspondence between the optical absorption features and the HI absorption suggests that one is sampling the same clouds in both cases. The derived spin temperatures and velocity widths are consistent with these clouds belonging to the same population as the standard cold diffuse clouds in the raisin-pudding model of the ISM. While it is conceivable that at low velocities one may merely be sampling the local gas (regardless of direction), statistical tests carried out by Habing (1969) suggest that this is unlikely.

2.2 *Non-coincident absorption feature*

As we have already encountered in the case of HD42087 (see Fig. 2), sometimes there is a mismatch between optical and radio spectrum even at low velocities. We mention two specific cases here.

HD37742

The HI absorption spectrum obtained by us (Fig. 3) shows a deep absorption feature at 9.5 km s^{-1}. There are no other absorption features down to an optical depth limit of 0.03. The optical absorption features are at 3.6 and –21 km s^{-1}. Since the radio source is only 12′ away from the star, given the distance estimate of 500 pc to the star the discrepancy between the optical spectrum and the HI absorption spectrum is significant and intriguing. While the gas seen strongly absorbing in HI could be located beyond the star, one is left wondering as to why one does not see the low velocity cloud seen in optical absorption.

HD119608

The optical absorption spectrum towards this star obtained by Munch and Zirrin (1961) shows two minima at 1.3 and 22.4 km s^{-1}. We have obtained HI absorption

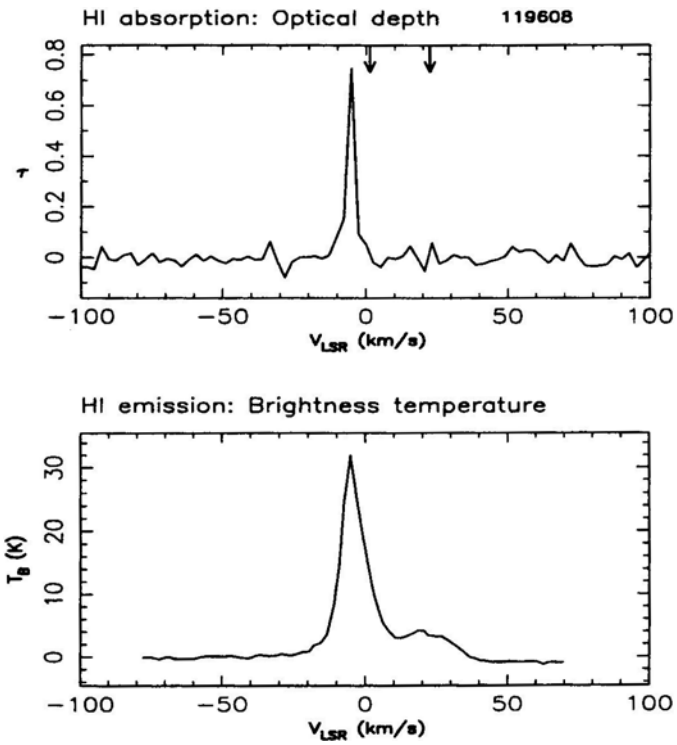

Figure 4. HI absorption (top) and emission (bottom) spectra towards HD119608. The arrows mark the velocities at which optical absorption is seen. The emission spectrum is from Habing (1968).

towards two strong radio sources in this field both within 15′ of the star. Both show a deep absorption feature at –5.4 km s^{-1} (Fig. 4). This agrees with the HI emission feature shown in the lower panel. However the HI emission spectrum also shows a broad feature peaking at ~ 20 km s^{-1}. This is also seen in the more recent measurement of Danly *et al.* (1992). If this feature is indeed to be identified with the optical absorption at 22.4 km s^{-1}, then this represents an interesting case where the gas in the line of sight to the star causing optical absorption manifests itself in HI emission but not absorption. This could happen for example if the spin temperature of this gas is sufficiently high as to make the HI optical depth below our detection limit. HD 119608 is a high latitude star and one is presumably sampling the halo gas, and warrants a deeper absorption study.

3. The high velocity clouds

Although in the previous section, we were primarily concerned with establishing the correspondence between the optical absorption features and the HI absorption spectra at low velocities, we did have occasion to comment on the *absence of HI absorption from the high velocity clouds* [The high velocity clouds we are discussing are those that populate the tail of the velocity distribution obtained by Blaauw (1952) and not those that are commonly referred to as HVCs in the literature]. It turns out that in all

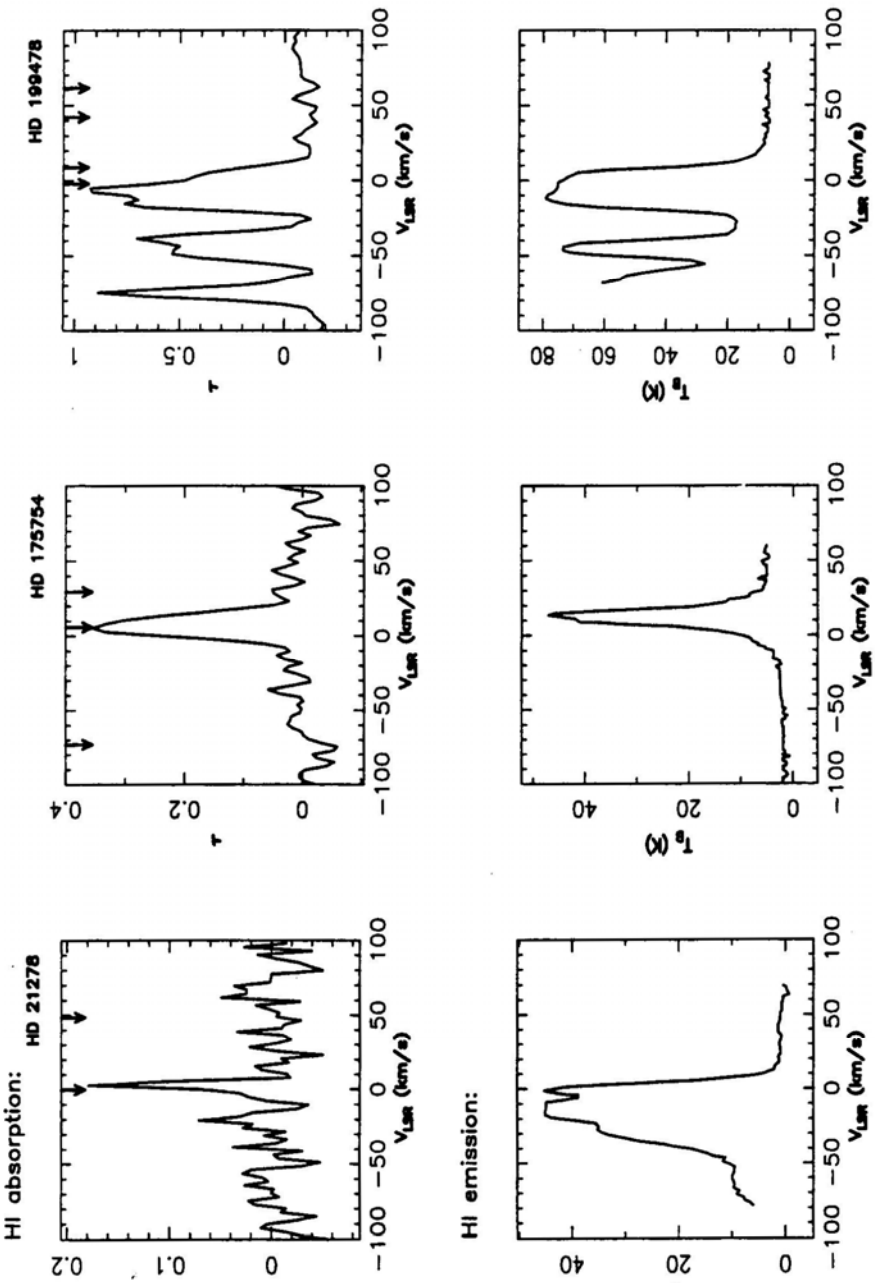

Figure 5. HI absorption (top) and emission (bottom) spectra towards three stars showing the lack of HI features corresponding to the high velocity optical absorption. The arrows on the velocity axis of the optical depth plot mark the velocities at which optical absorption is seen. The emission spectrum is from Habing (1968).

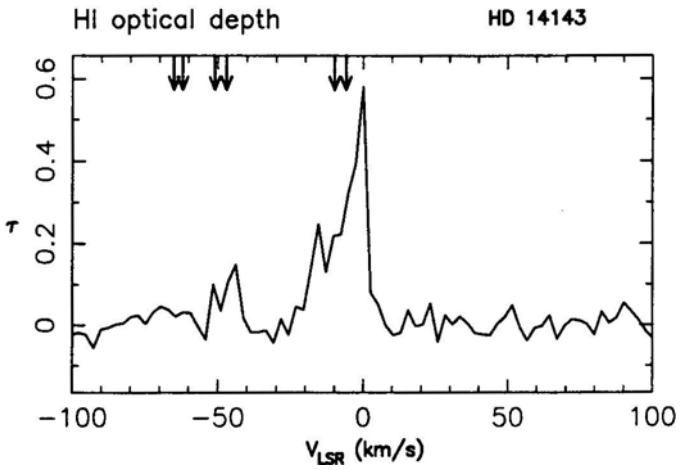

Figure 6. HI absorption spectra towards HD14143. The arrows mark the velocities at which optical absorption is seen.

but four cases, we fail to detect HI absorption at velocities corresponding to the high velocity ($\gtrsim$ 10 km s^{-1}) optical absorption lines. To illustrate this generic trend, we have shown some additional examples in Fig. 5. *It may be seen in the figure that the high velocity optical absorption features* (*indicated by arrows*) *are not seen in the HI emission spectra either.* A discussion of this will form the major part of section 5.

In only four out of the twenty four lines of sight have we detected HI absorption at velocities $\gtrsim$ 10km s^{-1} and which clearly correspond to the optical absorption lines. We discuss these below.

3.1 *Coincident absorption features at high velocities*

HD14134, HDI4143

These two stars (in the same field) are members of the *h* and *chi* Persei clusters (Münch 1957). There were three radio sources within our primary beam (all within 10′ of the star). The HI absorption features towards one of them is shown in Fig. 6. The prominent high velocity absorption features towards the three sources are at –52.8,–50.3 and –46.1 km s^{-1}, respectively(Table 1 of Paper I).These should be compared with the optical absorption features towards the two stars in question which are at –46.8 and –50.8 km s^{-1}. Thus there is reasonable coincidence between the optical and HI data. Nevertheless we wish to now point out that the high velocity may not represent random motion but rather systematic motion. While interpreting his pioneering observations Münch (1957) attributed the high velocity features in the optical spectra to anomalous motions in the Perseus arm. Since then it has generally been accepted that there are streaming motions in the Perseus arm with velocities ranging from –10 to –30 km s^{-1} (Blaauw & Tolbert 1966; Brand & Blitz 1993). For the sake of completeness we have listed in Table 2 the spin temperature of the gas derived by us by combining our measurements with existing HI emission measurements.

Table 2. Summary of coincident high velocities: Column 1 gives the HD number of the field. Column 2 lists the *high* velocity optical absorption seen towards the star. Column 3 is the "matching" HI absorption. Columns 4 and 5 give the fitted optical depth and width of the HI absorption features. The spin temperature is listed in column 6. As in the case of the low velocity features, we have used Habing(1968) and the Leiden-Green Bank survey for the emission temperatures needed to compute the spin temperature from the optical depth.

Field	V_{lsr}(optical)	V_{lsr}(HI)	τ	ΔV	T_s
	km s^{-1}	km s^{-1}		km s^{-1}	K
14143–14134	−50.8	−50.3	0.30	10.0	96
21291	−34.0	−31.2	0.40	3.3	181
159176	−22.5	−20.8	1.15	15.2	NA

HD21291

The spectrum towards this star near the Perseus arm has a prominent Na D line at a velocity of –34 km s^{-1} (Münch 1957). The HI absorption spectrum shows a feature at –31.2 km s^{-1}. The contribution to radial velocity from Galactic rotation can only be ~ 10 km s^{-1}, thus indicating significant peculiar motion of the gas. In our opinion one must attribute this to streaming motion of the gas as in the case discussed above. HI emission clearly shows spatially extended gas covering the longitude range from ~ 136° to 141° at the velocity of interest. This strengthens the conclusion that one must not attribute the observed velocity to random motions.

HD 159176

There is pronounced optical absorption at –22.5 km s^{-1} which might be identified with the HI absorption seen by us at –20.8 km s^{-1}. Given the longitude of 356°, it is difficult to attribute this to Galactic rotation. The measured velocity must correspond either to random velocity or systematic motion.

HD166937

In the case of this star, there is no strict coincidence (within 3 km s^{-1}) between the HI and optical absorption at high velocities. However we see two HI absorption features at velocities close to and straddling the optical feature at 41.1 km s^{-1}, so we include this field in our list of high velocity coincidences. It may be noted that this star is also close to the Galactic center direction.

4. Summary of results

In the preceding section we described the first attempt to directly compare HI absorption with optical absorption features arising in the ISM. We summarize below the main results:

(i) HI absorption measurements were carried out towards twenty four fields. Each field has existing optical absorption spectra towards a bright star. In twenty of these fields we detected HI absorption features.

(ii) In all but four of these twenty fields, the HI absorption features at low velocities (< 10 km s^{-1}) correspond to the optical absorption lines.
(iii) In most cases there is also corresponding HI emission.
(iv) The spin temperatures derived by us for the low velocity gas is consistent with the standard values for the cold diffuse HI clouds.
(v) This lends strong support to the hypothesis that (at least) the low velocity clouds seen in optical absorption belong to the same population as those sampled in extensive HI studies.
(vi) In twenty out of twenty four fields surveyed, we did not detect any HI absorption corresponding to optical absorption at high velocities (v > 10 km s^{-1}). It is unlikely that in all cases this is due to our line of sight not sampling the gas seen in optical absorption; in several cases the line of sight to the radio sources would have sampled this gas even if its linear size was of the order of 1 pc.
(vii) Curiously, the early emission measurements also failed to detect HI gas at high velocities (in these same lines of sight). Given the size of the telescopes used, beam dilution could have accounted for the non-detection if the gas was "clumpy". Our absorption measurements rule this out as a generic explanation.

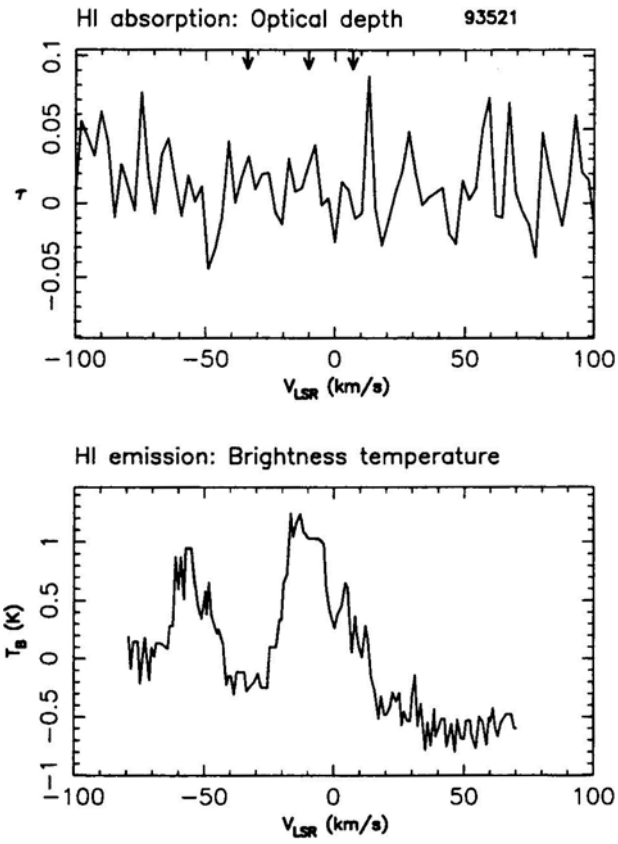

Figure 7. HI absorption (top) and emission (bottom) spectra towards HD93521. The arrows plot mark the velocities at which optical absorption is seen. The emission spectrum is from Habing (1968).

More recent and sensitive measurements indicate that the high velocity gas has much smaller column density than the low velocity gas ($N(HI) < 10^{18}$ cm^{-2}). If this is the case, then it is not difficult to reconcile why we do not see it in absorption since our sensitivity limit was $\tau \gtrsim 0.1$. But then the correlation between high velocity and low column density would have to be explained. We venture to offer some suggestions in the next section.

(viii) *Fields with no HI absorption:* We wish to record that in the fields containing the stars HD38666, HD93521, HD205637 and HD220172 *we did not detect any HI absorption -even at low velocities.* These are all high latitude stars. HI emission spectra also show only weak features. For illustration we show in Fig. 7 the HI absorption and emission spectrum towards HD93521. From very detailed investigations – the case of HD93521 is a good example -it has been concluded that most of the optical absorption arises from warm gas in the halo (detailed references may be found in Spitzer & Fitzpatrick 1993 and Welty, Morton & Hobbs 1996). The fact that we do not see HI absorption is consistent with the interpretation of this gas being warm. Weak HI emission indicates low column density also.

5. Discussion

As we have already argued, our absorption measurements, taken together with earlier emission measurements, establishes that the low velocity clouds seen in optical absorption are to be identified with the standard HI clouds–their column densities and spin temperatures match.

But the true nature of the high velocity clouds seen in optical absorption is still unclear. There are two questions to be addressed: (**1**) Do the high velocity clouds belong to a different population, and (**2**) is there a causal connection between their higher velocities and lower column densities? We wish to address these two questions below.

An unambiguous indication that the high velocity clouds may have very different properties compared to their low velocity counterparts comes from an HI absorption study towards the Galactic center (Radhakrishnan & Sarma 1980). Given the statistics of clouds derived from optical studies (8 to 12 perkpc), if the high velocity clouds had optical depths comparable to the low velocity clouds, then an absorption experiment towards the Galactic center should straightaway reveal a velocity distribution similar to the one derived by Blaauw (1952) from Adams' data. The velocity distribution derived by Radhakrishnan and Sarma from precisely such a study did not reveal a pronounced high velocity tail. The velocity dispersion of 5 km s^{-1} derived by them was in good agreement with the low velocity component of Blaauw's distribution. Instead of a pronounced high velocity tail seen in optical and UV studies, there was at best a hint of a high velocity population of very weakly absorbing clouds. Even this conclusion has remained controversial (Schwarz, Ekers & Goss 1982).

As for the possible correlation between higher velocities of clouds and lower column densities, fairly conclusive evidence comes from UV absorption studies. Since the UV absorption lines have larger oscillator strengths, they can be used to probe smaller column densities than is possible with optical absorption lines. The analysis of Hobbs (1984) seems to confirm this expectation–in several lines of sight

there is more high velocity UV absorption features than in the optical. A more direct inference can be drawn from the work of Martin & York (1982). For the two lines of sight they studied, there is a clear indication of lower column density (N(HI)) at higher velocities.

Over the years, three broad suggestions have been put forward in an attempt to elucidate the nature of the high velocity clouds.

5.1 *Circumstellar clouds*

According to an early suggestion due to Schlüter, Schmidt & Stumpf (1953), the high velocity clouds seen in optical absorption are to be identified with circumstellar clouds. This was an attempt to explain the predominance of *negative* velocities in the high velocity absorption features. If the clouds in the vicinity of massive stars are accelerated by the combined effect of stellar winds and radiation from the stars, then in an absorption study against the stars one would detect only those clouds accelerated towards us. A few years later, Oort & Spitzer (1955) developed the well known "rocket mechanism" in which the UV radiation from the star ionizes the near side of the cloud resulting in ablation and consequent acceleration of the cloud. This mechanism will naturally result in the higher velocity clouds having smaller mass and therefore smaller column density. The difficulty with this mechanism, however, is that one will have to invoke another mechanism to explain the large *positive* velocities which are also seen in absorption studies. In view of this we will not dwell any further on this scenario.

5.2 *Relic SNRs*

An alternative scenario was advanced by Siluk & Silk (1974). Their suggestion was that the high velocity optical absorption features arise in very old supernova remnants (SNRs) which have lost their identity in the ISM. Their primary objective in advancing this scenario was to explain the high velocity tail of the velocity distribution of optical absorption features. The point was that if the absorption features arise not in interstellar clouds but in SNRs in their very late stages of evolution, then it would result in a power law distribution of velocities; such a distribution according to them provided a good fit to the observations.

While this suggestion is quite attractive, it suffers from two drawbacks: (**1**) The early studies on the evolution of SNRs predicted the formation of very dense shells beyond the radiative phase. Such compressed shells were essential to explain the observed absorption features and the derived column densities. However, more recent studies which take into account the effects of the compressed magnetic field ands cosmic ray pressure in the shells suggest that either dense shells do not form or if they do, do not last long enough (Spitzer 1990; Slavin & Cox 1993). (**2**) Given a supernova rate of one per ~ 50 years in the Galaxy, the statistics of absorption features requires that the SNRs enter the radiative phase (and as a consequence develop dense shells) when they are still sufficiently small so as not to overlap with one another. This would indeed be the case if the intercloud medium into which the SNRs expand is dense enough ($n \sim 0.1$ cm^{-3}). But if a substantial fraction of the ISM is occupied by low density hot gas ($n \sim 0.003$ cm^{-3}; $T \sim 5 \times 10^5$ K) such as indicated by UV and soft X-ray observations then the supernova bubbles are likely to intersect with one another and perhaps

even burst out of the disk of the Galaxy before developing dense shells (Cowie & York 1978). In view of these two drawbacks, we do not favour this suggestion.

5.3 *Shocked clouds*

The third possibility is that the high velocity absorption features do arise in interstellar clouds but which have been engulfed and shocked by supernova blast waves. Indeed we feel that this is the most plausible explanation for it has support from several quarters. The earliest evidence that the high velocity gas may be "shocked" came from the Routly-Spitzer effect. The NaI/CaII ratio in the fast clouds was lower (sometimes by several orders of magnitude) than in the slow clouds. The variation in NaI/CaII ratio was primarily attributed to the variable *gas phase abundance* of calcium in these clouds. Due to its relatively high condensation temperature calcium is likely to be trapped in grains. Spitzer has argued that the observed trend in NaI/CaII ratio could be understood if the calcium is released back into the gas phase in the high velocity clouds due to sputtering. This is indeed what one would expect if the interstellar cloud is hit by an external shock, which in turn drives a shock into the clouds (Spitzer 1978). Supernova blast waves are the most likely candidates.

Earlier in this section we referred to an HI absorption study by Radhakrishnan & Sarma towards the Galactic center. While they did not find strong absorption at high velocities they did conclude that there must be a population of weakly absorbing high velocity clouds. Radhakrishnan & Srinivasan (1980) examined this more closely and advanced the view that in order to explain the optical depth profile centered at zero velocity one had to invoke *two distinct velocity distributions:* a standard narrow distribution witha velocity dispersion of ~ 5 km s^{-1}, and a second one with a much higher velocity dispersion of ~ 35 km s^{-1}. While arguing strongly for a high velocity tail, they stressed that the latter distribution must consist of a population of very weakly absorbing clouds. They went on to suggest that this population of weakly absorbing clouds might be those that have been shocked by expanding SNRs; the very process of acceleration by SNRs might have resulted in significant loss of material and heating of the clouds, leading to low HI optical depths.

To conclude this discussion we wish to briefly summarize the expected life history of a cloud hit by a supernova blast wave. The first consequence of a cloud being engulfed by an expanding SNR is that a shock will be driven into the cloud itself resulting in an eventual acceleration of the cloud. The effect of this shock and a secondary shock propagating in the reverse direction after the cloud has been overtaken by the blast wave, is to compress and flatten the cloud. Eventually various instabilities are likely to set in which will fragment the cloud.

The detailed history of the cloud depends upon two important timescales: the time taken for the cloud shock to cross the cloud and the evolutionary timescale of the SNR. If the former is much smaller than the latter, the cloud is likely to be destroyed. However if the reverse is true, then the shocked cloud will survive and be further accelerated as a consequence of the viscous drag of the expanding hot interior. *Clouds accelerated in such a manner will however suffer substantial evaporation due to heat conduction from the hot gas inside the SNR.* Partial fragmentation could further reduce the size of the cloud. For detailed calculation and discussion we refer to McKee & Cowie (1975); Woodward (1976); McKee, Cowie & Ostriker (1978); Cowie, McKee & Ostriker (1981) and a more recent paper by Klein, McKee & Woods (1995).

To summarize the above discussion, in our opinion the shocked cloud scenario has all the ingredients needed to explain the observational trends. In particular it would explain why the high velocity clouds seen so clearly in optical and UV absorption lines do not manifest themselves in HI observations. But this observation is predicated on the conjecture that the higher velocity clouds are not only warmer, but have smaller column densities. There is certainly an indication of this from optical and UV absorption studies. To recall, in UV observations which are sensitive to much smaller column densities than optical studies, the higher velocity absorption features are more pronounced. But it would be desirable to quantify the correlation between velocity and column densities. Reliable column densities are difficult to obtain from optical observations because of blending of lines and also depletion onto grains. The column densities derived from UV observations are also uncertain because of the effects of saturation of the lines. In view of these difficulties it would be rewarding to do a more systematic and much more sensitive HI absorption study, supplemented by emission studies.

References

Adams, W. A. 1949, *Astrophys. J.,* **109**, 131,354.
Blaauw, A. 1952, *Bull. Astr. Inst. Netherland,* **11**, 459.
Blaauw, A., Tolbert, C. R. 1966, *Bull Astr. Inst. Netherland,* **18**, 405.
Brand, J., Blitz, L. 1993, *Astr.Astrophys.,* **275**, 67.
Burton, W.B.1985, *Astr.Astrophys.Suppl.*, **62**, 365.
Cowie, L. L., McKee, C. F, Ostriker, J. P. 1981, *Astrophys. J.,* **247**, 908.
Cowie, L. L, York, D. G. 1978, *Astrophys. 1,* **223**, 876.
Danly, L., Lockman, F., Meade, M. R., Savage, B. D. 1992, *Astrophys. J. Suppl,* **81**, 125.
Habing, H. J. 1968, *Bull Astr. Inst. Netherland,* **20**, 120.
Habing, H.J.1969,*Bull.Astr. Inst. Netherland,* **20**, 171.
Hobbs, L. M. 1984, *Astrophys. J. Suppl,* **56**, 315.
Klein, R. I., McKee, C. F., Woods, D. T. 1995, in *The Physics of the InterstellarMedium and Intergalactic Medium* eds. A. Ferrara, C. F. McKee, C. Heiles, R R. Shapiro, ASP Conf. Ser. , Vol. 80.
Martin, E. R, York, D. G. 1982, *Astrophys. J.*, **257**, 135.
McKee, C. F., Cowie, L. L. 1975. *Astrophys. J.,* **195**, 715.
McKee, C. F., Cowie; L. L., Ostriker, J. P. 1978, *Astrophys. J. (Lett.),* **219**, L23.
Munch, G. 1957, *Astrophys. J.,* **125**, 42.
Münch, G., Zirrin, H. 1961, *Astrophys. J.,* **133**, 11.
Oort, J. H., Spitzer, L. 1955, *Astrophys. J.,* **121**, 6.
Radhakrishnan,V, Sarma,N.V.G.1980, *Astr.Astrophys.,* **85**, 249.
Radhakrishnan,V., Srinivasan,G. 1980, *J.Astrophys. Astr.,* **1**, 47.
Rajagopal, J., Srinivasan, G., Dwarakanath, K. S. 1998, *J. Astrophys.Astr,* 1998, **19**, 00-00 (Paper I).
Routly, P. M., Spitzer, L. Jr. 1952, *Astrophys. J.,* **115**, 227.
Schwarz, U. J., Ekers, R. D., Goss, W. M. 1982, *Astrophys. J.,* **110**, 100.
Schlüter A., Schmidt, H., Stumpf, P. 1953, Z *Ap.,* **33**, 194.
Sembach, K. R, Danks, A. C, Savage, B. D. 1993, *Astrophys. J. Suppl. Ser,* **100**, 107.
Siluk, R. S., Silk, J. 1974, *Astrophys. J.,* **192**, 51.
Slavin, J. D. Cox, D. P. 1993, *Astrophys.J.,* **417**, 187.
Spitzer, L. Jr. 1978, *Physical Processes in the Interstelllar Medium* (New York: Wiley-Interscience).
Spitzer, L. Jr. 1990, *Ann.Rev.Astr.Astrophys.,* **28**,71.
Spitzer, L. Jr. Fitzpatrick, E. L. 1993, *Astrophys. J.,* **409**, 299.
Welty, D. E., Morton, D. C, Hobbs, L. M. 1996, *Astrophys. J. Suppl,* **106**, 533.
Woodward, P. R. 1976, *Astrophys. J.,* **207**, 484.

J. Astrophys. Astr. (1998) **19,** 133–139

Quantum Fluctuations in Radiation Dominated Anisotropic Cosmology*

Thant Zin Naing[1] & J. V. Narlikar, *Inter-University Centre for Astronomy and Astrophysics*, *Post Bag 4* , *Pune 411 007*, *India*

Received 1998 December 8; accepted 1999 February 20

Abstract. Using the metric conformal transformation and simple path integral, Feynman propagator method, for computing its quantum fluctuations, we analyse the radiation dominated anisotropic Bianchi Type I cosmology. We proceed to show that the quantum conformal fluctuations diverge at the classical spacetime singularity, suggesting that a singularity free solution can exist in anisotropic cosmology in the quantum regime.

Key words. Quantum cosmology—quantum fluctuations—spacetime singularity.

1. Introduction

Quantum conformal fluctuations are supposed to play a fundamental role in the evolution and dynamics of the early universe. Narlikar (1978, 1979, 1981, 1984) had shown that the conformal degrees of freedom in metric can be quantized and that the procedure leads to the fluctuations around the solutions of the classical Einstein field equations. As the state of classical singularity is approached the quantum uncertainty diverges and within the range of quantum uncertainty non-singular final states are possible.

One of the simplest models of an anisotropic universe that describes a homogeneous and spatially flat universe is the Bianchi Type I Cosmology. Unlike the FRW model which has the same scale factor for each of the three spatial directions, the Bianchi Type I Cosmology has a different scale factor in each direction, which produces an anisotropy in expansion (Sahni 1988; Saha & Shikin 1997). Narlikar (op. cit.) had shown that the quantum conformal fluctuations of a dust driven model diverge at the spacetime singularity. The purpose of the present paper is to extend our study to quantum conformal fluctuations of radiation dominated universes which may probably be taken as much more realistic, since like the FRW models the Bianchi model is expected to be radiation driven rather than dust driven, near the classical singularity. We shall also investigate the behavior of conformal fluctuations in a radiation dominated cosmology and use the Feynman path integral method to compute the probability amplitudes.

This paper is organized as follows. In section 2 a brief account of the path integral approach to the study of conformal fluctuations is given. In section 3, the classical

* Since the December 1998 issue of this journal was delayed, we were able to include this paper in this issue.

[1] Permanent Address: Physics Department, Yangon University, Myanmar.

solution of a radiation dominated anisotropic Bianchi Type I cosmology is computed. In section 4 applications of the quantum conformal analysis of anisotropic Bianchi Type I Cosmology are discussed. The last section is devoted to the concluding remarks of our study.

2. The path integral and conformal degrees of freedom

One of the most tractable approaches to quantum gravity is via the Feynman path integral. The classical Einstein field equations are

$$R_{ik} - \frac{1}{2} g_{ik} R = -\frac{8\pi G}{c^4} T_{ik}, \tag{1}$$

where R is the scalar curvature, R_{ik} the Ricci tensor, g_{ik} the metric tensor, G the gravitational constant and c is the speed of light. In the path integral approach a unique geometry $\mathcal{G}$ obtained as the solution of (1) is replaced by a variety of geometries $\mathcal{G}$ which should be possible with specified end conditions. One treats each geometry as a path or 'history' with a probability amplitude (Feynman and Hibbs 1965),

$$\exp \frac{iS[\mathcal{G}]}{\hbar}$$

where S = classical action computed for geometry $\mathcal{G}$ $\hbar$ = Planck's constant. In the notation of 3-Geometries $\mathcal{G}$, the probability amplitude is provided by,

$$K[\mathcal{G}_2, \Sigma_2; \mathcal{G}_1, \Sigma_1] = \int \exp\left[\frac{i}{\hbar} S[\mathcal{G}]\right] \mathcal{D}\mathcal{G}, \tag{2}$$

here Σ_1 and Σ_2 are two spacelike hypersurfaces, $\mathcal{G}$ and $\mathcal{G}_2$ are three geometries and $\mathcal{D}\mathcal{G}$ is the measure of the integral on the right hand side. K is the quantum mechanical propagator. As was pointed out by DeWitt (1976), the conformal degrees of freedom provide a simple subset of all possible geometries. Suppose one denotes by an overbar the solution of the classical Einstein equations and writes a 'nonclassical' metric conformal tensor as

$$g_{ik} = (1 + \phi)^2 \bar{g}_{ik}, \tag{3}$$

where ϕ is a scalar function of the spacetime coordinates. The Hilbert action principle is given by,

$$S = \frac{c^3}{16\pi G} \int R\sqrt{-g}\,\mathrm{d}^4x + S_m, \tag{4}$$

where R = scalar curvature, g= determinant of g_{ik}, while S_m denotes the action of matter (and radiation) which gives rise to the energy momentum tensor in equation (1). From equations (3) and (4), one has,

$$\int R\sqrt{-g}\,\mathrm{d}^4x \sim \int [(1 + \phi)^2 \bar{R} - 6\phi_i \phi^i]\sqrt{-\bar{g}}\,\mathrm{d}^4x. \tag{5}$$

(The ~ indicates that the surface terms have been ignored. R, g refer to the classical solution.) The problem of computation of K can now be restated in the following form,

$$K[\phi_2, \Sigma_2; \phi_1, \Sigma_1] = \sum \exp \frac{i}{\hbar}\left(S_m + \frac{c^3}{16\pi G}\int [(1+\phi)^2 \bar{R} - 6\phi_i \phi^i]\sqrt{-\bar{g}}\,\mathrm{d}^4x\right) \tag{6}$$

The action of matter is given by

$$S_m = -\sum_a \int m_a ds_a, \tag{7}$$

where m_a = mass of ath particle and ds_a, the element of its propertime. If we assume that the universe is homogeneous, and continues to be so despite conformal fluctuations, then ϕ has only the time derivative. In the case of radiation dominated anisotropic cosmology, the curvature term vanishes simply because of the cancellation of trace in the stress tensor, and the matter term also vanishes (no massive particles exist). Then, the above equation (6) becomes,

$$K[\phi_2, \Sigma_2; \phi_1, \Sigma_1] = \sum \exp\left(\frac{3ic^3}{8\pi G\hbar}\int -\dot{\phi}^2\sqrt{-\bar{g}}d^4x\right). \tag{8}$$

If we integrate out the spatial part of equation (8),we get the 3-volume $\mathcal{V}$of the space and are left with only a one-dimensional path integral. We next apply these results to the Bianchi Type I model. Since we wish to explore the effect of quantum gravity, the model refers to the very early (near the spacetime singularity) universe when it was radiation dominated. We will consider such a model in the classical region first.

3. Radiation dominated anisotropic Bianchi Type I cosmology

The classical solution in this case is given by the line element,

$$\mathrm{d}s^2 = \mathrm{d}t^2 - X^2(t)(\mathrm{d}x)^2 - Y^2(t)(\mathrm{d}y)^2 - Z^2(t)(\mathrm{d}z)^2 \tag{9}$$

where X, Y and Z are functions of time only. The Einstein equations for $X(t)$, $Y(t)$ and $Z(t)$ corresponding to the metric can be written as

$$\left(T_1^1 - \frac{1}{2}T\right) = \frac{\ddot{X}}{X} + \frac{\dot{X}}{X}\left(\frac{\dot{Y}}{Y} + \frac{\dot{Z}}{Z}\right) = -\frac{8\pi\rho}{3}, \tag{10}$$

$$\left(T_2^2 - \frac{1}{2}T\right) = \frac{\ddot{Y}}{Y} + \frac{\dot{Y}}{Y}\left(\frac{\dot{Z}}{Z} + \frac{\dot{X}}{X}\right) = -\frac{8\pi\rho}{3}, \tag{11}$$

$$\left(T_3^3 - \frac{1}{2}T\right) = \frac{\ddot{Z}}{Z} + \frac{\dot{Z}}{Z}\left(\frac{\dot{X}}{X} + \frac{\dot{Y}}{Y}\right) = -\frac{8\pi\rho}{3}, \tag{12}$$

$$\left(T_0^0 - \frac{1}{2}T\right) = \frac{\ddot{X}}{X} + \frac{\ddot{Y}}{Y} + \frac{\ddot{Z}}{Z} = 8\pi\rho, \tag{13}$$

since $T_k^i = 8\mathrm{p}\pi\left(\rho, -\frac{\rho}{3}, -\frac{\rho}{3}, -\frac{\rho}{3}\right)$ and we take $c = G = 1$. From the continuity equations we have $T^i_{k;i} = 0$, hence $\rho\tau^{\frac{4}{3}}$ = constant, where $\tau = XYZ = \sqrt{-\bar{g}}$ From

Equations (10), (11) and (12) we have

$$\frac{X}{Y} = D_1 \exp\left(A_1 \int \frac{\mathrm{d}t}{\tau}\right), \tag{14}$$

$$\frac{Z}{Y} = D_2 \exp\left(A_2 \int \frac{\mathrm{d}t}{\tau}\right), \tag{15}$$

$$\frac{Z}{X} = D_3 \exp\left(A_3 \int \frac{\mathrm{d}t}{\tau}\right), \tag{16}$$

where D_1, D_2, D_3 and A_1, A_2, A_3 are constants . There are functional relations such that $D_2 = D_1 D_3, A_2 = A_1 + A_3$. Inserting equations (14), (15) and (16) into (13) gives us

$$\frac{\ddot{\tau}}{\tau} - \frac{2}{3}\left(\frac{\dot{\tau}}{\tau}\right)^2 + \frac{2}{3}\frac{C}{\tau^2} = -\kappa\rho, \tag{17}$$

where $C = A_1^2 + A_3 A_3^2$. For simplicity, we change the constant $\frac{2}{3} C$ into B and since $\kappa\rho\tau^{\frac{4}{3}}$ = constant, we denote this constant by A. Equation (17) now becomes,

$$\frac{\ddot{\tau}}{\tau} - \frac{2}{3}\left(\frac{\dot{\tau}}{\tau}\right)^2 + \frac{B}{\tau^2} + \frac{A}{\tau^{4/3}} = 0. \tag{18}$$

To solve the above differential equation, we use the conformal time coordinate,

$$\eta = \int \frac{\mathrm{d}t}{\tau(t)}, \text{ i.e, } \dot{\eta} = \frac{\mathrm{d}\eta}{\mathrm{d}t} = \frac{1}{\tau}. \tag{19}$$

The first and second derivatives of τ with respect to time t are,

$$\dot{\tau} = \frac{\mathrm{d}\tau}{\mathrm{d}\eta}\frac{\mathrm{d}\eta}{\mathrm{d}t} = \frac{\tau'}{\tau}, \tag{20}$$

$$\ddot{\tau} = \frac{\mathrm{d}\eta}{\mathrm{d}t}\frac{\mathrm{d}\dot{\tau}}{\mathrm{d}\eta} = \frac{1}{\tau}\left(\frac{\tau''}{\tau} - \frac{\tau'^2}{\tau^2}\right), \tag{21}$$

where $'$ denotes the differentiation with respect to η. Putting equations (20) and (21) into equation (18) gives us

$$\begin{aligned} &\frac{\tau''}{\tau^3} - \frac{5}{3}\frac{\tau'^2}{\tau^4} + \frac{B}{\tau^2} + \frac{A}{\tau^{4/3}} = 0, \quad \text{or} \\ &\tau''\tau - \frac{5}{3}\tau'^2 + B\tau^2 + A\tau^{8/3} = 0. \end{aligned} \tag{22}$$

Using the simple calculus one can show that the general solution to equation (22) is given by,

$$\tau^{-2/3} = \alpha e^{a\eta} + \beta e^{-a\eta} - \frac{A}{B}, \tag{23}$$

Here $\frac{A}{B}$ and, $a = \sqrt{\frac{2B}{3}}$ are constants. α and β are arbitrary constants. It is clear that whatever we choose for α and β the volume factor τ goes to zero at some stage. Thus singularity is inevitable. We want the asymptotic nature of the solution close to the singularity. Rewrite (23) as

$$\tau^{-2/3} = p\sinh(a\eta) + q\cosh(-a\eta) - \frac{A}{B}, \tag{24}$$

where p, q are arbitrary constants. Now look for the limit as $\eta \to -\infty$ and the asymptotic solution is given by,

$$\tau^{-2/3} \sim \frac{p}{2} e^{-a\eta}. \tag{25}$$

This is the relation between the scale factor and the conformal time coordinate close to the spacetime singularity ($\tau \to 0$) of the classical solution.

Hence, we have

$$a\eta = \text{const.} + \frac{2}{3}\ln\tau. \tag{26}$$

Since $= \dot{\eta} = \frac{1}{\tau}$, we have

$$t = \left(\frac{p}{2}\right)^{-\frac{3}{2}} \int e^{\frac{3}{2}a\eta} \mathrm{d}\eta. \tag{27}$$

Then, the conformal time for radiation dominated Bianchi Type I cosmology is given by,

$$\eta \sim \text{const.} + \frac{2}{3a}\ln t. \tag{28}$$

As described in section 2, the action functional for the radiation dominated cosmology is

$$S = -\frac{c^3}{16\pi G}\int 6\phi_i\phi^i\sqrt{-\bar{g}}\,\mathrm{d}^4x = -\frac{3c^3\mathcal{V}}{8\pi G}\int \dot{\phi}^2\tau(t)\mathrm{d}t. \tag{29}$$

Using the standard path integral techniques, the probability amplitude for the conformal fluctuations to evolve from ϕ_1 at $t = t_1$ to f_2 at $t = t_2$ is given by,

$$K[\phi_2, t_2; \phi_1, t_1] = \int \exp\left(-\frac{3\mathcal{V}i}{8\pi}\int \dot{\phi}^2\tau(t)\mathrm{d}t\right)\mathcal{D}\phi, \tag{30}$$

where we take $c = 1$, $G = 1$ and $\hbar = 1$ and $D\phi$ = measure of the integration (for details see Feynman and Hibbs 1965). Using the fact that $t = t(\eta)$ and $\phi = (\mathrm{d}\phi/\mathrm{d}\eta) \times (\mathrm{d}\eta/\mathrm{d}t) = \phi'\dot{\eta}$, we get

$$\int \dot{\phi}^2\tau(t)\mathrm{d}t = \int \phi'^2\dot{\eta}\tau(t)\mathrm{d}\eta = \int \phi'^2\mathrm{d}\eta \tag{31}$$

Now the propagator (30) can be written as

$$\begin{aligned} K[\phi_2, \eta_2; \phi_1, \eta_1] &= \int \exp\left(-\frac{3\mathcal{V}i}{8\pi}\int_{\eta_1}^{\eta_2} \phi'^2\mathrm{d}\eta\right)\mathcal{D}\phi \\ &= \frac{8\pi^2(\eta_2 - \eta_1)}{3\mathcal{V}}\exp\left(-\frac{3\mathcal{V}i(\phi_2 - \phi_1)^2}{8\pi(\eta_2 - \eta_1)}\right). \end{aligned} \tag{32}$$

It is more interesting to apply the above propagator to study the evolution of the wavefunction of the universe. We have,

$$\Psi(\phi_2, \eta_2) = \int K[\phi_2, \eta_2; \phi_1, \eta_1]\Psi(\phi_1, \eta_1)\mathrm{d}\phi_1, \tag{33}$$

which connects the wavefunction at epoch h1 to the wavefunction at epoch η_2.

Normally this technique is used to compute the probability amplitude for evolution of a wavefunction *forward* in time. Thus we normally have $t_2 > t_1$. Here, however, we use the Feynman propagator *backward* in time to compute the probability amplitude for the wavefunction to have evolved from a state ϕ_2 to a state ϕ_1 i.e. $t_2 < t_1$. This technique was used by Narlikar (1981) for estimating the probable range of states at an earlier epoch t_2 from which the universe could have evolved to its present state ϕ_1 at time t_1. Since the present state is very nearly classical, an appropriate expression for Ψ (ϕ_1, η_1) is a Gaussian wavepacket,

$$\Psi(\phi_1, \eta_1) = (2\pi\Delta_1^2)^{-1/4} \exp\left(-\frac{\phi_1^2}{4\Delta_1^2}\right). \tag{34}$$

Using (32) and (34) one can easily compute $\Psi(\phi_2, \eta_2)$. The early state was also a Gaussian wavepacket but its spread Δ_2 was much larger:

$$\Delta_2{}^2 = \Delta_1{}^2 + \frac{4\pi^2(\eta_2 - \eta_1)^2}{9\mathcal{V}^2\Delta_1{}^2}, \tag{35}$$

hence, since $\Delta_1 \ll 1$ and from equation (28), we get

$$\begin{aligned}\Delta_2 &\approx \frac{2\pi}{3\mathcal{V}\Delta_1}(\eta_2 - \eta_1) \\ &= \frac{4\pi}{9a\mathcal{V}\Delta_1}\ln\left(\frac{t_2}{t_1}\right).\end{aligned} \tag{36}$$

Thus Δ_2 diverges logarithmically as $t_2 \longrightarrow 0$. That is, close to the classical singularity, the quantum uncertainty diverges—a result found for dust dominated Bianchi Type I cosmologies also. This uncertainty therefore permits us to obtain non-classical non-singular solutions around the classical singular epoch, suggesting that a singularity free solution can exist in anisotropic radiation dominated cosmology in the quantum regime.

5. Concluding remarks

In the previous papers (Narlikar 1978, 1979, 1981, 1984), the quantum conformal fluctuations in a collapsing dust ball, the Schwarzschild spacetime and the Bianchi Type I dust dominated cosmology were investigated (see also Narlikar & Padmanabhan 1986). In the present paper we confined ourselves to radiation dominated anisotropic Bianchi Type I cosmology. The classical solution (relation between scale factor and conformal time) has been calculated and using this relation, quantum conformal fluctuations in the radiation dominated Bianchi Type I cosmology are obtained. The quantum dispersion diverges as $t_2 \longrightarrow 0$ (the classical

singular epoch) and it indicates that quantum fluctuations dominate as the classical solution approaches singularity. The classical solution thus ceases to be reliable, and non-singular finite solutions can be found if one enlarges the theory to include these conformal effects of quantum gravity. In our future investigations we shall be concerned with non-conformal fluctuations of the classical solution.

Acknowledgements

One of us (T.Z.N.) would like to express his gratitude to IUCAA for the hospitality and financial support which he received during his stay at IUCAA.

References

De Witt, B. 1976, *Ann. Phys.*, **97**, 307.
Feynman, R. P., Hibbs, A. R. 1965, *Quantum Mechanics and Path Integrals* (New York: McGraw-Hill).
Narlikar, J. V. 1978, *Mon. Not. R. Astr. Soc*, **183,** 159.
Narlikar, J. V. 1979, *Gen. Rel. Gra.*, **10**, 883.
Narlikar, J. V. 1981, *Found. Phys.*, **11,** 473.
Narlikar, J. V. 1984, *Found. Phys.*, **14**, 443.
Narlikar, J. V. Padmanabhan, T. 1986, *Gravity*, *Gauge Theory and Quantum Cosmology* (Dordrecht: D Reidel).
Saha, B., Shikin, G. N. 1997, *Class. Quan. Grav.*, **29**, 1099.
Sahni, V. 1988, *Class. Quan. Grav.*, **5**, L113.

J. Astrophys. Astr. (1998) **19,** 141–146

Nonconformal Fluctuations in Radiation Dominated Anisotropic Cosmology*

Thant Zin Naing[1] & J. V. Narlikar, *Inter-University Centre for Astronomy and Astrophysics*, *Post Bag 4*, *Pune 411 007*, *India.*

Received 1999 February 3; accepted 1999 March 2

Abstract. Using simple path integral, Feynman propagator method and the relation between conformal time η and scale factor τ, we investigate the non-conformal quantum fluctuations (of expansion and shear) and axisymmetric singularity case in radiation dominated anisotropic cosmology. We show that near the classical singularity the quantum fluctuations tend to diverge.

Key words. Quantum Cosmology—Anisotropic universes.

1. Introduction

It has been recently claimed that (Keifer *et al.* 1998) the epoch of the origin of the universe can be traced back to unavoidable fluctuations of some scalar field ϕ. As a consequence, these fluctuations, together with scalar fluctuations in the metric, are expected to lead to anisotropies in the cosmic background radiation. One would also expect that there are gravitational waves originating from tensor fluctuations in the metric. It is also generally assumed (Ellis and Wainwright 1997) that the quantum gravity epoch, occurred before the Planck epoch. Prior to this epoch the effects of classical general relativity may not be taken to be valid (Narlikar 1978, 1979, 1981, 1984). In an earlier paper (Naing & Narlikar 1998, hereafter Paper I) we had studied the quantum conformal fluctuations of radiation dominated Bianchi Type I models. This paper extends that work further to non-conformal fluctuations.

The Bianchi Type I models are the simplest anisotropically expanding cosmological models. As in the isotropic Friedmann models here too the universe is expected to be radiation dominated in the early epochs (close to $t = 0$). In this paper we shall therefore be concerned with the Bianchi Type I radiation dominated cosmology for our study of non-conformal quantum fluctuations. In section 2 we will give a brief account of the asymptotic behavior of our result obtained in Paper I. In section 3, applying the Feynman path integral method to Gaussian wavepackets describing non-conformal fluctuations (i.e., including expansion and shear) of these models we will show that classical singularity is made very unlikely. In section 4 an axisymmetric singularity case will be considered. The concluding remarks will be given in section 5.

* Since the December 1998 issue of this journal was delayed, we were able to include this paper in this issue.

[1] Permanent address: Physics Department, Yangon University, Myanmar.

2. Classical asymptotic solution for radiation dominated Bianchi Type I cosmology

One of the advantages of using the path integral method is that the Lagrangian density is *a scalar* quantity (Kashiwa *et al* 1997) that can be handled more simply than the Hamiltonian behaving as *a vector*, and that, symmetries in a system are simply incorporated in terms of *the classical Lagrangian.* Dealing with dynamical and curved spacetime is also conceptually easier with this approach. The use of the path integral method in quantum gravity is now well established and very common in literature. In our previous paper the notation we used for the probability amplitude or propagator K was

$$K[\mathcal{G}_2, \Sigma_2 : \mathcal{G}_1, \Sigma_1] = \int \exp\left[\frac{iS(\mathcal{G})}{\hbar}\right] \mathcal{D}\mathcal{G}, \tag{1}$$

where Σ_1 and Σ_2 are two spacelike hypersurfaces, $\mathcal{G}_1$, $\mathcal{G}_2$ three geometries, $S(\mathcal{G})$ the classical action computed for geometry $\mathcal{G}$, Planck's constant, and $\mathcal{D}\mathcal{G}$ the measure of the integration on the right hand side. This formal expression for K becomes considerably simplified in the case of homogeneous cosmologies. In our case K can even be explicitly evaluated. The classical solution for the anisotropic Bianchi Type I cosmology is given by the line element,

$$\mathrm{d}s = \mathrm{d}t^2 - X^2(t)\,(\mathrm{d}x)^2 - Y^2(t)\,(\mathrm{d}y)^2 - Z^2(t)\,(\mathrm{d}z)^2 \tag{2}$$

where X, Y and Z are functions of time only.
The 'non-classical' metric conformal tensor (DeWitt 1976) can be written as,

$$g_{ik} = (1+\phi)^2 \bar{g}_{ik}, \tag{3}$$

where g_{ik} is non-classical metric tensor, and g_{ik} classical metric tensor. The scalar ϕ, a function of the spacetime coordinates denotes the conformal fluctuation of the metric. The Hilbert Einstein action principle is given as,

$$S = \frac{c^3}{16\pi G}\int R\sqrt{-\bar{g}}\,\mathrm{d}^4x + S_m, \tag{4}$$

where R is the scalar curvature of the spacetime, c the speed of light, g the determinant of the metric g_{ik} while S_m denotes the action of the matter term. Making use of equations (4), (3), (2) in (1) gives,

$$K[\phi_2, \Sigma_2; \phi_1, \Sigma_1] = \sum \exp\left(\frac{3ic^3}{8\pi G\hbar}\int -\dot{\phi}^2\sqrt{-\bar{g}}\,\mathrm{d}^4x\right). \tag{5}$$

In getting the above equation, we assume that, in our case of radiation dominated cosmology, both the curvature term and the matter action term vanish or are negligible. It has been shown elsewhere (Saha *et al* 1997, also Paper I) that the second order differential equation for the expansion scale factor $\tau = XYZ = \sqrt{-\bar{g}}$ can be given as,

$$\frac{\tau''}{\tau^3} - \frac{5}{3}\frac{\tau'^2}{\tau^4} + \frac{B}{\tau^2} + \frac{A}{\tau^4/3} = 0,$$

or,

$$\tau''\tau - \frac{5}{3}\tau'^2 + B\tau^2 + A\tau^{8/3} = 0. \tag{6}$$

where $'$ denotes the differentiation with respect to η. A, B are constants. We use the conformal time coordinate,

$$\eta = \int \frac{\mathrm{d}t}{\tau(t)}, \quad \text{i.e,} \quad \dot{\eta} = \frac{\mathrm{d}\eta}{\mathrm{d}t} = \frac{1}{\tau}. \tag{7}$$

Using simple calculus we can show that the general solution of the equation (6) is given as,

$$\tau^{-2/3} = p\sinh(a\eta) + q\cosh(a\eta) - \frac{A}{B}, \tag{8}$$

where p, q are arbitrary constants. Now look for the limit as $\eta \to -\infty$ and the asymptotic solution is given by,

$$\tau^{-2/3} \sim \frac{p}{2}e^{-a\eta}. \tag{9}$$

This is the relation between the scale factor and the conformal time coordinate close to the spacetime singularity($\tau \longrightarrow 0$) of the classical solution. From equation (7), $\dot{\eta} = 1/\tau$, and we have,

$$\eta \sim \text{const.} + \frac{2}{3a}\ln t. \tag{10}$$

The above relation will be used in our next sections for computing the diffusion of Gaussian wavepackets.

3. Nonconformal fluctuations in radiation dominated anisotropic cosmology

The Bianchi Type I cosmology is characterized by two properties, namely, shear and expansion. In Paper I, quantum fluctuations in the expansion (scale factor) τ (t) or (η) were dealt with using the conformal techniques. To deal with the shear fluctuations we have to use a different technique. We will follow the transformations used by Misner (1972). One defines

$$X = e^{\xi+\zeta+\sqrt{3}\lambda}; \quad Y = e^{\xi+\zeta-\sqrt{3}\lambda};$$
$$Z = e^{\xi-2\zeta}; \quad \tau = XYZ = \sqrt{-\bar{g}} = e^{3\xi}, \tag{11}$$

where ξ, ζ and λ are functions of time. In our Paper I, we took into consideration the fluctuation of ξ, that is, only the expansion part. We will now consider the fluctuations in ζ and λ while ξ is kept at its classical value. Ignoring the surface term, the action functional integral over a 3-volume $\mathcal{V}$ now takes the form,

$$S \sim -\frac{3\mathcal{V}}{8\pi}\int_{t_1}^{t_2} e^{3\bar{\xi}}(\dot{\xi}^2 - \dot{\zeta}^2 - \dot{\lambda}^2)\mathrm{d}t$$

$$\sim -\frac{3\mathcal{V}}{8\pi}\int_{t_1}^{t_2}\tau(\eta)(-\dot{\zeta}^2-\dot{\lambda}^2)\mathrm{d}t, \tag{12}$$

where the ξ term does not produce any variable quantity and has been ignored. But, ζ and λ are functions of time (conformal time), hence

$$-(\dot{\zeta}^2+\dot{\lambda}^2)\mathrm{d}t = -(\zeta'^2+\lambda'^2)\dot{\eta}\,\mathrm{d}\eta$$

and $\dot{\eta} = 1/\tau$. Here $'$ denotes the differentiation with respect to η and, we have from (12)

$$S = \frac{3\mathcal{V}}{8\pi}\int_{\eta_1}^{\eta_2}(\zeta'^2+\lambda'^2)\,\mathrm{d}\eta. \tag{13}$$

The propagator (for details see Feynman and Hibbs 1965) for action (13) is,

$$K[\zeta_2,\lambda_2,\eta_2;\zeta_1,\lambda_1,\eta_1] = \int\int \exp\left[\frac{3i\mathcal{V}}{8\pi}\int_{\eta_1}^{\eta_2}(\zeta'^2+\lambda'^2)\mathrm{d}\eta\right]\mathcal{D}\zeta\mathcal{D}\lambda. \tag{14}$$

The solution of the above integral is,

$$K[\zeta_2,\lambda_2,\eta_2;\zeta_1,\lambda_1,\eta_1] = -\frac{8\pi^2}{3\mathcal{V}}(\eta_2-\eta_1)\exp 3i\mathcal{V}\left(\frac{(\zeta_2-\zeta_1)^2+(\lambda_2-\lambda_1)^2}{8\pi(\eta_2-\eta_1)}\right). \tag{15}$$

We now apply the above propagator to study the evolution of the wavefunction of the universe. We have,

$$\Psi(\phi_2,\eta_2) = \int K[\phi_2,\eta_2;\phi_1,\eta_1]\Psi(\phi_1,\eta_1)\mathrm{d}\phi_1, \tag{16}$$

which connects the wavefunction at epoch η_1 to the wavefunction at epoch η_2.

Normally this technique is used to compute the probability amplitude for evolution of a wavefunction *forward* in time. Thus we normally have $t_2 > t_1$. Here, however, we use the Feynman propagator *backward* in time to compute the probability amplitude for the wavefunction to have evolved from a state ϕ_2 to a state ϕ_1 i.e. $t_2 < t_1$. This technique was used by Narlikar (1981) for estimating the probable range of states at an earlier epoch t_2 from which the universe could have evolved to its present state ϕ_1 at time t_1 . Since the present state is very nearly classical, an appropriate expression for $\Psi(\phi_1, \eta_1)$ is a Gaussian wavepacket (expressed in the η-time coordinate),

$$\Psi(\phi_1,\eta_1) = (2\pi\Delta_1^2)^{-1/4}\exp\left(-\frac{\phi_1^2}{4\Delta_1^2}\right). \tag{17}$$

The wavepacket moves in the (ζ, λ) plane with the constant velocity $(\bar{\lambda}', \bar{\zeta}')$ and at the same time diffuses so that its dispersion at $\eta = \eta_2$ is Δ_2, where,

$$\Delta_2{}^2 = \Delta_1{}^2 + \frac{4\pi^2(\eta_2-\eta_1)^2}{9\mathcal{V}^2\Delta_1{}^2}. \tag{18}$$

In our case of the radiation dominated cosmology with the conformal time η given by equation (10) and, since $\Delta_1 \ll 1$, we get,

$$\Delta_2 \approx \frac{2\pi}{3\mathcal{V}\Delta_1}(\eta_2 - \eta_1)$$
$$= \frac{4\pi}{9a\mathcal{V}\Delta_1}\ln\left(\frac{t_2}{t_1}\right). \tag{19}$$

Thus, as in our previous case, Δ_2 diverges logarithmically as $t_2 \to 0$. In the case of the dust driven universe (Narlikar 1979) the dispersion Δ_2 is found to be,

$$\Delta_2 \approx \frac{4\pi}{27M\Sigma V\Delta_1}|\ln t_2|, \tag{20}$$

where M, Σ are constants > 0 and Δ_2 will diverge as $t_2 \longrightarrow 0$.

4. Axisymmetric singularity case

It is also interesting to examine whether a similar divergence of quantum uncertainty occurs in the axisymmetric case of radiation dominated cosmology. One of the possible methods to deal with the axisymmetric case with $X(t) = Y(t)$ is as follows. Define,

$$\alpha(t) = \tfrac{1}{2}\sqrt{X}(X+Z), \quad \beta(t) = \tfrac{1}{2}\sqrt{X}(X-Z). \tag{21}$$

where, α and β are functions of time.

The action functional for the radiation dominated universe becomes,

$$S \sim -\frac{\mathcal{V}}{6\pi}\int(\dot{\alpha}^2 - \dot{\beta}^2)\tau(t)\,\mathrm{d}t. \tag{22}$$

Since both α and β are functions of time η, we have

$$(\dot{\alpha}^2 - \dot{\beta}^2)\mathrm{d}t = (\alpha'^2 - \beta'^2)\dot{\eta}\,\mathrm{d}\eta,$$

and, the propagator K for the equation (22) is,

$$K[\alpha_2, \beta_2, \eta_2; \alpha_1, \beta_1, \eta_1] = \int\int \exp\left[-\frac{i\mathcal{V}}{6\pi}\int_{\eta_1}^{\eta_2}(\alpha'^2 - \beta'^2)\mathrm{d}\eta\right]\mathcal{D}\alpha\mathcal{D}\beta. \tag{23}$$

The solution of the equation (23) is,

$$K[\alpha_2, \beta_2, \eta_2; \alpha_1, \beta_1, \eta_1] = \frac{6\pi^2}{\mathcal{V}}(\eta_2 - \eta_1)\exp -i\mathcal{V}\left(\frac{(\alpha_2-\alpha_1)^2 - (\beta_2-\beta_1)^2}{6\pi(\eta_2 - \eta_1)}\right). \tag{24}$$

In our present case, the dispersion in probability grows as,

$$\Delta_2{}^2 = \Delta_1{}^2 + \frac{9\pi^2}{4\mathcal{V}^2\Delta_1{}^2}(\eta_2 - \eta_1)^2. \tag{25}$$

The classical singularity here is identified with $t_2 \longrightarrow 0$. Using the equation (9), and since $\Delta_1 \ll 1$, we get

$$\Delta_2 = \frac{3\pi}{2\mathcal{V}\Delta_1}(\eta_2 - \eta_1)$$
$$= \frac{\pi}{a\mathcal{V}\Delta_1}\ln\left(\frac{t_2}{t_1}\right). \tag{26}$$

Here again, Δ_2 diverges logarithmically as time $t \longrightarrow 0$, i.e. as t approaches its classical singularity. This scenario is exactly the same when one of us (J.V.N.) investigated the case of axisymmetric singularity for a dust driven universe.

5. Concluding remarks

In this paper we have investigated the non-conformal fluctuations in radiation dominated cosmology using the simple path integral method and Gaussian wavepackets. Here we considered the quantum fluctuations in the shear part (ζ and λ), while the volume expansion ξ is kept at its classical value. We also carried out our investigation of the axisymmetric singularity case. In both cases, it has been found that the quantum fluctuations around the classical singularity, are divergent and as a consequence, non-singular and finite solutions can exist near the classical spacetime singularity (see also Narlikar & Padmanabhan 1986). These investigations show that in the early universe (radiation and dust driven epochs etc.) the quantum effects are much more pronounced and classical relativity cannot be taken to be valid.

Acknowledgements

One of us (T.Z.N.) would like to express his gratitude to IUCAA for the hospitality and financial support which he received during his stay at IUCAA. J.V.N, acknowledges the Homi Bhabha Research Professorship of the Department of Atomic Energy.

References

DeWitt,B.S.1976,*Ann.Phys.*, **97**, 307.
Ellis, G.F.R., Wainwright,J.1997, *Dynamical Systems in Cosmology* (Cambridge:CUP).
Feynman, R. P., Hibbs, A. R. 1965, *Quantum Mechanics and Path Integrals* (New York: McGraw-Hill).
Kashiwa, T.,Ohnuki, Y.,Suziki, M. 1997, *Path Integral Methods* (New York:Clarendon).
Keifer,C,Polarski, D.,Starobinski,A. 1998, *Int. J. Mod.Phys.*,**D7**, 455.
Misner, C. W. 1972, In *Magic Without Magic*, ed. J. R. Klauder (San Francisco: W. H. Freeman), p. 441.
Naing, T. Z., Narlikar, J. V. 1998, *J. Astrophys.Astr*, **19**, 133.
Narlikar, J. V. 1978, *Mon. Not. R. Astr. Soc*, **183**, 159.
Narlikar, *J* V. 1979, *Gen. Rel. Gra.*, **10**, 883.
Narlikar, J.V.1981, *Found. Phys.*,**11**,473.
Narlikar, J.V.1984, *Found.Phys.*, **14**, 443.
Narlikar, J. V., Padmanabhan, T. 1986, *Gravity*, *Gauge Theory and Quantum Cosmology* (Dordrecht: D. Reidel).
Sana, B., Shikin, G. N. 1997, *Class. Quan. Grav.*, **29**, 1099.